Synthesis and reactivity of high-valent copper complexes and the design of copper monooxygenase model complexes

A Dissertation

SUBMITTED TO THE FACULTY OF THE

UNIVERSITY OF MINNESOTA

BY

Caitlin J. Bouchey

IN PARTIAL FULFILLMENT OF THE REQUIREMENTS

FOR THE DEGREE OF

DOCTOR OF PHILOSOPHY

William B. Tolman, Advisor

February 2022

Acknowledgements

I would like to start by thanking my advisor, Bill Tolman. Bill provided me with many experiences to grow as a person and a scientist. Under Bill's tutelage, I was able to travel across the world to share my science and move a lab across the Midwest. Bill crafted a group dynamic in which I was able to find true and lasting friendship and I'll always be grateful for that. Thank you, Bill, for your mentorship and your support.

Speaking of the Tolman group, I am tremendously grateful to have had such wonderful, collaborative, and enjoyable colleagues. Truly, our group dynamic was my favorite part of graduate school. Dr. Hussnain Sajjad, Dr. Mahesh Krishnan, Dr. Appie Peterson, Dr. Dimitar Shopov, Prof. Megan Fieser, Emma Zhong, Peter Koetting, Tedd Wiessner, Dr. Wen Wu, Dr. Evanta Kabir, Dr. Leon Lillie, Dr. Justin Barry, thank you for many lengthy lab conversations, a tremendous amount of help with my research, and an abundance of fun outside of the lab. I am very thankful to the undergraduates that I was privileged enough to mentor: Yilenda Dong, Jack Klein, Dylan Bodner, and Aaron Gruen. And thank you to my mentor at Michigan State University, Dr. Tanner McDaniel. I wouldn't have succeeded in the lab without the training I received from him in my undergraduate research.

I would like to give special appreciation to my friends that contributed to my life in graduate school in significant ways. Dr. Courtney Elwell and Prof. Annie Luke, you two came into my life when I never knew I needed you. You both are so motivating, inspiring caring, and entertaining. I always have the best time of my life with you two and I am so grateful to know we'll keep having those times in the future. When I needed a family the most, the following five people (and a doggie) stepped up and took me in. Prof. Wilson Bailey, Cecily Ferguson, and India, our times spent together are amongst my most precious memories. Dr. Yanay Popowski, Adi Popowski, and Ben Popowski, I will be forever indebted to your generosity. To all these friends, thank you, I love you, and I miss you!

My family means the whole world to me. I owe everything to my mom, dad, Leigh, and Mike. These four have always had the utmost faith and trust in me to accomplish my goals, but that faith and trust are the only reasons I've been able to accomplish all that I have. Thank you for being the support system I need: you know, four parents are definitely

better than two. Madison and Campbell, my sisters, are two of my favorite people in this world. My heart wasn't whole until they entered in my life. My brothers, Cameron, Alec, Carson, and Justin couldn't be more different from each other. However, they do have one thing in common: driving my competitive spirit. Thank you, my brothers, because that spirit was necessary to get me through graduate school. I wouldn't have been able to finish this dissertation if it wasn't for y'all. My nieces and nephews, Braeden, Karter, Zander, and Millie simultaneously make me want to graduate, get a job, and be a role model for them AND make me want to quit everything just to spend all my time with them. I love you four with all my heart. The love my grandparents have for me makes me feel so special that I can only hope that I make them as proud. The unwavering love and support from my aunts, uncles, and cousins mean so much to me. Thank you all. 15 years of friendship with me deserves to be praised and I want David, Derek, and Ike to know how much it means to me. Thank you, guys, for always picking up right where we left off. And the Beaumier family, they have made me feel so loved over the past 8 years. I appreciate everything they have ever done for me and all our time together. I am so happy to have them in my life.

Mr. Peanutbutter, I love you Mr. Man. You make my heart swell every time I look at or even think about you. Thank you for being the sweetest boy with the loudest bark. Finally, Evan, you are my patient, intelligent, funny, kind, loving life partner. Thank you for helping me check in my glassware to my organic chemistry lab drawer all those years ago. Seriously, without that interaction I wouldn't be here right now. You have profoundly impacted my life. I knew from the beginning you were the one I wanted to spend my life with because you always made me want to be better: a better scientist, a better daughter, a better friend, a better fantasy football player, a better person. Everything is better when I'm with you. I can't wait to marry you.

Dedicated to my mom, dad, Leigh, Mike, and Evan

Abstract

Copper plays a vital role in various enzymatic and catalytic transformations. Specifically, copper-oxygen and high-valent copper species are implicated as intermediates in oxidations by metalloenzymes and catalysts. In order to study the nature and the role of copper in these transformations, copper model complexes have been sought after and investigated for their properties and reactivities. This thesis describes several such copper model complexes. Chapter 1 outlines the biological precedence of copper-oxygen complexes in a monooxygenase enzyme and a class of copper complexes that mimic the monooxygenase active site. Additionally, the literature relevant to high-valent copper complexes discussed herein is reviewed. In chapter 2, the development of two biomimetic, monoanionic ligands and their copper complexes is discussed. The characterization of the ligands and complexes and efforts to access copper-oxygen complexes bearing the monoanionic ligands are shown. Chapter 3 details the generation of a new high-valent copper-nitrite complex and its oxidative proton-coupled electron transfer (PCET) and anaerobic phenol nitration reactivity. Mechanistic considerations for the unusual anaerobic phenol nitration are made. Lastly, chapter 4 describes the synthesis and characterization of two copper-amidate complexes and the generation of their high-valent counterparts. The PCET reactivity of the high-valent copper-amidate complexes are contrasted with each other and previous high-valent copper-oxygen complexes. The results from the projects described herein provide insights into copper coordination chemistry, electronic structure, and reactivity, which helps augment the knowledge of copper enzymes and catalysts.

Table of contents

List of tables

List of figures and schemes

List of abbreviations

$AcFcBArF_{24}$	Acetylferrocenium tetrakis(3,5-bis(trifluoromethyl)phenyl)borate
AIBN	Azobis(isobutyronitrile)
BDE	Bond dissociation enthalpy
^{13}C NMR	Carbon nuclear magnetic resonance
CASSFC	Complete active space self-consistent field
CHD	1,4-Cyclohexadiene
cPCET	Concerted proton-coupled electron transfer
CPET	Concerted proton-electron transfer
18-crown-6	1,4,7,10,13,16-Hexaoxacyclooctadecane
CuNIR	Copper nitrite reductase
Cumyl	α,α-Dimethylbenzyl
CV	Cyclic voltammetry
DFB	1,2-Difluorobenzene
DHA	9-10-Dihydroanthracene
DMF	Dimethylformamide
DMSO	Dimethyl sulfoxide
DTBP	2,4-Di-*tert*-butylphenol
2,6-DTBP	2,6-Di-*tert*-butylphenol
EPR	Electron paramagnetic resonance
ET	Electron transfer
Fc	Ferrocene
Fc*	Decamethylferrocene
$FcBArF_{24}$	Ferrocenium tetrakis(3,5-bis(trifluoromethyl)phenyl)borate
GC-MS	Gas chromatography-mass spectrometry
^{1}H NMR	Proton nuclear magnetic resonance
HAA	Hydrogen atom abstraction
HAT	Hydrogen atom transfer
HDMS	bis(trimethylsilyl)amide

HR ESI-MS	high-resolution electrospray ionization-mass spectrometry
KHMDS	Potassium bis(trimethylsilyl)amide
KIE	Kinetic isotope effect
Krypt	Kryptofix 222 or 4,7,13,16,21,24-Hexaoxa-1,10-diazabicyclo[8.8.8]hexacosane
L	Bis(2,6-diisopropylphenylcarboxamido)pyridine
LMCT	Ligand-to-metal charge transfer
LPMO	Lytic polysaccharide monooxygenase
*m*CBA	*m*-chlorobenzoate
MeCN	Acetonitrile
MeOH	Methanol
Nuc or Nu	Nucleophile
PCET	Proton-coupled electron transfer
PDB	Protein Data Bank
PPA	2-Phenylpropionaldehyde
PPN	Bis(triphenylphosphine)iminium
PT	Proton transfer
PT/ET	Stepwise proton transfer followed by electron transfer
RC	Radical combination
TACN	1,4,7-Triisopropyl-1,4,7-triazacyclononane
TBAP	Tetrabutylammonium hexafluorophosphate
TD-DFT	Time dependent-density functional theory
TEMPO•	(2,2,6,6-Tetramethylpiperidin-1-yl)oxyl
TEMPO–H	1-Hydroxy-2,2,6,6-tetramethyl-piperidine
THF	Tetrahydrofuran
TPP	5,10,15,20-tetraphenyl-21H,23H-porphine
TTBP	2,4,6-Tri-*tert*-butylphenol
UV-vis	Ultraviolet-visible
X	Anionic ligand

XAS	X-ray absorption spectroscopy

Introduction

1.1 Introduction

Nature evolved to use metal ions to perform vital transformations.[1] Metalloproteins are a class of proteins where metal ions in specific chemical environments aid in specific functions. Copper is one such metal ion and metalloproteins containing copper can perform various transformations, such as electron transfer (ET), binding and reduction of O_2, NO_2^-, and N_2O, and oxidation of substrates.[2] Copper is a choice metal ion for these transformations because of its ability to access multiple oxidation states. Studies of copper protein active sites have revealed information about their structures, their mechanisms, and how they shuttle between oxidation states and there is an ongoing goal to develop a deeper understanding of these topics.[2]

A method of learning more about copper protein active sites is to synthesize copper complexes to mimic active site structures and/or reactivity patterns. For example, lytic polysaccharide monooxygenase (LPMO), an enzyme that oxidizes polysaccharides, has been a target for model complexes that mimic the LPMO active site and reactivity.[3,4] Additionally, the various intermediates proposed in the oxidation mechanism of LPMO have been investigated by synthesizing and studying the reactivity of discrete Cu-oxygen complexes. For example, an intermediate proposed to attack strong C–H bonds in polysaccharides contains the $[Cu–OO]^+$ unit.[5,6] The $[Cu–OO]^+$ core has been studied in many model complexes and those complexes have been reacted with O–H and C–H substrates to understand their oxidation chemistry.[7,8]

Generating reactive Cu-oxygen complexes and studying the intricate mechanistic details of their reactivity has been a fruitful route for expanding the knowledge of the bioinorganic field. To preface Chapter 2, a background on the biological precedence for Cu-oxygen species will be presented. The copper-containing enzymes, LPMOs, will be discussed in depth to set precedence for trying to access copper-oxygen complexes supported by monoanionic ligands. Chapter 2 discusses a project which focuses on monoanionic ligands, which are differ from the dianionic ligand bis(2,6-diisopropylphenylcarboxamido)pyridine (L^{2-}) that has been used extensively by the Tolman group. Thus, to put my work into context, the literature on Cu-oxygen complexes supported by L^{2-} (Figure 1.1), mimics for proposed Cu-oxygen species in the LPMO enzymatic cycle, will be presented. This background knowledge also provides background on the routes available for accessing synthetic Cu-oxygen complexes. The first Cu-oxygen complex reviewed is $[LCuOO]^-$, and its reactivity and the implications on the LPMO mechanism will be considered. Additionally, high-valent copper-oxygen complexes LCuOOR and LCuOH, motifs that are implicated a models for possible copper-oxygen cores in the process of O_2 activation at monocopper site, will be examined.

An ongoing goal of the Tolman group is to study ligand perturbations on Cu(III) complexes and proton-coupled electron transfer (PCET) reactivity of those complexes. In Chapters 3 and 4, new LCu(III)–X (X = anionic ligand) complexes are presented. To put this work into perspective, the characterization data for previously studied LCuX complexes (X = OOR, OH, O_2CR, F, Cl, and Br) are described in this chapter. Additionally, the LCuX system (Figure 1.1) has been extended to X ligands that are not necessarily biomimetic but provide valuable information about PCET chemistry. In particular, the properties and detailed PCET reactivity of $LCuO_2CR$, LCuF, LCuCl, and LCuBr will be discussed. Furthermore, Chapters 3 and 4 describe two projects in which the X ligand is nitrite or amides, respectively. To set the stage for the nitrite work, the enzymes copper nitrite reductases (CuNIRs) and Cu(I)- and Cu(II)-nitrite model complexes will be discussed here. Lastly, an introduction to Chapter 4 will explore the chemistry relevant to Cu-nitrogen complexes, including C–N coupling reactions and C–H amination reactions.

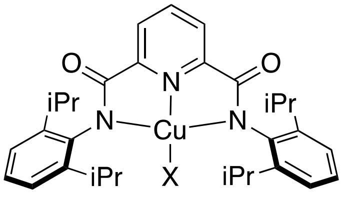

LCuX

Figure 1.1. The structure of LCuX

1.2 Lytic polysaccharide monooxygenase

Lytic polysaccharide monooxygenases (LPMO) are monocopper enzymes that use molecular oxygen, O_2, to oxidize recalcitrant polysaccharide substrates, incorporating a hydroxyl group into the polysaccharide (Figure 1.2). The oxidized products are susceptible to glycosidic cleavage, resulting in oligomers.[9–11] LPMOs boost the degradation of polysaccharides, such as lignocellulosic biomass, a process useful in biofuel formation.[12] LPMOs are now being added to enzymatic cocktails in biorefineries, reducing costs for the industrial processes.[13] Because of the important applications of LPMOs, they have been widely studied in order to gain an understanding of their structures and functionality. This introduction will discuss the LPMO active site, the proposed mechanisms for O_2 activation at the copper center, and the critical oxidation process for polysaccharide degradation.

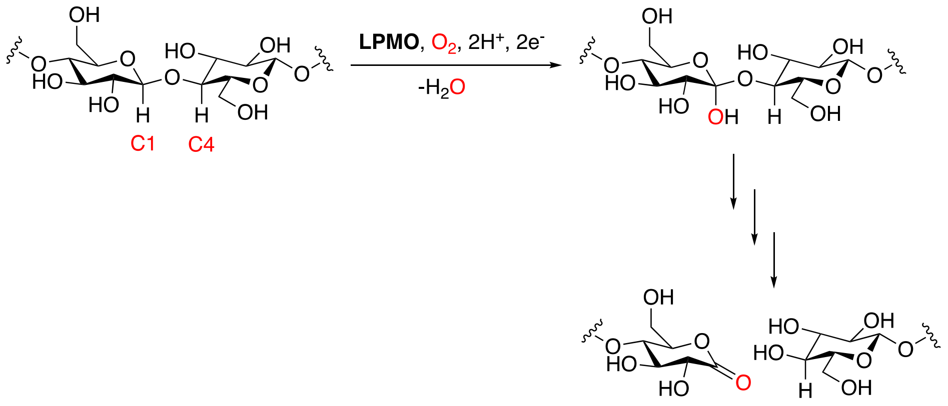

Figure 1.2. Oxidative cleavage of cellulose by LPMO. Adapted from ref. 9.

1.2.1 LPMO active site

The active sites of LPMOs are located on the periphery of the enzymes (Figure 1.3), a consequence of the substrate of the enzymes, crystalline polysaccharide.[9] Many crystal structures and electron paramagnetic resonance (EPR) spectroscopy studies on LPMOs reveal a diverse secondary-coordination sphere, differing in H-bonding networks that control various factors like substrate interactions.[14] However, a highly conserved binding motif is found for the copper ions. Across the different classes of LPMOs, a t-shaped binding motif about the copper is consistently observed and is termed the “histidine brace” (Figure 1.3). The histidine brace includes two histidine imidazolyl groups, with one histidine being at the terminus of the protein. A third ligand is the amino terminus $–NH_2$.[14]

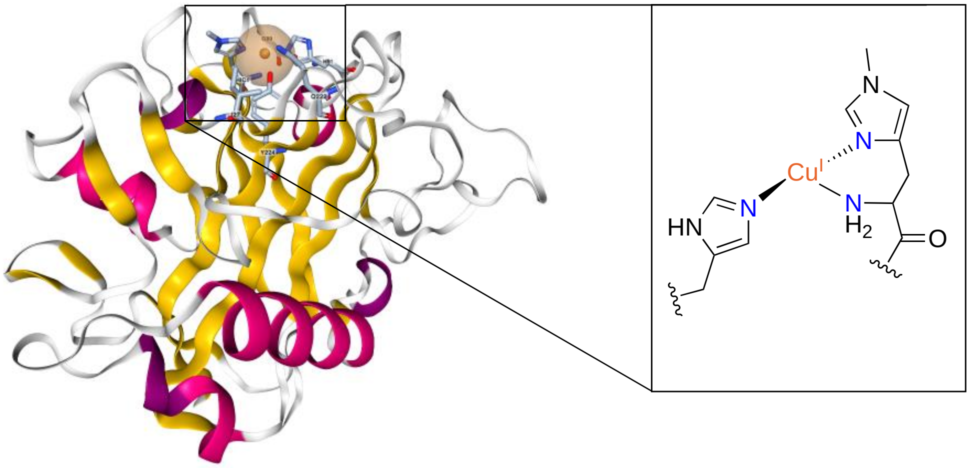

Figure 1.3. The crystal structure of an LPMO enzyme with 1.5 Å resolution and a detailed depiction of the enzyme active site (structure taken from the Protein Data Bank, data from ref. 15).

The histidine brace is now recognized as a common framework in oxygen-activating enzymes,[16,17] and is capable of supporting the formation of reactive copper-oxygen species. The three N-donors of the histidine brace supply sufficient electron density to the Cu(I) ion to make its reaction with O_2 kinetically and thermodynamically favored. When dioxygen reacts with LPMO, the histidine brace forces the molecule to bind equatorially putting the oxygen ligand trans to the amino terminus ligand.[14] The protonation state of the amino terminus is ambiguous but, it has been hypothesized that if the ligand trans to the oxygen ligand was anionic, it could help stabilize Cu-oxygen species (*vide infra*). Furthermore, the pK_a of this group could be modulated by H-bonding networks in the presence of substrate and/or by the generation of high-valent Cu-oxygen complexes during catalysis.[14] Some evidence for the amino terminus being deprotonated has come from neutron diffraction studies.[18] Together, these results provide a rationale for modelling the LPMO active site with ligands that feature three N-donors in a *mer* geometry with a single negative charge.

1.2.2 Proposed mechanisms for LPMO

The resting state of the LPMO enzyme contains the copper ion in the Cu(II) oxidation state.[9] In a cofactor dependent electron transfer,[19] the active state, T-shaped Cu(I), is generated. The Cu(I) center reduces O_2 to yield a Cu(II)-superoxide adduct, [Cu–

$OO]^+$, which has been identified in LPMO by XAS and X-ray crystallography.[18,20] From the Cu(II)-superoxide adduct, two possible mechanisms have been proposed that differ by which species performs the arduous task of C–H bond cleavage via a hydrogen-atom transfer (HAT) step, a type of PCET.[5]

One proposed mechanism depicts the Cu(II)-superoxide adduct (S) performing HAT directly (Figure 1.4, left). The products of this oxidation are a Cu(II)-hydroperoxide adduct (HP) and a C-based substrate radical. According to this pathway, the Cu(II)-hydroperoxide species (HP) undergoes O–O bond cleavage after introduction of a proton from the medium and an electron to yield a putative Cu(II)-oxyl adduct (Ox). The Cu(II)-oxyl adduct (Ox) combines with the substrate radical and a proton to yield the hydroxylated substrate and the T-shaped Cu(I).[5]

Another proposed mechanism invokes the Cu(II)-superoxide adduct (S) reacting with a proton and an electron to yield a Cu(II)-hydroperoxide adduct (HP) (Figure 1.4, right). Cleavage of the O–O bond in this adduct upon addition of another proton and another electron to release water and the Cu(II)-oxyl species (Ox). The Cu(II)-oxyl adduct (Ox) is then suggested to be the species that performs HAT from the substrate. The products of this reaction are a Cu(II)-hydroxide adduct (HOx) and the C-based substrate radical, which combine in a “rebound” step to yield the hydroxylated substrate and the T-shaped Cu(I) again.[5] These proposed mechanisms have provided synthetic chemists with Cu-oxygen cores to target, notably the Cu(II)-superoxide and the Cu(II)-oxyl, in studies aimed at evaluating their properties and reactivity.

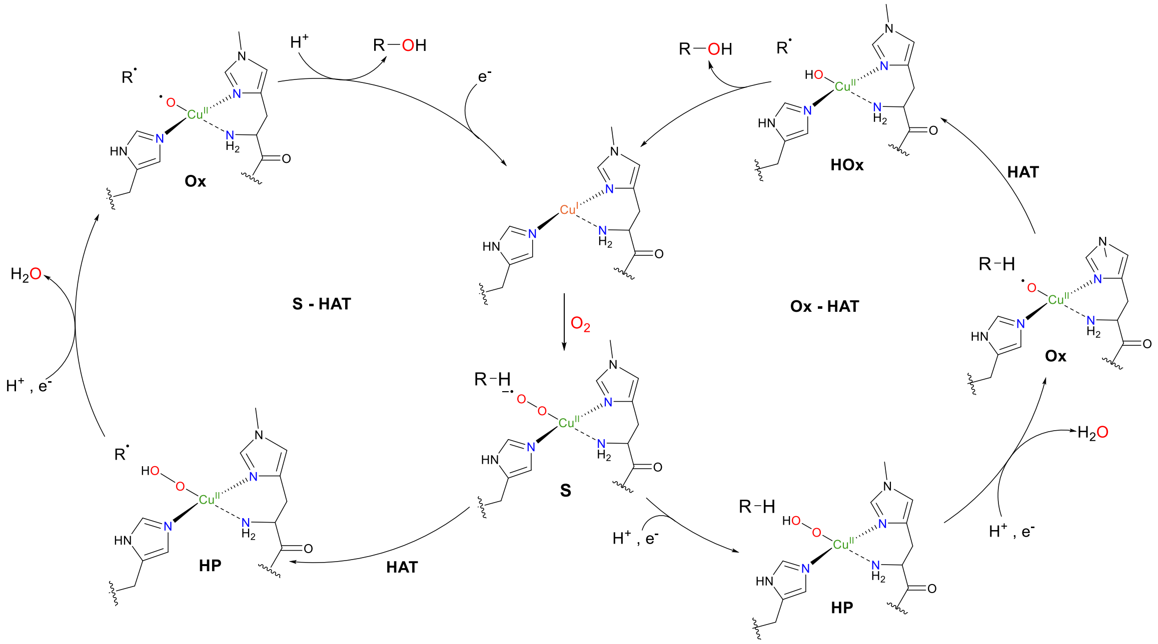

Figure 1.4. Two proposed catalytic cycles for the oxidation of substrate performed by LPMO. Adapted from ref. 5.

1.2.3 Possible copper-oxygen cores

In addition to the copper-oxygen cores mentioned above, others may be considered. When Cu(I) binds O_2 to form the Cu(II)-superoxide adduct, a series of cascading proton and electron transfers can occur, either separately or in a coupled fashion (PCET). So, when thinking about which copper-oxygen cores to study synthetically, we can map out the species that would form after discrete proton and electron transfers from the Cu(II)-superoxide core (Figure 1.5).

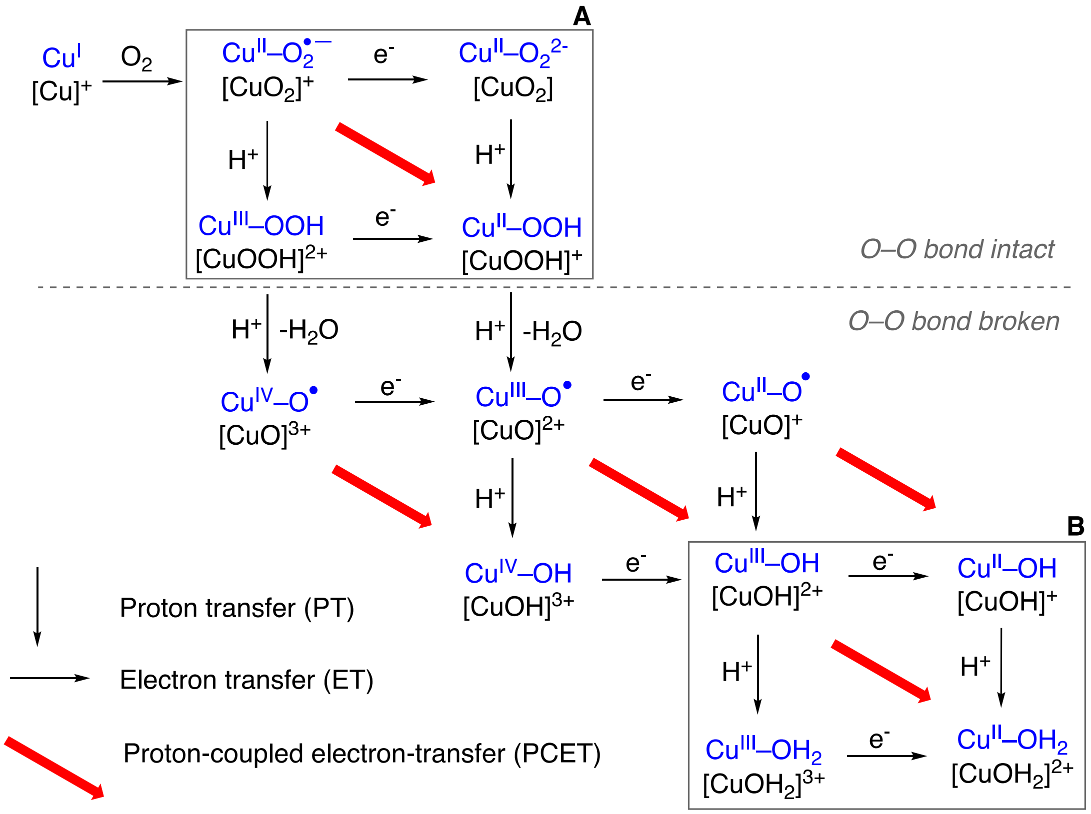

Figure 1.5. Proposed intermediates for O_2 activation at a monocopper site. Proton transfers (vertical arrows), electron transfers (horizontal arrows), and proton-coupled electron transfers (diagonal arrows) are indicated. Two formulaic representations of the Cu complexes are shown, formal oxidations states (upper blue formulation) and core with overall charge (lower black formulation). Boxes **A** and **B** emphasize square schemes that are discussed more in depth in text. Adapted from ref. 21.

Thus, each set of proton and electron transfers can be pictured in a "square scheme" that depicts electron transfers occurring horizontally, proton transfers vertically, and proton-coupled electron transfer diagonally. For example, an electron can be transferred to the Cu(II)-superoxide adduct to form a Cu(II)-peroxide adduct. Subsequently, a proton can be transferred to the Cu(II)-peroxide adduct to form a Cu(II)-hydroperoxide species. Alternatively, a proton can be transferred to the Cu(II)-superoxide adduct first to form a Cu(III)-hydroperoxide species, which an electron transfer would transform to the product Cu(II)-hydroperoxide. The diagonal transformation represents a direct proton-coupled electron transfer from the Cu(II)-superoxide adduct to the Cu(II)-hydroperoxide product.

The Cu-hydroperoxide species are the final species with the O–O bond intact along the Cu-mediated reduction of O_2 path that ultimately releases water (one of the byproducts of LPMO oxidations). For example, a proton transfer to the Cu(II)-hydroperoxide adduct releases water and yields a Cu(III)-oxyl adduct. An electron transfer to this species would result in a Cu(II)-oxyl species, one of the proposed species to perform HAT in the previously discussed LPMO mechanisms. The Cu(II)-oxyl core has only been observed in gas phase and is thought to be very reactive.[22] Computational studies have suggested that the Cu(II)-oxyl species is a potent oxidant for polysaccharide C–H bonds.[6] However, because of its innate reactivity it is difficult to study in discrete synthetic molecules.

After O–O scission, another copper-oxygen species relevant to oxidation reactions is revealed, the Cu(III)-hydroxide adduct. The Cu(III)-hydroxide species can be viewed as a "masked Cu(II)-oxyl" as it is the protonated form of the Cu(II)-oxyl core. As seen in Figure 1.5, the Cu(III)-hydroxide adduct also has an associated square scheme, representing its potential for oxidation reactions. The Cu(III)-hydroxide core has been shown to be a potent oxidant[23–25] and is discussed in depth in section 1.3.3. Ultimately, the square scheme treatment reveals several biologically relevant copper-oxygen cores to study: $[Cu–OO]^+$, $[Cu–OOH]^+$ and $[Cu–OOH]^{2+}$ (or $[Cu–OOR]^+$ and $[Cu–OOR]^{2+}$), and $[Cu\text{-}OH]^{2+}$.

1.3 Pyridine dicarboxamide copper complexes

The molecule bis(2,6-diisopropylphenylcarboxamido)pyridine (H_2L) can be doubly deprotonated to yield a dianionic pincer ligand, L^{2-}. The anionic carboxamide groups are highly electron donating and can support electron deficient metal centers, such as Cu(III). The large amount of negative charge can also be delocalized into the carboxamide π-system to bind a metal ion that is not as electron deficient, such as Cu(II). However, a disadvantage of L^{2-} is its lesser ability to support electron rich metals, such as Cu(I). The ligand also contains two flanking aryl groups with steric bulk installed as isopropyl groups in the 2- and 6- positions. The flanking aryl rings provide enough steric influence to prevent dimerization of two copper complexes. The steric bulk also helps enforce a square planar orientation about the copper ion, inhibiting the binding of a fifth ligand.

A Cu(II) complex of L^{2-} may be prepared by reacting H_2L with 2 eq. of NaOMe and $Cu(OTf)_2$ in methanol. After dissolving the initially formed species MeCN and recrystallization from MeCN/toluene, LCuMeCN forms.[26] It is a suitable starting material for some $[LCuX]^-$ complexes. Other $[LCuX]^-$ may be generated from protonolysis reactions with $[LCuOH]^-$, which can be synthesized by reacting LCuMeCN with a hydroxide salt in ethereal solvents.[23]

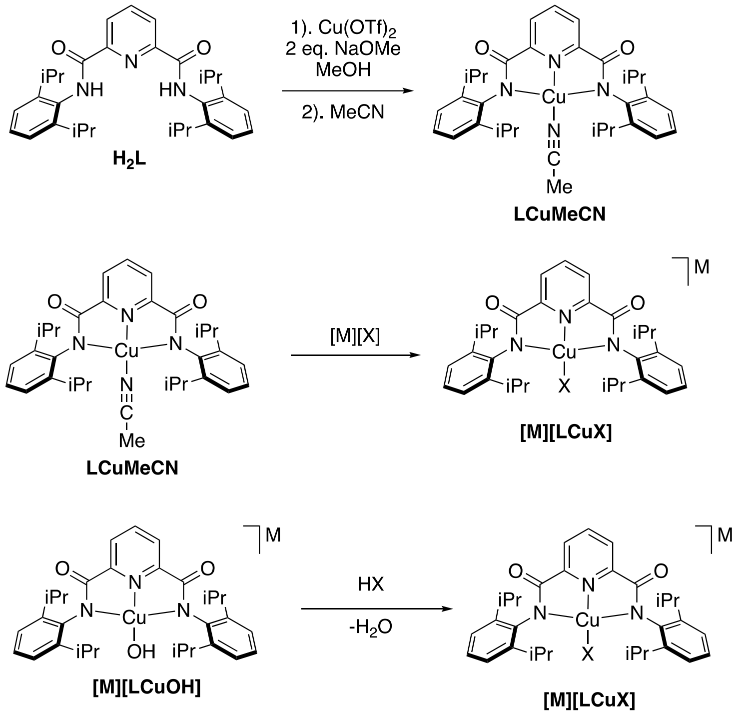

Figure 1.6. General syntheses for LCuMeCN and [M][LCuX] complexes.[23,26–31]

1.3.1 [LCuOO]- complexes

A $[Cu–OO]^+$ adduct is implicated as an HAT-active species in a proposed mechanism for LPMO oxidation. Therefore, model complexes containing a $[Cu–OO]^+$ core have been synthesized to understand the propensity for HAT by the core. There are many 1:1 $Cu:O_2$ adducts in the literature that are typically formed by reacting O_2 with a Cu(I) complex at low temperature in inert conditions.[7] When Cu(I) binds O_2 the electronic structure of the resulting product can exist on a spectrum where the extremes are formulated as a Cu(II)-superoxide and a Cu(III)-peroxide (Figure 1.7). The O_2 ligand can also bind end-on, η^1, or side-on, η^2 (Figure 1.7). The electronic structure of the complex can be determined by the nature of the O–O bond. X-ray crystallography and/or resonance Raman have been used to examine the bond length/energy of the O–O bond to understand how much electron density has been transferred from the Cu(I).[7]

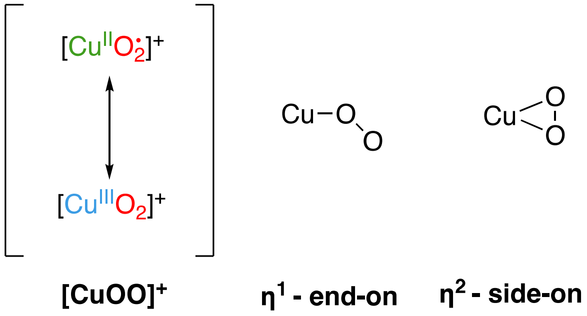

Figure 1.7. The two extreme electronic structures for 1:1 Cu/O2 complexes and the possible binding motifs for dioxygen ligands to Cu.

However, thus far, a Cu(I) complex supported by the ligand L^{2-} has not been reported, presumably because of the 2- charge of the ligand. Therefore, a route using Cu(II) and superoxide salts were used to generate a Cu(II)-superoxide supported by L^{2-}. In 2010, the first report of the generation of [K(18-crown-6)][LCuOO] by reacting LCuMeCN with KO_2 in the presence of 18-crown-6 in 1:1 DMF/THF mixtures at -80 °C was reported.[26] Unfortunately, this method was problematic in investigating the reactivity of $[LCuOO]^-$ because the limited solubility of KO_2, requiring the use of DMF, rendered the metastability of the complex poor and controlling the stoichiometry of the superoxide salt difficult.

In 2019, an alternative method for generating $[LCuOO]^-$ was reported using Kryptofix 222 (Krypt) as the phase transfer agent rather than 18-crown-6, which eliminated that need for DMF as a solvent and allowed for better control of the stoichiometry of KO_2:LCuMeCN.[32] The new method granted the reexamination of the nucleophilic reactivity of $[LCuOO]^-$ and mechanistic studies of the reactions between $[LCuOO]^-$ and phenols.[21,32]

The 2010 report described a dark blue solution with a characteristic UV-vis peak at 627 nm ($\varepsilon \sim 1700$ M^{-1} cm^{-1}) developed when LCuMeCN was added to a slurry of KO_2/18-crown-6 in 1:1 THF/DMF at -80 °C. This peak was assigned by time-dependent density functional theory (TD-DFT) as a ligand-to-metal charge transfer (LMCT) from the end-on superoxide π^* orbital to an antibonding orbital with components from the Cu(II) d_{x2-y2} orbital and the four ligand σ-donors.[26] The nature of the superoxide ligand was explored with resonance Raman using an excitation wavelength to irradiate the LMCT of [LCuOO]$^-$. An isotopically sensitive peak at 1104 cm^{-1} ($\Delta_{16O\text{-}18O}$ = 60 cm^{-1}) was identified, which is a result consistent with a superoxide ligand.[7,26] The EPR spectrum of [LCuOO]$^-$ was found to be silent, a result consistent with either an *S* = 1 or *S* = 0 complex. The triplet *S* = 1 state was corroborated experimentally, by the absence of peaks in the ^{1}H NMR spectrum of the complex, and computationally.[26]

In 2019, different experimental conditions to generate [LCuOO]$^-$ were reported. An MeCN solution of 1:1 KO_2/Krypt was added to a THF solution of LCuMeCN at -80 °C to generate [K(Krypt)][LCuOO], which exhibited the same UV-vis, resonance Raman, and EPR spectra as [K(18-crown-6)][LCuOO]. The clean generation of [K(Krypt)][LCuOO] was demonstrated by titration experiments of the MeCN solution of 1:1 KO_2/Krypt to a THF solution of LCuMeCN, indicating only 1 eq. of K(Krypt)O_2 was needed to fully form [K(Krypt)][LCuOO]. Additionally, the new method increased the stability of [LCuOO]$^-$ significantly: no decay > 1 day for [K(Krypt)][LCuOO] (-80 °C in 19:1 THF/MeCN) vs decay in a few hours for [K(18-crown-6)][LCuOO] (-80 °C in 1:1 THF/DMF).[32]

Examination of the reactions of the Cu(II)-superoxide with O–H substrates was enabled after the clean generation of [LCuOO]$^-$ was discovered. [K(Krypt)][LCuOO] reacted with TEMPO–H at -80 °C to yield TEMPO• and [LCuOOH]$^-$, determined by EPR and UV-vis spectroscopy and the independent generation of [LCuOOH]$^-$. [K(Krypt)][LCuOO] was also treated with *p*-substituted phenols (^{X}ArOH) at -60 °C, and a Hammett plot revealed a mechanistic dichotomy (Figure 1.18). When [K(Krypt)][LCuOO] was reacted with *p*-substituted phenols with electron-donating substituents (X = NMe_2, OMe, *t*Bu, Me), a faster rate with increasing σ_p was observed, and a concerted proton-electron transfer (CPET) pathway was proposed (Figure 1.9). When *p*-substituted phenols with electron-withdrawing substituents (X = Cl, CF_3, NO_2) were used, a faster rate with increasing σ_p was also observed, and a PT/ET mechanism was proposed (Figure 1.9). However, the *p*-substituted phenols near the mechanistic crossover point (X = *t*Bu, Me, H) most likely operate by both mechanisms as the thermodynamic driving forces for either mechanism appear to be similar at the crossover point. The identification of [LCuOO]$^-$ operating via a PT/ET mechanism points to the basic nature of the complex.[21]

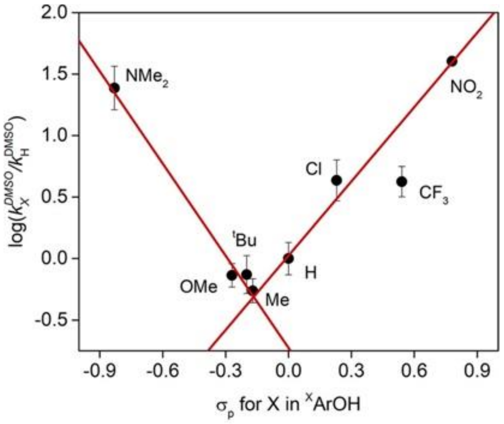

Figure 1.8. Hammett plot of $\log(k_X^{DMSO}/k_H^{DMSO})$ vs σ_p for ^{X}ArOH,(X = NMe_2, OMe, *t*Bu, Me , H, Cl, CF_3, and NO_2). Separate linear fits are shown for X = NMe_2, OMe, *t*Bu, and Me (slope $\rho = -2.5$, $R^2 = 0.97$) and for X = Me, H, Cl, CF_3, and NO_2 (slope $\rho = 2.0$, $R^2 = 0.96$). Reprinted with permission from ref. 21. Copyright 2019 American Chemical Society.

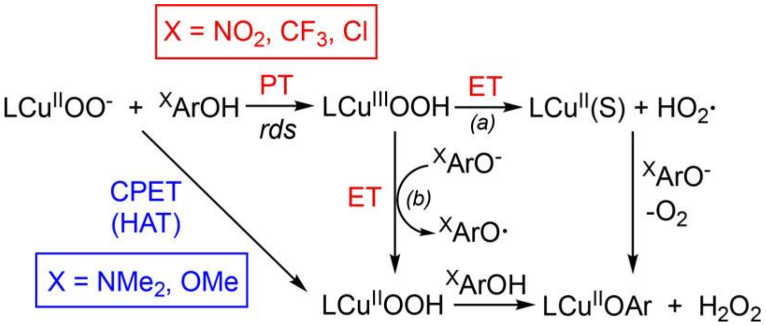

Figure 1.9. Proposed mechanisms for reactions with phenols with electron-donating substituents (top PT/ET route) and with electron-withdrawing substituents (bottom CPET route). Reprinted with permission from ref. 21. Copyright 2019 American Chemical Society.

The PCET reactions of $[LCuOO]^-$ with substrates can be described by a square scheme. The steps depicted by a square scheme can be understood by thermodynamic values associated with the steps. The horizontal electron transfers can be described with the $E_{1/2}$ of the redox couples represented and the vertical proton transfers can be described with the pK_a values of the acid/base pairs. These values can be used in equation 1.1 to calculate the bond dissociation enthalpy (BDE) of the bond being formed in the square scheme. Equation 1.1 shows that a more basic and/or more oxidizing complex results in a stronger bond, or a more thermodynamically favored species.[24]

$$\mathrm{BDE_{O–H}} = 1.37\mathrm{p}K_\mathrm{a} + 23.06\mathrm{E}_{1/2} + C_\mathrm{H} \qquad \text{Eq. 1.1}$$

To fill out some of the thermodynamic values in the square scheme for $[\mathrm{LCuOO}]^-$ (Figure 1.10), the $\mathrm{E}_{1/2}$ of the $[\mathrm{LCuOOH}]^{0/-}$ couple was measured. This oxidation potential was determined to be -215 mV vs $\mathrm{Fc}^{0/+}$ (THF, 25 °C) by cyclic voltammetry (CV) experiments of *in situ* generated $[\mathrm{LCuOOH}]^-$ from $[\mathrm{LCuOH}]^-$ and H_2O_2. Unfortunately, the $\mathrm{p}K_\mathrm{a}$ of LCuOOH could not be measured directly. However, by assuming that the mechanistic crossover point is where the thermodynamic driving force of PCET and PT are equal enable estimation using Equations 1.2 – 1.6 of a $\mathrm{p}K_\mathrm{a}$ value of ~ 19. These data led to an estimated BDE of the O–H bond in $[\mathrm{LCuOOH}]^-$ of ~ 87 kcal mol^{-1}.[21]

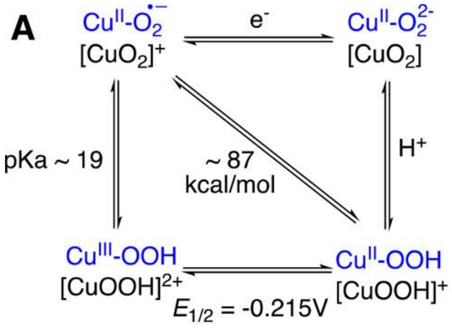

Figure 1.10. Square scheme for [LCuOO]- with associated thermodynamic values. Reprinted with permission from ref. 21. Copyright 2019 American Chemical Society.

$$\Delta\mathrm{G_{CPET}} = \mathrm{BDE_{MeArO–H}} - \mathrm{BDE_{CuOO–H}} \qquad \text{Eq. 1.2}$$

$$\mathrm{BDE_{CuOO–H}} = 1.37\ \mathrm{p}K_\mathrm{a} + 23.06\mathrm{E}_{1/2} + C_\mathrm{H} \qquad \text{Eq. 1.3}$$

$$\Delta\mathrm{G_{CPET}} = 25.18 - 1.37\mathrm{p}K_{\mathrm{a(CuOO–H)}} \qquad \text{Eq. 1.4}$$

$$\Delta\mathrm{G_{PT}} = 2.303RT(\mathrm{p}K_{\mathrm{a(MeArO–H)}} - \mathrm{p}K_{\mathrm{a(CuOO–H)}}) \qquad \text{Eq. 1.5}$$

$$\Delta\mathrm{G_{PT}} = 18.43 – 0.975\mathrm{p}K_{\mathrm{a(CuOO–H)}} \qquad \text{Eq. 1.6}$$

1.3.2 LCuOOR complexes

The $[\mathrm{Cu–OOH}]^{+/2+}$ cores are proposed intermediates in the oxidation of polysaccharides by LPMO, but due to difficulties encountered in attempts to cleanly generate the complexes $[\mathrm{LCuOOH}]^{-/0}$, $[\mathrm{CuOOR}]^{+/2+}$ species were studied as models. The studies of the oxidized complexes also contributed to our collective knowledge of Cu(III) complexes, aiding in the characterization of new Cu(III) species, like the ones in Chapters 3 and 4. The complexes [NBu$_4$][LCuOOR] (R = tBu, Cumyl) were synthesized via protonolysis reactions between the respective HOOR materials and [NBu$_4$][LCuOH]. The one electron products, LCuOOR (Figure 1.11), were characterized and the reactivity of LCuOOCumyl complexes with O–H substrates was explored.[28]

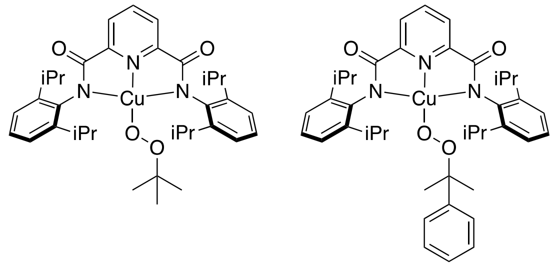

LCuOO*t*Bu **LCuOOCumyl**

Figure 1.11. The structures of LCuOOR complexes.

The oxidized complexes LCuOOR (R = *t*Bu, cumyl) were generated with the addition of FcBArF$_{24}$ since the E$_{1/2}$ values were found to be -154 mV and -205 mV vs. Fc$^{0/+}$ for [LCuOO*t*Bu]$^{-/0}$ and [LCuOOCumyl]$^{-/0}$, respectively. The formation of the LCuOOR species was monitored by UV-vis spectroscopy, revealing three intense absorption features each between about 500 and 800 nm. TD-DFT was used to assign these transitions as LMCTs, specifically L aryl π to Cu d_{x2-y2} transitions. Maximum absorption features for LCuOOCumyl were reached when 1 eq. of FcBArF$_{24}$ and the features could be reversibly generated with subsequent additions of FcBArF$_{24}$ and Fc*.[28]

EPR spectra of LCuOO*t*Bu and LCuOOCumyl exhibited no signal, consistent with either $S = 0$ (Cu^{III} or Cu^{II}-ligand radical antiferromagnetically coupled) or $S = 1$ (Cu^{II}-ligand radical ferromagnetically coupled). The resonance Raman spectrum of LCuOOCumyl shows an isotopically sensitive peak at 831 cm^{-1} ($\Delta_{16O-18O}$ = 18 cm^{-1}), supporting the retention of the alkylperoxide ligand in the oxidized species. The collective UV-vis data, EPR and resonance Raman spectra, and computations support the formal Cu(III) oxidation state for the LCuOOR complexes.[28]

LCuOOCumyl was treated with a suite of O–H and C–H substrates but only reacted appreciably with substrates containing weak O–H bonds (TEMPO-H and 4-

dimethylaminophenol or ^{NMe2}ArOH). LCuOOCumyl reacted with TEMPO-H (k_2 = 2.4 M^{-1} s^{-1}) in THF at -80 °C and yielded TEMPO•, consistent with a PCET reaction. LCuOOCumyl reacted with ^{NMe2}ArOH in THF at -80 °C and yielded LCuOAr^{NMe2}, a species designated as a Cu(II)-phenoxyl radical. The overall reaction represents a proton transfer and ligand exchange, although the exact mechanism for the reaction was not determined.

1.3.3 LCuOH complexes

As previously discussed, the [Cu–OH]$^{2+}$ core is a proposed intermediate in LPMO oxidation chemistry and may be considered as a protonated version of the highly reactive [Cu–O]$^{+}$ core. Accessing the [Cu–OH]$^{2+}$ species in a discrete molecule would allow us to understand the viability of the core in LPMO and oxidation catalysis and to study PCET reactivity in detail. In 2011, the generation of LCuOH and its reactivity with 9,10-dihydroanthracene (DHA) in acetone at -80 °C was reported.[23] After this initial report, several journal articles detailing derivatives of LCuOH varying in the supporting ligand (^{Y}L),[29,33,34] and the detailed mechanistic nuances of its PCET reactivity have been published.[24,25]

The complex LCuOH ($E_{1/2}$ = -76 mV vs Fc$^{0/+}$ in acetone) was generated using FcBArF$_{24}$. UV-vis spectroscopy experiments revealed a new highly absorbing peak at 540 nm that fully formed after addition of 1 eq. of FcBArF$_{24}$ and that could be bleached with the addition of Fc*. UV-vis spectra were generated by TD-DFT for all possible electronic structures, singlet LCu(III)–OH, singlet LCu(II)–•OH, and triplet LCu(II)–•OH, and it was found that the calculations for singlet LCu(III)–OH were most consistent with the experimental data.[23]

X-ray absorption spectroscopy (XAS) was performed on samples of [NBu$_4$][LCuOH] and LCuOH to further understand the electronic structure of the oxidized product. The Cu k-edge data had a difference of 1.7 eV in the pre-edge positions of the two complexes and a difference of 1.1 eV in the rising edge energies of the two complexes. These results indicate a metal-based oxidation and a total increase of effective nuclear charge on the metal center. Furthermore, the extended X-ray absorption fine structure (EXAFS) data revealed a 0.1 Å shortening of the bond lengths between the Cu ions and the primary ligand sphere atoms, typical results for a 1-electron oxidation at Cu. The bond contractions are consistent with DFT results.[23]

Resonance Raman spectroscopy revealed an isotopically sensitive peak at 633 cm^{-1} ($\Delta_{16O\text{-}18O}$ = 18 cm^{-1}) for frozen CH_2Cl_2 samples of LCuOH. This peak was identified as a υ(Cu–O), which was confirmed by DFT calculations. Since a crystal structure of LCuOH was elusive, a normalized Badger's rule, an equation relating vibrational frequencies to bond lengths, was used to estimate a Cu–O bond length of 1.80 Å.[35] The estimates from the resonance Raman experiments and DFT calculations were ultimately confirmed by recent X-ray structural data of a variant of LCuOH, ^{OMe}LCuOH (methoxy-substituted pyridine in L^{2-}).[29]

Finally, a relatively small reorganization energy, λ, for the $[LCuOH]^{-/0}$ couple was calculated to be 0.95 eV, only slightly larger than type 1 Cu proteins known to facilitate electron transfers. Both inner sphere and outer sphere contributions are included in this value and the outer sphere reorganization accounts for just over half of the value. The calculated λ is consistent with minimal structural change from the Cu(II) to Cu(III) state, consistent with the proposed minimal contraction of the Cu–O/N bonds.[36]

Initial studies of the reaction between LCuOH and DHA (Scheme 1.1) in acetone at -80 ºC indicated the formation of anthracene, confirmed by UV-vis spectroscopy and gas chromatography-mass spectrometry (GC-MS), and $LCuOH_2$, confirmed by UV-vis spectroscopy. The reaction proceeded with second-order kinetics at relatively fast rates (k_2 = 1.1 M^{-1} s^{-1}) with a kinetic isotope effect (KIE) at -70 °C of 44, signifying C–H bond cleavage in the rate-determining step. Temperature dependent KIE experiments were performed allowing the KIE at 25 °C to be calculated as 29, indicating possible tunneling components during hydrogen atom abstraction.[23] LCuOH was also found to react with various other C–H bonds (-25 °C, 1,2-difluorobenzene), ranging from DHA (BDE = 76.3 kcal mol^{-1}) to cyclohexane (BDE = 99.8 kcal mol^{-1}).[24]

Scheme 1.1. The reaction between LCuOH and DHA.

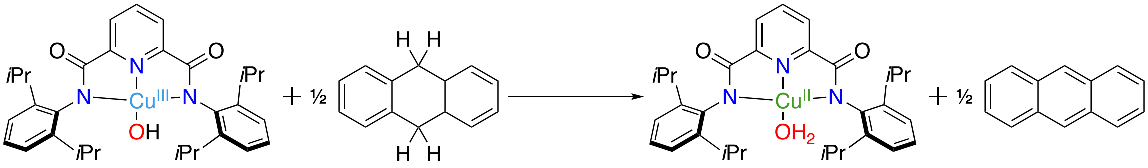

The BDE of the O–H bond in $LCuOH_2$ was sought after to aid in understanding the fast HAT kinetics of LCuOH, requiring the determination of some of the thermodynamic values in the square scheme (Figure 1.12). The $E_{1/2}$ of the $[LCuOH]^{-/0}$ couple was remeasured in THF as -74 mV vs $Fc^{0/+}$. The pK_a of $LCuOH_2$ was measured through UV-vis titrations as 18.8 ± 1.8. The BDE of $LCuOH_2$ was calculated to be 90 ± 3 kcal mol^{-1}, a value higher than most BDEs of O–H bonds formed through HAA reactions of various metal-oxo/hydroxo complexes. The thermodynamic values suggest that although LCuOH is a poor oxidant, the high basicity of LCuOH accounts for its fast HAT rates.[24]

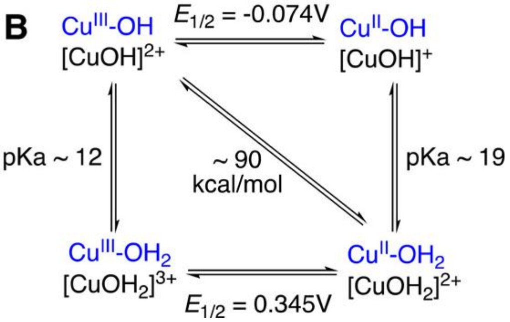

Figure 1.12. Square scheme for LCuOH with associated thermodynamic values. Reprinted with permission from ref. 21. Copyright 2019 American Chemical Society.

LCuOH was reacted with a series of *p*-substituted phenols (^{X}ArOH, X = NMe_2, OMe, Me, H, Cl, CF_3, NO_2) and monitored by low-temperature stopped flow UV-vis spectroscopy. Linear free energy relationships revealed that the reaction of LCuOH with most phenols follows a similar mechanism. However, a different mechanism appears to occur between the reaction of LCuOH and the most acidic phenol, ^{NO2}ArOH, as apparent in the phenol pK_a vs log k plot (Figure 1.13). The results suggest that the HAA reaction of LCuOH and most phenols follows a CPET mechanism and the reaction between LCuOH and ^{NO2}ArOH follows a PT/ET mechanism.[25]

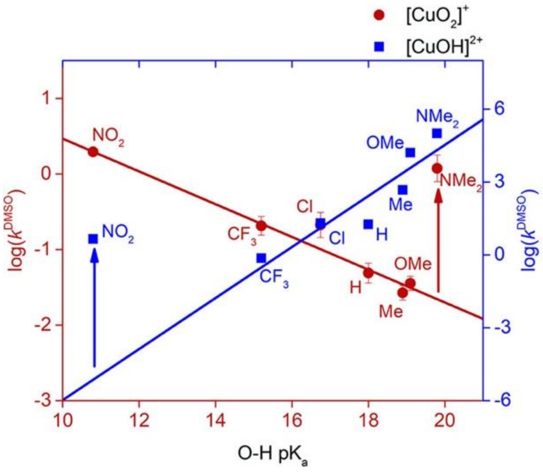

Figure 1.13. Log(k_{DMSO}) vs ^{X}ArOH pK_a plot for $[CuOO]^+$ (red circles, −60 °C) and $[CuOH]^{2+}$ (blue squares, −80 °C) cores. The red and blue lines are fits to the data for all X except NMe_2 (red, $R^2 = 0.992$, slope = −0.22) or NO_2 (blue, $R^2 = 0.811$, slope = 1.1). Reprinted with permission from ref. 21. Copyright 2019 American Chemical Society.

When an H-atom is abstracted from a substrate, the overall transformation involves a proton and an electron, but where they travel to can differ. When the proton and electron travel from one place to another together, this is called a hydrogen atom transfer (HAT). When the proton and electron travel together from one site to two different sites, the reaction is termed concerted proton-coupled electron transfer (cPCET). Computations of the reactions between LCuOH and DHA and 2,6-di-*t*-butylphenol (2,6-DTBP) were performed to determine mechanistic details of these reactions. Looking at electronic structures of the reactants along the reaction coordinate revealed the change in dipole moment for the reaction between LCuOH and DHA to be relatively small and between LCuOH and 2,6-DTBP to be relatively large (Figure 1.14). A small change in dipole moment suggests a HAT mechanism, the DHA reaction, and a large change in dipole moment suggests a cPCET mechanism, the 2,6-DTBP reaction. These mechanisms are further corroborated by intrinsic bond orbital analysis, which depicted the proton and electron both travel from DHA to the hydroxyl ligand (Figure 1.15). However, the proton and electron travel from 2,6-DTBP to separate locations: the proton travels to the hydroxyl ligand and the electron travels to the Cu ion (Figure 1.15).[37]

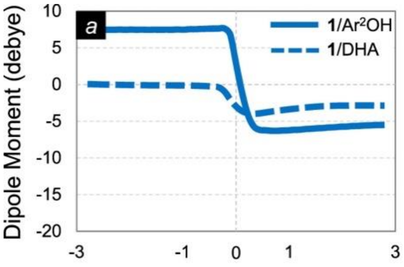

Figure 1.14. The total dipole moment as the HAA reaction proceeds for LCuOH with 2,6-DTBP (solid line) and DHA (dashed line). Reprinted with permission from ref. 30. Copyright 2019 American Chemical Society.

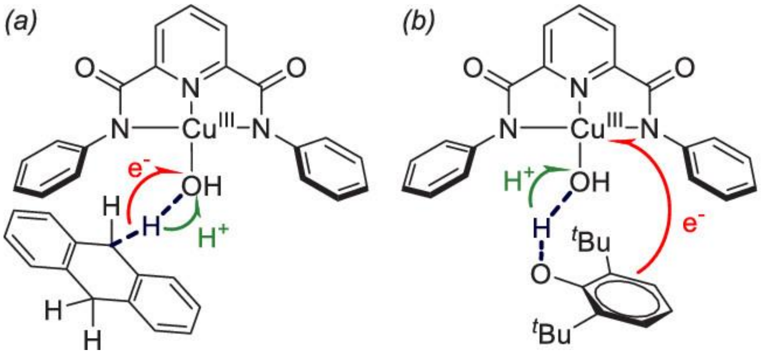

Figure 1.15. Representation of the proton and electron transfers during the HAA reactions of LCuOH with DHA (a) and 2,6-DTBP (b). Reprinted with permission from ref. 30. Copyright 2019 American Chemical Society.

Modifications of the L^{2-} ligand were performed to study the effects on the thermodyanamic values and HAT kinetics of the [Cu–OH]$^{2+}$ core. For example, electron-withdrawing -NO$_2$ substituents were added to the *para* position of the flanking aryl rings and the pyridine ring was reduced to a piperidine group and the N was methylated (Figure 1.16). The formally Cu(III) complexes were generated using 1 eq. of suitable oxidant and the UV-vis spectra for ^{NO2}LCuOH and ^{PipMe}LCuOH were found to be similar to that of LCuOH, supporting similar formulations for the new complexes.[34]

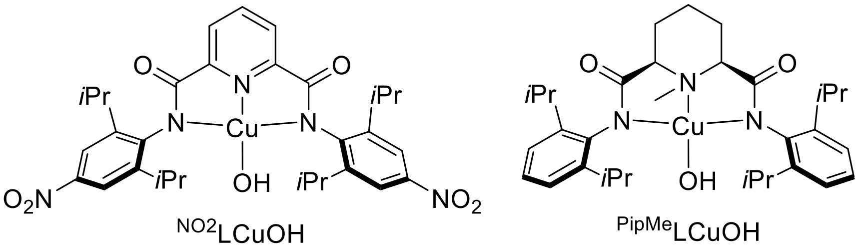

Figure 1.16. Cu-hydroxide complexes explored for effects of electronic ligand perturbations.[34]

The reactions of ^{NO2}LCuOH and ^{PipMe}LCuOH with C–H substrates showed that the complexes were also potent at HAA. Of note, the k_2 values of the reactions between ^{NO2}LCuOH, LCuOH, and ^{PipMe}LCuOH with DHA (-25 ˚C, DFB) were found to be 346(52), 50(8), and 25(4) M^{-1} s^{-1}, respectively. This trend correlates with the BDEs found for the O–H bonds formed in the HAA reactions. The O–H BDEs in ^{Y}LCuOH$_2$ were found to be 88 ± 3, 90 ± 3, and 91 ± 3 kcal mol^{-1} for ^{NO2}LCuOH$_2$, LCuOH$_2$, and ^{PipMe}LCuOH$_2$, respectively. The electronic modifications resulted in only slight differences in thermodynamic values and a more pronounced HAA rate difference for ^{NO2}LCuOH. Ultimately, clear trends were difficult to discern between the three complexes because of varying degrees of tunnelling contributions in the HAA reactions.[34]

The overall charge of the Cu–OH complex was perturbed as well by installing -NMe_3^+ or -$SO3^-$ groups to the *para* position of the flanking aryl rings (Figure 1.17). When the respective Cu(II)-hydroxide complexes were oxidized by 1 electron, typical Cu(III) UV-vis features were observed for the dianionic [^{SO3}LCuOH]$^{2-}$ and dicationic [^{NMe3}LCuOH]$^{2+}$ complexes. Interestingly, the BDE values of the O–H bonds that were measured for the charged Cu(II)-aqua complexes were found to be nearly identical to each other: 91.5 kcal mol^{-1} for [^{SO3}LCuOH][K(18-crown-6)]$_2$ and 91 kcal mol^{-1} for [^{NMe3}LCuOH][BArF$_{24}$]$_2$. However, a large difference was found in the second-order rate constants for the reactions between the complexes and DHA (-25 ˚C, DFB): 2.8(7) M^{-1} s^{-1} for [^{NMe3}LCuOH][BArF$_{24}$]$_2$ and 400(22) M^{-1} s^{-1} for [^{SO3}LCuOH][K(18-crown-6)]$_2$ (~150 times faster). The slow HAA kinetics observed for [^{NMe3}LCuOH][BArF$_{24}$]$_2$ were explained by the steric crowding of the bulky [BArF$_{24}$]$^-$ anions that are associated with the Cu(III) complex. This conclusion was corroborated by reacting [^{NMe3}LCuOH][BArF$_{24}$]$_2$ with 1,4-

cylcohexadiene (CHD), similar C–H BDE to DHA but overall a smaller substrate, in identical conditions and the rate was found to be 10 times faster with CHD than the rate with DHA.[33]

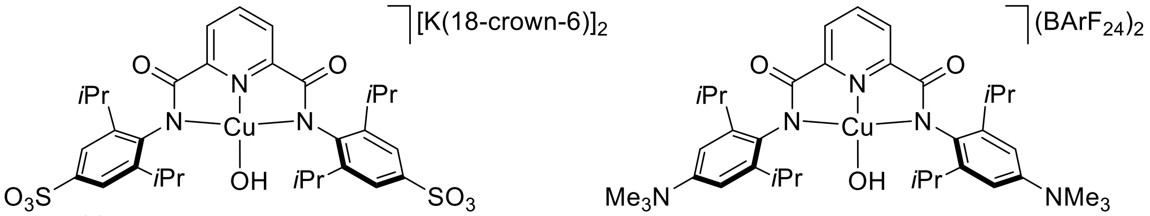

$[^{SO3}LCuOH][K(18\text{-}crown\text{-}6)]_2$ $[^{NMe3}LCuOH][BArF_{24}]_2$

Figure 1.17. Cu-hydroxide complexes explored for charge effects.[33]

1.3.4 *LCuO$_2$CR complexes*

While the LCuX system provides an apt platform for studying copper-oxygen complexes that are closely biomimetic, the system has been extended to X ligands that are not necessarily ligands expected in biological oxidations. The exploration of X ligands provides information of the generality of the LCuX chemistry in oxidation processes. One X ligand of note that was studied was *m*-chlorobenzoate (*m*CBA). The complex [NBu$_4$][LCu*m*CBA] was synthesized via the protonolysis reaction between *m*-chlorobenzoic acid and LCu*m*CBA was prepared by a 1-electron oxidation. The reactions between LCu*m*CBA and C–H and O–H substrates were studied experimentally and computationally, which revealed mechanistic nuances of the oxidations.[37] Furthermore, other LCuO$_2$CR complexes (Figure 1.18) were generated, and the electronic influences of the carboxylate ligands on the properties of the complexes and their reactivities were examined.[31]

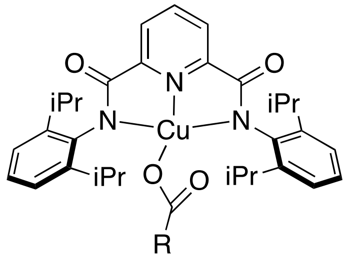

R = CH_3, $C_6H_4(OMe)$, C_6H_5,
$C_6H_4(m\text{-}Cl)$, $C_6H_4(NO_2)$, C_6F_5

LCuO$_2$CR

Figure 1.18. Structure of LCuO$_2$CR complexes.

Notably, cyclic voltammogram experiments revealed the oxidation potential of the [LCu*m*CBA]$^{-/0}$ couple as 157 mV vs Fc$^{0/+}$. The addition of 1 eq. of [AcFc][BArF$_{24}$] to THF solutions of [NBu$_4$][LCu*m*CBA] at -80 °C generated two new highly absorbing features at 650 and 830 nm. These features were assigned as LMCTs from the amide and flanking aryl π-system to the Cu d_{x2-y2} orbital. As expected for oxidized copper species, the EPR spectrum was silent. The experimental and computational data, along with precedence, are taken as confirmation for the assignment of the Cu(III) state for LCu*m*CBA.[37]

The PCET reactivity of LCu*m*CBA was probed using two substrates, 2,4,6-tri-*t*-butylphenol (TTBP) and DHA. The reaction between LCu*m*CBA and TTBP in THF at -80 °C yielded LCuTHF, as determined by UV-vis spectroscopy, and the TTBP phenoxyl radical, which was identified by EPR spectroscopy. The products of the reaction are consistent with a PCET reaction, and the second-order rate constant was calculated to be 3×10^{-1} M^{-1} s^{-1}. When LCu*m*CBA was treated with DHA in DFB at -25 °C, the PCET product of anthracene was detected by GC-MS, and the second-order rate constant was calculated as 1.1×10^{-1} M^{-1} s^{-1}.[37] DFT was used to understand which O-atom is the preferred site for HAA since both atoms could be the reactive site because of conjugation. Free energies of activation were calculated for the HAA at either site and suggested the distal carbonyl O-atom is the preferred site for HAA from TTBP and DHA by 8.7 and 4.5 kcal mol^{-1}, respectively.[37]

The mechanism of HAA by LCu*m*CBA was studied in detail computationally by looking at the electronic structures along the reaction coordinate. The change in the dipole moment over the reaction coordinate reveal the separation of the proton and electron from each other is relatively large along the reactions of LCu*m*CBA and TTBP and DHA, implicating cPCET mechanisms with both substrates (Figure 1.19). An understanding of the mechanisms was further developed by intrinsic bond orbital analysis, which depicted the proton transfer occurred from the substrates to the carboxylate ligand and electron transfer occurred from the substrates to the Cu metal through the flanking aryl π-system (Figure 1.20). Furthermore, proton-coupled electron transfers can occur with the proton and electron transferring together (synchronous), the proton transfer character can dominate early in the transition state (basic asynchronous), or the electron transfer character can dominate early in the transition state (oxidative asynchronous). The asynchronicity factor of the reactions revealed the reactions to be oxidative asynchronous, in accordance with the high oxidation potential measured for [LCu*m*CBA], and could be, in part, responsible for its HAA reactivity since asynchronous PCET reactions are known to have accelerated rates compared to synchronous reactions.[37]

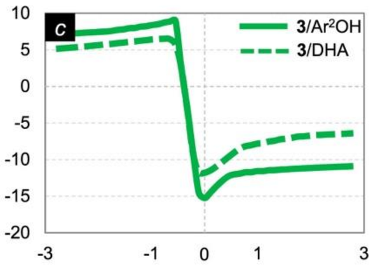

Figure 1.19. The total dipole moment as the HAA reaction proceeds for LCu*m*CBA with 2,6-DTBP (solid line) and DHA (dashed line). Reprinted with permission from ref. 30. Copyright 2019 American Chemical Society.

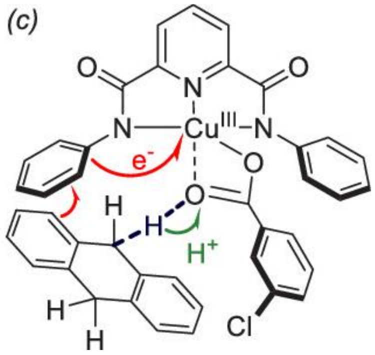

Figure 1.20. Representation of the proton and electron transfers during the HAA reactions of LCuOH with DHA. Reprinted with permission from ref. 30. Copyright 2019 American Chemical Society.

Previously, ligand perturbation experiments for the LCuOH complexes were borne out through functionalizing the L ligand. However, the carboxylate ligands allowed for electronic modifications on the fourth ligand. Various substituted benzoates and acetate were explored and their Cu(III) complexes displayed typical Cu(III) spectroscopic features. Several interesting trends were observed. Firstly, the oxidation potentials of the $[LCuO_2CR]^{-/0}$ couples (THF, vs $Fc^{0/+}$) were found to be smaller with increasing RCO_2H aqueous pK_a values (Figure 1.21), depicting the trade-off between the oxidation potential of the complex and its basicity.

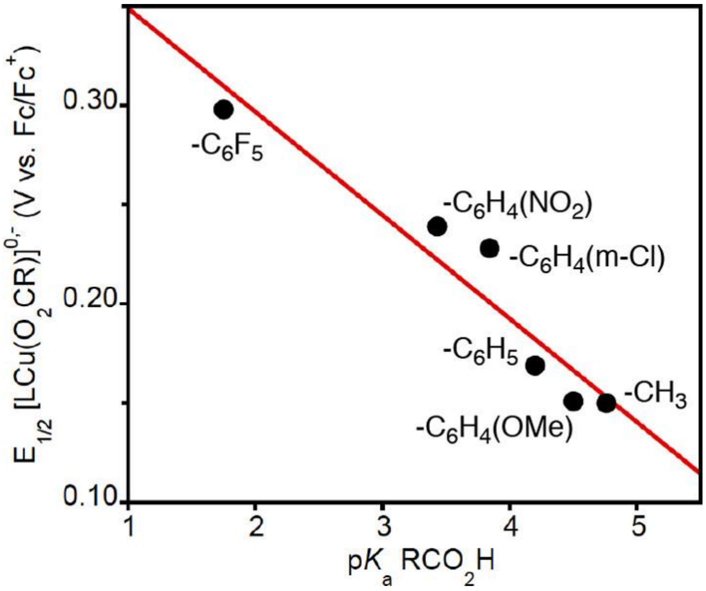

Figure 1.21. Plot of $E_{1/2}$ for the $[LCuO_2CR]^{0/-}$ couple (THF) vs the pK_a of RCO_2H (aqueous). The red line is a linear fit to the data ($R^2 = 0.91$). Reprinted with permission from ref. 31. Copyright 2019 American Chemical Society.

Additionally, the position of the lowest energy LMCT peak in the Cu(III)-carboxylate UV-vis spectra was dependent on the RCO_2H aqueous pK_a values (Figure 1.22). This trend is consistent with a more acidic RCO_2H resulting in a more electron-withdrawing ligand and a more electrophilic Cu center. Lastly, the second-order rate constants of the reactions between $LCuO_2CR$ and TTBP (-80 ˚C, THF) increased with higher $E_{1/2}$ values for the $[LCuO_2CR]^{0/-}$ couples (THF, vs $Fc^{0/+}$) (Figure 1.23). These results are consistent with faster HAA rates for the complexes that are more oxidizing.[31]

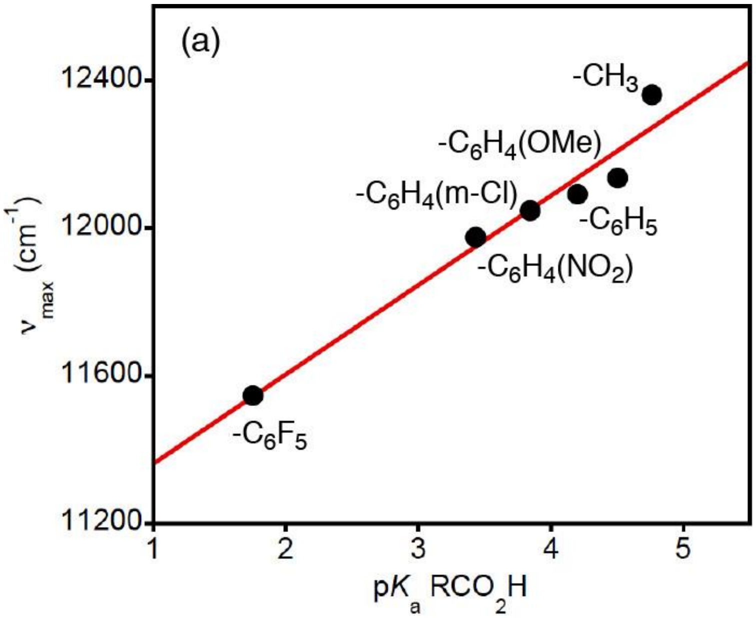

Figure 1.22. Plot of ν_{max} for the lowest energy feature in the UV-vis spectra for LCuO$_2$CR complexes (THF) vs the pK_a of RCO$_2$H (aqueous). The red line is a linear fit to the data ($R^2 = 0.96$). Reprinted with permission from ref. 31. Copyright 2019 American Chemical Society.

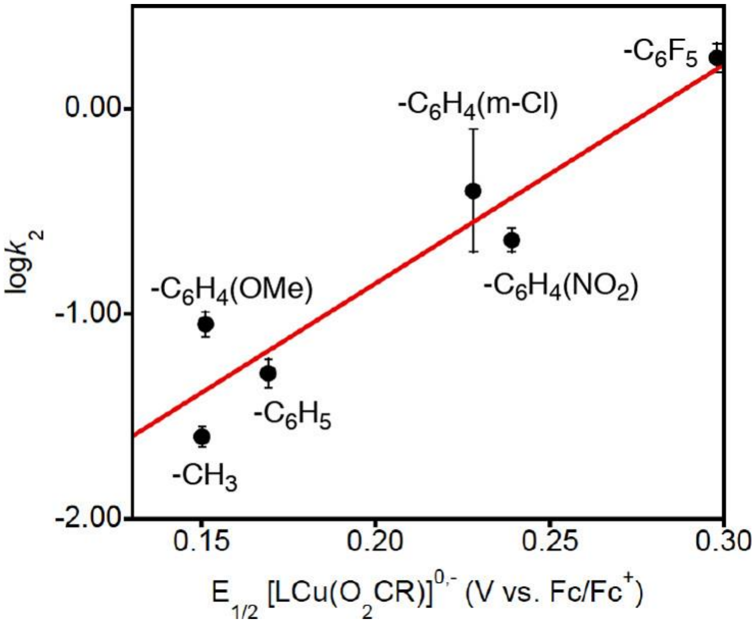

Figure 1.23. Plot of logk_2 for the reactions between LCuO$_2$CR complexes and TTBP (-80 ˚C, THF) vs the $E_{1/2}$ for the [LCuO$_2$CR]$^{0/–}$ couple (THF). The red line is a linear fit to the data ($R^2 = 0.90$). Reprinted with permission from ref. 31. Copyright 2019 American Chemical Society.

1.3.5 LCuX (X = halides) complexes

LCuX (X = F, Cl, and Br) were sought after to explore C(sp^3)–H halogenation. Cu(II) chloride and bromide salts are known to induce C(sp^3)–H halogenation but Cu(II) fluoride salts are not.[27] However, the [Cu-F]$^{2+}$ moiety was hypothesized to have the ability to perform C(sp^3)–H fluorination because of reports of hole-type character on the ligands of oxidized copper species, i.e. copper nitrene complexes.[38,39] The [NBu$_4$][LCuX] (X = F, Cl, and Br) complexes were synthesized by reacting the corresponding [NBu$_4$][X] salt with LCuMeCN. LCuX (X = F, Cl, and Br), were accessed using a potent oxidizing agent and were characterized using spectroscopic techniques and X-ray crystallography. The hydrogen-atom abstraction (HAA) and radical capture (RC) reactivity of the LCuX (X = F, Cl, and Br) complexes were explored along with the ability of LCuF to perform C(sp^3)–H fluorination.[27]

The oxidation potentials of the [LCuX]$^{-/0}$ (X = F, Cl, and Br) couples were measured as 465 mV for X = F and 525 mV for both X = Cl and Br (vs Ag/AgNO$_3$ in CH$_2$Cl$_2$). Therefore, a stronger oxidant like [NAr$_3$]PF$_6$ was needed to generate the LCuX (X = F, Cl, and Br) species. The oxidized species exhibit at least two highly absorbing UV-vis peaks each between 400 and 1000 nm (CH$_2$Cl$_2$, -80 °C) that red-shift with decreasing donor strengths of the X ligand. TD-DFT identified these transitions, in accordance with the previously discussed Cu(III) complexes, to LMCTs from halide orbitals to the Cu d$_{x2-y2}$ orbital.[27]

The thermal stabilities of the LCuX complexes were relatively high so the complexes were examined using ^{1}H NMR spectroscopy, a technique usually not used with Cu(III) complexes because the spectra start to broaden out with traces of paramagnetic Cu(II). However, the ^{1}H NMR spectra of the thermally stable LCu-halide complexes exhibited sharp resonances in the 0 – 9 ppm range, signifying an $S = 0$ ground state. X-ray crystallography was also a viable technique for the LCuX complexes because of their stabilities. The crystal structures established the generation of LCuX complexes as there were no counterions present in the structures. Additionally, the Cu(III) metal centers displayed square planar geometries, the same geometry as seen in the Cu(II) complexes, again substantiating the low reorganization energy from the Cu(II) to Cu(III) in LCuX complexes.[27,36]

The electronic structures of the Cu(III)-halide complexes were probed with XAS, looking at the Cu K-edge. The rising edge shift from the Cu(II) complexes to the oxidized species was found to be 1.4 eV for all the Cu-halides, confirming the species is oxidized.[27] However, the exact electronic structures, Cu(III)-X^- character or Cu(II)-X• character, is disputed by the differing interpretations of CASSFC calculations and XAS rising edge shifts.[27,40]

A hypothetical mechanism for C(sp^3)–H fluorination by LCuF was determined to be subsequent HAA/RC reactions, so those processes were investigated. The HAA reactivity of LCuX (X = F, Cl, and Br) was researched using the substrate DHA. It was found that LCuF (k_2 = 6.7 x 10^{-1} M^{-1} s^{-1}) reacts with DHA in CH_2Cl_2 at -30 ºC much faster (200 times) than LCuCl (k_2 = 2.3 x 10^{-3} M^{-1} s^{-1}) and LCuBr (k_2 = 3.0 x 10^{-3} M^{-1} s^{-1}) under the same conditions. The rapid rate of HAA reactivity by LCuF must be of consequence of the higher basicity of LCuF since LCuCl and LCuBr are more oxidizing species than LCuF. This concept is again illustrated when you compare the HAT rates of LCuF with DHA (k_2 = 6.7 x 10^{-1} M^{-1} s^{-1}, CH_2Cl_2 at -30 ºC) to LCuOH with DHA (k_2 = 24 M^{-1} s^{-1}, acetone at -30 ºC) and the pK_a of F^- (15) to the pK_a of OH^- in DMSO (30).[27]

The propensity for LCuX (X = F, Cl, and Br) to do RC was investigated by using substrates that are carbon-based radical precursors. The Cu(II)- and Cu(III)-halides were reacted with azobis(isobutyronitrile) (AIBN) in CH_2Cl_2 at 80 ºC. The Cu(II) complexes did not react with AIBN but the Cu(III) complexes yielded the 2-haloisobutyronitriles in modest yields. Additionally, the Cu(III)-halides were reacted with Gomberg's dimer, which is in equilibrium with the trityl radical in solution, in CH_2Cl_2 at -80 ºC and produced the triphenylmethyl halide products in good yields (Figure 1.24). The rates of the RC reactions with the trityl radical were similar for all the Cu(III) complexes but differences appear in the reaction pathways (Figure 1.24). LCuF reacts with the trityl radical directly, or synchronously, where the UV-vis traces of the reactions of LCuCl and LCuBr with the trityl radical reveal an intermediate, the triphenylmethane cation. Therefore, it was concluded that LCuCl and LCuBr react with the trityl radical in a stepwise fashion, an electron transfer followed by halide transfer.[27]

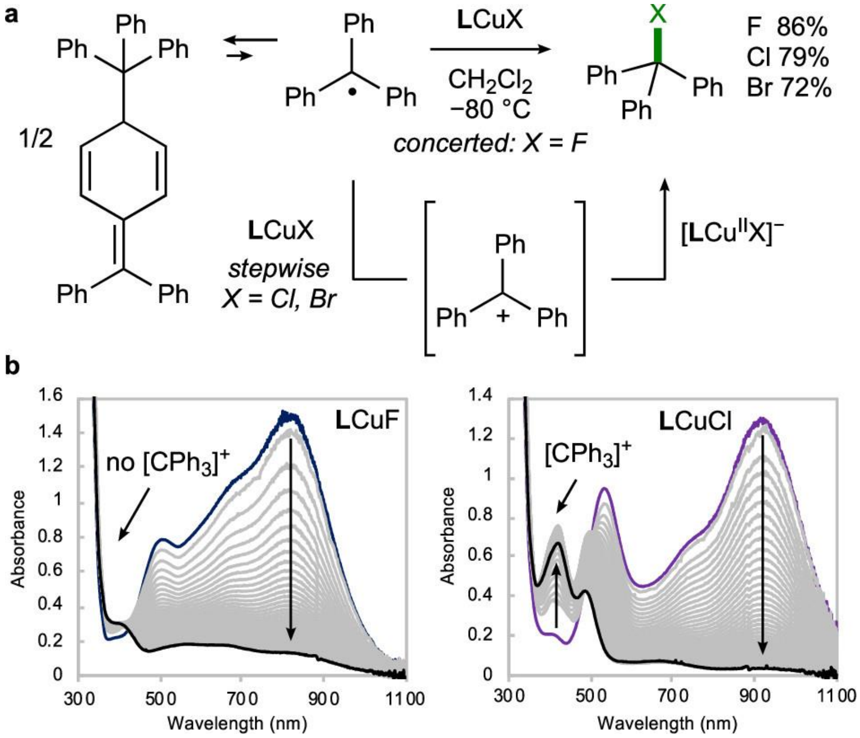

Figure 1.24. LCuX reactivity with Gomberg's dimer. Reprinted with permission from ref. 27. Copyright 2020 American Chemical Society.

The capability of LCuF to perform HAA and RC set precedence for LCuF to perform C(sp^3)–H fluorination. A variety of C(sp^3)–H substrates were treated with 2 eq. of LCuF, necessary stoichiometry to induce HAA and RC, to yield fluorinated products. The substrate scope included α-ether, allylic, and benzylic C–H containing molecules, all formed in low to moderate yields. This report was the first to demonstrate that LCuX complexes are capable of "rebound" reactions, a pivotal step in LPMO oxidations.[27]

1.4 Copper-nitrite chemistry

Copper-nitrite complexes have been studied as mimics for the enzymes copper nitrite reductases (CuNIRs).[41] CuNIRs, enzymes critical in the biogeochemical nitrogen cycle (Figure 1.25), catalyze the one electron reduction of nitrite to NO.[41,42] The structure and function of CuNIRs are well known and the field has been bolstered by model complexes as discussed in the following sections.

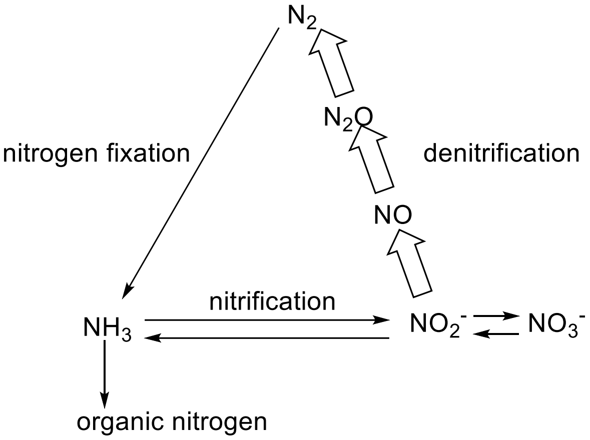

Figure 1.25. Biogeochemical nitrogen cycle. Adapted from ref. 42.

1.4.1 Copper nitrite reductase enzymes (CuNIRs)

The biogeochemical nitrogen cycle represents the redox chemistry of inorganic nitrogen on Earth (Figure 1.25), which directly impacts the available nitrogen for living organisms. Overall, atmospheric dinitrogen, N_2, is transformed to ammonia, NH_3, by nitrogen fixation, which is the source of bioavailable nitrogen. Ammonia undergoes nitrification to yield nitrite, NO_2^-, (or nitrate, NO_3^-) which is converted back to N_2 via denitrification. The first step in denitrification is the transformation of NO_2^- to NO, a step mediated by bacterial nitrite reductases. Two types of nitrite reductases are known, multi-heme and copper.[42]

X-ray structures of CuNIRs reveal the enzyme is a trimer with two Cu sites in each monomer. One Cu site is a type 1 Cu, which is responsible for the highly absorbing, low energy UV-vis spectroscopic features that give the enzymes their blue or green color. This site is bound to two histidine residues, a methionine, and a cysteine (Figure 1.26). The cysteine ligand gives rise to the previously mentioned UV-vis features, characterized as a S(Cys) to Cu charge transfer. This Cu site performs an electron transfer in the reduction of nitrite. The second Cu site is a type 2 Cu site bound to three histidine residues and a water (in the absence of substrate) to form a distorted tetrahedral geometry about the Cu (Figure 1.26). This Cu site is the binding site for nitrite, as observed in X-ray structures of oxidized CuNIR crystals grown in the presence of nitrite.[41,42] The nitrite ion is bound to the type 2 Cu(II) through both O atoms in an asymmetric fashion (Figure 1.27). The Cu–O bond distances differ from structure to structure,[41,42] but recent high-resolution data revealed lengths of 1.98(2) Å and 2.13(6) Å in one structure and 2.13(2) Å and 2.22(5) Å in another.[43] Structures of substrate-bound reduced CuNIR enzymes have been reported also showing asymmetric binding of nitrite to Cu(I) through the two O atoms,[41] a stark difference to common Cu(I)-nitrite model complexes (*vide infra*).[41,44–47] Lastly, the structures reveal conserved H-bonding networks, which can aid in the proton-assisted nitrite reduction.[42,48]

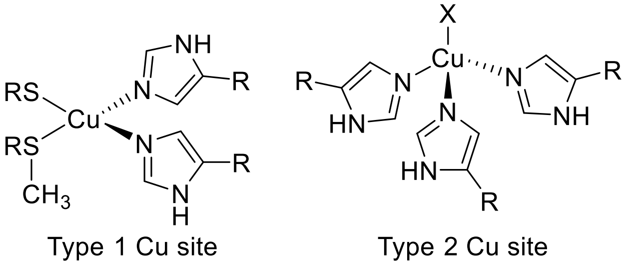

Figure 1.26. Type 1 and Type 2 Cu coordination environments in CuNIR enzymes. Adapted from ref. 49.

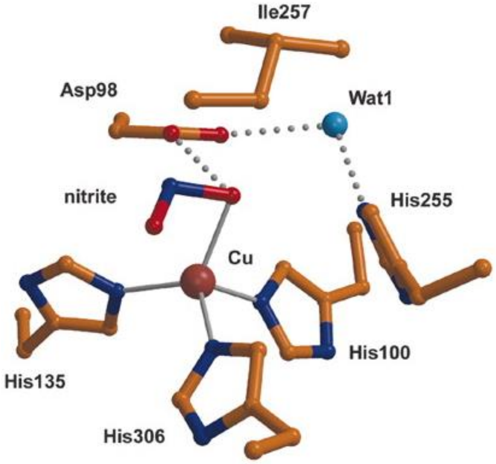

Figure 1.27. Nitrite-bound type 2 Cu(II) in a CuNIR enzyme. PDB: 1SJM. Reprinted with permission from ref. 50. Copyright 2004 American Association for the Advancement of Science.

The overall reaction for CuNIR enzymes is a one-electron, two-proton reduction of NO_2^- to NO and H_2O.[41,42] Many mechanisms have been proposed based on structures obtained from CuNIR enzymes and model complexes and these have been reviewed.[41] One commonly proposed mechanism (Figure 1.28) for this reaction begins with the type 2 Cu(II) site binding NO_2^-, forming a Cu(II)-nitrite adduct. An electron from the type 1 Cu complex reduces the type 2 site forming a Cu(I)-nitrite species that subsequent proton-transfer transforms to a Cu(I)-HNO_2 adduct. N–O bond cleavage in the Cu(I)-HNO_2 adduct is facilitated by a proton transfer, releasing NO regenerating the water-ligated type 2 Cu(II).[41,42] Other proposed mechanisms differ in when the electron transfer occurs (before or after nitrite coordination) and whether NO is bound to the Cu after the N–O bond cleavage step since NO bound CuNIR adducts have been observed.[41]

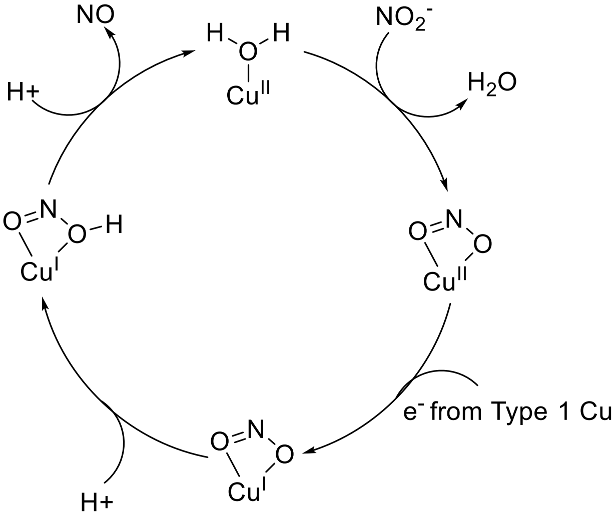

Figure 1.28. Proposed mechanism for CuNIR mediated reduction of nitrite. Adapted from ref. 41.

1.4.2 *Model Cu-nitrite complexes*

Model complexes for CuNIR have included Cu(I)- and Cu(II)-nitrite complexes. The supporting ligands for these complexes vary widely but the nitrite binding tends to be N-bound for Cu(I) and N- or O-bound for Cu(II). Nitrite has multiple coordination modes: η^1-NO_2, η^1-ONO, and η^2-ONO and all have been observed in Cu-nitrite complexes (Figure 1.29). The reactivity of the Cu-nitrite complexes typically mimics that of CuNIR, NO release, but oxygen-atom transfer, proton-coupled electron transfer, and nitrosation of nucleophiles have all been explored as well.

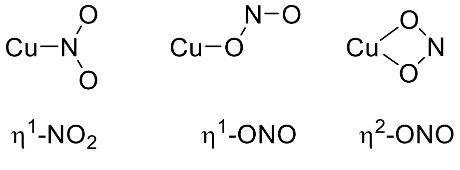

Figure 1.29. Possible coordination modes of nitrite to copper.

In one example, a Cu(I)-nitrite complex supported by an isopropyl-substituted TACN ligand (TACN = 1,4,7-triisopropyl-1,4,7-triazacyclononane) showed the NO_2^- ligand coordinated through its N atom. This nitrite coordination mode was found in other Cu(I)-nitrite structures where the range of Cu–N bond lengths is 1.883 – 2.087 Å.[44,46,51] At least two Cu(I)-nitrite complexes, supported by phosphine ligands, contain a η^2-ONO bound nitrite ligand in their structures.[52,53] There are numerous Cu(II)-nitrite complexes that have been synthesized, characterized, and previously reviewed.[41] All three binding modes of nitrite have been observed in Cu(II)-nitrite complexes.[41] The bond lengths for η^1-ONO bound Cu(II)-nitrites are outlined in Chapter 3, Section 3.2.1.

As Cu(I)-nitrite complexes are proposed key intermediates in the reduction of NO_2^- by CuNIR, reactions of synthetic Cu(I)-nitrite complexes were examined to understand if the complexes could act as functional mimics of CuNIR. When ^{iPr3}TACN-Cu(I)-NO_2 was reacted with 2 eq. of acetic acid, NO and ^{iPr3}TACN-Cu(O_2CCH_3)$_2$ were detected (Scheme 1.2).[47] Other Cu(I)-nitrite complexes were also found to similarly release NO,[46,52–59] supporting the notion that synthetic Cu(I)-nitrite complexes are functional models of CuNIR and that a Cu(I)-nitrite adduct is a viable intermediate in the CuNIR mechanism. Another example of a CuNIR model reaction used a Cu(I) complex with a tripodal ligand containing aryl hydroxyl groups in proximity of the open coordination site of the Cu (Figure 1.30). When the complex was treated with nitrite, NO and a new Cu(II)-aqua complex with the doubly oxidized tripodal ligand were detected.[60] This is a unique example of nitrite reduction by a Cu(I) site via a proton and electron transfer facilitated by the proton-responsive ligand.

Scheme 1.2. Reaction of ^{iPr3}TACN-Cu(I)-NO_2 with 2 eq. of acetic acid[47]

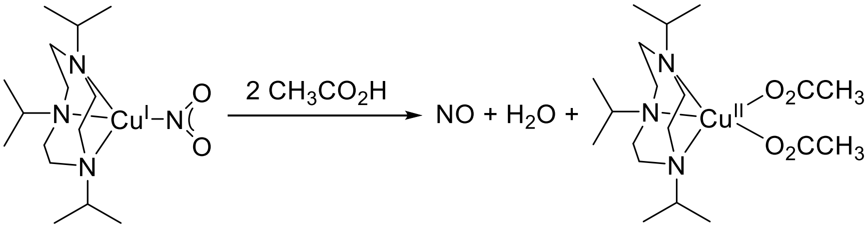

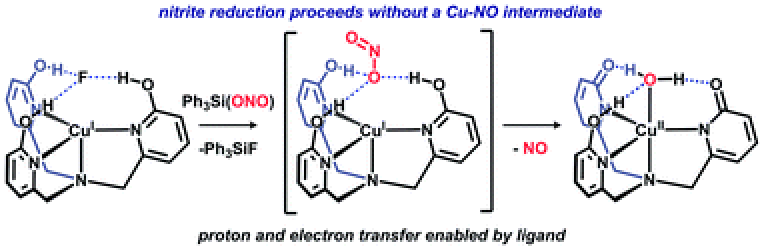

Figure 1.30. Ligand-assisted nitrite reduction reactivity of a Cu(I)-nitrite complex. Reprinted with permission from ref. 60. Copyright 2015 Royal Society of Chemistry.

Diverse reactivity of Cu(II)-nitrite complexes has been reported (Figure 1.31). Cu(II)-nitrite complexes have shown oxygen atom transfer reactivity with substrates such as phosphines and isocyanides.[51,61] Additionally, reaction of a Cu(II)-nitrite complex with nucleophiles resulted in nitrosated products via a nucleophilic attack by the substrate on the nitrite ion in the complex.[62,63] Another Cu(II)-nitrite complex with a tripodal ligand containing a cryptand cap was found to react with phenols to form NO, a Cu(II)-hydroxide adduct, and the oxidized phenol products. The reaction products and kinetic isotope effect experiments indicated this reaction proceeds via a PCET pathway. Lastly, when the cryptand-capped Cu(II)-nitrite complex was protonated then treated with phenol, the oxidized phenol product and, interestingly, the nitrated phenol were observed. This was a unique example of phenol nitration by a Cu(II)-nitrite complex.[64]

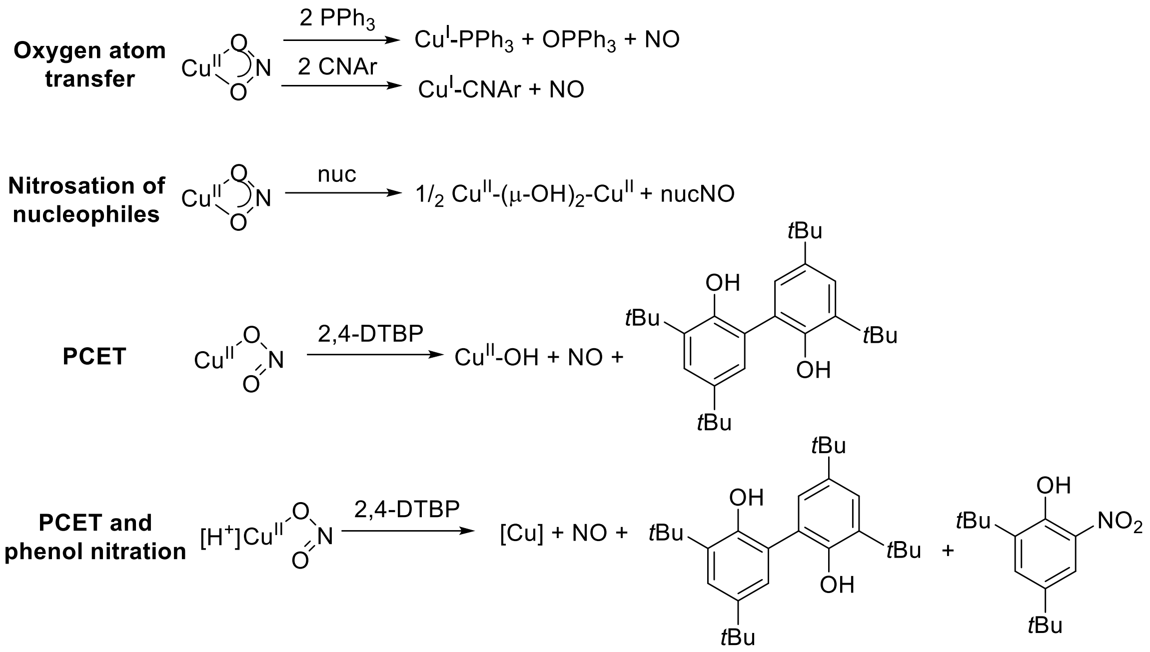

Figure 1.31. Examples of Cu(II)-nitrite reactivity.

1.5 Copper-nitrogen complexes

C–N bond formation is an invaluable transformation in synthetic chemistry for making natural products,[65,66] pharmaceuticals,[67–69] commodity chemicals,[70] and materials.[71,72] Copper has been identified as a metal suitable for multiple routes to form C–N bonds, which often include copper-nitrogen complexes delivering the N-unit. These routes include C–N bond coupling and C–H amination reactions. C–N bond coupling reactions often invoke Cu-amide intermediates[73] and C–H amination reactions often invoke Cu nitrenoid intermediates.[74] These intermediates have been studied extensively and will be discussed in this introduction.

1.5.1 Copper-amide species and C–N coupling reactions

Copper mediated C–N bond coupling reactions are facile and convenient transformations that have become commonly used synthetic tools. Two examples are Chan-Evans-Lam coupling reactions (Scheme 1.3 top), where Cu(II) salts couple arylboronic acids and nucleophiles (C–H, N–H, S–H, and P–H),[75] and Ullmann coupling reactions (Scheme 1.2 bottom), which use Cu(0), Cu(I), or Cu(II) sources to couple aryl halides and nucleophiles (C–H, N–H, O–H, S–H, and P–H).[76] Many mechanisms have been considered for the two reactions[75,77] but a common mechanism proposed involves the

Cu(I)/Cu(II)/Cu(III) oxidation states in an oxidative addition-reductive elimination cycle. Notably, Cu(II)- and Cu(III)-amide species are proposed intermediates in this mechanism when considering N–H nucleophiles.[75,77] The oxidative addition-reductive elimination cycle, Cu(II)-amide complexes, and an example of modelling the proposed Cu(III)-amide intermediate are outlined in Chapter 4, Section 4.1.

Scheme 1.3. General reactions for Chan-Evans-Lam coupling reactions (top) and Ullmann coupling reactions (bottom)

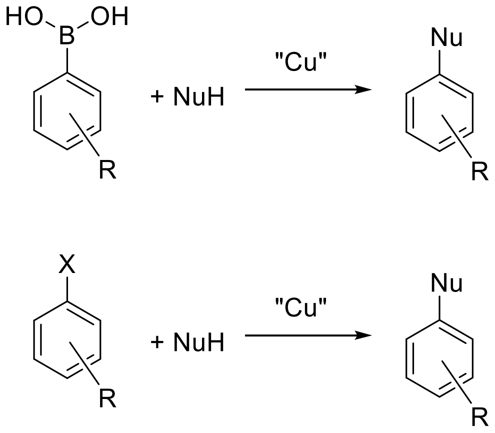

1.5.2 *Copper nitrenoid species and C–H amination reactions*

Copper(I) complexes have been shown to oxidize C–H substrates in the presence of nitrene sources (Scheme 1.4). Nitrene sources (“NR”) include iminoiodinanes and azides, among others.[74] It is proposed that the nitrene source oxidizes the Cu(I) and forms a transient copper nitrenoid species. The electronic structure of these species is not entirely clear.[78] Examples of dicopper bridged nitrenoids have been observed[74,79–82] (proposed to be in equilibrium with a mononuclear nitrenoid through reactivity)[79,83] and a recent example of a Cu(I)-inverted nitrene has been isolated.[78] Formally, the transient copper nitrenoid species is proposed to react with relatively weak C–H bonds via a hydrogen atom abstraction and radical rebound pathway to form the products, the aminated substrate and the Cu(I) starting material. Mechanistic work has shown this transformation to occur stepwise rather than concerted.[79]

Scheme 1.4. A general depiction of the oxidation of R–H substrates in the presence of nitrene sources and Cu(I).

$$\text{R'-H} + \text{"NR"} \xrightarrow{\text{Cu}^{\text{I}}} \text{R-NHR'} + \text{Cu}^{\text{I}}$$

1.6 Research objectives

A guiding principle for my projects is to investigate how ligand perturbations impact copper complexes and their reactivity. In the second chapter of my dissertation, I discuss the development of monoanionic ligands as alternatives to L^{2-} for the synthesis of biomimetic copper-oxygen complexes. The monoanionic ligands discussed in Chapter 2 mimic the active site of LPMO more closely than L^{2-}. The synthesis and characterization of Cu(I) and Cu(II) complexes bearing the new monoanionic ligands are discussed. The attempts at accessing Cu-oxygen complexes are also detailed.

The third chapter of my dissertation features the synthesis and characterization of a new $[LCuX]^-$ complex, $[LCuNO_2]^-$. The 1-electron oxidation of $[LCuNO_2]^-$ to $LCuNO_2$ is described and the evidence for the formulation of LCu(III)-NO_2 is elaborated. Many Cu(II)-nitrite complexes have been studied in the past; however, the Cu(III)-nitrite adduct in Chapter 3 is the first example of its type. The reactivity of $LCuNO_2$ with phenols is also explored. We found that $LCuNO_2$ can perform PCET with 2,4,6-tri-*t*-butylphenol and can perform unusual anaerobic phenol nitration with 2,4-di-*t*-butylphenol. Mechanistic hypotheses for phenol nitration are deliberated.

In the fourth chapter of this dissertation, the LCuX system is extended to X = amides. Two different ligands were explored, N-methylbenzamide and acetanilide. The synthesis and characterization of the Cu(II) compounds, the 1-electron oxidation of the Cu(II) compounds, and the PCET reactivity with 2,4,6-tri-*t*-butylphenol are all discussed. All these aspects are compared with the results of studies from copper-oxygen complexes. Together, the results of the studies described herein provide important fundamental insights into (a) the copper coordination chemistry of monoanionic ligands that mimic the active site of LPMO and (b) electronic structure, bonding, and reactivity of oxidized, formally Cu(III) complexes with nitrite and amide ligands. This knowledge will inform efforts to understand oxidation catalysis and possible pathways for organic transformations that use copper catalysts.

Chapter 2

Cu complexes supported by monoanionic N,N’,N’’ ligands: Modeling the tridentate ligand set of LPMO

2.1 Introduction

In the subject area of challenging substrate oxidations, lytic polysaccharide monooxygenase (LPMO) is an important biological example of a catalyst capable of activating dioxygen to cleave strong C–H bonds, in this case those in cellulose and associated polymers to yield short chain oligomers.[15,84–87] While the structure of LPMO and its active site is well known,[9,14] the precise mechanism of oxygen activation and subsequent oxidation of the cellulose substrate and how the structural motif of the active site of LPMO supports these processes remains the subject of extensive research efforts.

It is known that the active site of LPMO contains a mononuclear copper center with three conserved coordinating groups: two histidine residues and a more unusual third group, the amine terminus of the protein chain (Figure 2.1). This terminus belongs to one of the coordinating histidine residues, thereby forming a metalacyclic moiety dubbed the “histidine brace”.[14] The enzyme is unreactive when the Cu center is in the +2 oxidation state, but upon reduction to Cu(I) the active site can react with O_2 to generate oxidizing species.[20] As is typically the case with metalloenzymes, the protonation state of the ligands is ambiguous, although neutral or monoanionic environments are usually proposed.[6,18] Specifically, the deprotonated amino terminus, which has been observed in neutron diffraction studies,[18] yields a monoanionic ligand set about the Cu ion placing the anionic site *trans* to the oxygen binding site. This electronic environment would stabilize highly oxidized species that are proposed as intermediates in LPMO.[14] Even though the specific Cu species responsible for the proposed rate-determining step of hydrogen atom transfer (HAT) from saccharide substrates is unknown, several Cu-oxygen cores have been implicated, such as $[\text{Cu-OO}]^+$, $[\text{Cu-OH}]^{2+}$, and $[\text{Cu-O}]^+$.[6,9,88,89] These cores have been studied in model complexes, in the gas-phase, and/or computationally and have been shown to be competent at HAT from various O–H and C–H bonds.[5,9,11–27]

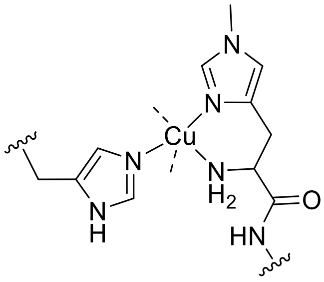

Figure 2.1. Active site of lytic polysaccharide monooxygenase (LPMO) enzymes, showing only the conserved ligands.

We have previously demonstrated that formally Cu(III)-OH species using a family of dianionic pyridine dicarboxamide pincer ligands (Figure 2.2) can be prepared, and that they perform rapid proton-coupled electron transfer (PCET) reactions.[23–25,29,34] However, due to the very strongly donating nature of these ligands, which is proposed to be required for accessing the high oxidation state, Cu(I) complexes of this ligand appear not to be accessible. As a result, it is not possible to use O_2 directly to produce reactive oxidizing species, a reaction that is a cornerstone of many bioinorganic processes.[8] Instead, introduction of free superoxide to the Cu(II) complexes of the ligand is required to produce $[Cu–OO]^+$ species.[21,26,32] These systems are not closely biomimetic with regard to LPMO, which can access Cu(I) and does not have a highly anionic ligand environment. To achieve a more biomimetic system, we sought to design ligands that placed a carboxamido group in the central position with flanking neutral N donors. We hypothesized this donor set would sufficiently decrease the overall donor strength, which would allow us to access to the Cu(I) state, enabling reactions with O_2 to be observed while potentially retaining the accessibility of the formally Cu(III) state.

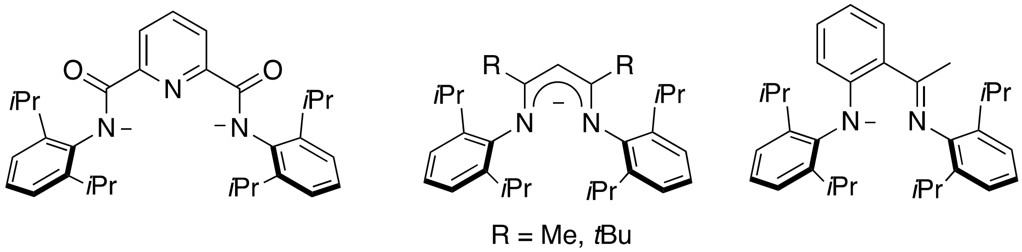

Pyridine dicarboxamide β-diketiminate anilido-imine

Figure 2.2. Previously studied ligands for Cu-oxygen chemistry.

In support of this hypothesis, many mononuclear Cu-O_2 adducts that are formed by the reaction of Cu(I) complexes with dioxygen feature monoanionic bidentate supporting ligands, although these are typically bidentate, such as β-diketiminates or anilido-imines (Figure 2.2).[7,96,97] These adducts typically exist as transient species or side-on species with properties intermediate between Cu(II)-superoxo and Cu(III)-peroxo moieties that are unreactive with hydrocarbon substrates.[7,98,99] We suspected that adding a third arm to a similar ligand motif could force the formation of biomimetic end-on copper-dioxygen species by blocking the extra coordination position of the Cu center.

Thus inspired, we designed two novel N,N',N'' ligands that provide a ligand donor environment more in line with the active site of LPMO, employing a central amide group within a tridentate framework. These ligands, **HL^1** and **HL^2** (Figure 2.3) feature the pyridine carboxamide fragment paired with a substituted pyrazolyl group. This design places the amide in the middle position similar to what is present in LPMO, from where it could, in principle, promote back-bonding to dioxygen via the *trans* effect.

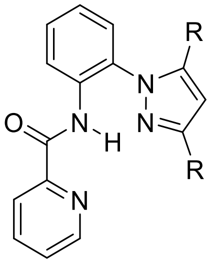

HL^n
n = 1 : R = Me
n = 2 : R = *i*Pr

Figure 2.3. Ligands studied in this work.

As described in the following discussion, we succeeded in synthesizing the target ligands and exploring their copper coordination chemistry. Ultimately, however, we faced several issues with these systems which thwarted our main goal of generating reactive copper-oxygen species. Nonetheless, we believe that the development of new ligands and complexes is significant. Specifically, the literature examples of Cu complexes with monoanionic N,N',N'' ligands employing a central anionic group are fairly limited,[34–64] and further modification of the ligand scaffolds presented here could yield future successes with copper-oxygen chemistry.

2.2 Synthesis and characterization of **HL^1** and **HL^2**

The pyridine-carboxamide-pyrazole proligands **HL^1** and **HL^2** were synthesized in three steps according to Scheme 2.1. A previous report detailed the synthesis of 2-aminophenyl-1*H*-pyrazole and the installation of the group to various aroyl moieties.[131] We mimicked these syntheses to access **HL^1** and **HL^2** by using 3,5-disubstituted pyrazoles, instead of unsubstituted pyrazole, and 2-picolinic acid, instead of other aryl carboxylic acids. In the syntheses of **HL^1** and **HL^2**, the first step yielded the 2-nitrophenyl-1*H*-3,5-disubstituted pyrazoles via a nucleophilic aromatic substitution of 1-fluoro-2-nitrobenzene with NaH and the 3,5-disubstituted pyrazoles in dry THF. The reactions proceeded at room temperature for 2 h each at which point they were quenched, and an aqueous wash removed the salt byproducts. Column chromatography was necessary to isolate the 2-nitrophenyl-1*H*-3,5-disubstituted pyrazoles away from the 1-fluoro-2-nitrobenzene, resulting in modest isolated yields of 73% for 2-nitrophenyl-1*H*-3-5-dimethylpyrazole and 66% for 2-nitrophenyl-1*H*-3-5-diisopropylpyrazole. The following data confirmed that the 2-nitrophenyl-1*H*-3,5-disubstituted pyrazoles were successfully synthesized and isolated: the ^{1}H NMR spectra (Figures 2.4 and 2.5) did not contain the pyrazole N–H protons, the ^{1}H NMR spectra show the methyl group resonances were in an asymmetric environment, ^{13}C NMR spectroscopy revealed 11 resonances for 2-nitrophenyl-1*H*-3-5-dimethylpyrazole (Figure 2.6) and 13 resonances for 2-nitrophenyl-1*H*-3-5-diisopropylpyrazole (Figure 2.7), and the elemental analysis results were within 0.5% of the theoretical values for the compounds.

Scheme 2.1. Syntheses of **HL**^{1} and **HL**^{2}.

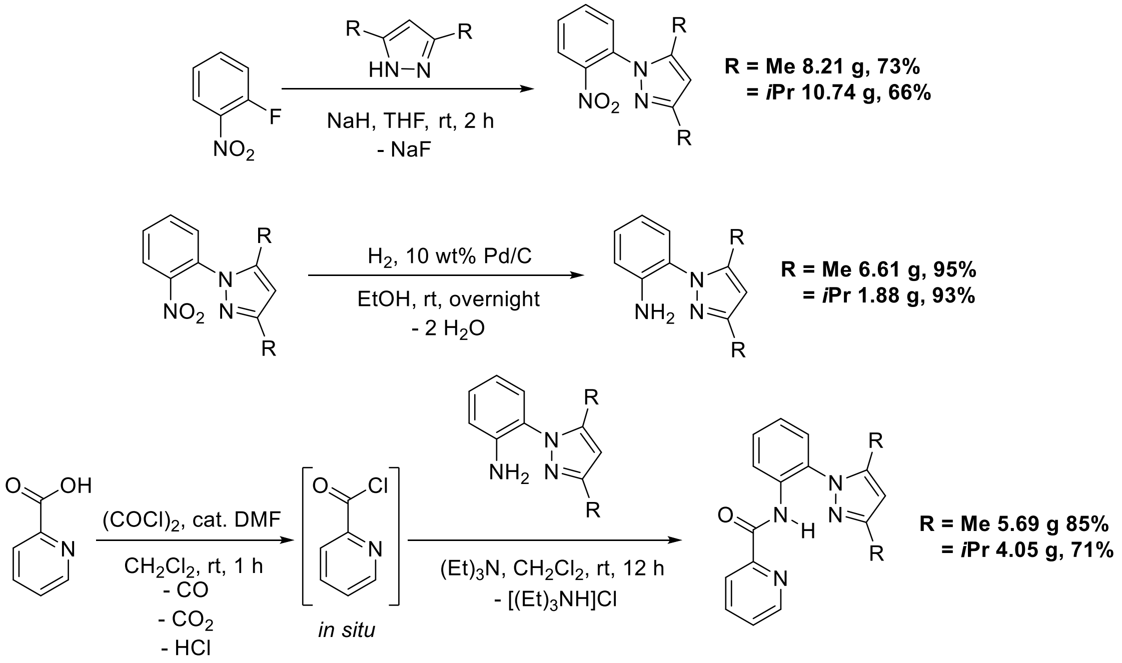

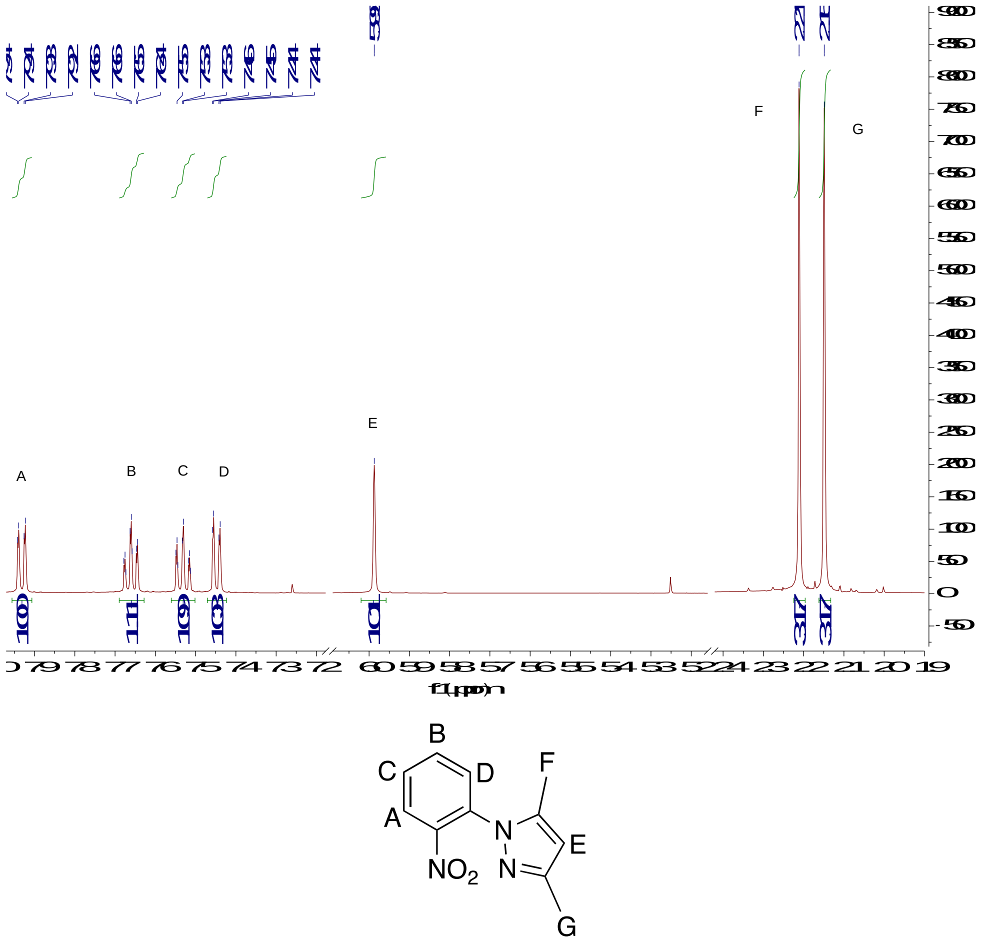

Figure 2.4. ^{1}H NMR spectrum of 2-nitrophenyl-1*H*-3-5-dimethylpyrazole.

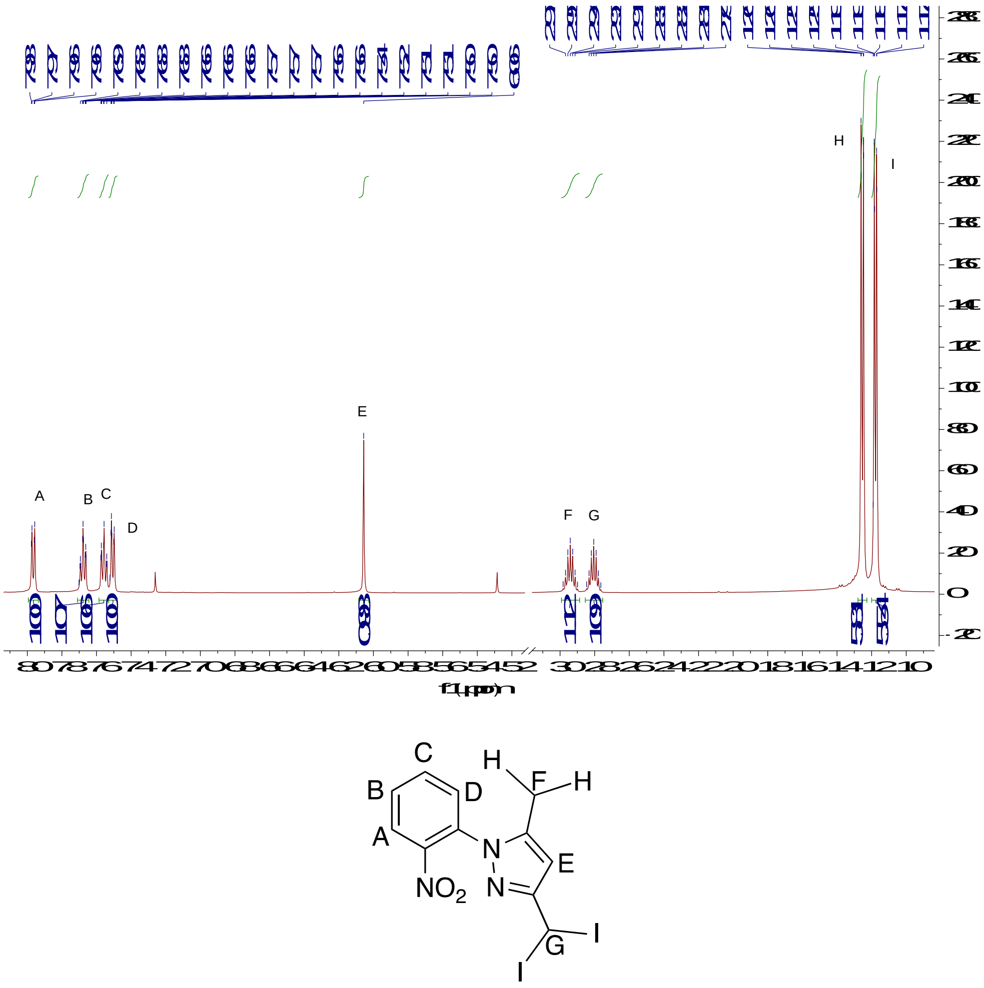

Figure 2.5. ^{1}H NMR spectrum of 2-nitrophenyl-1*H*-3-5-dimethylpyrazole.

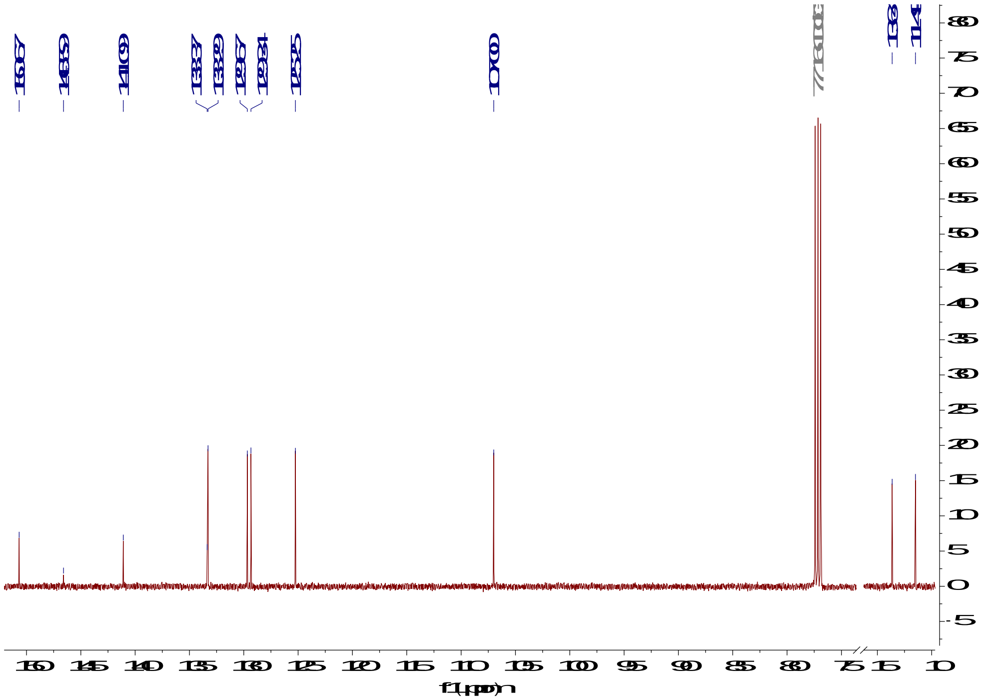

Figure 2.6. ^{13}C NMR spectrum of 2-nitrophenyl-1*H*-3-5-dimethylpyrazole.

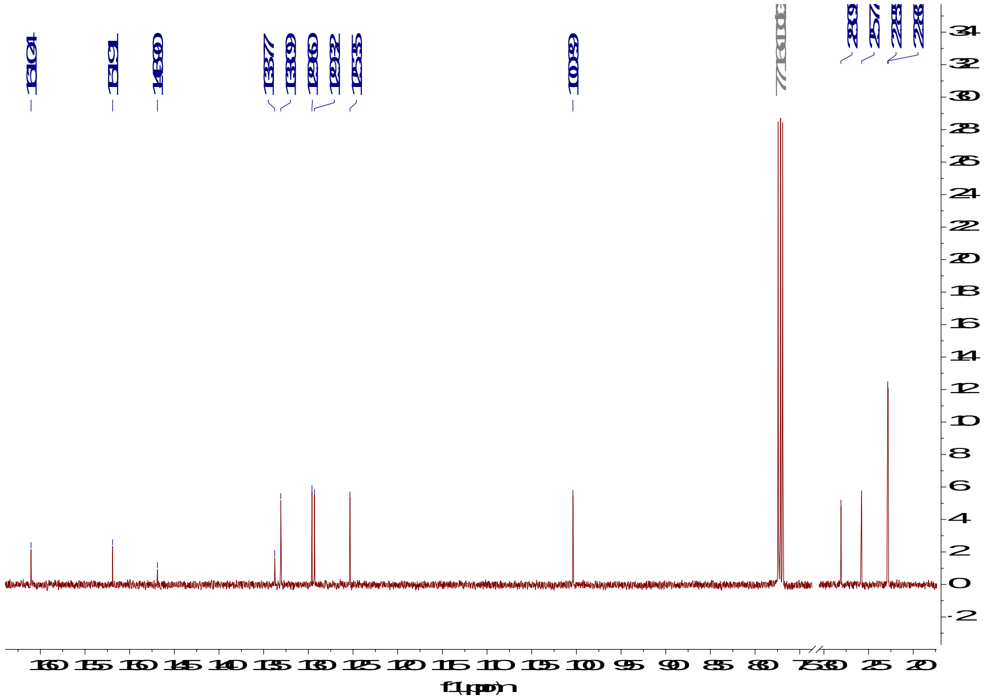

Figure 2.7. ^{13}C NMR spectrum of 2-nitrophenyl-1*H*-3-5-diisopropylpyrazole.

Next, the 2-nitrophenyl-1*H*-3,5-disubstituted pyrazoles were reduced to 2-aminophenyl-1*H*-3,5-disubstituted pyrazoles via palladium-catalyzed hydrogenation in ethanol. While 100 psi H_2 was used overnight for the synthesis of 2-aminophenyl-1*H*-3,5-diisopropylpyrazole, we found 24 h under atmospheric pressures of H_2 yielded 2-aminophenyl-1*H*-3,5-dimethylpyrazole in similar yields, forgoing the need for a pressurized reaction vessel (*note: A safety shield should be placed in front of pressurized systems*). The heterogeneous reaction mixtures were filtered through celite to remove the Pd/C (*note: Residual Pd/C should be wetted with water after filtration to prevent ignition of the solid*). Removing the ethanol thoroughly from the filtrates afforded the clean products in high yields: 2-aminophenyl-1*H*-3,5-dimethylpyrazole as a brown solid in 95% yield and 2-aminophenyl-1*H*-3,5-diisopropylpyrazole as a white solid in 93% yield. The following data indicated the successful syntheses of the 2-aminophenyl-1*H*-3,5-disubstituted pyrazoles: the ^{1}H NMR spectra (Figures 2.8 and 2.9) contained new resonances associated with the aniline N–H protons, the ^{1}H NMR spectra showed an upfield shift of the aromatic resonances, the methyl group resonances in the ^{1}H NMR spectra remained asymmetric, ^{13}C NMR spectroscopy revealed 11 resonances for 2-aminophenyl-1*H*-3-5-dimethylpyrazole (Figure 2.10) and 13 resonances for 2-aminophenyl-1*H*-3-5-diisopropylpyrazole (Figure 2.11), and the elemental analysis results were within 0.5% of the theoretical values for the compounds.

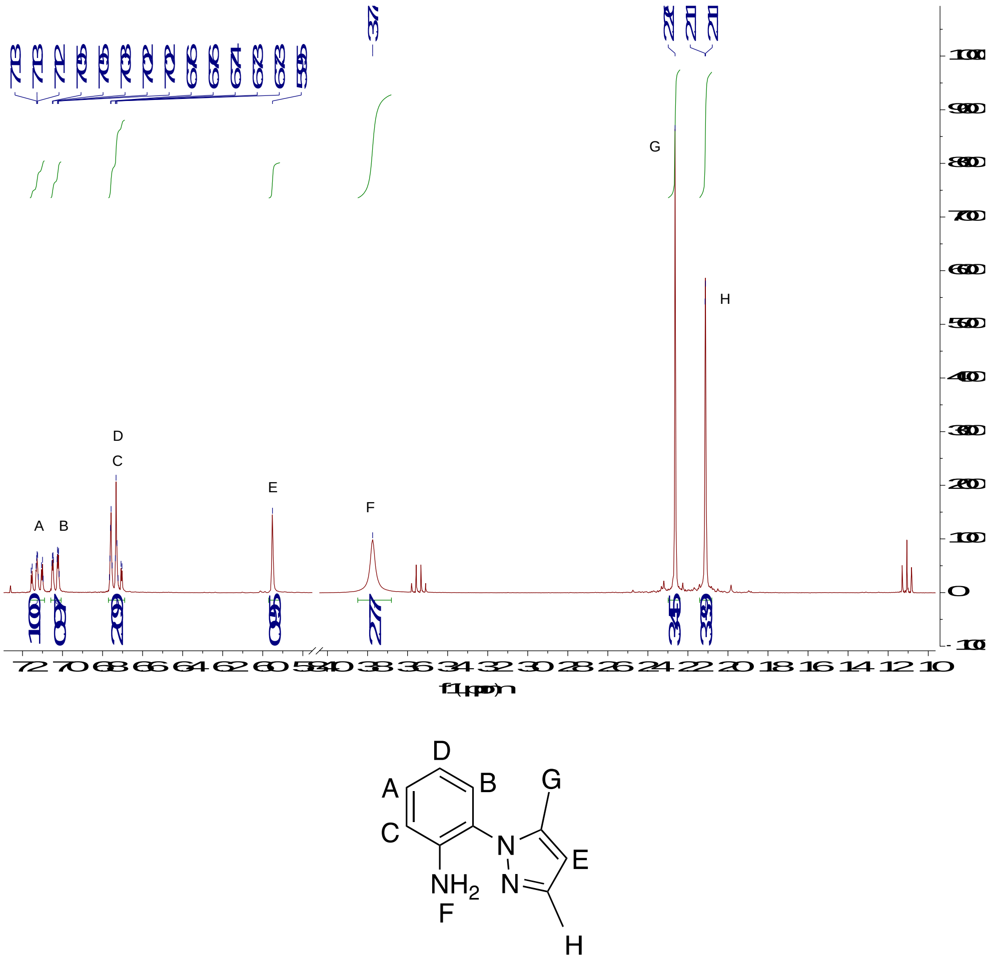

Figure 2.8. ^{1}H NMR spectrum of 2-aminophenyl-1*H*-3-5-dimethylpyrazole.

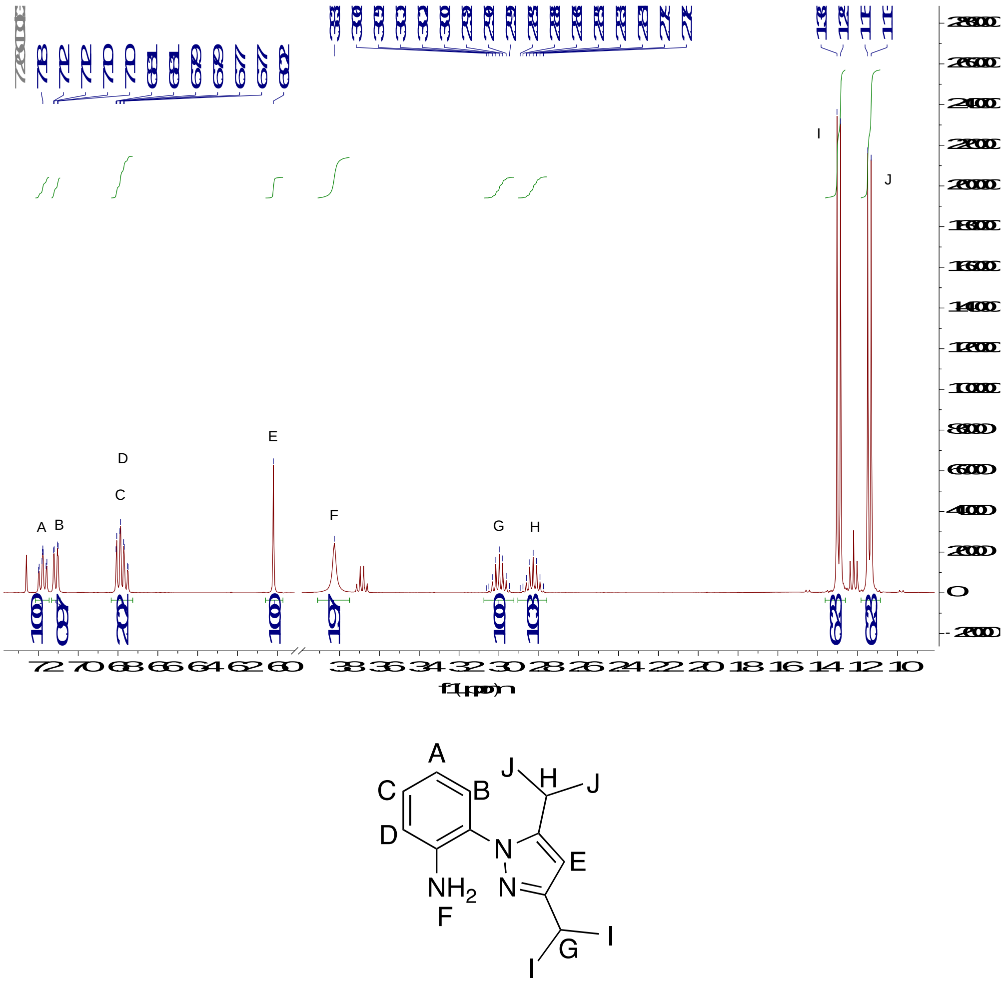

Figure 2.9. ^{1}H NMR spectrum of 2-aminophenyl-1*H*-3-5-diisopropylpyrazole.

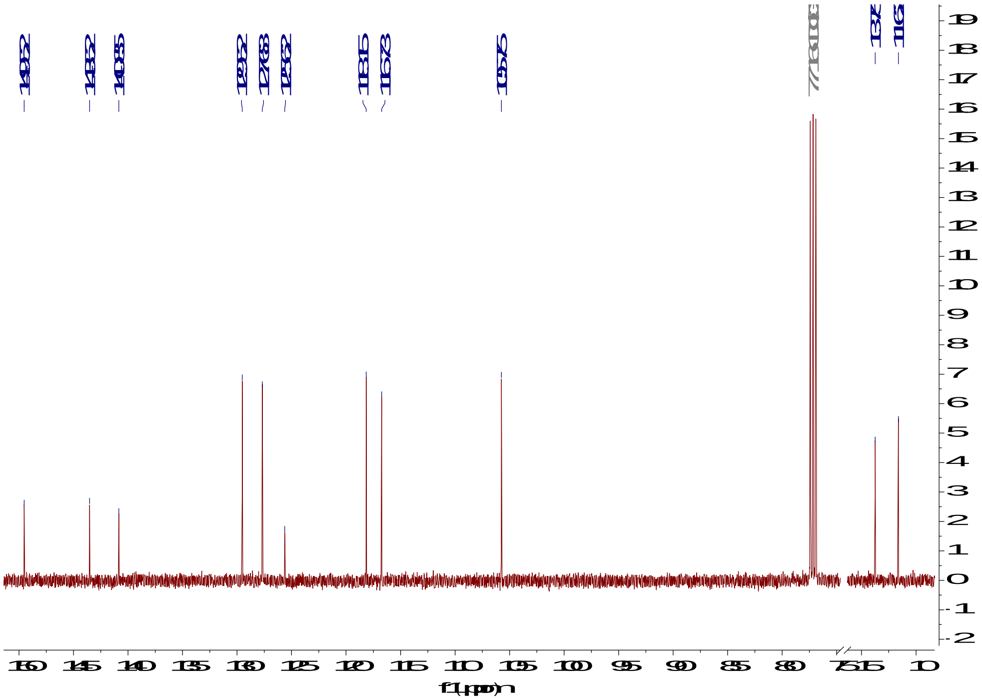

Figure 2.10. ^{13}C NMR spectrum of 2-aminophenyl-1*H*-3-5-dimethylpyrazole.

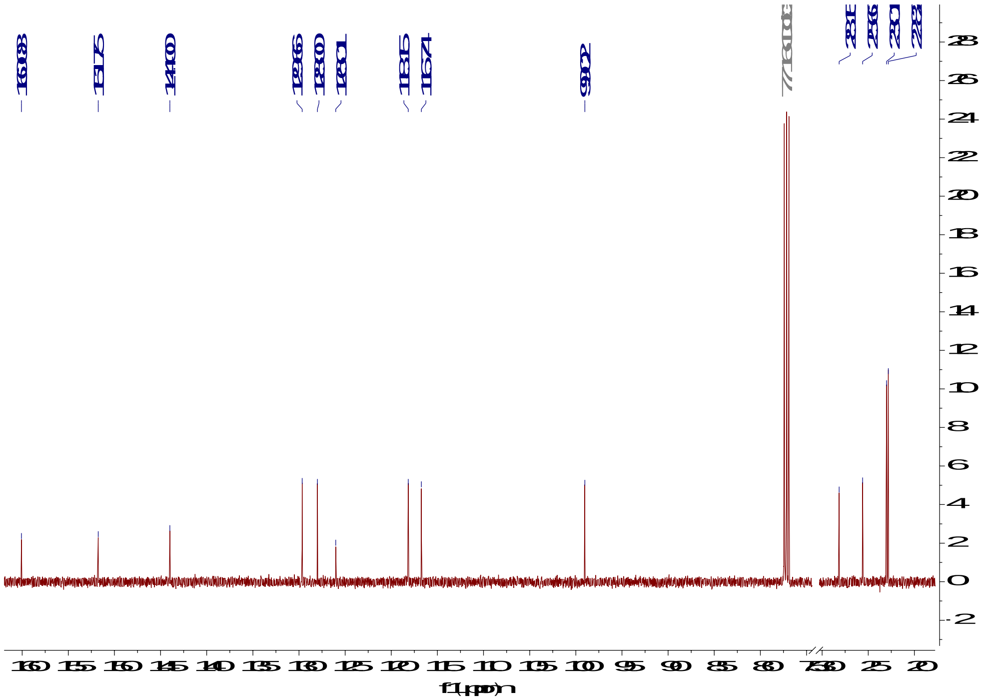

Figure 2.11. ^{13}C NMR spectrum of 2-aminophenyl-1*H*-3-5-diisopropylpyrazole.

Lastly, in the third step, picolinic acid was first transformed to the acyl chloride *in situ* using oxalyl chloride and DMF in CH_2Cl_2. After removal of excess oxalyl chloride (*note: the excess oxalyl chloride was collected in an external trap to be quenched with a saturated aqueous solution of sodium bicarbonate*), the 2-aminophenyl-1*H*-3,5-disubstituted pyrazoles were reacted with the acyl chloride in the presence of triethylamine in CH_2Cl_2. After aqueous washes, column chromatography yielded the proligands $\mathbf{HL^1}$ and $\mathbf{HL^2}$ in 85% and 71% yields, respectively. $\mathbf{HL^2}$ was a white solid while $\mathbf{HL^1}$ was initially yielded as an orange oil that, interestingly, spontaneously solidified into a brown solid months after it was synthesized. Nevertheless, several pieces of data confirmed the successful synthesis and isolation of clean compounds: the ^1H NMR spectra (Figures 2.12 and 2.13) revealed amide N–H protons at the most downfield resonances, new resonances in the ^1H NMR spectra from the pyridine rings were observed at consistent integral ratios, the methyl group resonances in the ^1H NMR spectra remained asymmetric, the ^{13}C NMR spectra had resonances consistent with amide carbonyl shifts and at different values than the picolinic acid carboxylic acid carbon, ^{13}C NMR spectroscopy revealed 17 resonances for $\mathbf{HL^1}$ (Figure 2.14) and 19 resonances for $\mathbf{HL^2}$ (Figure 2.15), and the elemental analysis results were within 0.5% of the theoretical values for the compounds. With confidence in the attainment and purity of $\mathbf{HL^1}$ and $\mathbf{HL^2}$, we sought to use the proligands to prepare copper complexes.

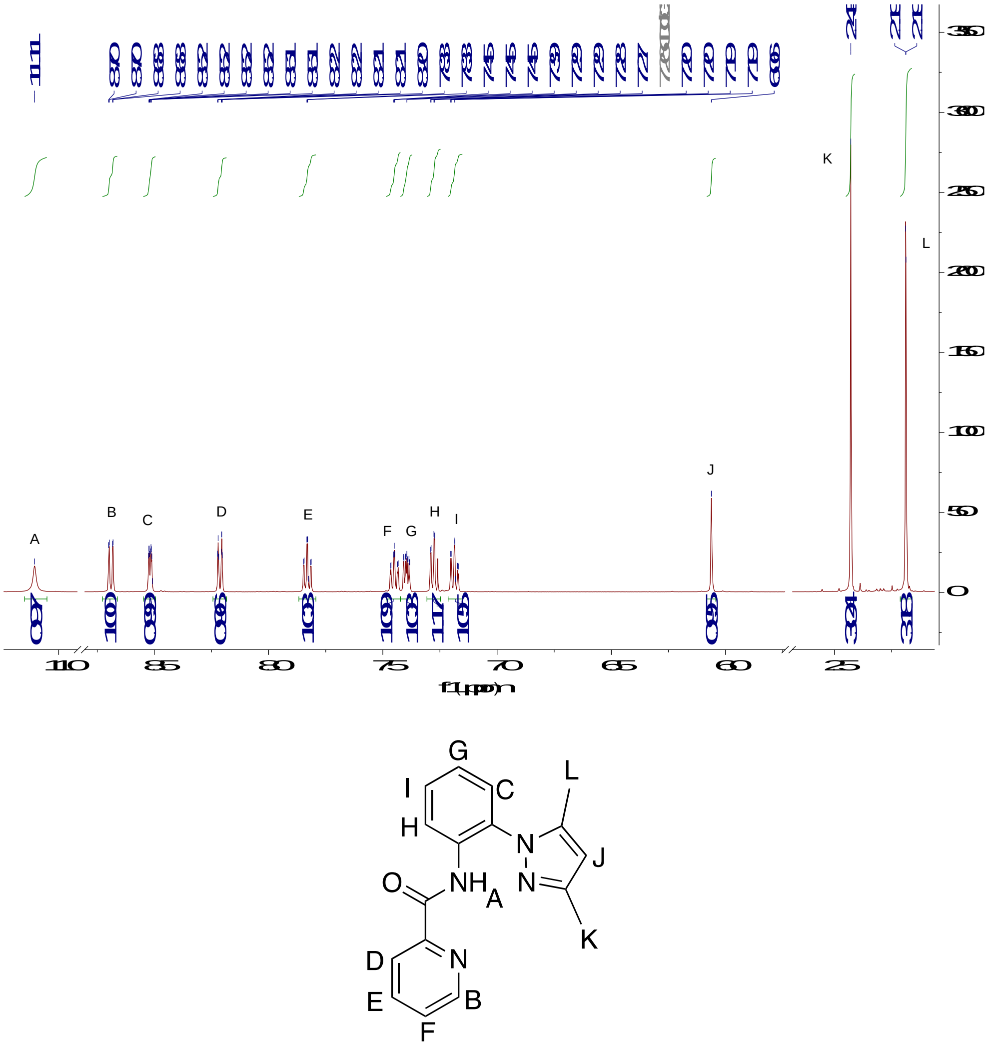

Figure 2.12. ^{1}H NMR spectrum of **HL^1**.

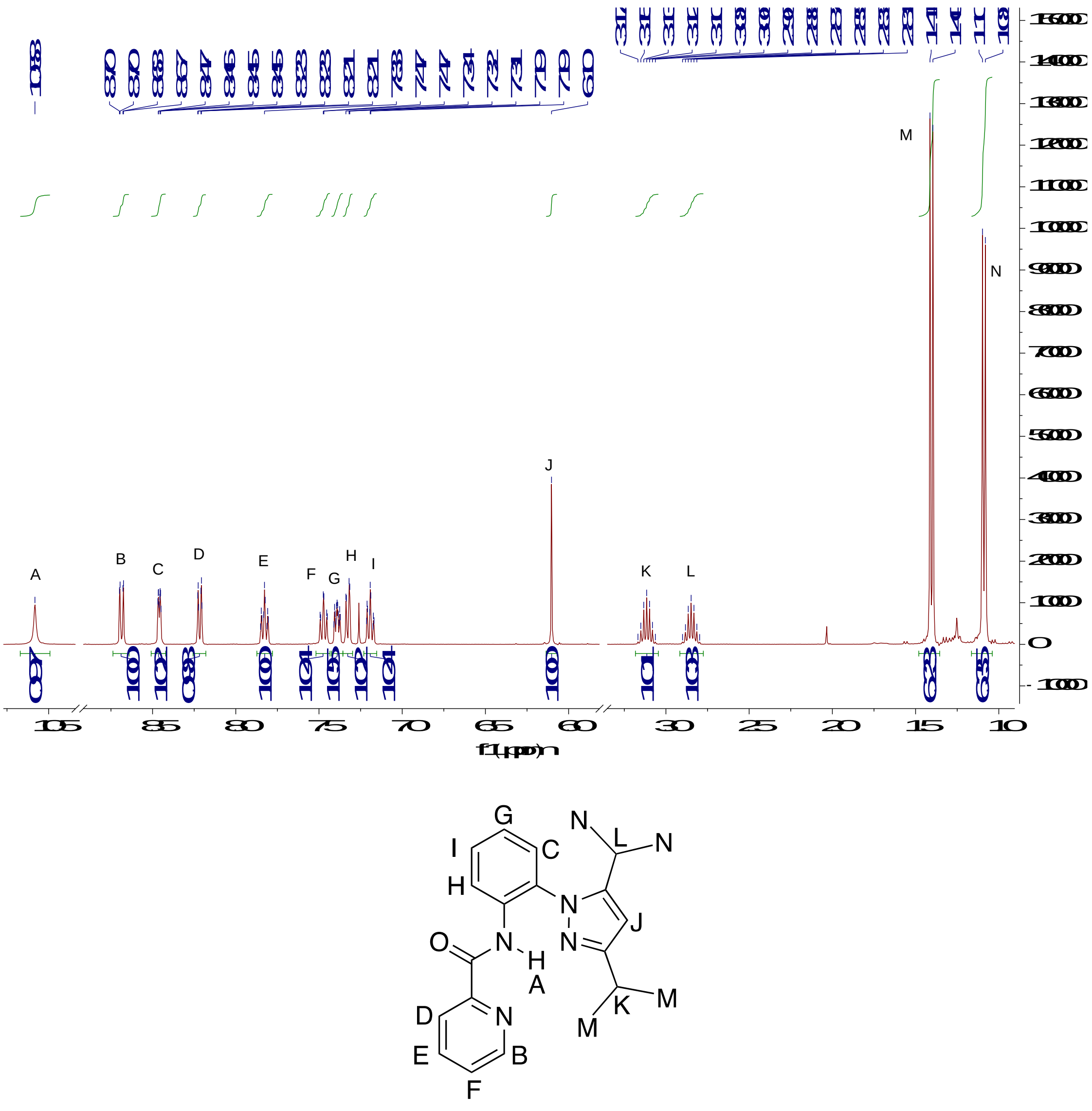

Figure 2.13. ^{1}H NMR spectrum of **HL^2**.

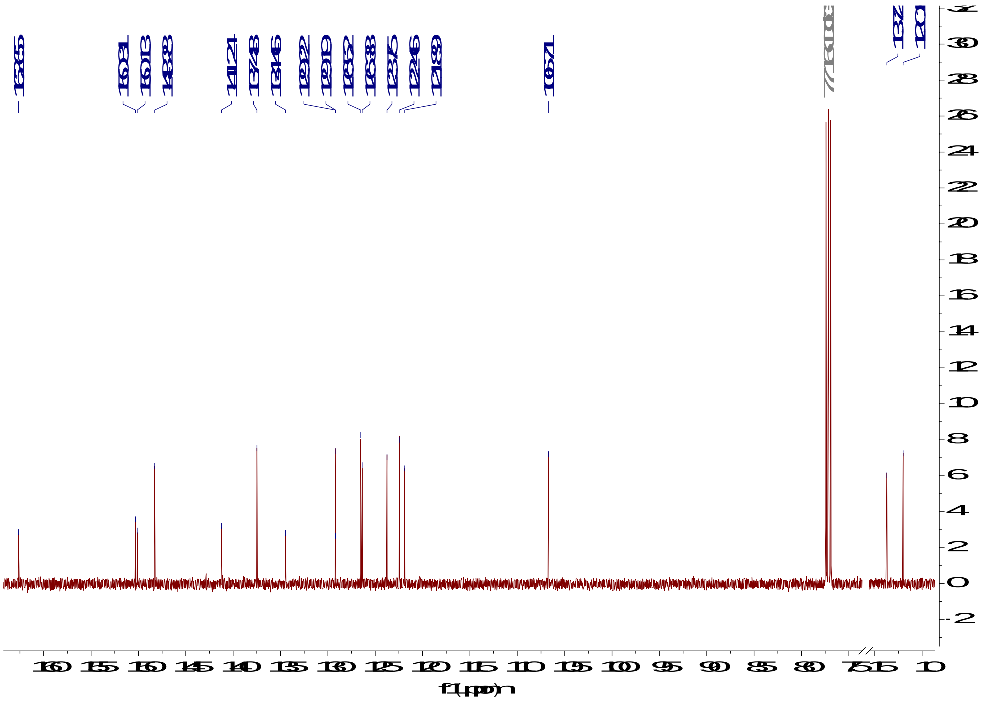

Figure 2.14. ^{13}C NMR spectrum of **HL^1**.

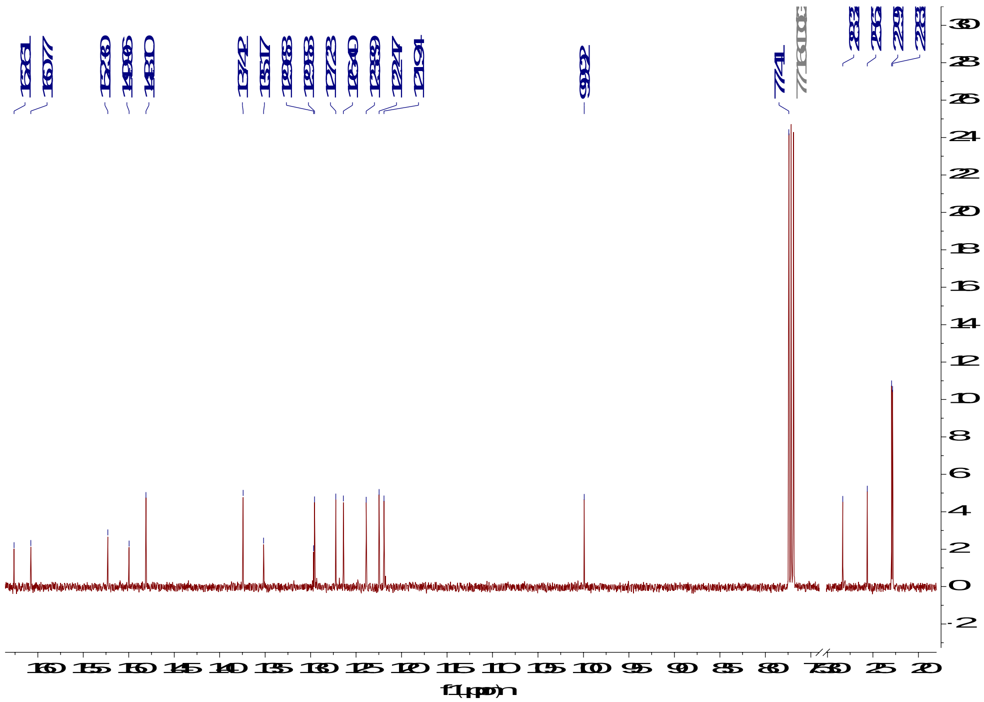

Figure 2.15. ^{13}C NMR spectrum of **HL^2**.

2.3 Synthesis and characterization of $(L^2Cu)_2$

Since the active site of LPMO uses a Cu(I) center to reduce oxygen, we sought to synthesize a mononuclear Cu(I) complex by reacting **HL^2** with KHMDS and $Cu(MeCN)_4OTf$ in MeCN(Scheme 2.2). After addition of the reagents, an orange powder precipitated out of solution and was isolated, rinsed with MeCN, and dried in *vacuo* resulting in 33% yield of the product. Orange crystalline blocks were obtained from a THF/pentane vapor diffusion. The resulting compound was characterized by ^1H and ^{13}C NMR spectroscopy, UV-visible spectroscopy, cyclic voltammetry, elemental analysis, and X-ray diffraction. The ^1H NMR spectrum (Figure 2.16) of the new species depicted a loss of the amide N–H peak and an upfield shift relative to the spectrum of **HL^2** for all peaks, indicating deprotonation and coordination to the copper ion. The ^1H NMR spectrum also shows a splitting of the isopropyl methyl resonances into four doublets, where the proligands only have two doublets. The ^{13}C NMR spectrum of the complex displays 21 resonances (Figure 2.16), consistent with all four methyl groups in **HL^2** being magnetically inequivalent. The UV-vis spectrum of the orange product (Figure 2.18) has features at 426 nm (ε = 16490 M^{-1} cm^{-1}) and 592 nm (ε = 1365 M^{-1} cm^{-1}). Combined, the data support coordination of the ligand to Cu(I).

Scheme 2.2. Metalation of **HL^2** with Cu(I).

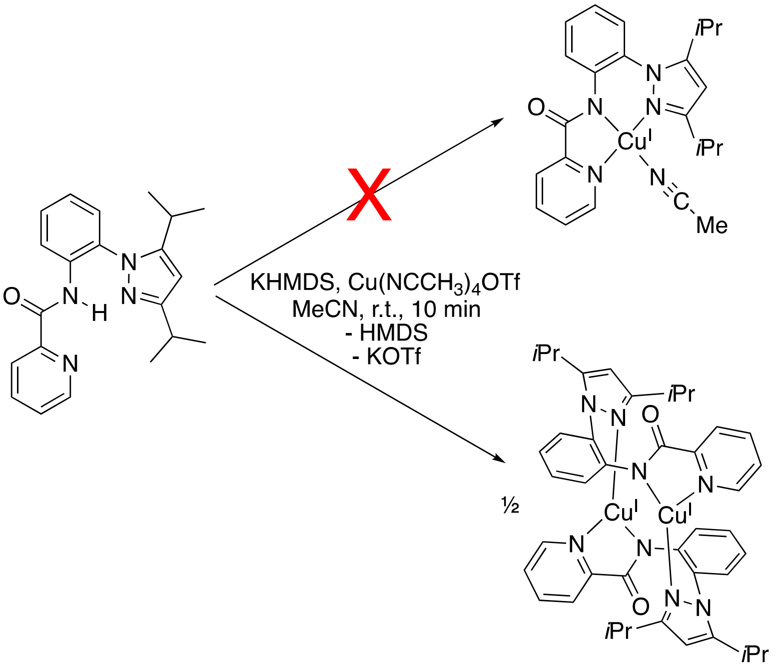

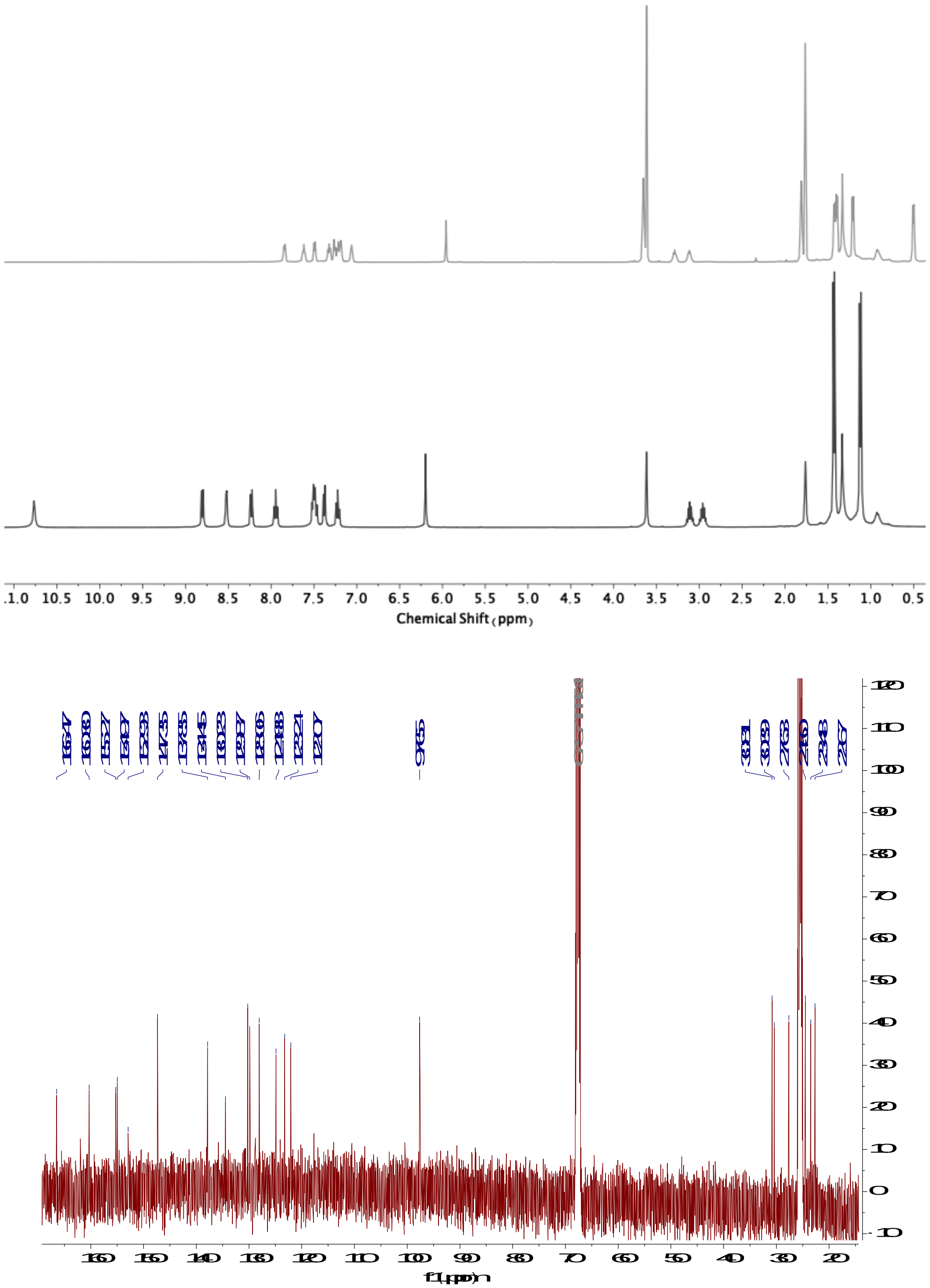

Figure 2.16. ^{1}H NMR spectra overlay of **HL_2** (black, middle) and **$(L^2Cu)_2$** (gray, top) and ^{13}C NMR spectrum of **$(L^2Cu)_2$** (THF-d^8).

The X-ray crystal structure (Figure 2.17) revealed that instead of being mononuclear, the compound is a dimer, **($L^2Cu)_2$**, where each ligand bridges the two copper ions in a (κ^1, κ^2) fashion. The Cu(I) ions adopt distorted trigonal planar geometries. The Cu–N lengths are typical for Cu(I) complexes with N,N,N ligands,[102,114,126,127] and the Cu–Cu distance is 2.7509(7) Å, which is too long for significant bonding interactions between the two metals.[132] The complex contains an inversion center between the two coppers and two ligands resulting in a symmetric dimer. There is another molecule of **($L^2Cu)_2$** in the solid-state unit cell that adopts the same dimer configuration but with slightly different bond lengths.

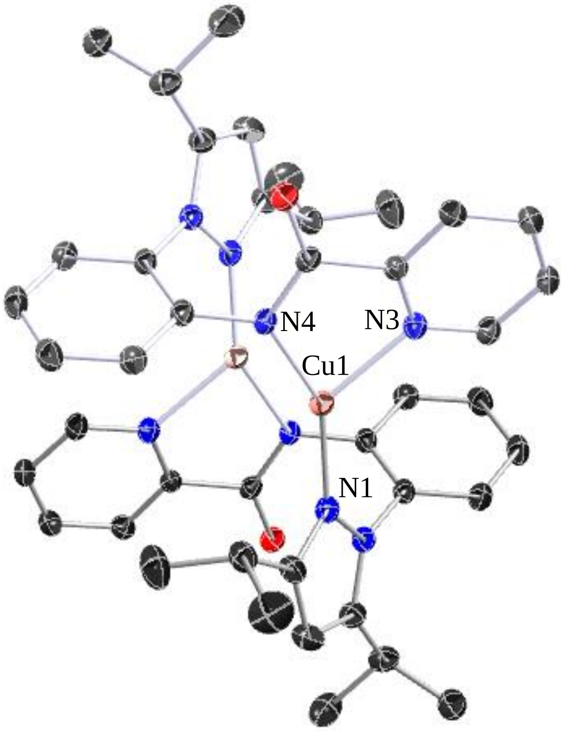

Figure 2.17. X-ray crystal structure of **($L^2Cu)_2$** with the THF molecules and H atoms omitted for clarity. Atoms are shown as 30% thermal ellipsoids. Selected bond distances (Å) and angles (deg): Cu1–N1, 1.909(2); Cu1–N3, 1.935(2); Cu1–N4, 2.151(2); N1–Cu1–N3, 155.79(9); N1–Cu1–N4, 118.13(9); N3–Cu1–N4, 81.90(9).

Although the solid-state structure shows the formation of a dimer for the 1:1 Cu(I)/**L^2** complex, it is not clear if the dimeric structure is retained in solution. The NMR solution-state data is consistent with both the monomer in Scheme 2.2 and **($L^2Cu)_2$**, since the symmetry of the solid-state dimer structure would result in only one set of ligand resonances. Cu(I) complexes, like tris(pyrazolyl)hydroborate Cu(I) complexes, have been shown to crystallize as dimers but the solution-state data suggests the dimers can dissociate in solution to monomeric units.[133,134] Furthermore, Cu(I) dimers can be used to react with and activate small molecules.[45,135] Thus, in an attempt to access and stabilize a 1:1:1 $\mathbf{L^2}$/Cu/O_2 adduct, we bubbled gaseous O_2 into a THF solution of $\mathbf{(L^2Cu)_2}$ at -80 °C for 2 min. There were no apparent changes in the spectrum, indicating no reaction with O_2 at this temperature (Figure 2.18). Additionally, no spectral changes were observed upon warming the solution in the presence of O_2. The lack of reactivity of the Cu(I) complex contrasts with the reactivity of other species supported by tridentate monoanionic N-donor ligands,[136,137] the reasons for which are unknown.

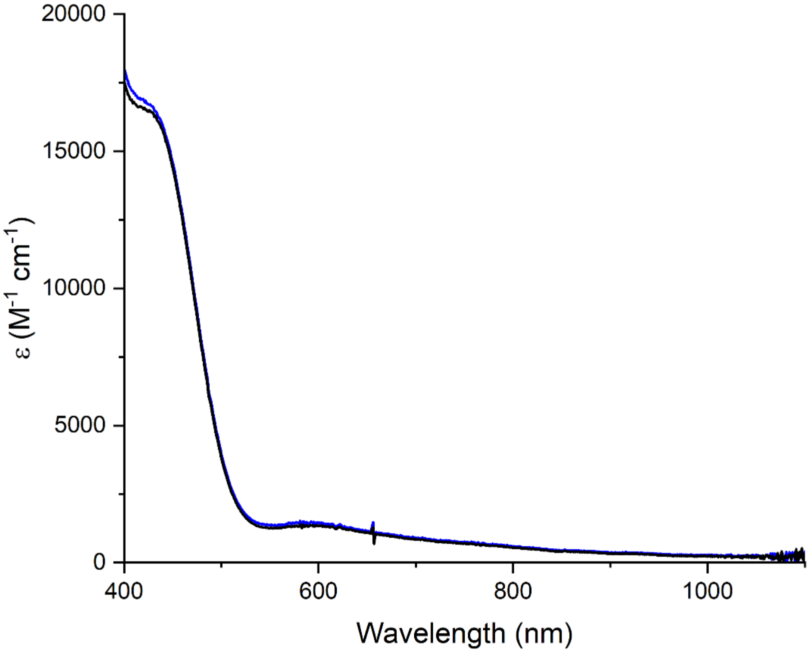

Figure 2.18. UV-vis spectrum of $\mathbf{(L^2Cu)_2}$ (black) and the spectrum produced after bubbling O_2(g) into a THF solution of $\mathbf{(L^2Cu)_2}$ for 2 min (blue).

Cyclic voltammetry experiments revealed an irreversible oxidation event at 170 mV vs Fc/Fc^+ at 100 mV s^{-1} in THF (Figure 2.19). We found that when cycling past this oxidation event, another irreversible reduction event occurs on the reducing sweep at -83 mV vs $Fc^{0/+}$. However, this reduction event is not observed when performing the reductive sweep without first undergoing oxidation. This is suggestive of a highly hysteretic Cu(I/II) redox process whereby oxidation generates a Cu(II) complex that undergoes a chemical transformation to a species that is then reduced at the low potential. We speculate that this species may be a monomeric Cu(II) compound on the basis of observed formation of such complexes in synthetic reactions (*vide infra*). The lack of O_2 reactivity and reversible redox chemistry for **($L^2Cu)_2$** led us to synthesize Cu(II) complexes containing **$^-L^1$** and **$^-L^2$**, which provide alternative routes to accessing copper-oxygen complexes.

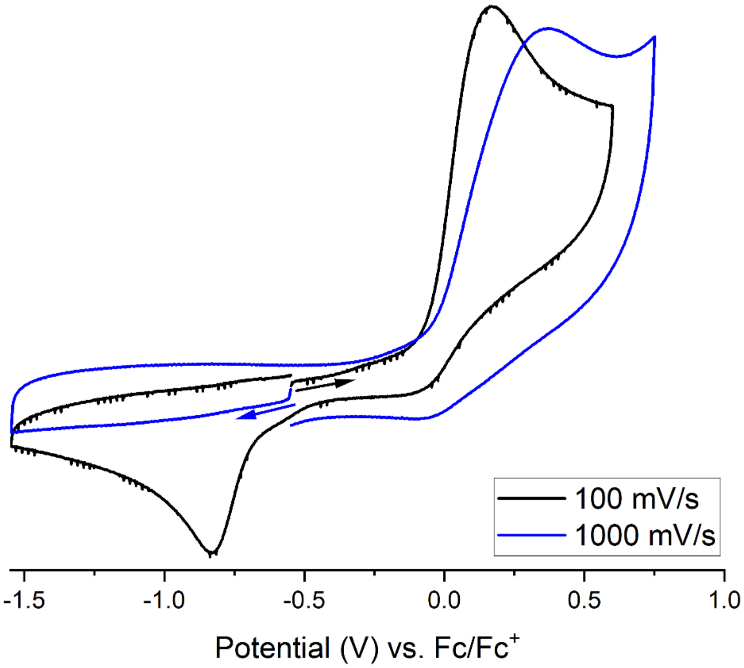

Figure 2.19. Cyclic voltammogram of **($L^2Cu)_2$**. Conditions: 2 mM [Cu dimer], 0.3 M TBAP, THF, 25 ˚C, glassy-carbon working electrode.

2.4 Synthesis and characterization of Cu(II) complexes bearing L^1 and L^2

2.4.1 Synthesis and characterization of L^nCuCl (n = 1 and 2)

We reacted **HL^1** and **HL^2** with multiple Cu(II) sources to access mononuclear copper complexes. Deprotonation of **HL^1** and **HL^2** with KHMDS and reaction with anhydrous $CuCl_2$ in THF yielded dark green solutions (Scheme 2.3). The THF and HMDS byproduct were removed *in vacuo*, successive filtrations using CH_2Cl_2 and then MeCN were performed, and the green oily materials were triturated with diethyl ether. A green powder was afforded for **L^1CuCl** after purification in 31% yield and a green/brown powder for **L^2CuCl** was afforded in 60% yield. The complexes, **L^1CuCl** and **L^2CuCl,** were characterized by UV-vis and EPR spectroscopy, elemental analysis, and X-ray crystallography.

Scheme 2.3. Syntheses of **L^{1}CuCl** and **L^{2}CuCl**.

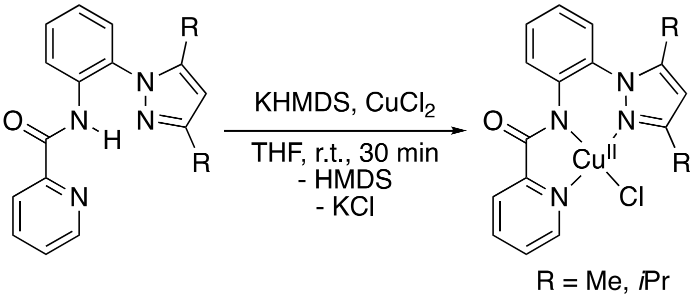

Crystalline complexes that were suitable for X-ray diffraction were attained using MeCN/diethyl ether layering for **L^{1}CuCl** and by a CH_2Cl_2/heptane layering for **L^{2}CuCl**. The structures (Figure 2.20) revealed that the products, **L^{1}CuCl** and **L^{2}CuCl**, were 1:1:1 **L^n**:Cu:Cl (**n** = 1 and 2) species. In the solid state, **L^{2}CuCl** exists as a dimer composed of two **L^{2}CuCl** units where the Cl from one unit has a weak interaction in the axial position of the Cu in the other unit (2.7025(9) Å and 2.7464(9) Å), a motif seen in other Cu(II)-halide complexes supported by tridentate ligands.[121,122,138–143] On the other hand, **L^{1}CuCl** does not exhibit the same phenomenon, remaining monomeric in the solid state, as seen in other Cu(II)-halide complexes with tridentate ligands.[101,112,125,144,145] The bond lengths are comparable between the two complexes, but all the bond lengths were slightly shorter in **L^{1}CuCl**. The geometry index value, τ_4, describes a 4-coordinate atom on a spectrum from 0, square planar, to 1, tetrahedral, based on the equation: $[360° – (\alpha + \beta)]/[360° – 2(109.5°)]$ where α and β are the largest angles about the central atom.[146] The τ_4 values of the metal centers are 0.37 and 0.31 for **L^{1}CuCl** and **L^{2}CuCl**, respectively, indicating a moderate deviation from a square planar geometry.

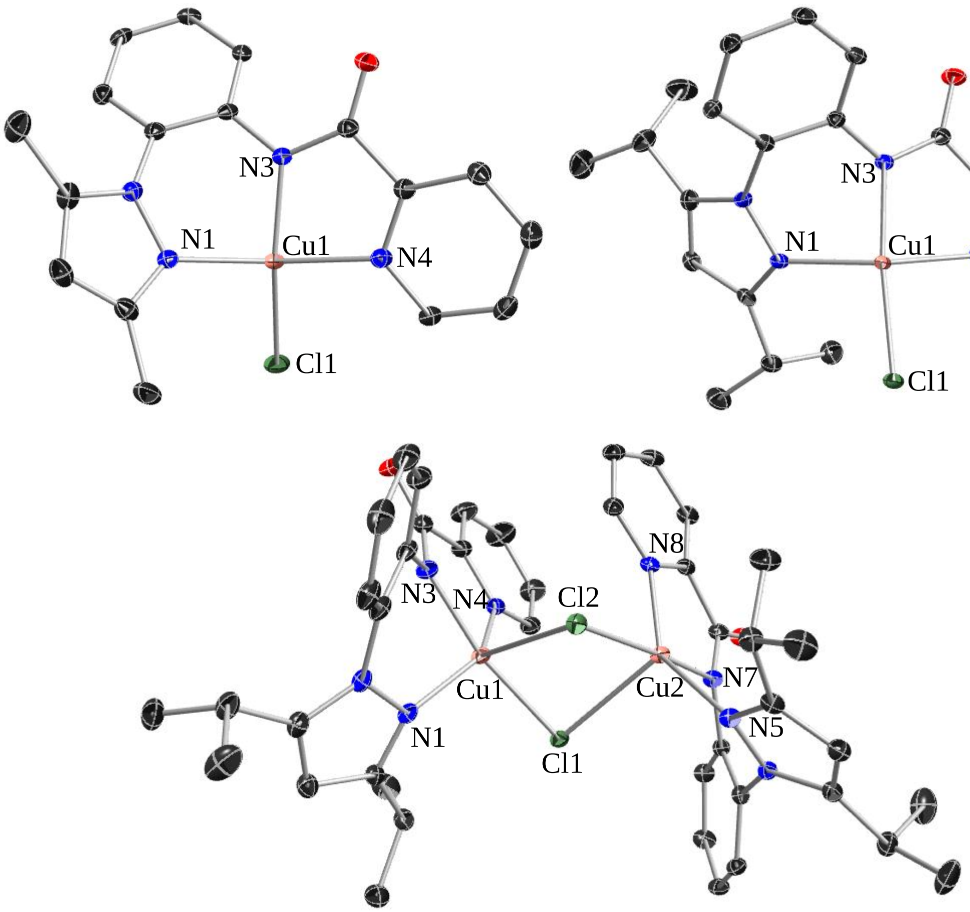

Figure 2.20. X-ray crystal structures of **L^{1}CuCl** (top left) and **L^{2}CuCl** (top right) and a representation of the solid-state electrostatic dimer of **L^{2}CuCl** (bottom). H atoms are omitted for clarity, and all non-H atoms are shown as 30% thermal ellipsoids. Selected bond distances (Å) and angles (deg) for **L^{1}CuCl**: Cu1–N1, 1.9909(16); Cu1–N3, 1.9341(15); Cu1–N4, 1.9999(17); Cu1–Cl1, 2.2059(5); N1–Cu1–N4, 149.41(7); N3–Cu1–Cl1, 158.01(5). Selected bond distances (Å) and angles (deg) for **L^{2}CuCl**: Cu1–N1, 2.032(3); Cu1–N3, 1.947(3); Cu1–N4, 2.030(3); Cu1–Cl1, 2.2701(9); Cu1–Cl2, 2.7025(9); N1–Cu1–N4, 144.64(12); N3–Cu1–Cl1, 171.00(9).

L^{1}CuCl and **L^{2}CuCl** were also characterized by EPR spectroscopy (THF, X-band, 30 K, Figure 2.21) which showed signals typical for tetragonal, monomeric Cu(II) complexes. While the solid-state structure of **L^{2}CuCl** depicted a dimer, the EPR spectrum of **L^{2}CuCl** was indicative of a mononuclear species in frozen solution. Both EPR spectra show Cu hyperfine and N superhyperfine splitting. Simulations of the EPR spectra were performed and the resulting parameters can be seen in Table 2.1. The UV-vis spectrum of **L^{1}CuCl** in MeCN (Figure 2.22) has low absorbing peaks at 463 nm (ε = 358 M^{-1} cm^{-1}), 604 nm (ε = 152 M^{-1} cm^{-1}), and 775 nm (ε = 198 M^{-1} cm^{-1}), and the UV-vis spectrum of **L^2CuCl** in MeCN has similar peaks at 458 nm (ε = 325 M^{-1} cm^{-1}), 606 nm (ε = 105 M^{-1} cm^{-1}), and 815 nm (ε = 177 M^{-1} cm^{-1}). The low absorbing peaks are typical for *d*-*d* transitions in Cu(II) complexes. Elemental analysis results for **L^1CuCl** were within 0.5% for H and N but were too high in C by 1.8%. Unfortunately, including different solvents into the fit did not agree with the H and N values. The high C composition is inconsistent with contamination by $CuCl_2$ and at this juncture we do not know the source of the analysis discrepancy. The elemental analysis results for **L^2CuCl** were within 0.5% of the theoretical values, indicating high purity of the complex. Ultimately, we demonstrated that mononuclear Cu(II) complexes containing $^-$**L^1** and $^-$**L^2** could be synthesized, confirming the desired tridentate coordination of the ligands yielding typical Cu(II) complex structures.

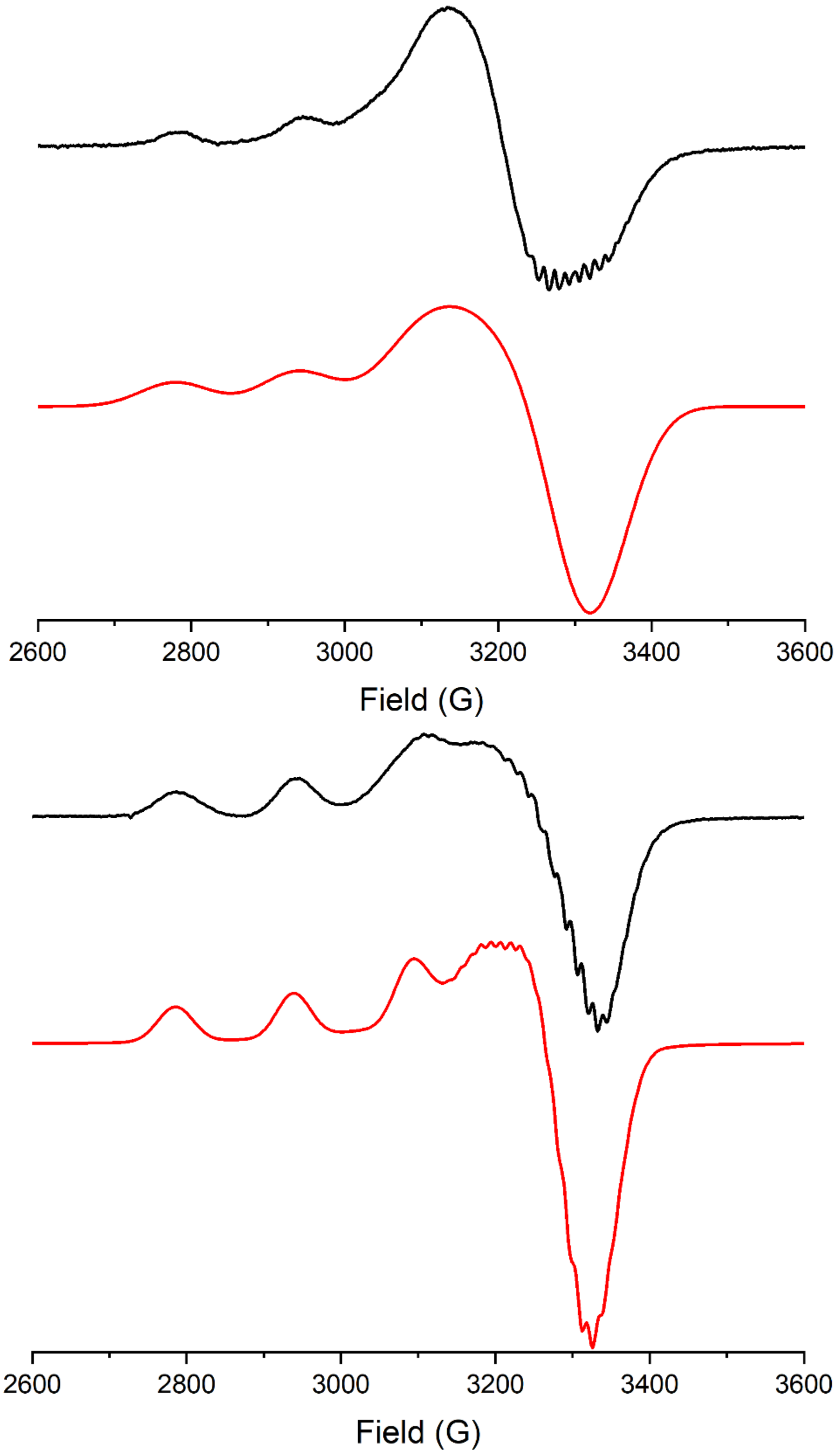

Figure 2.21. (top) Continuous wave X-band EPR spectrum of 1 mM **L^1CuCl** in THF at 30 K (black) and the simulation of **L^1CuCl** (red). Parameters: 30 K; microwave frequency 9.38 GHz; microwave power 0.0002 mW; modulation amplitude 9.8 G; modulation frequency 100 kHz. Parameters from the simulation are listed in Table 2.1. (bottom) Continuous wave X-band EPR spectrum of 1 mM **L^2CuCl** in THF at 30 K (black) and the

simulation of **L^2CuCl** (red). Parameters: 30 K; microwave frequency 9.38 GHz; microwave power 0.0002 mW; modulation amplitude 9.8 G; modulation frequency 100 kHz. Parameters from the simulation are listed in Table 2.1.

Table 2.1. Simulated g-values and hyperfine/superhyperfine parameters (MHz) for Cu, N^1, N^2, N^3, and Cl nuclei for **L^1CuCl** and **L^2CuCl** in THF at 30 K.

Compound	**L^1CuCl**	**L^2CuCl**
g_x	2.105	2.100
g_y	2.152	2.135
g_z	2.285	2.285
$A^{Cu}{}_x$	45	55
$A^{Cu}{}_y$	45	55
$A^{Cu}{}_z$	495	480
$A^{N1}{}_x$	45	40
$A^{N1}{}_y$	45	45
$A^{N1}{}_z$	30	30
$A^{N2}{}_x$	45	50
$A^{N2}{}_y$	45	55
$A^{N2}{}_z$	40	40
$A^{N3}{}_x$	45	40
$A^{N3}{}_y$	45	35
$A^{N3}{}_z$	30	30
$A^{Cl}{}_x$	45	45
$A^{Cl}{}_y$	45	45
$A^{Cl}{}_z$	30	30

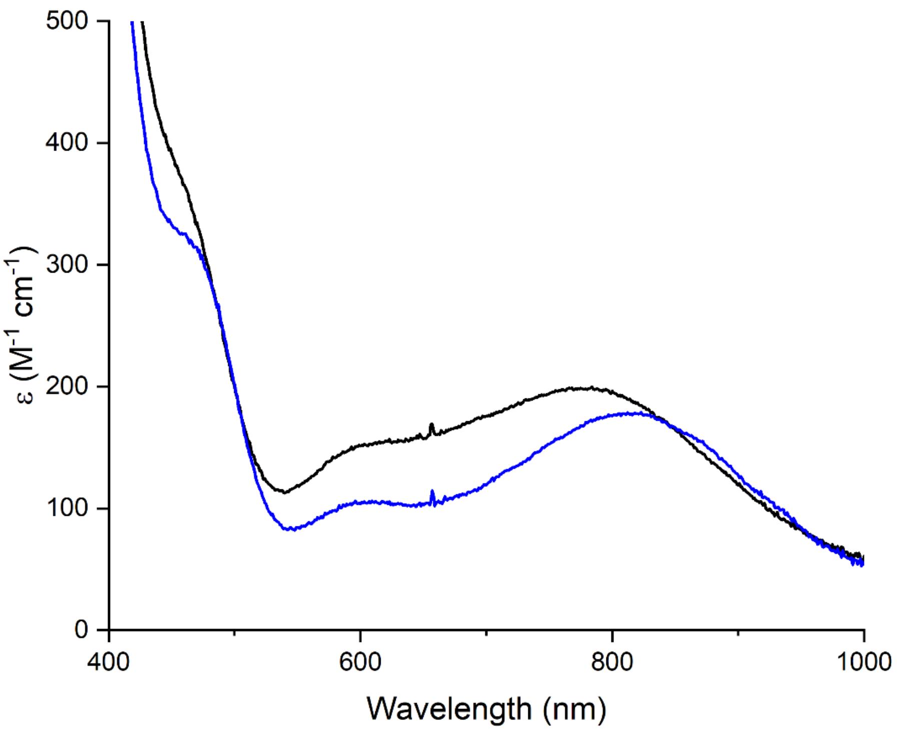

Figure 2.22. UV-vis spectra of **L^{1}CuCl** (black) and **L^{2}CuCl** (blue) in MeCN at room temperature.

2.4.2 Synthesis and characterization of [L^{n}CuMeCN][SbF$_6$] (n = 1 and 2)

While the chloro complexes are stable and useful for structural assessment, we sought compounds that could more readily convert to various copper-oxygen species by virtue of a labile ligand such as MeCN. To this end, we deprotonated **HL^1** and **HL^2** with KHMDS in MeCN and then added [Cu(MeCN)$_5$][SbF$_6$]$_2$ to the solutions (Scheme 2.4), resulting in dark green reaction mixtures. We isolated green powders in quantitative yields after removing the MeCN and HMDS byproduct *in vacuo* and precipitating the product from concentrated MeCN solutions with diethyl ether, leaving the salt byproduct in solution. The resulting green products were characterized by EPR and UV-vis spectroscopy, elemental analysis, and high-resolution electrospray ionization-mass spectrometry (HR ESI-MS), and on this basis we tentatively propose the following formulations: [**L^{1}CuMeCN**][SbF$_6$] and [**L^{2}CuMeCN**][SbF$_6$]. The EPR spectra (Figure 2.23) reveal the unpaired spins are localized on the Cu(II) ions, as evidenced by the hyperfine interactions in the g_{parallel} region of the axial signal, but superhyperfine splitting from the N atoms is not apparent. The simulated parameters can be seen in Table 2.2.

Scheme 2.4. Syntheses of [$\mathbf{L^1CuMeCN}$][SbF_6] and [$\mathbf{L^2CuMeCN}$][SbF_6].

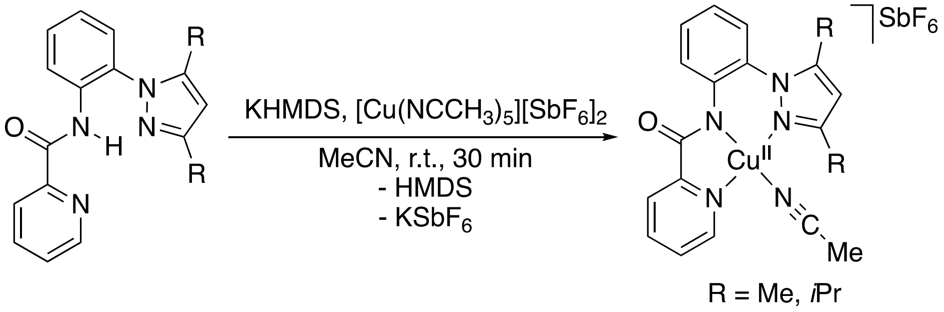

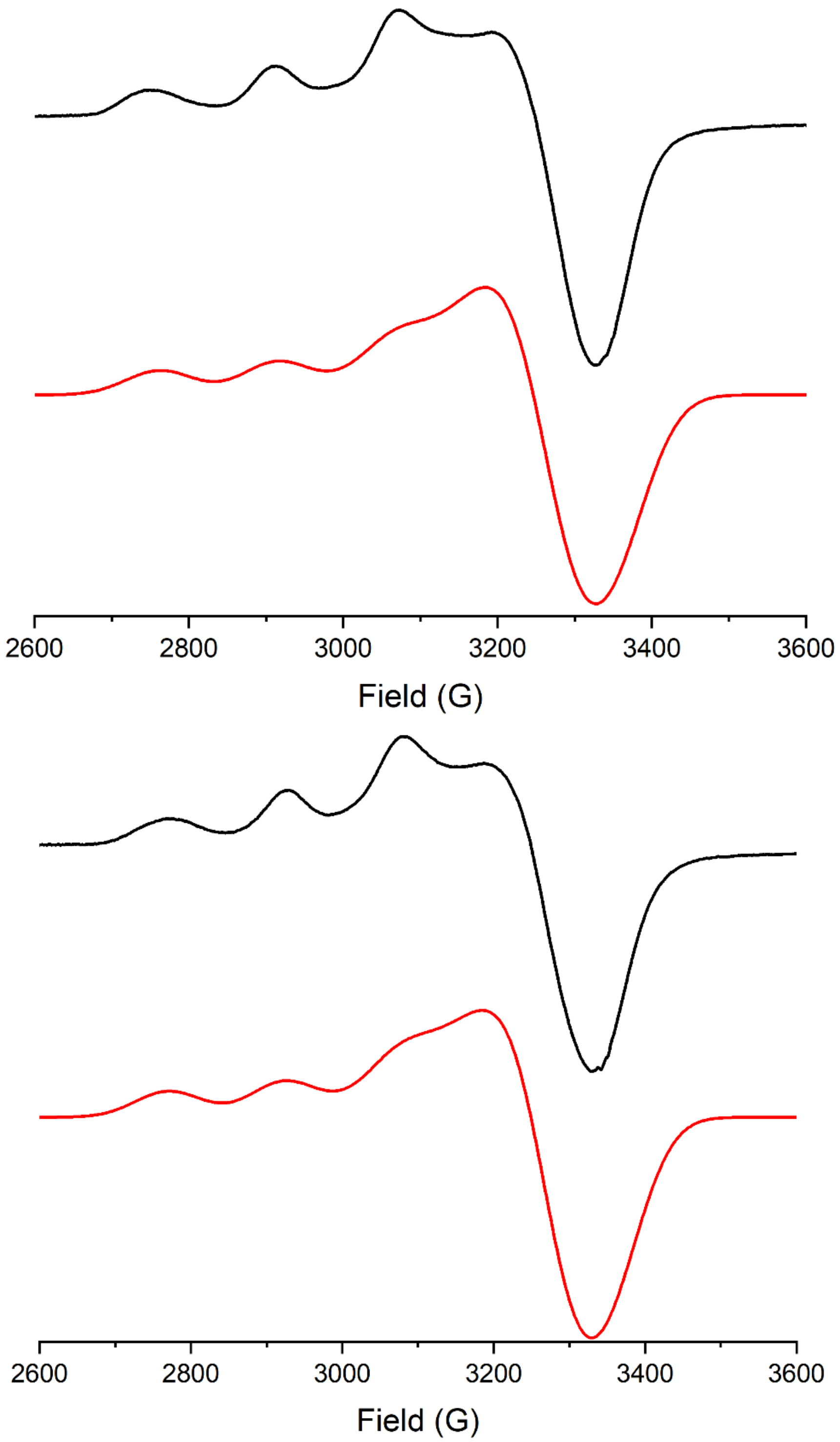

Figure 2.23. (top) Continuous wave X-band EPR spectrum of 1 mM [**L^{1}CuMeCN**][SbF$_6$] in 1:4 MeCN/THF at 30 K (black) and the simulation of [**L^{1}CuMeCN**][SbF$_6$] (red). Parameters: 30 K; microwave frequency 9.38 GHz; microwave power 0.0002 mW; modulation amplitude 9.8 G; modulation frequency 100 kHz. Parameters from the

simulation are listed in Table 2.2. (bottom) Continuous wave X-band EPR spectrum of 1 mM [**L^{2}CuMeCN**][SbF$_6$] in 1:4 MeCN/THF at 30 K (black) and the simulation of [**L^{2}CuMeCN**][SbF$_6$] (red). Parameters: 30 K; microwave frequency 9.38 GHz; microwave power 0.0002 mW; modulation amplitude 9.8 G; modulation frequency 100 kHz. Parameters from the simulation are listed in Table 2.2.

Table 2.2. Simulated g-values and hyperfine/superhyperfine parameters (MHz) for Cu, N^1, N^2, and N^3 nuclei for [**L^{1}CuMeCN**][SbF$_6$] and [**L^{2}CuMeCN**][SbF$_6$] in 1:4 MeCN/THF at 30 K.

Compound	[**L^{1}CuMeCN**][SbF$_6$]	[**L^{2}CuMeCN**][SbF$_6$]
g_x	2.080	2.080
g_y	2.150	2.150
g_z	2.305	2.298
A^{Cu}_x	55	55
A^{Cu}_y	55	55
A^{Cu}_z	480	480
A^{N1}_x	40	40
A^{N1}_y	45	45
A^{N1}_z	30	30
A^{N2}_x	50	50
A^{N2}_y	55	55
A^{N2}_z	40	40
A^{N3}_x	30	30
A^{N3}_y	35	35
A^{N3}_z	30	30

The UV-vis spectrum of [**L^{1}CuMeCN**][SbF$_6$] in MeCN shows peaks at 466 nm (ε = 390 M^{-1} cm^{-1}) and 731 nm (ε = 220 M^{-1} cm^{-1}) and similar peaks were observed in the [**L^{2}CuMeCN**][SbF$_6$] UV-vis spectrum in MeCN at 462 nm (ε = 255 M^{-1} cm^{-1}) and 752 nm (ε = 122 M^{-1} cm^{-1}) (Figure 2.24). These low absorbing peaks are consistent with *d-d* transitions typical in Cu(II) complexes although they are different than the features found for **L^{1}CuCl** and **L^{2}CuCl**, indicating the fourth ligand perturbing the electronics of the metal center. Elemental analysis results were inconsistent with the proposed structure and could not be fit to a combination of metals, ligands, solvents, and contaminants, possibly due to a variety of ligands being present in the fourth coordination site of the copper (i.e. other solvents or a carbonyl from a neighboring molecule), or additional solvent coordination on the fifth position. High resolution ESI-MS data were collected for acetonitrile solutions of the complexes and yielded masses in positive mode that may be assigned to 1:1 **L^n**/Cu (**n** = 1 and 2) species with no bound acetonitrile. Unfortunately, crystal structures of [**L^{n}CuMeCN**][SbF$_6$] (**n** = 1 and 2) were never realized despite exhaustive efforts to grow crystals suitable for X-ray diffraction and micro-crystal electron diffraction. Additionally, these starting materials never yielded tractable copper-oxygen species, such as LCu(II)OH, when treating the compounds with NBu$_4$OH under an inert atmosphere, and LCu(II)OO (*vide infra*), methods known to work for pyridine dicarboxamide copper complexes. Ultimately, the nature of the species formed in solution was never certain, so alternative syntheses to discrete species were explored.

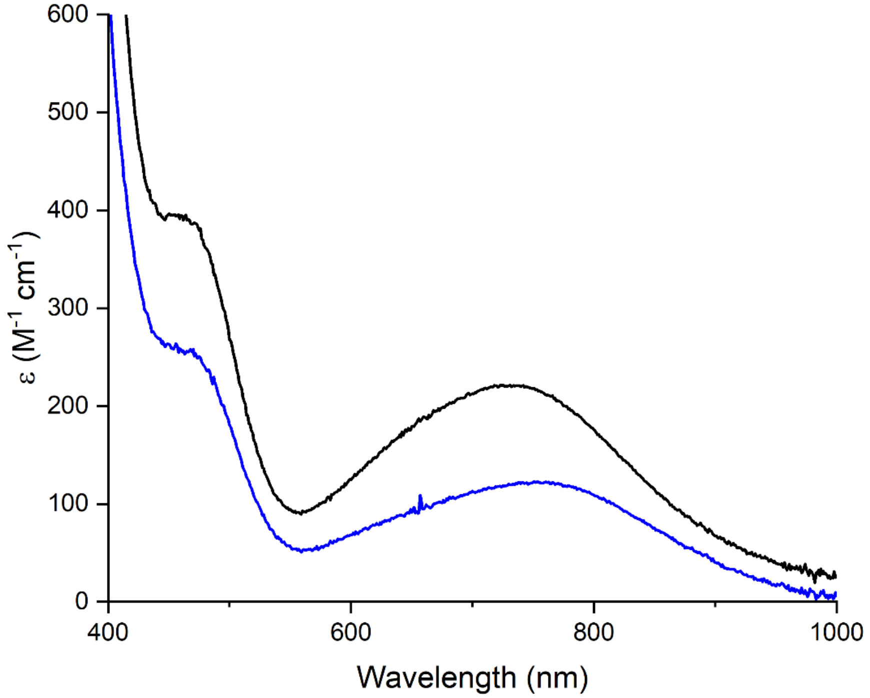

Figure 2.24. UV-vis spectra of [**L^{1}CuMeCN**][SbF$_6$] (black) and [**L^{2}CuMeCN**][SbF$_6$] (blue) in MeCN at room temperature.

2.4.3 Synthesis and characterization of L^{n}CuOAc (n = 1 and 2)

A different synthetic route, we reacted **HL^1** and **HL^2** with Cu(OAc)$_2$·H$_2$O in the presence of 3 Å molecular sieves in MeCN (Scheme 2.5) resulting in vibrant green-blue solutions. The former reaction yielded green crystalline plates isolated in 85% yield after filtering the reaction mixture and removing the solvent *in vacuo* and recrystallizing the material from a THF/diethyl ether vapor diffusion. In the case of the latter reaction, the product mixture was filtered, and the solvent was removed *in vacuo*. Trituration of the green oil with hexanes and removal of the solvent produced a green-blue solid in 77% yield. Crystalline blue blocks of the material were afforded after a THF/diethyl ether vapor diffusion. Both products were characterized by X-ray crystallography, EPR and UV-vis spectroscopy, and elemental analysis, which showed them to be **L^{1}CuOAc** and **L^{2}CuOAc**. The X-ray crystal structures (Figure 2.25) show acetate ligands bound to the copper in monodentate fashion with a weak interaction from the second carboxylate oxygen in the axial position of the copper. This interaction differs between the two complexes (Cu–O3 lengths 2.611(5) Å for **L^{1}CuOAc** and 2.3310(19) Å for **L^{2}CuOAc).** The geometric parameter, τ_4, of the metal center is about equal for each complex: 0.33 for **L^{1}CuOAc** and 0.36 for **L^{2}CuOAc**. All other bond lengths in the two compounds are similar.

Scheme 2.5. Syntheses of **L^{1}CuOAc** and **L^{2}CuOAc**.

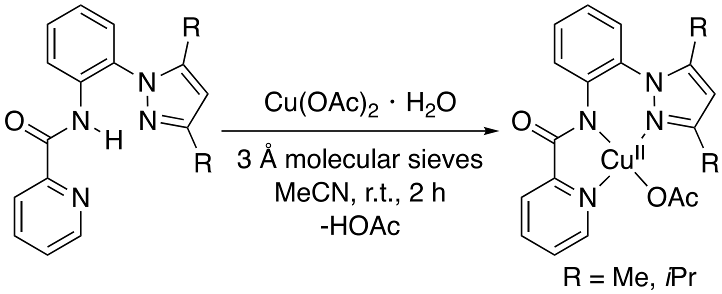

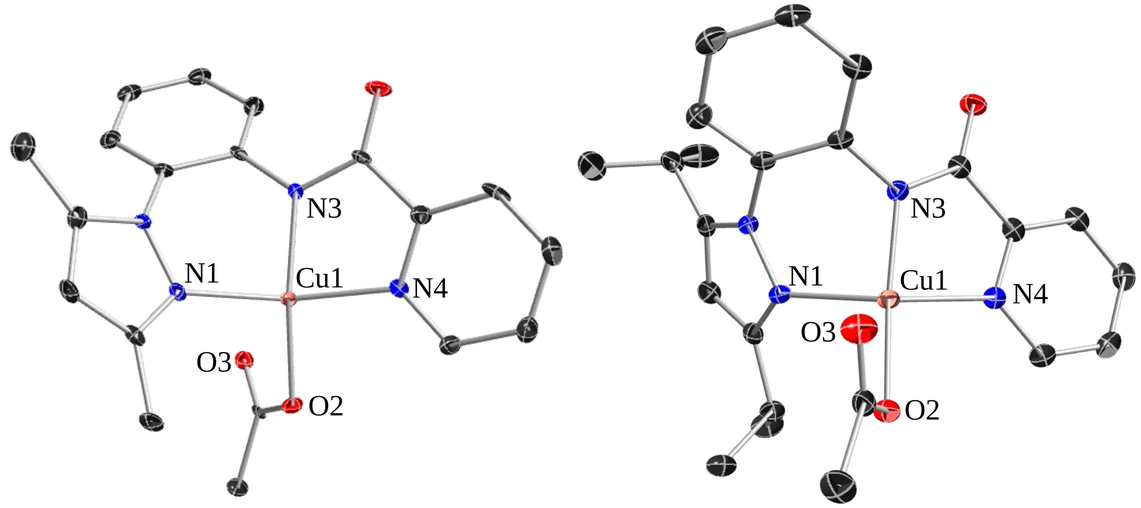

Figure 2.25. X-ray crystal structures of **L^{1}CuOAc** (left) and **L^{2}CuOAc** (right). H atoms are omitted for clarity, and all non-H atoms are shown as 30% thermal ellipsoids. Selected bond distances (Å) and angles (deg) for **L^{1}CuOAc**: Cu1–N1, 2.018(6); Cu1–N3, 1.923(6); Cu1–N4, 2.015(6); Cu1–O2, 1.921(5); Cu1–O3, 2.611(5); N1–Cu1–N4, 146.1(3); N3–Cu1–O2, 166.8(3). Selected bond distances (Å) and angles (deg) for **L^{2}CuCl**: Cu1–N1, 2.044(2); Cu1–N3, 1.914(2); Cu1–N4, 2.002(2); Cu1–O2, 1.9500(17); Cu1–O3, 2.3296(18); N1–Cu1–N4, 141.48(8); N3–Cu1–O2, 167.67(8).

The solid-state structures resemble those of other Cu(II)-acetate complexes supported by tridentate ligands.[107,110,113,117,120,124,125,128,147,148] The Cu–N distances found for **L^{n}CuOAc** (**n** = 1 and 2) are similar to previously published structures and the Cu–O2 bond lengths of 1.920 and 1.9492 Å are within the range of the known Cu–O(proximal)OCH_3 bond lengths (1.92 - 2.08 Å). The Cu–O(distal)OCH_3 lengths of 2.611(5) and 2.3310(19) Å are also within or very similar to the range found for the previously reported Cu(II)-acetate structures (2.37 - 2.85 Å).

The complexes were also characterized by EPR spectroscopy (Figure 2.26). As with the previously discussed Cu(II) complexes, the EPR spectra of **L^{1}CuOAc** and **L^{2}CuOAc** reveal axial signals that are indicative of a tetragonal Cu(II) complex. Cu hyperfine and N superhyperfine couplings are observed in both spectra. The spectra were simulated and the parameters can be seen in Table 2.3. The UV-vis spectra for **L^{1}CuOAc** and **L^{2}CuOAc** in MeCN (Figure 2.27) have peaks at 694 nm (ε = 208 M^{-1} cm^{-1}) and 694 nm (ε = 292 M^{-1} cm^{-1}), respectively. Again, these features are typical for *d-d* transitions of Cu(II) complexes but different than the features found for **L^{1}CuCl**, **L^{2}CuCl**, and [**L^{1}CuMeCN**][SbF_6], and

[**L^{2}CuMeCN**][SbF$_6$]. Elemental analysis results for **L^{1}CuOAc** were consistent with the structure determined by X-ray diffraction, indicating high purity. The elemental analysis results for **L^{2}CuOAc** showed the C composition was 1% higher than the theoretical value. The experimental C, H, and N values could not be fit to added solvents, acetic acid, or Cu(OAc)$_2$. Additionally, the solid-state structure of **L^{2}CuOAc** did not contain any molecules other than the desired molecule, so we concluded the sample was suitable for further experiments.

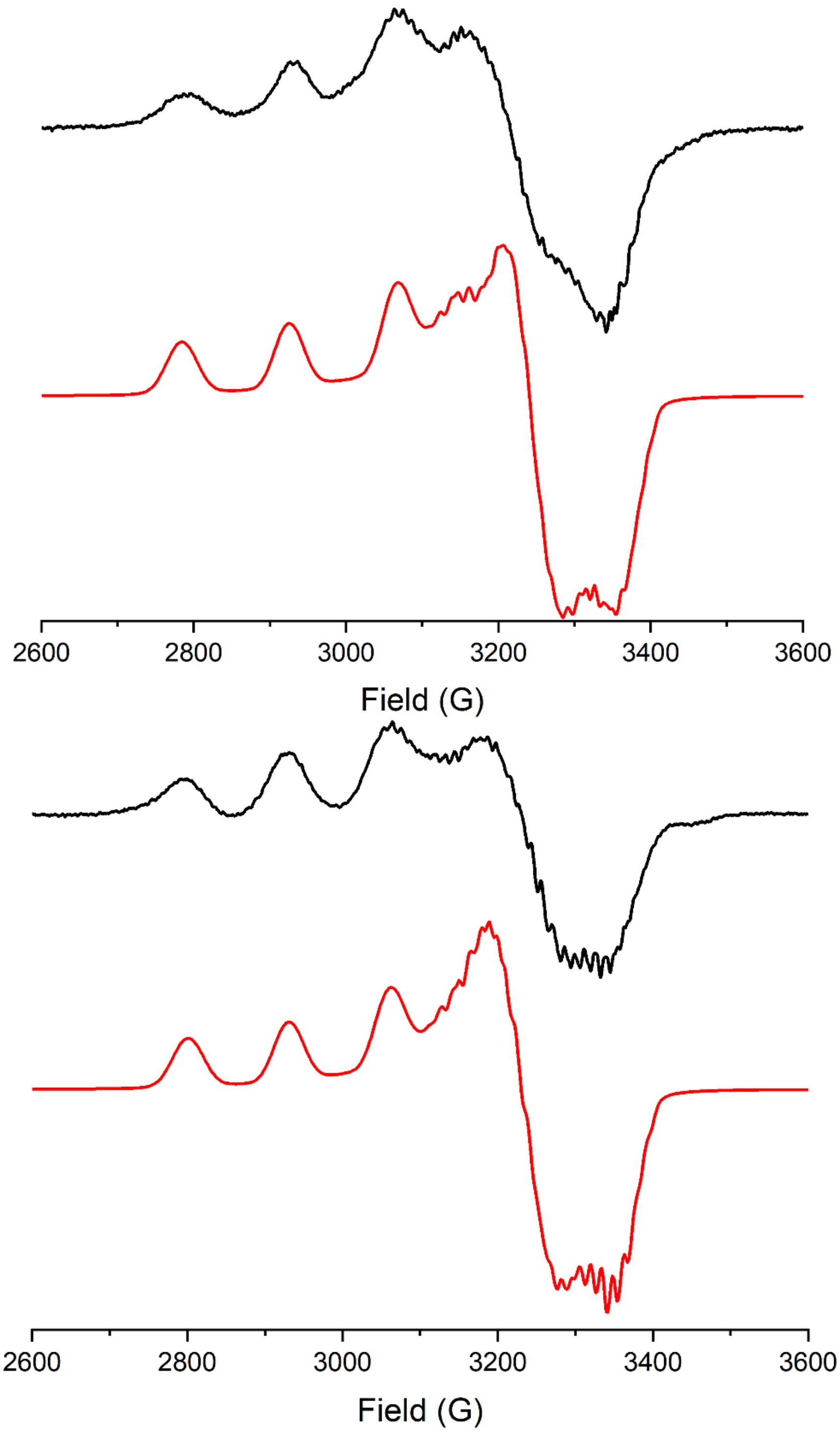

Figure 2.26. (top) Continuous wave X-band EPR spectrum of 1 mM **L^{1}CuOAc** in THF at 30 K (black) and the simulation of **L^{1}CuOAc** (red). Parameters: 30 K; microwave frequency 9.38 GHz; microwave power 0.0002 mW; modulation amplitude 9.8 G; modulation frequency 100 kHz. Parameters from the simulation are listed in Table 2.3. (bottom) Continuous wave X-band EPR spectrum of 1 mM **L^{2}CuOAc** in THF at 30 K

(black) and the simulation of **L^{2}CuOAc** (red). Parameters: 30 K; microwave frequency 9.38 GHz; microwave power 0.0002 mW; modulation amplitude 9.8 G; modulation frequency 100 kHz. Parameters from the simulation are listed in Table 2.3.

Table 2.3. Simulated g-values and hyperfine/superhyperfine parameters (MHz) for Cu, N^1, N^2, and N^3 nuclei for **L^{1}CuOAc** and **L^{2}CuOAc** in THF at 30 K.

Compound	**L^{1}CuOAc**	**L^{2}CuOAc**
g_x	2.075	2.075
g_y	2.162	2.160
g_z	2.300	2.300
$A^{Cu}{}_x$	55	55
$A^{Cu}{}_y$	55	55
$A^{Cu}{}_z$	445	410
$A^{N1}{}_x$	40	40
$A^{N1}{}_y$	45	45
$A^{N1}{}_z$	30	30
$A^{N2}{}_x$	50	45
$A^{N2}{}_y$	55	55
$A^{N2}{}_z$	40	40
$A^{N3}{}_x$	30	35
$A^{N3}{}_y$	35	35
$A^{N3}{}_z$	30	30

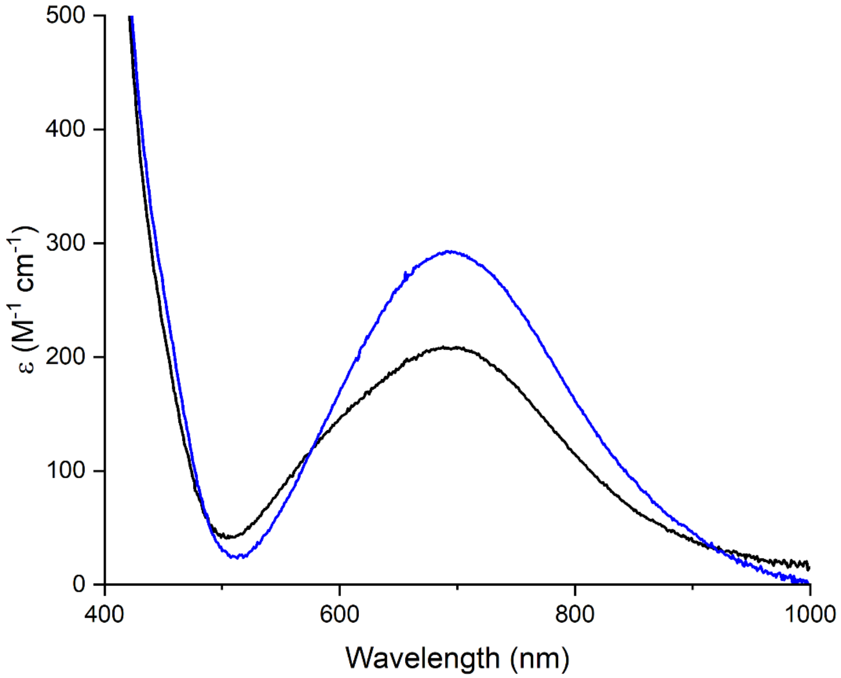

Figure 2.27. UV-vis spectra of **L^{1}CuOAc** (black) and **L^{2}CuOAc** (blue) in MeCN at room temperature.

2.5 Electrochemistry of Cu complexes

We investigated the accessibility of additional oxidation states in the six Cu(II) complexes, **L^{1}CuCl**, **L^{2}CuCl**, and [**L^{1}CuMeCN**][SbF$_6$], [**L^{2}CuMeCN**][SbF$_6$], **L^{1}CuOAc**, and **L^{2}CuOAc** with cyclic voltammetry (0.3 M tetrabutylammonium hexafluorophosphate as the supporting electrolyte, MeCN, glassy-carbon working electrode, Figure 2.28). No reversible oxidation or reduction events were observed for any of the compounds, with several irregular irreversible oxidative features at or beyond 1 V vs. Fc$^{0/+}$, most consistent with oxidative degradation of the compounds. We therefore conclude that highly oxidized Cu complexes supported by $^-$**L^1** and $^-$**L^2** were not feasible species to access and observe due to their apparent instabilities. Irreversible reductive features are observed below 0 V vs. Fc$^+$/Fc; based on our Cu(I) metalation experiments, we suspect that these most likely correspond to Cu(I) reduction accompanied by extensive coordinative rearrangement to form dimeric or polymeric aggregates like **(L^{2}Cu)$_2$**.

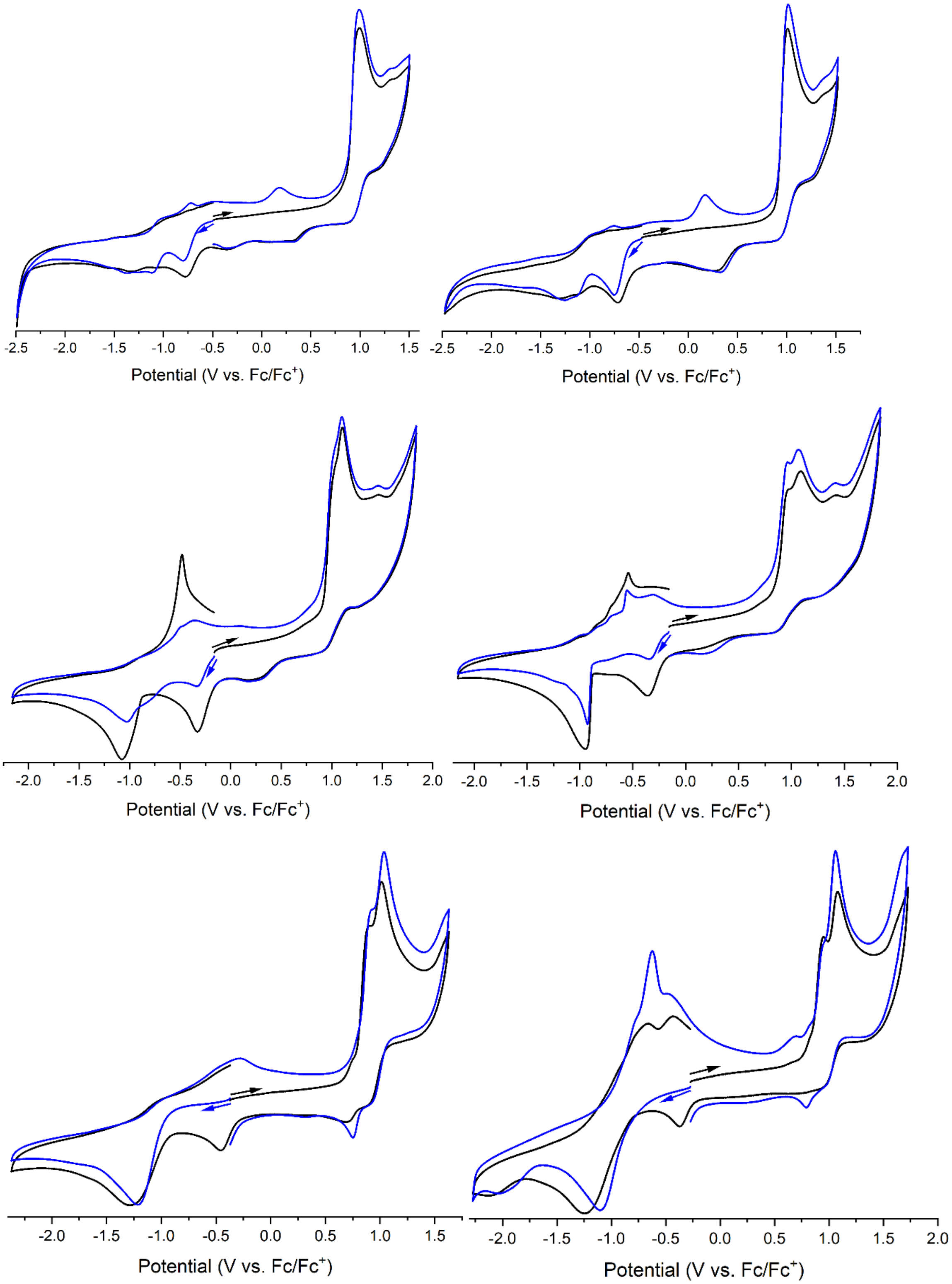

Figure 2.28. Cyclic voltammograms collected of **L^{1}CuCl** (top left), **L^{2}CuCl** (top right), [**L^{1}CuMeCN**][SbF$_6$] (middle left), [**L^{2}CuMeCN**][SbF$_6$] (middle right), **L^{1}CuOAc**

(bottom right), and **L^2CuOAc** (bottom left). Conditions: 2 mM [Cu], 0.3 M TBAP, MeCN, 25 °C, glassy-carbon working electrode, 100 mV/s scan rate.

2.6 Superoxide reactivity of [L^nCuMeCN][SbF_6] (n = 1 and 2)

Since neither mononuclear Cu(I) nor Cu(III) states were accessible for reactivity studies, we sought to produce mononuclear Cu(II)-oxygen species, specifically, copper-superoxide complexes. In a method analogous to that used in previous work with Cu(II) pyridine dicarboxamide systems, we reacted [**L^nCuMeCN**][SbF_6] (**n** = 1 and 2) in THF with [K(Krypt)][O_2] in 4:1 THF/MeCN at -80 ˚C.[21,32] However, we did not observe the formation of new spectroscopic features upon addition of the superoxide salt to the Cu(II) complexes under these conditions (Figures 2.29 and 2.30). Therefore, we concluded controlled formation of Cu-oxygen species supported by **$^{-}L^1$** and **$^{-}L^2$** was not practical.

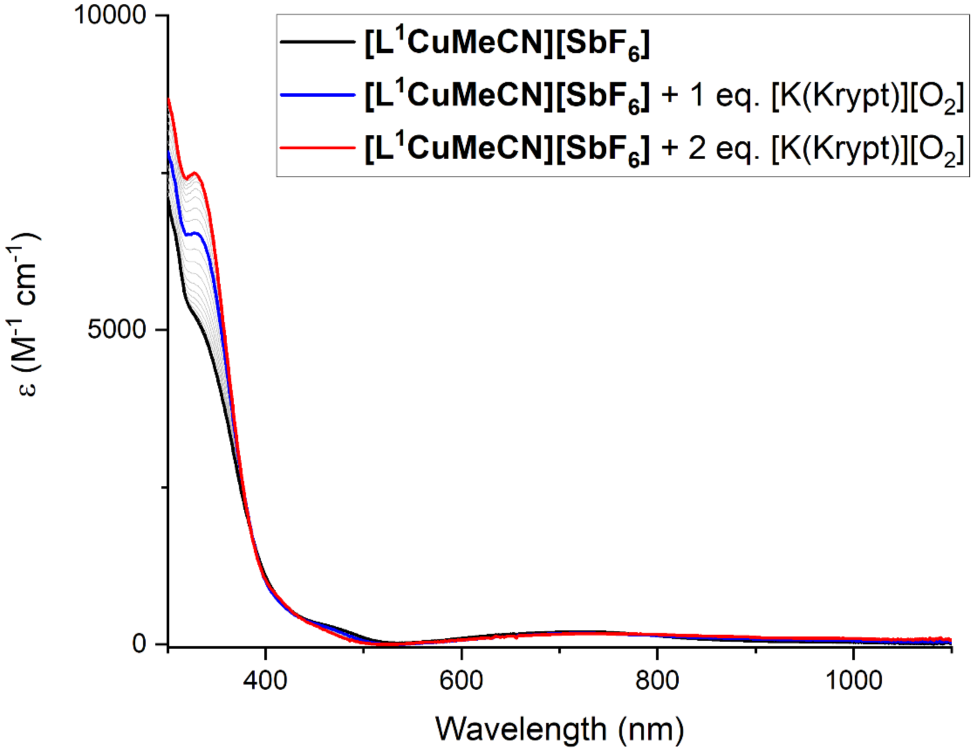

Figure 2.29. UV-vis spectra of the titration of [K(Krypt)][O_2] in 4:1 THF/MeCN into [**L^1CuMeCN**][SbF_6] in THF at -80 ˚C.

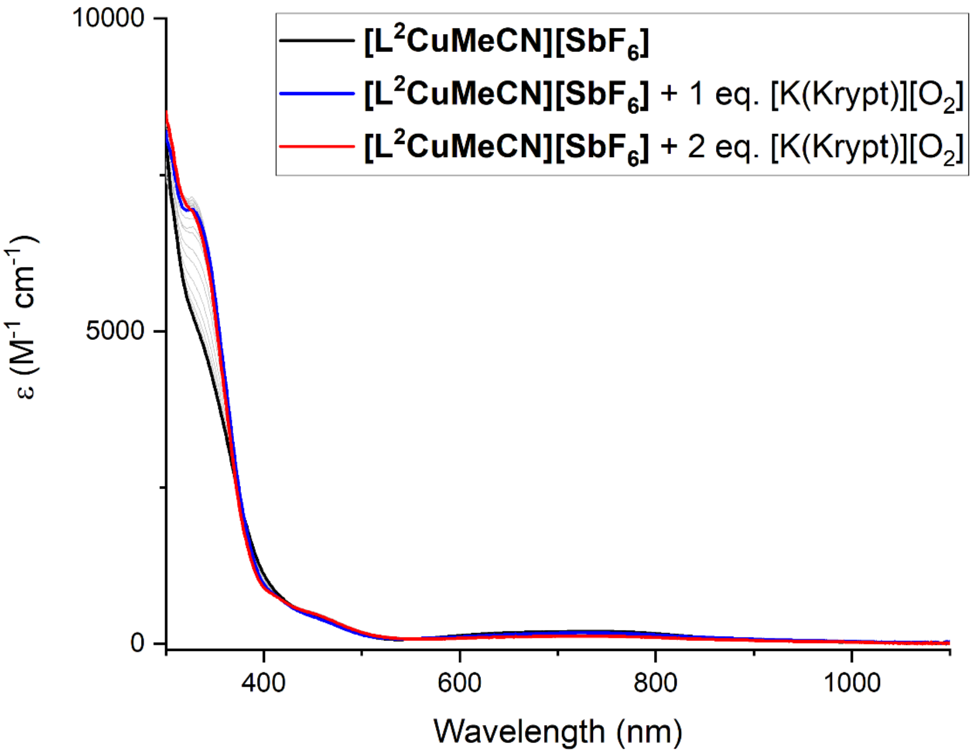

Figure 2.30. UV-vis spectra of the titration of [K(Krypt)][O_2] in 4:1 THF:MeCN into [**L^{1}CuMeCN**][SbF_6] in THF at -80 ˚C.

2.7 Summary and conclusions

We prepared two new monoanionic N,N’,N’’ ligands with central amide groups to develop more structurally and electronically similar analogues to the LPMO active site. A Cu(I) dimer ligated by $^-$**L^2** was isolated from an attempt to synthesize a mononuclear Cu(I) complex. Yet, observation of a 1:1 Cu/O_2 complex was sought after by reacting **(L^{2}Cu)$_2$** with O_2 but with no success. The ligands afforded a number of tetragonal Cu(II) complexes in which a variety of neutral or anionic ligands fourth ligands were employed, leading to mononuclear or dinuclear species. We found that the ligands bind in a tridentate fashion, but either to one metal ion or two. In the mononuclear complexes, there exists a fourth ligand that binds monodentate with, in the case for the carboxylate complexes, an additional weak interaction to the carboxylate. The challenges we faced with both obtaining copper-oxygen species as well as oxidizing them to a formally Cu(III) state prevented us from studying substrate oxidation reactivity with [CuOR]$^{2+}$-type species. While we had hoped that the lower donor strength of these ligands would lend access to O_2-reactive Cu(I) species, the lack of which is a major drawback of the pyridine dicarboxamide ligand framework, we observed a tendency to form unreactive clusters. We speculate this may be due to a steric insufficiency or high flexibility in the explored ligands. Bulkier modifications to these frameworks could alleviate this issue and are targets for further investigation. Nonetheless, the ligands presented in this work give access to a relatively unexplored coordination environment for Cu and could be useful in other lines of coordination chemistry research.

2.8 Experimental section

2.8.1 Materials and methods

All air-sensitive manipulations were carried out in a dinitrogen-filled glovebox or under argon using Schlenk techniques. All reagents and solvents were purchased from commercial vendors and used as received unless otherwise noted. Tetrahydrofuran, dichloromethane, acetonitrile, pentane, diethyl ether, and heptane were passed through activated alumina columns and used directly or plumbed into a glovebox. Tetrahydrofuran, dichloromethane, and acetonitrile were stored over activated 3 Å molecular sieves in a dinitrogen-filled glovebox and, prior to use in spectroscopy and cyclic voltammetry experiments, filtered using a 25 mm diameter, 0.2 mm hydrophobic polytetrafluoroethylene (PTFE) syringe filter. 3,5-diisopropylpyrazole was either made according to the previously published synthesis[149] or purchased from Tokyo Chemical Industry Co., Ltd. and used without further purification. KHMDS was purchased from Sigma-Aldrich and was recrystallized from toluene at -35 °C, filtered, and dried *in vacuo* before use. $Cu(MeCN)_4OTf$[150] and $[Cu(MeCN)_5][SbF_6]_2$[151] were synthesized according to the previously published procedures. 3,5-dimethylpyrazole, 1-fluoro-2-nitrobenzene, picolinic acid, and anhydrous $CuCl_2$ were purchased from Sigma-Aldrich and used without further purification.

UV-vis spectra were collected using a HP8453 (190 – 1100 nm) diode array spectrophotometer equipped with a Unisoku low-temperature UV-vis cell holder. EPR spectra were collected on frozen 1 mM samples with a CW Elexsys E500 EPR spectrometer using X band (9.38 GHz) radiation at 35 dB and 30 K with the following conditions: microwave power, 0.0002 mW; modulation amplitude, 9.6 G; and modulation frequency, 100 kHz. NMR spectra were collected on a Bruker Avance III HD nanobay AX-400, a Bruker Avance III HD-500, or an Agilent DD2 (500 MHz) spectrometer. Deuterated tetrahydrofuran was purchased from Cambridge Isotopes Laboratories, degassed, and dried over 3 Å molecular sieves prior to use. Cyclic voltammograms were recorded using an EC Epsilon potentiostat from BASi, a glassy carbon working electrode, and a Ag wire pseudoreference electrode. All cyclic voltammograms were performed in THF or MeCN with 0.3 M tetrabutylammonium hexafluorophosphate (TBAP) electrolyte, which was recrystallized several times from ethanol and dried under high vacuum before use and were internally referenced to the ferrocene/ferrocenium (Fc/Fc^+) couple. The spectra were converted vs. the standard Fc/Fc^+ couple using standard conversion factors.[152] Elemental analysis was performed by the CENTC Elemental Analysis Facility (University of Rochester). ESI-HR-MS data is supplied by instruments funded by NIH grant 8P41GM103422.

For X-ray crystallography experiments, crystals were placed onto the tip of a MiTeGen cryoloop and mounted on a Bruker D8 VENTURE diffractometer equipped with a Photon III CMOS. The data collections were carried out using Mo Kα source using normal parabolic mirrors as monochromators at 173 K. Structure solutions were performed with SHELXT[153] using ShelXle[154] as a graphical interface. The structures were refined against F^2 on all data by full-matrix-least-squares with SHELXL.[155]

2.8.2 Experimental procedures

Synthesis of 3,5-dimethyl-1-(2-nitrophenyl)-1*H*-pyrazole. The following preparation was adapted from a previously published synthesis.[131] Under an argon atmosphere, a flame-dried 500 mL Schlenk flask containing dry THF (100 mL) was charged with NaH (60% in mineral oil, 1.931 g, 48.3 mmol) then cooled to 0 °C using an ice bath. The slurry was stirred while a solution of 3,5-dimethylpyrazole (5.00 g, 52.0 mmol) in dry THF (100 mL) was added dropwise via an addition funnel over 30 min. After the addition was complete, a solution of 1-fluoro-2-nitrobenzene (5.49 mL, 7.339 g, 52.0 mmol) in dry THF (100 mL) was added dropwise via an addition funnel over 30 min. The ice bath was removed, and the orange solution was allowed to stir at rt for 2 h under argon. The reaction was transferred to a separatory funnel and slowly quenched with a saturated aqueous NH_4Cl solution (100 mL). After separation of the phases, the aqueous layer was extracted with ethyl acetate (2 x 200 mL). The organic layers were combined, washed with brine (50 mL), dried with Na_2SO_4, decanted, and the solvents were removed *in vacuo*. The resulting orange residue was purified via column chromatography on silica gel (50% CH_2Cl_2, 50% ethyl acetate) affording the pure product as an orange oil (8.209 g, 73% yield). ^1H NMR (500 MHz, $CDCl_3$) δ (ppm):7.93 (dd, J = 8.1, 1.5 Hz, 1H), 7.66 (td, J = 7.8, 1.5 Hz, 1H), 7.53 (td, J = 7.8, 1.4 Hz, 1H), 7.45 (dd, J = 7.9, 1.4 Hz, 1H), 5.99 (s, 1H), 2.21 (s, 3H), 2.15 (s, 3H). ^{13}C NMR (500 MHz, $CDCl_3$) δ (ppm): 150.67, 146.59, 141.09, 133.37, 133.29, 129.67, 129.34, 125.25, 107.00, 13.64, 11.49. Anal. Calcd for $C_{11}H_{11}N_3O_2$: C 60.82, H 5.1, N 19.34. Found: C 60.57, H 5.15, N 19.02.

Synthesis of 3,5-diisopropyl-1-(2-nitrophenyl)-1*H*-pyrazole. The following preparation was adapted from a previously published synthesis.[131] Under an argon atmosphere, a flame-dried 500 mL Schlenk flask containing dry THF (100 mL) was charged with NaH (60% in mineral oil, 3.941 g, 104.5 mmol) then cooled to 0 °C using an ice bath. The slurry was stirred while a solution of 3,5-diisopropylpyrazole (10.00 g, 65.7 mmol) in dry THF (100 mL) was added dropwise via an addition funnel over 30 min. After the addition was complete, a solution of 1-fluoro-2-nitrobenzene (6.93 mL, 9.268 g, 65.7 mmol) in dry THF (100 mL) was added dropwise via an addition funnel over 30 min. The ice bath was removed, and the orange solution was allowed to stir at rt for 2 h under argon. The reaction was transferred to a separatory funnel and slowly quenched with a saturated aqueous NH_4Cl solution (150 mL). After separation of the phases, the aqueous layer was extracted with ethyl acetate (2 x 200 mL). The organic layers were combined, washed with brine (50 mL), dried with Na_2SO_4, decanted, and the solvents were removed *in vacuo*. The resulting orange residue was purified via column chromatography on silica gel (80% hexanes, 20% ethyl acetate) affording the pure product as an orange oil (10.735 g, 66% yield). ^1H NMR (400 MHz, $CDCl_3$) δ (ppm): 7.97 (dd, J = 8.1, 1.5 Hz, 1H), 7.68 (td, J = 7.7, 1.2 Hz, 1H), 7.56 (td, J = 7.9, 1.2 Hz, 1H), 7.51 (dd, J = 8.0, 1.2 Hz, 1H), 6.06 (s, 1H), 2.94 (sept, J = 6.9 Hz, 1H), 2.81 (sept, J = 6.9 Hz, 1H), 1.25 (d, J = 6.9 Hz, 6H), 1.18 (d, J = 6.9 Hz, 6H). ^{13}C NMR (500 MHz, $CDCl_3$) δ (ppm): 161.04, 151.91, 146.90, 133.77, 133.09, 129.60, 129.32, 125.35, 100.39, 28.09, 25.77, 22.85, 22.80. Anal. Calcd for $C_{15}H_{19}N_3O_2$: C 65.91, H 7.01, N 15.37. Found: C 66.09, H 7.23, N 15.27.

Synthesis of 2-(3,5-dimethyl-1*H*-pyrazol-1-yl)aniline. The following preparation was adapted from a previously published synthesis.[131] Under argon, a Schlenk flask was charged with 3,5-dimethyl-1-(2-nitrophenyl)-1*H*-pyrazole (8.097 g, 37.3 mmol), 10 wt% Pd/C (0.282 g, 0.265 mmol), and 200 proof ethanol (50 mL). The flask was flushed with H_2 then stirred at rt for 24 h under a balloon of H_2, refilling the H_2 balloon when deflated. The reaction mixture was filtered through celite and the solids were washed with ethanol (50 mL). *Note: Residual Pd/C should be wetted with water after filtration to prevent ignition of the solid.* Solvent was removed *in vacuo* yielding the pure product as a brown solid (6.609 g, 95% yield). ^{1}H NMR (400 MHz, $CDCl_3$) δ (ppm): 7.13 (ddd, *J* = 8.1, 7.3, 1.6 Hz, 1H), 7.04 (dd, *J* = 7.6, 1.6 Hz, 1H), 6.78 – 6.68 (m, 2H), 5.95 (s, 1H), 3.77 (s, 2H), 2.26 (s, 3H), 2.11 (s, 3H). ^{13}C NMR (500 MHz, $CDCl_3$) δ (ppm): 149.52, 143.52, 140.85, 129.52, 127.68, 125.62, 118.15, 116.73, 105.75, 13.75, 11.62. Anal. Calcd for $C_{11}H_{13}N_3$: C 70.56, H 7.00, N 22.44. Found: C 70.56, H 7.09, N 22.37.

Synthesis of 2-(3,5-diisopropyl-1*H*-pyrazol-1-yl)aniline. The following preparation was adapted from a previously published synthesis.[131] Under argon, a Fisher Porter tube was charged with 3,5-diisopropyl-1-(2-nitrophenyl)-1*H*-pyrazole (2.264 g, 8.28 mmol), 10 wt% Pd/C (0.063 g, 0.059 mmol), and 200 proof ethanol (15 mL). The system was sealed and flushed with H_2 through 3 pressurization/vent cycles then pressurized once more to 100 psi H_2 and stirred at rt overnight. The vessel was repressurized once during the reaction. *Note: A safety shield should be placed in front of the Fisher Porter tube during this reaction.* Residual pressure in the vessel was vented before filtering the reaction mixture through celite and washing the solids with ethanol (15 mL). *Note: Residual Pd/C should be wetted with water after filtration to prevent ignition of the solid.* Solvent was removed *in vacuo* to yield the product as a white solid (1.876 g, 93% yield). ^{1}H NMR (400 MHz, $CDCl_3$): δ_H 7.18 (ddd, *J* = 8.1, 7.3, 1.5 Hz, 1H), 7.11 (dd, *J* = 7.8, 1.5 Hz, 1H), 6.78 (m, 2H), 6.02 (s, 1H), 3.83 (s, 2H), 3.00 (sept, *J* = 6.9 Hz, 1H), 2.83 (sept, *J* = 6.9 Hz, 1H), 1.29 (d, *J* = 6.9 Hz, 6H), 1.14 (d, *J* = 6.9 Hz, 6H). ^{13}C NMR (500 MHz, $CDCl_3$) δ (ppm): 160.08, 151.75, 144.00, 129.66, 128.00, 126.01, 118.15, 116.74, 99.02, 28.15, 25.60, 23.01, 22.82. Anal. Calcd for $C_{15}H_{21}N_3$: C 74.03, H 8.70, N 17.27. Found: C 74.54, H 8.93, N 17.40.

Synthesis of *N*-(2-(3,5-dimethyl-1*H*-pyrazol-1-yl)phenyl)picolinamide (HL^1). The following preparation was adapted from a previously published synthesis.[131] In a 250 mL Schlenk flask under argon, a solution of picolinic acid (3.117 g, 25.3 mmol) in CH_2Cl_2 (35 mL) was cooled to 0 °C using an ice bath. With stirring, DMF (5 drops) was added dropwise to the solution, followed by another dropwise addition of oxalyl chloride (2.96 mL, 34.5 mmol). The purple solution was brought to rt and stirred for 1 h. The solvent and excess oxalyl chloride were removed *in vacuo* to yield the acid chloride as a dark black/brown oily solid. *Note: the excess oxalyl chloride was collected in an external trap to be quenched with a saturated aqueous solution of sodium bicarbonate.* To the same flask under argon, the acid chloride was dissolved in CH_2Cl_2 (35 mL) and cooled back to 0 °C using an ice bath. A solution of 2-(3,5-dimethyl-1*H*-pyrazol-1-yl)aniline (4.310 g, 23.0 mmol) in CH_2Cl_2 (35 mL) was added to the flask, followed by the addition of triethylamine (3.53 mL, 25.3 mmol). The flask was removed from the ice bath and the reaction was stirred at rt for 12 h. The reaction mixture was filtered into a separatory funnel and washed with a saturated aqueous ammonium chloride solution (2 x 20 mL) and brine (30 mL). The organic layer was dried with Na_2SO_4, decanted, then concentrated *in vacuo*. The crude product was purified by via column chromatography on silica gel (90% hexanes, 10% ethyl acetate;) affording the pure product as an yellow/orange oil (5.686 g, 85% yield). Over a few months, the oil solidified into a brown solid. ^1H NMR (400 MHz, $CDCl_3$): δ_H 11.11 (s, 1H), 8.69 (dd, J = 8.3, 1.4 Hz, 1H), 8.52 (ddd, J = 4.8, 1.7, 1.0 Hz, 1H), 8.21 (dt, J = 7.9, 1.1 Hz, 1H), 7.83 (td, J = 7.7, 1.7 Hz, 1H), 7.45 (ddd, J = 8.6, 7.6, 1.6 Hz, 1H), 7.40 (ddd, J = 7.6, 4.7, 1.2 Hz, 1H), 7.28 (dd, J = 7.9, 1.6 Hz, 1H), 7.19 (td, J = 7.7, 1.4 Hz, 1H), 6.06 (s, 1H), 2.43 (s, 3H), 2.19 (s, 3H). ^{13}C NMR (500 MHz, $CDCl_3$) δ (ppm): 162.65, 150.31, 150.13, 148.28, 141.24, 137.48, 134.46, 129.22, 129.19, 126.52, 126.38, 123.75, 122.46, 121.89, 106.71, 13.72, 12.01. Anal. Calcd for $C_{17}H_{16}N_4O$: C 69.85, H 5.52, N 19.17. Found: C 69.64, H 5.52, N 19.17.

Synthesis of *N*-(2-(3,5-diisopropyl-1*H*-pyrazol-1-yl)phenyl)picolinamide (HL^2). The following preparation was adapted from a previously published synthesis.[131] In a 100 mL Schlenk flask under argon, a solution of picolinic acid (2.230 g, 18.1 mmol) in CH_2Cl_2 (25 mL) was cooled to 0 °C using an ice bath. With stirring, DMF (5 drops) was added dropwise to the solution, followed by another dropwise addition of oxalyl chloride (2.11 mL, 24.7 mmol). The purple solution was brought to rt and stirred for 1 h. The solvent and excess oxalyl chloride were removed *in vacuo* to yield the acid chloride as a dark black/brown oily solid. *Note: the excess oxalyl chloride was collected in an external trap to be quenched with a saturated aqueous solution of sodium bicarbonate.* To the same flask under argon, the acid chloride was dissolved in CH_2Cl_2 (25 mL) and cooled back to 0 °C using an ice bath. A solution of 2-(3,5-diisopropyl-1*H*-pyrazol-1-yl)aniline (4.000 g, 16.4 mmol) in CH_2Cl_2 (25 mL) was added to the flask, followed by the addition of triethylamine (2.52 mL, 18.1 mmol). The flask was removed from the ice bath and the reaction was stirred at rt for 12 h. The reaction mixture was filtered into a separatory funnel and washed with a saturated aqueous ammonium chloride solution (2 x 10 mL) and brine (20 mL). The organic layer was dried with Na_2SO_4, decanted, then concentrated *in vacuo*. The crude product was purified by via column chromatography on silica gel (90% hexanes, 10% ethyl acetate) affording the pure product as a white solid (4.050 g, 71% yield). ^{1}H NMR (400 MHz, $CDCl_3$): δ_H 10.58 (s, 1H), 8.69 (dd, J = 8.3, 1.4 Hz, 1H), 8.46 (ddd, J = 4.8, 1.8, 1.0 Hz, 1H), 8.22 (dt, J = 7.9, 1.1 Hz, 1H), 7.83 (tt, J = 7.7, 1.7 Hz, 1H), 7.47 (td, J = 7.9, 1.5 Hz, 1H), 7.39 (ddt, J = 7.6, 4.8, 1.4 Hz, 1H), 7.33 (dd, J = 7.8, 1.6 Hz, 1H), 7.19 (td, J = 7.6, 1.3 Hz, 1H), 6.10 (s, 1H), 3.12 (sept, J = 7.0 Hz, 1H), 2.85 (sept, J = 6.8 Hz, 1H), 1.40 (d, J = 7.0 Hz, 6H), 1.09 (d, J = 6.9 Hz, 6H). ^{13}C NMR (500 MHz, $CDCl_3$) δ (ppm): 162.61, 160.77, 152.30, 149.96, 148.10, 137.42, 135.17, 129.68, 129.58, 127.23, 126.40, 123.89, 122.47, 121.94, 99.92, 28.32, 25.62, 22.95, 22.83. Anal. Calcd for $C_{21}H_{24}N_4O$: C 72.39, H 6.94, N 16.08. Found: C 72.41, H 7.20, N 15.95.

Synthesis of ($L^2Cu)_2$. In a glovebox, a solution of KHMDS (32 mg, 0.16 mmol) in MeCN (3 mL) was added dropwise to a solution of HL^2 (50 mg, 0.14 mmol) in MeCN (2 mL) in a 20 mL scintillation vial while stirring. After complete addition of the base, a solution of $Cu(MeCN)_4OTf$ in MeCN (2 mL) was added dropwise to the vial with stirring, and a bright orange powder started to precipitate from the solution. After 10 min of stirring, the MeCN was decanted from the vial. The solid was rinsed with MeCN (2 x 3 mL), decanted, and dried *in vacuo* to afford the pure compound (39 mg, 33%). X-ray quality crystals (orange blocks) were formed upon slow diffusion of pentane into a concentrated THF solution of $(L^2Cu^I)_2$ at -35 °C. ^1H NMR (400 MHz, THF-d_8): δ_H 7.80 (app d, *J* = 7.8 Hz, 1H), 7.57 (app t, *J* = 7.6 Hz, 1H), 7.45 (app d, *J* = 7.6 Hz, 1H), 7.32 – 7.11 (m, 4H), 7.01 (app t, *J* = 6.0 Hz, 1H), 5.91 (s, 1H), 3.27 (sept, *J* = 6.9 Hz, 1H), 3.09 (sept, *J* = 6.7 Hz, 1H), 1.38 (overlapping doublets, *J* = 6.8 Hz, 6H), 1.17 (d, *J* = 6.9 Hz, 3H), 0.47 (d, *J* = 6.9 Hz, 3H). ^{13}C NMR (500 MHz, THF-*d8*) δ (ppm): 166.47, 160.30, 155.27, 154.97, 152.93, 147.35, 137.85, 134.45, 130.23, 129.87, 128.06, 124.88, 123.24, 122.07, 97.65, 30.81, 30.39, 27.63, 24.50, 23.48, 22.67. UV-vis (THF, -80 °C) [λ_{max}, nm (ε, M^{-1} cm^{-1})]: 426 (16490), 592 (1365). Anal. Calcd for $C_{42}H_{46}Cu_2N_8O_2$: C 61.37, H 5.64, N 13.63. Found: C 60.83, H 5.62, N 13.29.

Synthesis of L^1CuCl. In a glovebox, a 50 mL Schlenk flask was charged with a solution of HL^1 (111.2 mg, 0.38 mmol) in THF (4 mL). A solution of KHMDS (75.9 mg, 0.38 mmol) in THF (4 mL) was added dropwise to the flask with stirring. After complete addition of the base, a slurry of anhydrous $CuCl_2$ (49.1 mg, 0.37 mmol) in THF (4 mL) was added to the flask with stirring, producing a dark green reaction mixture. After stirring at rt for 30 min, the solvent and HMDS byproduct were removed *in vacuo*. CH_2Cl_2 (5 mL) was added to the flask, and the solution was filtered into a 20 mL scintillation vial using a 25 mm diameter, 0.2 mm hydrophobic PTFE syringe filter. The solvent was removed *in vacuo*. MeCN (5 mL) was used to dissolve the product and then filtered into a 20 mL scintillation vial using a 25 mm diameter, 0.2 mm hydrophobic PTFE syringe filter. The solvent was removed *in vacuo* and the resulting green oil was triturated with diethyl ether (2 x 5 mL) resulting in a green powder (44.6 mg, 31%). Crystalline material of the title product was obtained by dissolving the green oil in a minimum amount of MeCN and layering with diethyl ether at rt, which afforded dark green plates that were suitable for X-ray diffraction. UV-vis (MeCN, 25 °C) [λ_{max}, nm (ε, M^{-1} cm^{-1})]: 463 (358), 604 (152), 775 (198). Anal. Calcd for $C_{17}H_{15}CuN_4OCl$: C 52.31, H 3.87, N 14.35. Found: C 54.18, H 4.13, N 14.61.

Synthesis of L^2CuCl. In a glovebox, a 50 mL Schlenk flask was charged with a solution of HL^2 (95.1 mg, 0.27 mmol) in THF (4 mL). A solution of KHMDS (54.4 mg, 0.27 mmol) in THF (4 mL) was added dropwise to the flask with stirring. After complete addition of the base, a slurry of anhydrous $CuCl_2$ (35.2 mg, 0.26 mmol) in THF (4 mL) was added to the flask with stirring, producing a dark green reaction mixture. After stirring at rt for 30 min, the solvent and HMDS byproduct were removed *in vacuo*. CH_2Cl_2 (5 mL) was added to the flask, and the solution was filtered into a 20 mL scintillation vial using a 25 mm diameter, 0.2 mm hydrophobic PTFE syringe filter. The solvent was removed *in vacuo*. MeCN (5 mL) was used to dissolve the product and then filtered into a 20 mL scintillation vial using a 25 mm diameter, 0.2 mm hydrophobic PTFE syringe filter. The solvent was removed *in vacuo* and the resulting green oil was triturated with diethyl ether (2 x 5 mL) resulting in a green/brown powder (70.0 mg, 60%). Crystalline material of the title product was obtained by dissolving the green oil in a minimum amount of CH_2Cl_2 and layering with heptane at -20 °C, which resulted in an oil that was subsequently allowed to sit at rt overnight resulting in dark green plates that were suitable for X-ray diffraction. UV-vis (MeCN, 25 °C) [λ_{max}, nm (ε, M^{-1} cm^{-1})]: 458 (325), 606 (105), 815 (177). Anal. Calcd for $C_{21}H_{23}CuN_4OCl$: C 56.50, H 5.19, N 12.55. Found: C 57.02, H 5.24, N 12.53.

Synthesis of [L^1Cu(MeCN)][SbF_6]. In a glovebox, a 50 mL Schlenk flask was charged with a solution of HL^1 (50 mg, 0.17 mmol) in MeCN (4 mL). A solution of KHMDS (34 mg, 0.17 mmol) in MeCN (4 mL) was added dropwise to the flask with stirring. After complete addition of the base, a solution of $[Cu(MeCN)_5][SbF_6]_2$ (122 mg, 0.16 mmol) in MeCN (4 mL) was added dropwise to the flask with stirring, producing a dark green reaction mixture. After stirring at rt for 30 min, the solvent and HMDS byproduct were removed *in vacuo*. The title product was obtained as a green solid after precipitating the compound out of MeCN (0.5 mL) with diethyl ether (10 mL) several times, decanting the liquid, and drying the solid *in vacuo* (108 mg, 104%). UV-vis (MeCN, 25 °C) [λ_{max}, nm (ε, M^{-1} cm^{-1})]: 466 (390), 731 (220). HR-MS (ESI, acetonitrile, positive ion) *m/z*: $[L^1Cu+SbF_6+H]^+$ Calcd For $[C_{17}H_{16}CuN_4OSbF_6]^+$ (without acetonitrile) 591.96; Found 591.9591. Anal. Calcd for $C_{19}H_{18}CuN_5OSbF_6$ (with acetonitrile): C 36.13, H 2.87, N 11.09. Found: C 38.18, H 3.32, N 10.77.

Synthesis of [L^2Cu(MeCN)][SbF_6]. In a glovebox, a 50 mL Schlenk flask was charged with a solution of HL^2 (50 mg, 0.14 mmol) in MeCN (4 mL). A solution of

KHMDS (29 mg, 0.14 mmol) in MeCN (4 mL) was added dropwise to the flask with stirring. After complete addition of the base, a solution of $[Cu(MeCN)_5][SbF_6]_2$ (102 mg, 0.14 mmol) in MeCN (4 mL) was added dropwise to the flask with stirring, producing a dark green reaction mixture. After stirring at rt for 30 min, the solvent and HMDS byproduct were removed *in vacuo*. The title product was obtained as a green solid after precipitating the compound out of MeCN (0.5 mL) with diethyl ether (10 mL) several times, decanting the liquid, and drying the solid *in vacuo* (89 mg, 94%). UV-vis (MeCN, 25 °C) [λ_{max}, nm (ε, M^{-1} cm^{-1})]: 462 (255), 752 (122). HR-MS (ESI, acetonitrile, positive ion) *m/z*: $[L^2Cu+SbF_6+H]^+$ Calcd For $[C_{21}H_{24}CuN_4OSbF_6]^+$ (without acetonitrile) 648.02; Found 648.0219. $[L^2Cu]^+$ Calcd For $[C_{21}H_{23}CuN_4O]^+$ (without acetonitrile) 410.12; Found 410.1185. Anal. Calcd for $C_{23}H_{26}CuN_5OSbF_6$ (without acetonitrile): C 40.17, H 3.81, N 10.18. Found: C 41.73, H 4.17, N 9.98.

Synthesis of L^1CuOAc. A solution of HL^1 (100 mg, 0.34 mmol) in anhydrous MeCN (3 mL) was added dropwise into a 20 mL scintillation vial containing $Cu(OAc)_2$•H_2O (74 mg, 0.37 mmol), anhydrous MeCN (3 mL), and 3 Å molecular sieves (500 mg). The reaction was stirred for 2 h at rt, resulting in a green-blue solution, which was filtered into a clean 20 mL scintillation vial using a 25 mm diameter, 0.2 mm hydrophobic PTFE syringe filter. The solvent was removed *in vacuo*. Crystalline material of the title product was obtained by vapor diffusion of anhydrous diethyl ether into a concentrated dry THF solution of L^1CuOAc at rt, which afforded green plate crystals that were suitable for X-ray diffraction (120 mg, 85%). UV-vis (MeCN, 25 °C) [λ_{max}, nm (ε, M^{-1} cm^{-1})]: 694 (208). Anal. Calcd for $C_{19}H_{18}CuN_4O_3$: C 55.13, H 4.38, N 13.54. Found: C 55.01, H 4.36, N 13.36.

Synthesis of L^2CuOAc. A solution of HL^2 (100 mg, 0.29 mmol) in anhydrous MeCN (4 mL) was added dropwise into a 20 mL scintillation vial containing $Cu(OAc)_2$•H_2O (62.5 mg, 0.31 mmol), anhydrous MeCN (2 mL), and 3 Å molecular sieves (1 cm). The reaction was stirred for 2 h at rt, resulting in a green-blue solution, which was filtered into a clean 20 mL scintillation vial using a 25 mm diameter, 0.2 mm hydrophobic PTFE syringe filter. The solvent was removed *in vacuo*. The green oil was allowed to stir in hexanes (5 mL) overnight, which was then decanted, and was then triturated with hexanes (2 x 5 mL). The residual solvent was removed *in vacuo* yielding a green-blue solid (103.4 mg, 77%). Crystalline material of the title product was obtained by vapor diffusion of anhydrous diethyl ether into a concentrated dry THF solution of L^2CuOAc at rt, which afforded blue block crystals that were suitable for X-ray diffraction. UV-vis (MeCN, 25 °C) [λ_{max}, nm (ε, M^{-1} cm^{-1})]: 694 (292). Anal. Calcd for $C_{23}H_{26}CuN_4O_3$: C 58.77, H 5.58, N 11.92. Found: C 59.77, H 5.85, N 11.76.

Chapter 3

Involvement of a formally Cu(III) nitrite complex in PCET and nitration of phenols[a]

[a] The results presented in this chapter were previously published in:

Bouchey, C. J.; Tolman, W. B. Involvement of a Formally Copper(III) Nitrite Complex in Proton-Coupled Electron Transfer and Nitration of Phenols. *Inorg. Chem.* **2022**, Article ASAP.

3.1 Introduction

Copper-nitrite complexes have been studied extensively as models for the active sites of the copper-containing nitrite reductases (CuNIRs),[1–24] key enzymes in global denitrification and mammalian and plant signaling pathways.[166] These model complexes contain Cu(I) or Cu(II), often in coordination geometries relevant to the CuNIR active site, and they typically reduce NO_2^- to NO, a reaction also performed by the enzymes. It has been proposed for CuNIR that the one-electron reduction of NO_2^- to NO involves an initial proton transfer facilitated by neighboring amino acid residues.[42,48,167–169] Inspired by this notion, recent work has probed the ability of Cu(II)-nitrite complexes to perform proton-coupled electron transfer (PCET).[49,52,54,56–59,160–162] Notably, PCET was invoked in a reaction of a Cu(II)-nitrite complex with 2,4-di-*t*-butylphenol (DTBP) that underwent subsequent nitration, an unusual anaerobic transformation.[162] Such a process is relevant to tyrosine nitration, which normally occurs via attack by peroxynitrite.[170–172]

Considering that higher oxidation state species generally exhibit enhanced PCET reactivity,[173–175] we sought to prepare a complex with a $[CuNO_2]^{2+}$ core (formally containing Cu(III)) that would represent a rare example of a high valent metal-nitrite species.[176–178] Specifically, previous success in using the hindered dianionic ligand bis(2,6-diisopropylphenylcarboxamido)pyridine (L^{2-}) to prepare reactive complexes with cores $[CuX]^{2+}$ (X = OR,[23–25,29,33,34] SR,[40] OOR,[28] O_2CR,[31,37] F, Cl, and Br[27]) led us to target $LCuNO_2$. Herein, we describe the successful generation and spectroscopic characterization of this novel high valent metal-nitrite species, as well as preliminary studies of PCET reactivity with phenolic substrates that results in an unusual anaerobic nitration.

3.2 Synthesis and characterization of [M][LCuNO$_2$] (M = NBu4$^+$ or PPN$^+$)

Addition of the corresponding nitrite salt [M][NO$_2$] to LCu(MeCN) in THF resulted in the formation of the Cu(II) complexes [M][LCuNO$_2$] (M = NBu$_4^+$ or PPN$^+$), which were isolated as powder blue solids and characterized by elemental analysis, UV-vis and EPR spectroscopy, and X-ray crystallography for M = PPN$^+$ (Scheme 3.1). Elemental analysis of [PPN][LCuNO$_2$] revealed the expected CHN composition, implying high purity of the sample. However, the elemental composition of the sample containing [NBu$_4$][LCuNO$_2$] fit when one eq. of water was included in the molecular formula. The introduction of water to the sample could have occurred upon sample shipping/handling to the elemental analysis facilities since the crystalline material, which was used for elemental analysis and spectroscopy experiments, displayed identical spectroscopic (UV-vis, EPR) markers to [PPN][LCuNO$_2$]. If water persisted in the spectroscopic experiments, we would have expected to see different molar absorptivity values in the Cu(II) UV-vis spectra (*vide infra*) and possibly a contamination of [LCuOH]$^-$. Additionally, the reagents used in the synthesis of [NBu$_4$][LCuNO$_2$] are anhydrous and the synthesis was performed in an inert glovebox. Therefore, we concluded that the purity of [NBu$_4$][LCuNO$_2$] was sufficient for further experiments.

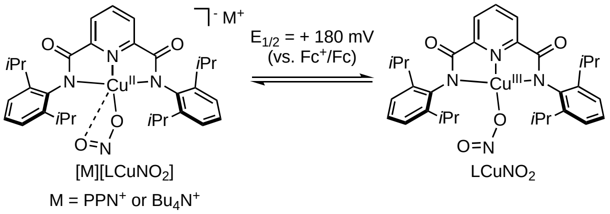

Scheme 3.1. Copper complexes discussed in this work, with formal oxidation states indicated. Reprinted with permission from ref. 179. Copyright 2022, American Chemical Society.

3.2.1 X-ray crystallography of [PPN][LCuNO$_2$]

High quality crystals could not be obtained for [NBu$_4$][LCuNO$_2$]; however, navy blue/gray crystalline plates of [PPN][LCuNO$_2$], grown from THF/diethyl ether vapor diffusion, resulted in a high resolution crystal structure. The X-ray structure of [PPN][LCuNO$_2$] shows nitrite bound strongly to the Cu ion through one oxygen atom (Cu1–O3 = 1.9667(13) Å) with an additional weak interaction through the second oxygen atom (Cu1-O4 = 2.4622(14) Å; Figure 3.1). This binding geometry is similar to that observed for carboxylate ligands in the series [NBu$_4$][LCu(O$_2$CR)],[31,37] and the N–O bond distances are comparable to those in other complexes containing Cu^{II}(η^1-ONO) cores.[44,57,58,157,160–162,61,180–185] The Cu ion adopts a square planar geometry (τ_4 = 0.16),[146] and the Cu1–N1, –N2, and –N3 bond lengths are similar to those in previously reported [LCuX]$^-$ complexes.[23,25,27–31,33,40]

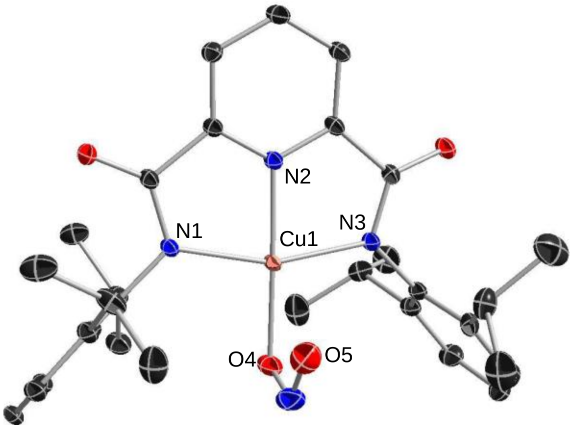

Figure 3.1. X-ray crystal structure of [PPN][LCuNO$_2$] with the PPN cation and H atoms omitted for clarity. All non-hydrogen atoms are shown as 30% thermal ellipsoids. Selected bond distances (Å) and angles (deg): Cu1–O3, 1.9667(13); Cu1–O4, 2.4622(14); Cu1–N1, 1.9987(13); Cu1–N2, 1.9242(14); Cu1–N3, 1.9985(13); N1–Cu1–N3, 160.25(6); N1–Cu1–N2, 80.26(5); N2–Cu1–N3, 80.48(6); N2–Cu1–O3, 178.01(6). Reprinted with permission from ref. 179. Copyright 2022, American Chemical Society.

3.2.2 EPR and UV-vis spectroscopy for [M][LCuNO$_2$] (M = NBu$_4^+$ or PPN$^+$)

The X-band EPR spectra for [M][LCuNO$_2$] (M = NBu$_4^+$ or PPN$^+$) in THF at 30 K are nearly identical and exhibit typical signals for S = ½ square-planar Cu(II) complexes (Figures 3.2). Spectral parameters were estimated by simulation, with the best match to the 17-line experimental superhyperfine pattern resulting when only 3 nitrogen atoms were included (Table 3.1). From these results and the similarity of the spectrum to those of other [LCuX]$^-$ complexes,[23,27–31,33,34,40]we conclude that little spin density is present on the nitrite N atom and that the superhyperfine coupling arises from interactions with the N atoms of L^{2-}. The UV-vis spectra for [M][LCuNO$_2$] (M = NBu$_4^+$ or PPN$^+$) in THF show typical *d-d* transitions (λ_{max} ~586 nm, ε ~ 480 M^{-1}cm^{-1}; Figure 3.3).

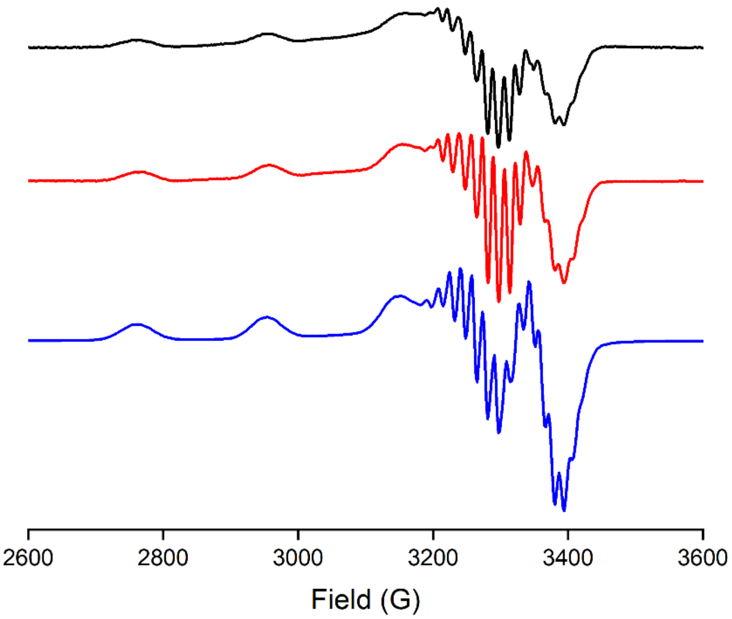

Figure 3.2. Continuous wave X-band EPR spectrum of 1 mM [NBu$_4$][LCuNO$_2$] in THF at 30 K (black), 1 mM [PPN][LCuNO$_2$] in THF at 30 K (red), and the simulation of [LCuNO$_2$]$^-$ (blue). Parameters: 30 K; microwave frequency 9.38 GHz; microwave power 0.0002 mW; modulation amplitude 9.8 G; modulation frequency 100 kHz. Parameters from the simulation are listed in Table 3.1. Reprinted with permission from ref. 179. Copyright 2022, American Chemical Society.

Table 3.1. Simulated g-values and hyperfine/superhyperfine parameters (MHz) for Cu, N^{pyridine}, and N^{amide} nuclei for [PPN][LCuNO$_2$] in THF at 30 K.

[PPN][LCuNO$_2$]											
g_x	g_y	g_z	A^{Cu}_x	A^{Cu}_y	A^{Cu}_z	A^{py}_x	A^{py}_x	A^{py}_z	A^{am}_x	A^{am}_y	A^{am}_z
2.09	2.11	2.26	55	60	595	33	50	40	48	50	40

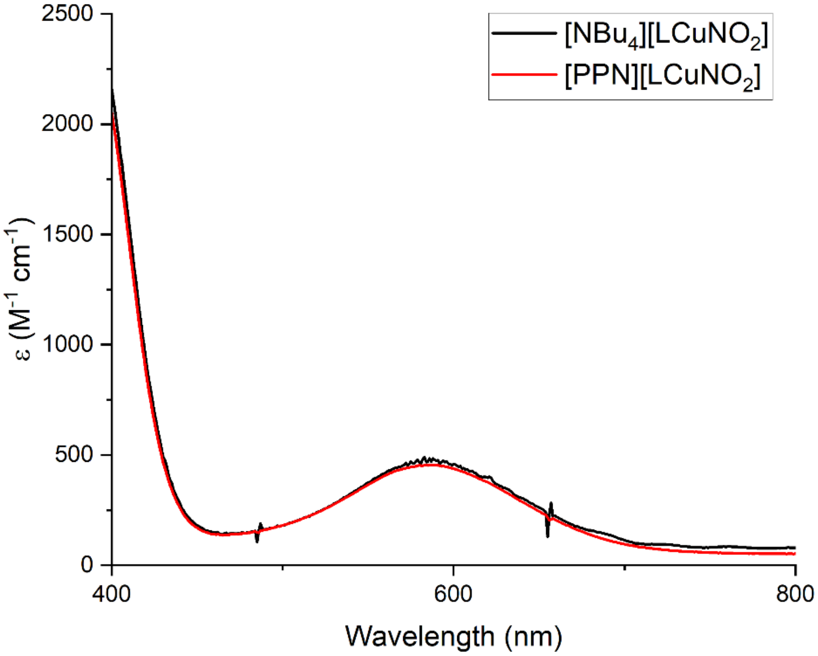

Figure 3.3. Overlay of the UV-vis spectra of [NBu$_4$][LCuNO$_2$] (black) and [PPN][LCuNO$_2$] (red) in THF at -80 ˚C. Reprinted with permission from ref. 179. Copyright 2022, American Chemical Society.

3.2.3 Electrochemistry of [NBu$_4$][LCuNO$_2$]

Cyclic voltammetry for [NBu$_4$][LCuNO$_2$] in THF (0.3 M [NBu$_4$][PF$_6$]) revealed a pseudoreversible wave with $E_{1/2}$ = +180 mV vs. Fc/Fc$^+$ (linear plot of i_{pa} vs. $\nu^{1/2}$, Figure 3.4). This oxidation potential is similar to those measured for the [LCu(O$_2$CR)]$^{-/0}$ series (range = 150 - 298 mV)[31] and 347 mV higher than that for [LCuOH]$^{-/0}$,[29] all which track inversely with the basicity of the anionic "X" ligands (greater basicity, lower potential; Table 3.2).

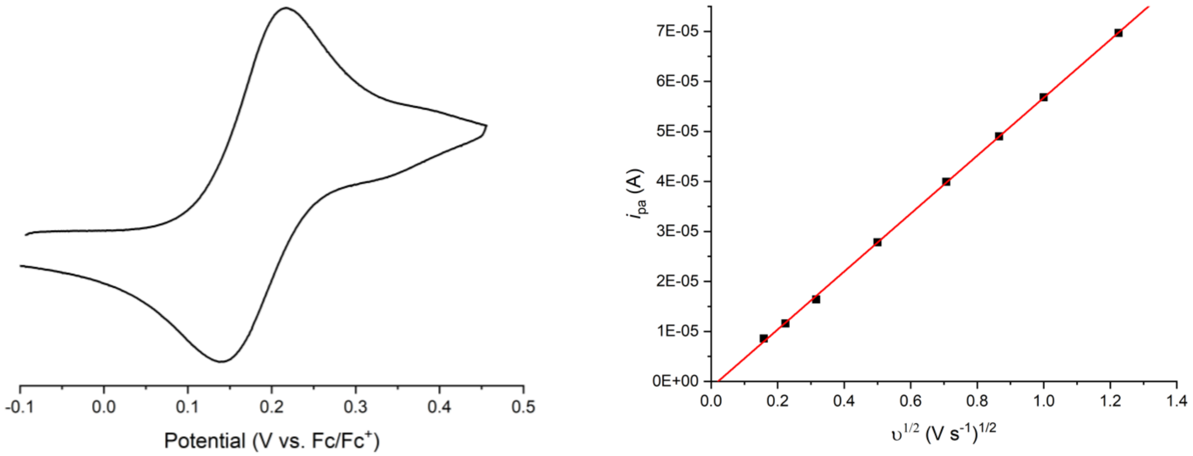

Figure 3.4. (Left) Cyclic voltammogram collected of [NBu$_4$][LCuNO$_2$]. Conditions: 2 mM [LCuNO$_2$], 0.3 M TBAP, THF, 25 °C, glassy-carbon working electrode, 100 mV/s scan rate. (Right) Anodic current response as a function of the square root of the scan rate. Reprinted with permission from ref. 179. Copyright 2022, American Chemical Society.

Table 3.2. Cyclic voltammetry data^a for [LCuX]$^{-/0}$

Complex	$E_{1/2}$ (mV)	Ref.
[LCuSPh]$^-$	-251	40
[LCuSH]$^-$	-209	40
[LCuOOtBu]$^-$	-205	28
[LCuOH]$^-$	-167	29
[LCuOOCMe$_2$Ph]$^-$	-154	28
[LCuOCH$_2$CF$_3$]$^-$	37	29
[LCuO$_2$CCH$_3$]$^-$	150	31
[LCuO$_2$CC$_6$H$_4$(OMe)]$^-$	151	31
[LCuO$_2$CC$_6$H$_5$]$^-$	169	31
[LCuNO$_2$]$^-$	180	this work
[LCuO$_2$CC$_6$H$_4$(Cl)]$^-$	228	30,31
[LCuO$_2$CC$_6$H$_4$(NO$_2$)]$^-$	239	31
[LCuO$_2$CC$_6$F$_5$]$^-$	298	31

^{a}Measured in THF with TBAP as the supporting electrolyte using a glassy-carbon electrode

3.3 Synthesis and characterization of LCuNO$_2$

Addition of 1 eq. of [AcFc][BArF$_{24}$] to a solution of [NBu$_4$][LCuNO$_2$] in THF at -80 °C resulted in immediate development of a deep Prussian blue color and the appearance of intense features at 478 (e = 5350 M^{-1}cm^{-1}), 655 (e = 9170 M^{-1}cm^{-1}), and 816 (e = 7180 M^{-1}cm^{-1}) nm in the UV-vis spectrum (Figure 3.5 a). Variation of the amount of [AcFc]$^+$ between 0.2-1.8 eq. showed attainment of maximum absorbance for the new features when 1 eq. of [AcFc]$^+$ was added (Figure 3.5 b and 3.6). Also, addition of 1 eq. of decamethylferrocene (Fc*) bleached the solution to yield the spectrum of $[LCuNO_2]^-$, a process that could be repeated (2x) (Figure 3.7). Taken together, the evidence supports reversible 1-electron oxidation of $[NBu_4][LCuNO_2]$.

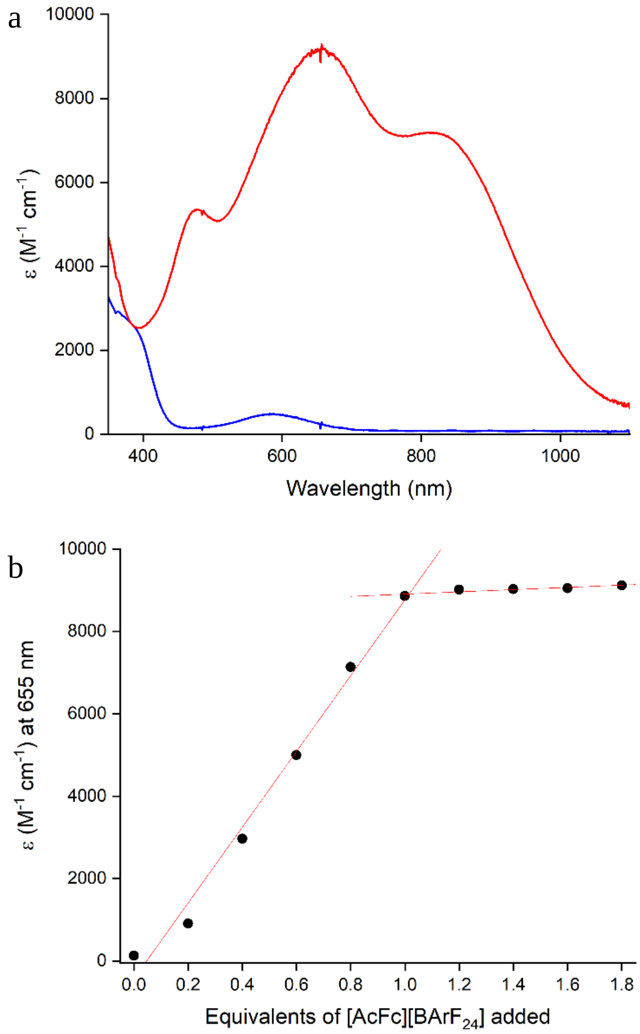

Figure 3.5. (a) Overlay of UV-vis spectra of $[NBu_4][LCuNO_2]$ (blue) and the species generated upon addition of 1 eq. of $[AcFc][BArF_{24}]$ to $[NBu_4][LCuNO_2]$ (red). Conditions: -80 °C in THF. (b) Plot of corresponding molar absorptivity values at λ = 655 nm vs. equivalents of $[AcFc][BArF_{24}]$ added to $[NBu_4][LCuNO_2]$ at -80 °C in THF. Reprinted with permission from ref. 179. Copyright 2022, American Chemical Society.

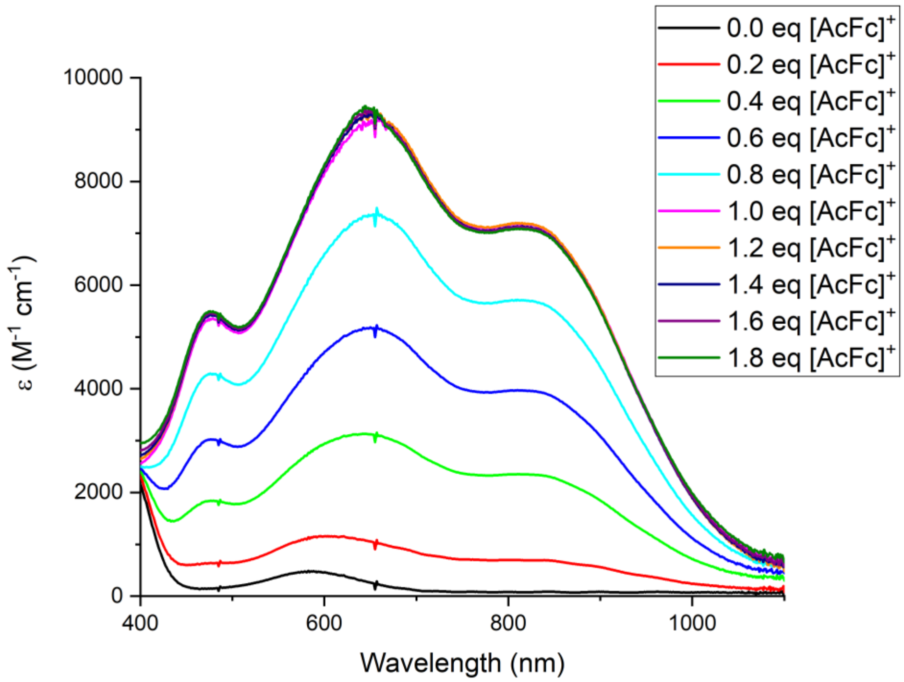

Figure 3.6. Overlay of UV-vis spectra upon addition of incremental equivalents of [AcFc][BArF$_{24}$] to [NBu$_4$][LCuNO$_2$] at -80 °C in THF. Reprinted with permission from ref. 179. Copyright 2022, American Chemical Society.

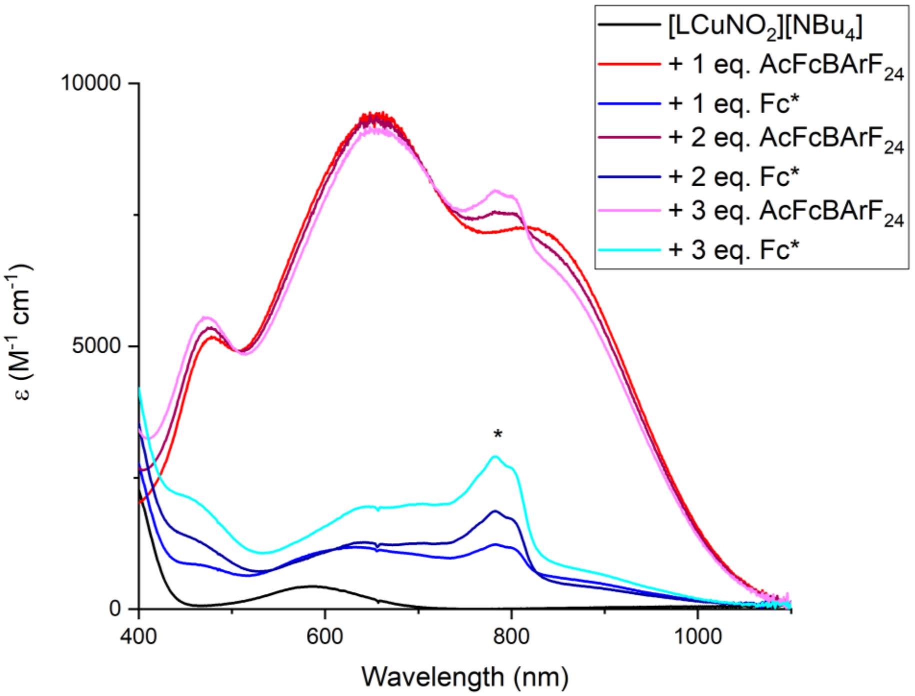

Figure 3.7. UV-vis chemical oxidation/reduction titration where up to 3 eq. of [AcFc][BArF$_{24}$] and Fc* were added to [NB$_{u4}$][LCuNO$_2$] in THF at -80 °C (*denotes Fc*$^+$ signal). Reprinted with permission from ref. 179. Copyright 2022, American Chemical Society.

The new UV-vis features that appear upon oxidation of [NBu$_4$][LCuNO$_2$] are similar to those seen for other LCuX complexes, and bear particular resemblance to those found for the LCuO$_2$CR series.[31] These features were assigned using TD-DFT to Ligand-to-Metal Charge Transfers (LMCTs) involving N-aryl $\pi \rightarrow$ Cu d and N-amide $\pi \rightarrow$ Cu d transitions.[30] Consistent with these assignments, the energy of these transitions is inversely proportional to the electron withdrawing characteristics of the carboxylate ligand. Thus, for example, LCuO$_2$CC$_6$F$_5$, with the most electron withdrawing carboxylate and the lowest carboxylic acid aqueous pK_a of 1.48,[186] yields the most electrophilic Cu ion and the lowest energy feature at 866 nm, whereas LCuO$_2$CCH$_3$ with its absorption feature at 809 nm has the least electrophilic Cu ion in the series with a carboxylic acid aqueous pK_a of 4.8.[31] The lowest energy peak for the product of 1-electron oxidation of [NBu$_4$][LCuNO$_2$] has λ_{max} = 816 nm, intermediate in the LCuO$_2$CR series, consistent with the nitrous acid aqueous pK_a of 3.16, and in line with an analogous LMCT assignment.[187] Finally, a peak at 634 cm^{-1}

was observed in the resonance Raman spectrum of $LCuNO_2$ (λ_{ex} = 660 nm), which we assign as ν(Cu–O) based on nearly identical peaks present in previously measured spectra for LCuX with X = O-based ligands (Figure 3.8).[28,29,35] Taken together, the UV-vis and resonance Raman spectra and titration/stoichiometry/reversibility data support formation of $LCuNO_2$ upon 1-electron oxidation of $[NBu_4][LCuNO_2]$.

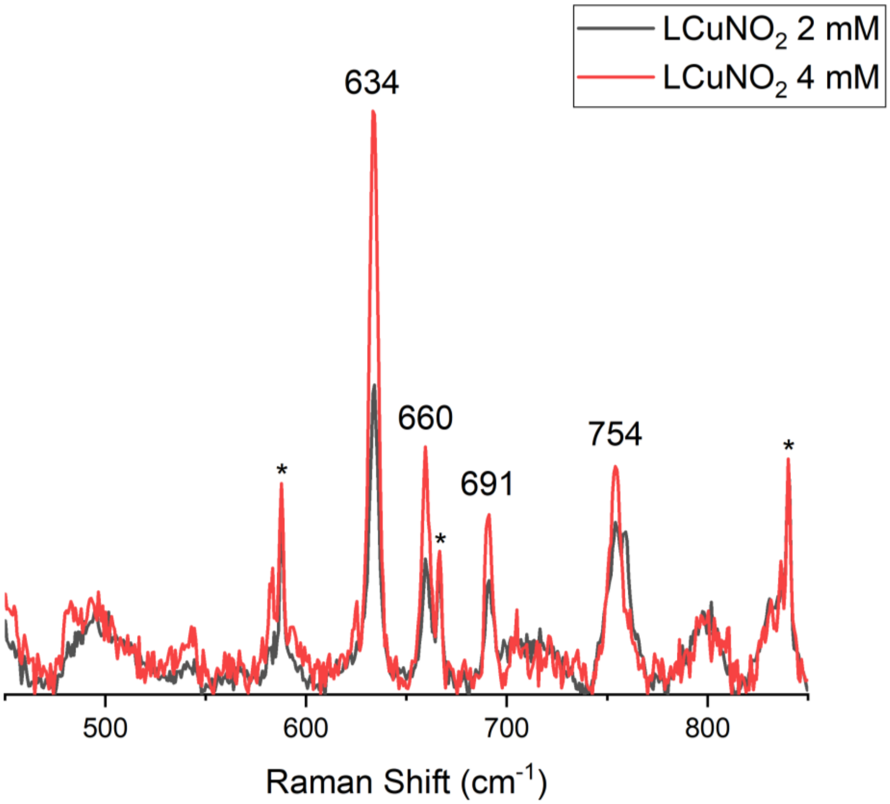

Figure 3.8. Resonance Raman spectra (λ_{ex} = 660 nm) of frozen $LCuNO_2$ samples in THF (2 mM, black and 4 mM, red). Peaks with concentration dependence are labelled (* denotes solvent). Reprinted with permission from ref. 179. Copyright 2022, American Chemical Society.

3.4 PCET reactivity of $LCuNO_2$

Treatment of $LCuNO_2$ with 2,4,6-tri-*t*-butylphenol (TTBP, 50 eq.) in THF at -80 °C led to decay of the absorptions associated with $LCuNO_2$. This decay was monitored over ~40 min and a global fit of the decay spectra to a second order reaction model using ReactLab Kinetics[188] yielded a k_2 of $1(1) \times 10^{-1}$ M^{-1} s^{-1}. The UV-vis spectrum of the product solution (Figure 3.9) indicated formation of the 2,4,6-tri-*t*-butylphenoxyl radical (characteristic peaks around 400 and 660 nm)[189,190] and LCu(THF) (*d-d* transition at 570 nm).[30] The radical was also identified by EPR spectroscopy and from integration a yield of 61% was determined (Figure 3.10). In a separate experiment designed to detect possible coproduct NO, a solution of TTBP (50 eq.) was added to a solution of $LCuNO_2$ at -40 °C and allowed to warm to room temperature in the presence of a solution of CoTPP (TPP = 5,10,15,20-tetraphenyl-21H,23H-porphine).[51,62,163,177] Subsequent analysis of the latter solution by UV-vis spectroscopy revealed formation of (NO)CoTPP in an amount corresponding to ~15% yield of NO from the PCET reaction (Figure 3.11). We presume that HNO_2 also forms in the PCET reaction, but decays via unidentified processes, which might also lead to NO. Interpreted as a control experiment, we attempted to detect NO formation from the decay of $LCuNO_2$ (albeit in the presence of phosphine that was added in an unrelated experiment) in THF at -40 °C for 2 h. The starting material $LCuNO_2$ decayed, and NO formation was not detected, so we concluded the presence of phenol is necessary for the formation of NO. An alternative PCET pathway (analogous to one identified previously in a reaction of a Cu(II)-NO_2 complex)[162] would involve initial formation of NO and $LCu^{III}OH$, but the latter would be expected to react further with TTBP and generate an additional equivalent of the phenoxyl radical (Scheme 3.2). The observed low yield of the radical and the low yield of NO argues against this pathway being the dominant HAT step.[191,192]

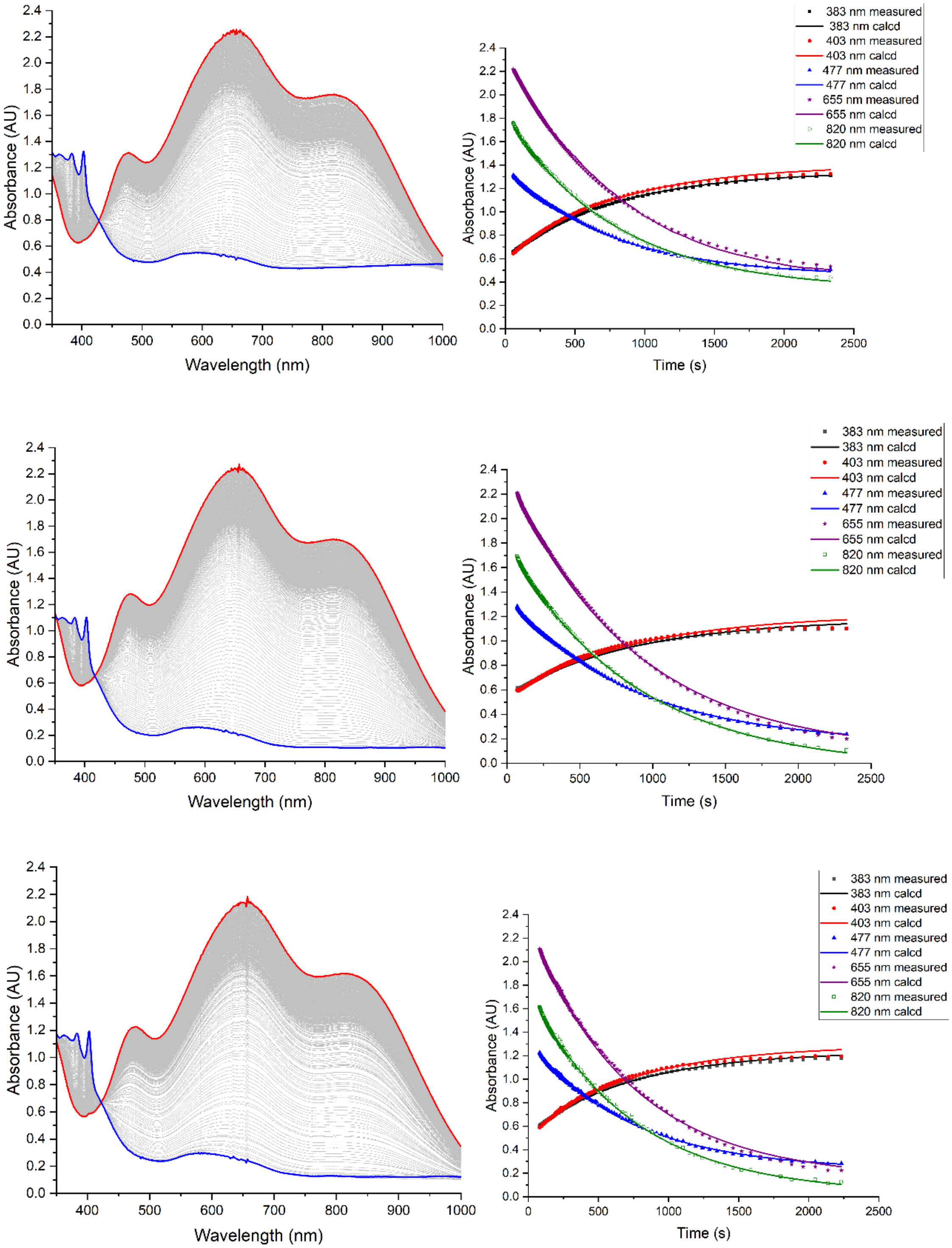

Figure 3.9. (Left column) Triplicate UV-vis spectra as a function of time for the reactions of LCuNO$_2$ (red) with TTBP (50 eq.) in THF at -80 °C. The product spectrum (blue) is assigned as LCuTHF and the phenoxyl radical of TTBP. (Right column) Plots of

absorbance vs. time at representative wavelengths (λ = 383, 403, 477, 655 and 820 nm) for the respective decay plots in the right column. The plots contain an overlay of experimental (scatter plots) and calculated (lines) data to represent the accuracy of the fit from ReactLab Kinetics, which was used to calculate the k_2 value discussed in the text. Reprinted with permission from ref. 179. Copyright 2022, American Chemical Society.

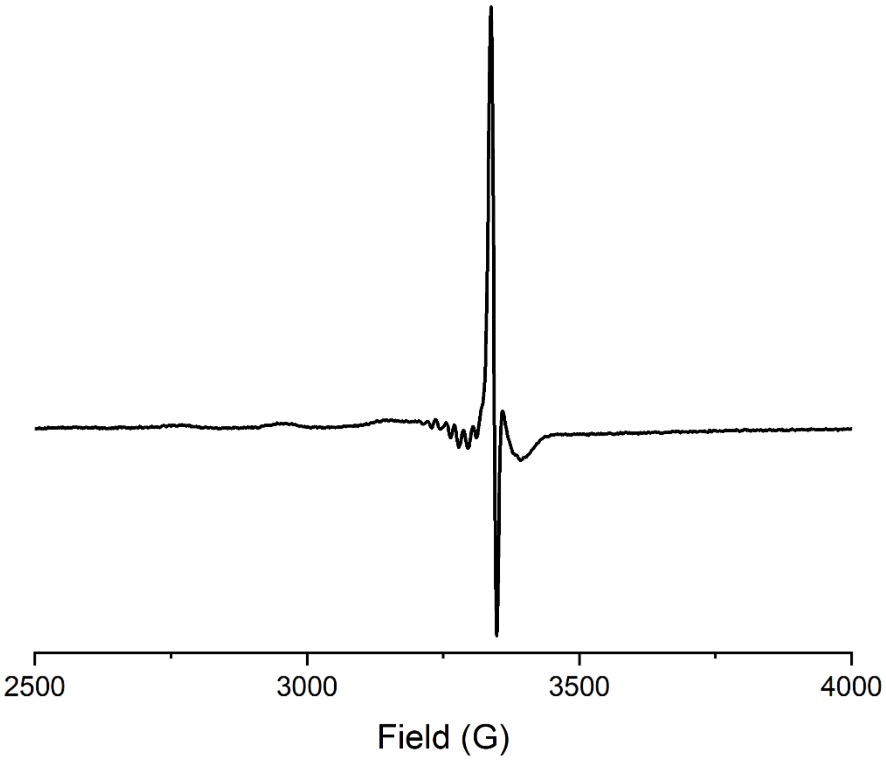

Figure 3.10. Continuous wave X-band (9.38 GHz) EPR spectrum of the products of the reaction between 0.1 mM $LCuNO_2$ and 50 eq. of TTBP in THF at 30 K. Reprinted with permission from ref. 179. Copyright 2022, American Chemical Society.

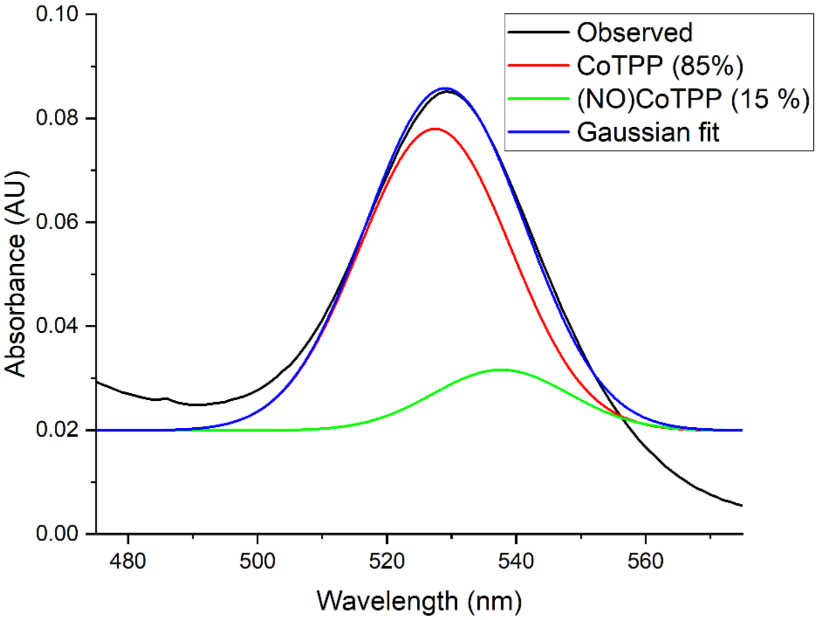

Figure 3.11. UV-vis spectrum and Gaussian fits of the CH_2Cl_2 solution containing CoTPP after exposure to the headspace of the reaction between $LCuNO_2$ and TTBP. Reprinted with permission from ref. 179. Copyright 2022, American Chemical Society.

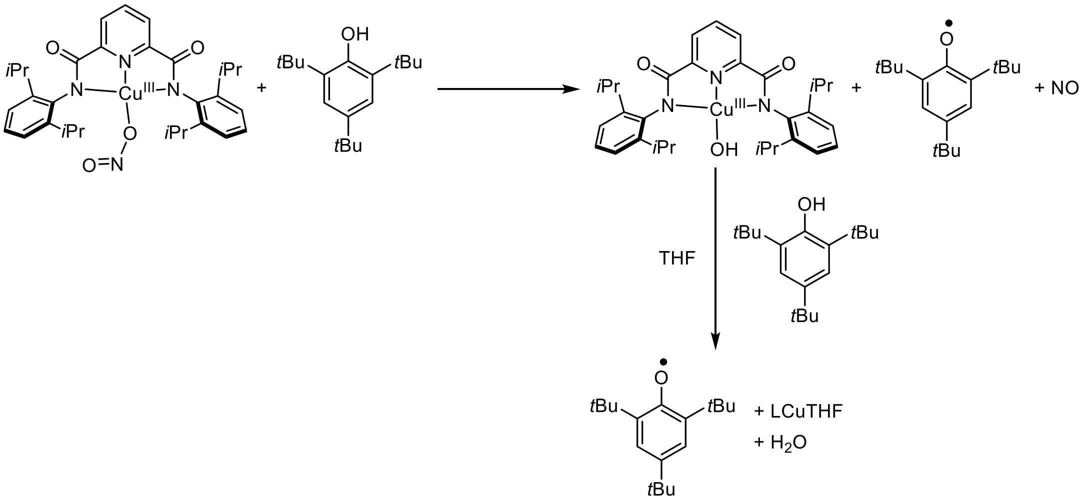

Scheme 3.2. An alternative mechanism of the PCET reaction of $LCuNO_2$ and TTBP where $LCuNO_2$ abstracts an H-atom from TTBP resulting in O–N bond cleavage to give products LCuOH, the phenoxyl radical, and NO. LCuOH is known to quickly react with TTBP so this mechanism would result in two eq. of the phenoxyl radical product in the presence of excess TTBP. Reprinted with permission from ref. 179. Copyright 2022, American Chemical Society.

The rate constant found for the reaction of TTBP with $LCuNO_2$ is similar to the rate constant for the reaction with $LCuO_2CC_6H_4(Cl)$ under the same conditions (k_2 = 3(1) x 10^{-1} M^{-1} s^{-1}), but it is ~100 times smaller than that for the reaction with LCuOH (k_2 = 2(1) x 10^1 M^{-1} s^{-1}).[30] These rate constants are in line with thermodynamic considerations, particularly $E_{1/2}$ and pK_a values. Thus, the $[LCuNO_2]^{-/0}$ $E_{1/2}$ of 180 mV vs. Fc/Fc^+ and the pK_a of HNO_2 of 3.16[187] fall close to the corresponding $E_{1/2}$ and carboxylic acid pK_a values for the series $[LCuO_2CR]^{-/0}$, and the former $E_{1/2}$ values correlate with the log k_2 values for reaction with TTBP (Figure 3.12).[31] These relationships support similar driving forces for the PCET reactions. Likewise, the greater basicity of LCuOH that results in formation of a stronger O-H bond underlies its faster PCET reactions.[24]

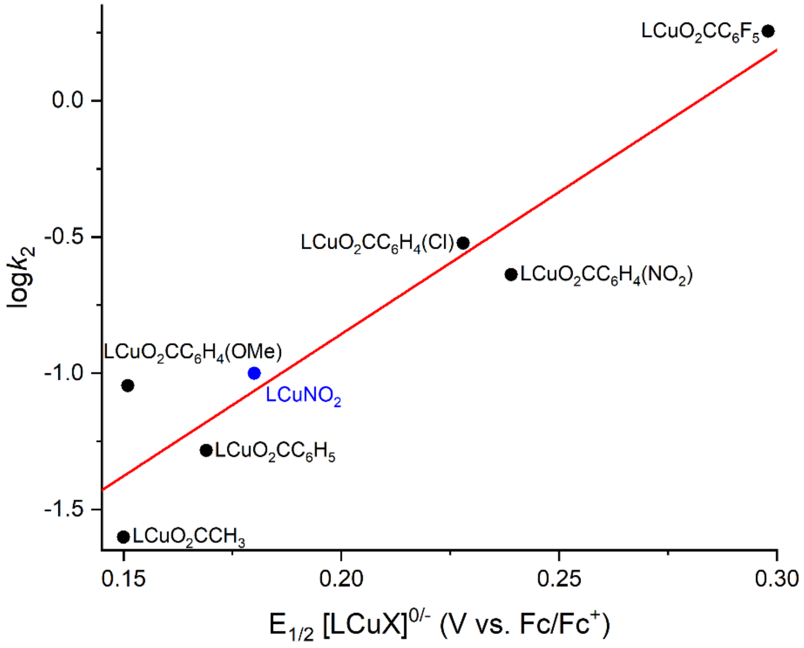

Figure 3.12. Plot of $E_{1/2}$ for the $[LCuX]^{0/-}$ couple in THF vs the log k_2 values for the reactions between LCuX and TTBP at -80 ˚C in THF. Figure reproduced from reference [31]. Reprinted with permission from ref. 179. Copyright 2022, American Chemical Society.

3.5 Nitration reactivity of $LCuNO_2$

UV-vis monitoring of the reactions between $LCuNO_2$ and varying amounts of 2,4-di-t-butylphenol (DTBP) (1 – 60 eq.) in THF at -40 °C resulted in $t_{1/2}$ values of 613, 318, 252, and 176 s in the presence of 1, 20, 40, and 60 eq. of substrate, respectively (Figure 3.13). While the trend in $t_{1/2}$ values indicate a dependence of the rate on the DTBP concentration, the decay data could not be fit to simple kinetic models (i.e., pseudo-first order; Figure 3.13 c, f, i, and l). These findings suggest a more complicated reaction occurs with DTBP compared to TTBP. Product analysis was performed in attempt to understand the results from the kinetic experiments. A peak at 570 nm in the final UV-vis spectrum suggests formation of LCu(THF). To identify the organic products, reactions were performed on larger scale (2.67 mM) at -40 °C in THF using 0.5 or 1 eq. DTBP for 2 h or 10 eq. DTBP for 1 h, and the residues were analyzed by ^{1}H NMR spectroscopy (Figure 3.14-3.16). Two products were identified: the coupled bisphenol product, 3,3′,5,5′-tetra-*t*-butyl-[1,1′-biphenyl]-2,2′-diol, and 2,4-di-*t*-butyl-6-nitrophenol (Scheme 3.3). The yields of the bisphenol and 2,4-di-*t*-butyl-6-nitrophenol and the amount of unreacted DTBP varied with differing equivalents of DTBP (Table 3.3). The data show that the yield of nitrated product and the conversion of substrate increase in the reactions with fewer equivalents of DTBP used. We interpret these results (greater nitration when $LCuNO_2$ is in excess) to indicate that nitration involves multiple equivalents of $LCuNO_2$.

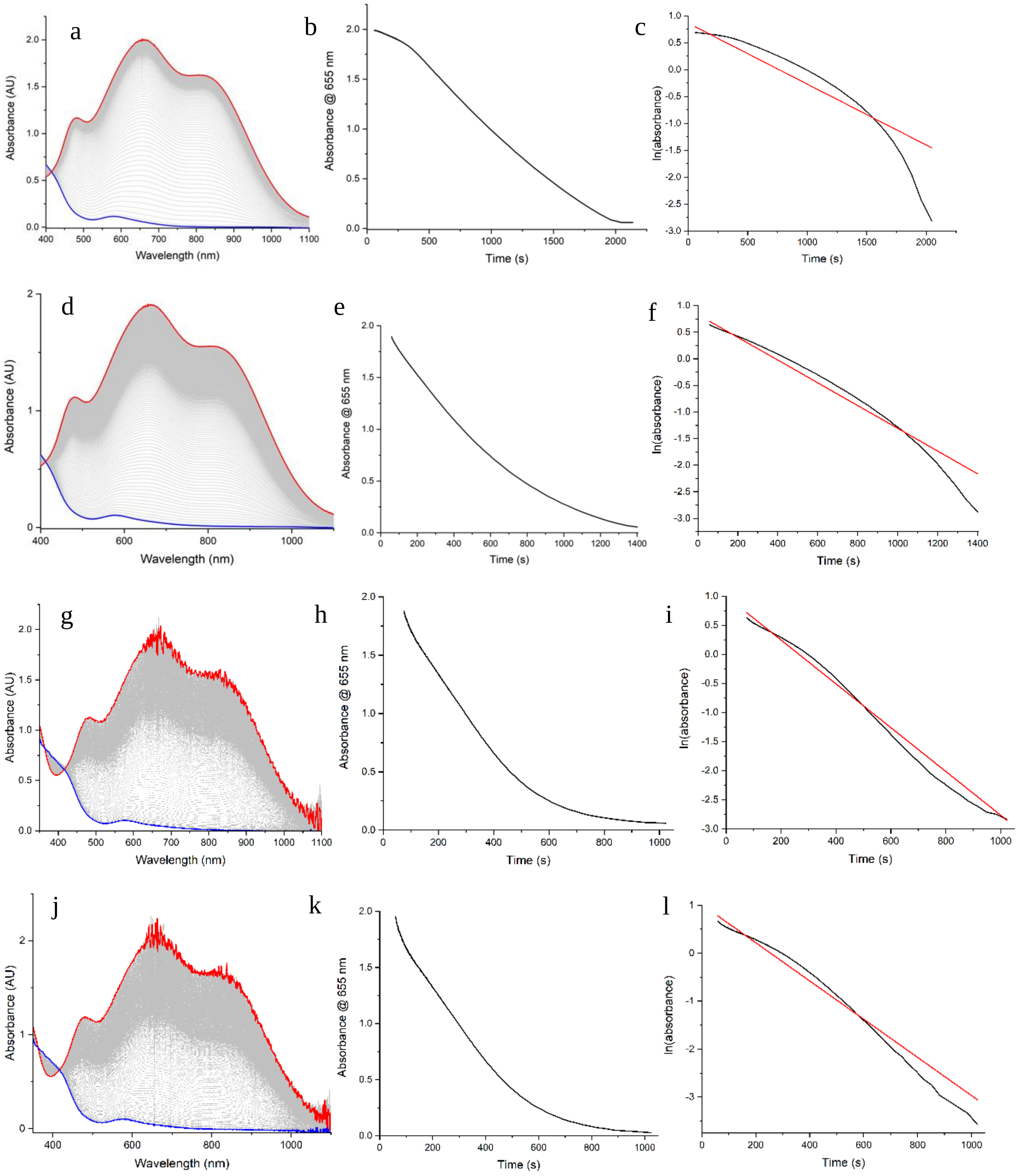

Figure 3.13. (a, d, g, j) UV-vis spectra as a function of time for the reaction between $LCuNO_2$ (red) and DTBP (a, d, g, j: 1 eq., 20 eq. 40 eq. 60 eq.) in THF at -40 °C. The product spectrum (blue) is assigned as LCuTHF. (b, e, h, k) Plot of absorbance vs. time at 655 nm for the reaction between $LCuNO_2$ and DTBP in THF at -40 °C (b, e, h, k: 1 eq., 20 eq. 40 eq. 60 eq.: $t_{1/2}$ = 613, 318, 252, 176 s). (c, f, i, l) Plot of ln(absorbance) vs. time at 655 nm (black) and a linear fit (red) for the reaction between LCuNO2 and DTBP (c, f, i, l: 1 eq., 20 eq. 40 eq. 60 eq.) in THF at -40 °C. Reprinted with permission from ref. 179. Copyright 2022, American Chemical Society.

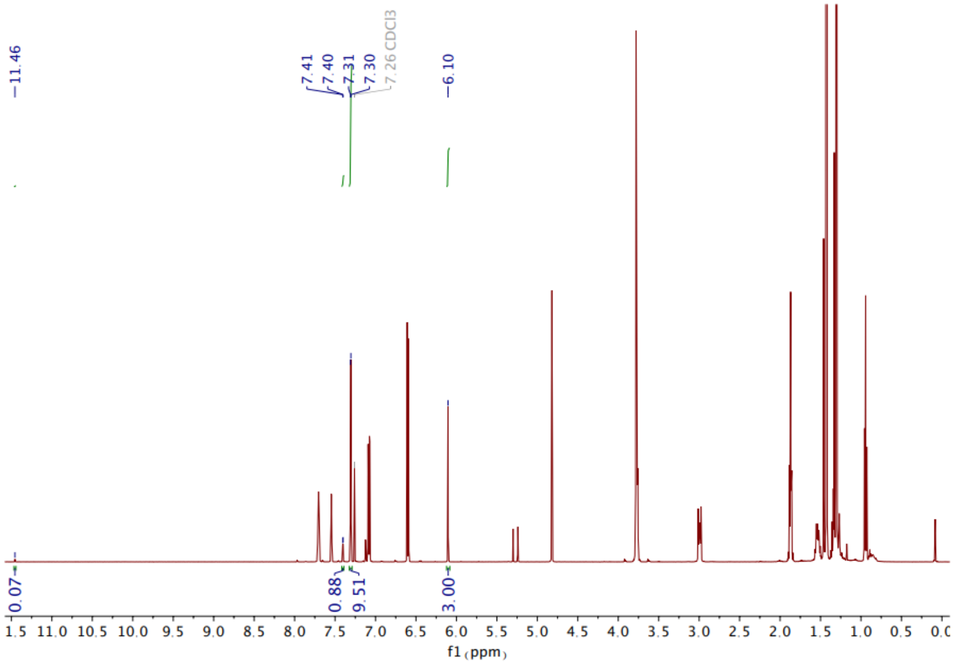

Figure 3.14. Representative ^{1}H NMR spectrum of the products from the reaction between $LCuNO_2$ and 10 eq. of DTBP. Reprinted with permission from ref. 179. Copyright 2022, American Chemical Society.

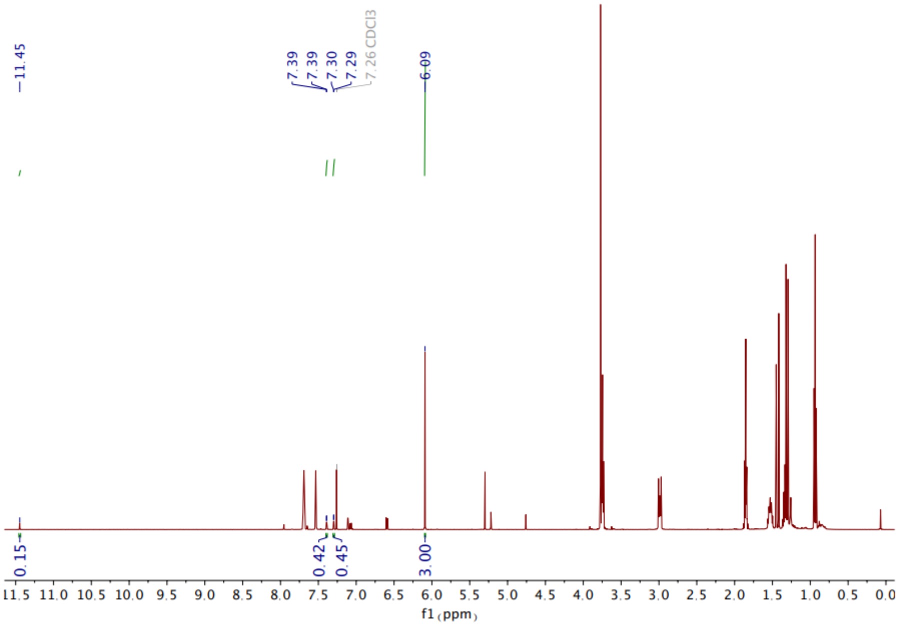

Figure 3.15. Representative ^{1}H NMR spectrum of the products from the reaction between $LCuNO_2$ and 1 eq. of DTBP. Reprinted with permission from ref. 179. Copyright 2022, American Chemical Society.

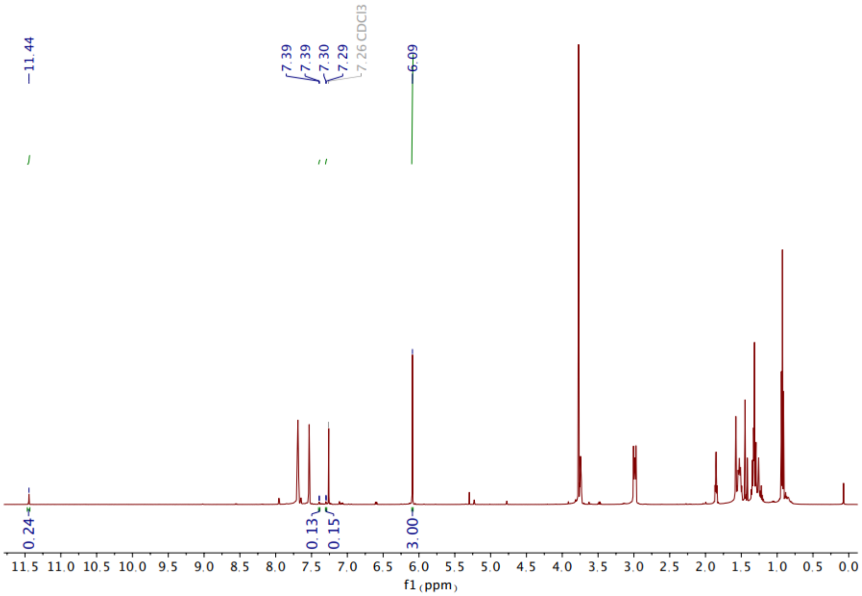

Figure 3.16. Representative ^{1}H NMR spectrum of the products from the reaction between $LCuNO_2$ and 0.5 eq. of DTBP. Reprinted with permission from ref. 179. Copyright 2022, American Chemical Society.

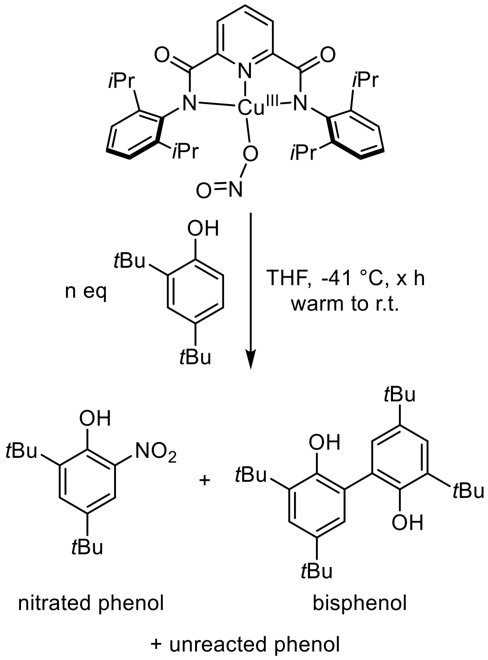

Scheme 3.3. The observed reactants and products when $LCuNO_2$ is reacted with DTBP. Reprinted with permission from ref. 179. Copyright 2022, American Chemical Society.

Table 3.3. Results from product analysis of the reactions between $LCuNO_2$ and various equivalents of DTBP.[a]

equivalents	nitrated phenol % yield	bisphenol % yield[b]	% of unreacted phenol	mass balance[c] (%)	% phenol converted[d]
10	0.5	8.2	94	102.7	8.5
	0.7	8.8	95	104.5	9.1
1	15	42	45	102	56
	17	43	42	102	59
0.5	48	26	30	104	71
	46	24	28	98	71

[a] All data were from ^1H NMR spectrum integrations using the integration of the trimethoxybenzene peak at 6.09 ppm (3 protons) as a standard. All values are based on DTBP loading. [b] Values take into consideration that 2 moles of DTBP are required to form 1 mole of bisphenol. [c] Mass balance values over 100% are due to standard error in ^1H NMR integration values. [d] Calculated by the equation: (nitrated phenol % yield + bisphenol % yield)/mass balance.

The product 2,4-di-*t*-butyl-6-nitrophenol could be formed from the reaction between $LCuNO_2$ and DTBP via multiple possible mechanisms. $LCuNO_2$ could abstract an H-atom from DTBP resulting in a [$LCuHNO_2$] adduct (which presumably decays to LCuTHF and HNO_2) and the phenoxyl radical of DTBP, which could react with another equivalent of $LCuNO_2$ in a 'rebound' type of reaction to form LCuTHF and nitrated phenol product (Scheme 3.4, path A). There is precedence to support the "rebound" pathway given that LCuF was reported to functionalize substrates via hydrogen-atom abstraction and radical capture, or "rebound".[27] Conversely, multiple pathways where free NO_2 is liberated are possible (Scheme 3.4), and free NO_2 has been studied for its oxidation and nitration chemistry with DTBP.[193] If $LCuNO_2$ does disproportionate into LCuTHF and free NO_2, then this is an unusual transformation of mildly oxidizing nitrite to NO_2. The results of the stoichiometry experiments are taken as evidence for Scheme 3.4, path A being the predominant nitration mechanism, because the dependence of the nitrated product yield on stoichiometry of $LCuNO_2$ suggests that limiting consumption of $LCuNO_2$ by PCET favors nitration.

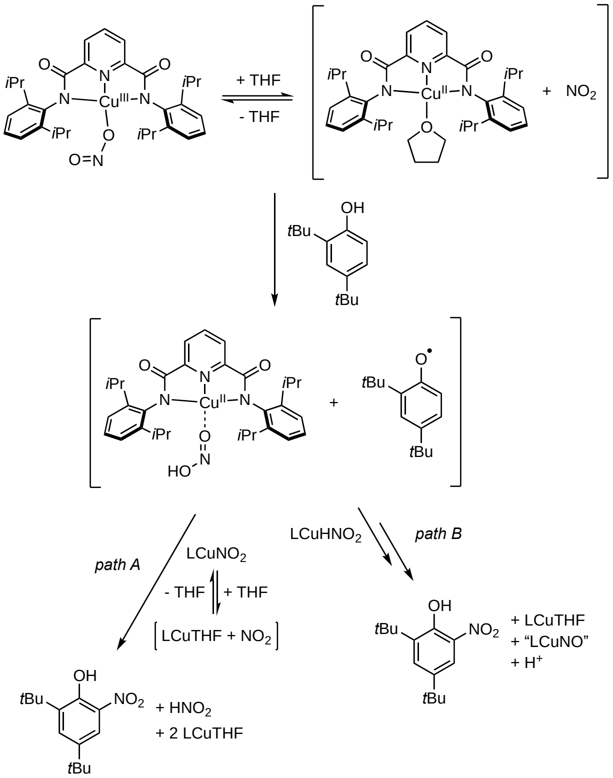

Scheme 3.4. Possible mechanisms of phenol nitration by $LCuNO_2$. Reprinted with permission from ref. 179. Copyright 2022, American Chemical Society.

$LCuNO_2$ could be involved in the generation of the phenoxyl radical of DTBP via a nucleophilic attack of the phenol on the nitrite ligand of $LCuNO_2$, as seen for a Cu^{II}-NO_2 compound previously (Scheme 3.5).[62,63] The products of the nucleophilic attack would be O-nitrosated DTBP and $LCu^{III}OH$, which would react with another equivalent of DTBP to form the bisphenol. The O-nitrosated DTBP would then release NO and the phenoxyl radical of DTBP, which could then combine to form 2,4-di-*t*-butyl-6-nitrophenol.[63] The stoichiometry experiments do not support this nitration mechanism because it does not use more than 1 eq. of $LCuNO_2$ to nitrate the phenol. However, we cannot rule out nucleophilic attack of the phenol on $LCuNO_2$ to form the phenoxyl radical of DTBP, which then could react with another equivalent of $LCuNO_2$ via the "rebound" mechanism.

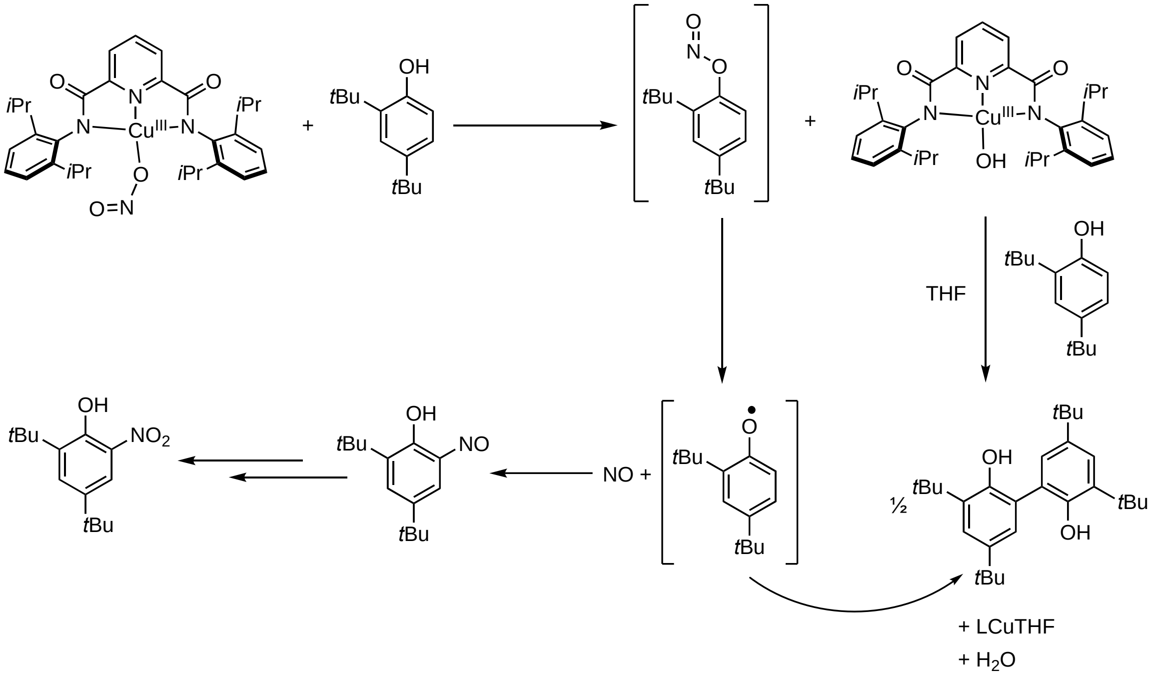

Scheme 3.5. An alternative mechanism for nitration of DTBP by $LCuNO_2$ involving nucleophilic attack of the phenol on the nitrite ligand of $LCuNO_2$. Reprinted with permission from ref. 179. Copyright 2022, American Chemical Society.

Alternatively, the [$LCuHNO_2$] adduct could functionalize DTBP directly, resulting in the nitrated phenol product of DTBP (Scheme 3.4, path B). This mechanism is consistent with the stoichiometry experiments and there is literature precedence for the involvement of a nitrous acid adduct, $[CoHNO_2]^{2+}$,[194] nitrating DTBP. However, we view this mechanism unlikely for [$LCuHNO_2$] since one of the products would be an unprecedented $\{CuNO\}^{10}$ complex.

Yet another pathway to generate 2,4-di-*t*-butyl-6-nitrophenol from $LCuNO_2$ and DTBP would involve one electron oxidation of DTBP by $LCuNO_2$, with the resulting cation radical phenol species reacting with free nitrite, as proposed for the protonated cryptand-capped tripodal Cu^{II}-NO_2 compound.[162] We performed reactions between $LCuNO_2$ and DTBP (THF, -40 ˚C) in the presence of excess nitrite (10 eq.) and observed almost instantaneous decay of the complex, and organic product analysis revealed no PCET product or nitrated phenol from these reactions. We currently do not understand why excess nitrite facilitates the decay of $LCuNO_2$. We rule this pathway out because the reported E_{ox} of DTBP is 1.03 V vs. Fc/Fc^+ (converted from 1.43 V vs. SCE),[195] which is about 800 mV higher than the $E_{1/2}$ found for the $[LCuNO_2]^{-/0}$ couple. As discussed for the protonated cryptand-capped tripodal Cu^{II}-NO_2 compound, phenol nitration typically occurs via O_2-dependent pathways through metal-peroxynitrite species. The reactions of the compounds $LCuNO_2$ and the protonated cryptand-capped tripodal Cu^{II}-NO_2 species are two recent examples of phenol nitration that occur through uncommon anaerobic pathways.[162]

3.6 Summary and conclusions

The Cu(II)-nitrite starting materials, $[M][LCuNO_2]$ ($M = NBu_4^+$ or PPN^+) were prepared, characterized by UV-vis and EPR spectroscopy, CHN analysis, and X-ray crystallography. Electrochemical and chemical oxidations of $[LCuNO_2]^-$ revealed a reversible one-electron oxidation to an intriguing $[CuNO_2]^{2+}$ core, and $LCuNO_2$ was characterized low temperatures by UV-vis and resonance Raman spectroscopies. To our knowledge, this complex is a unique example of a high-valent copper-nitrite complex. The reaction between $LCuNO_2$ and TTBP revealed that $LCuNO_2$ can abstract H-atoms from O–H substrates at rates comparable to $LCuO_2CR$ complexes.[31] Interestingly, the reaction between $LCuNO_2$ and DTBP yielded not only the expected PCET product but the ortho-nitrated phenol as well. Although there are multiple possible mechanisms that could result in the nitrated phenol, the detection of the nitrated product indicates $LCuNO_2$ (or a derivative) can functionalize substrates, a type of transformation that has only been demonstrated by X = halides for LCuX complexes.[27] These results provide an alternative pathway of understanding Cu-mediated oxidation and nitration chemistry.

3.7 Experimental section

3.7.1 Materials and methods

Metal complexes were synthesized and handled under a dinitrogen atmosphere in a Vacuum Atmospheres glovebox or an argon atmosphere using Schlenk techniques. All reagents and solvents were purchased from commercial sources unless otherwise noted. Tetrahydrofuran, acetonitrile, diethyl ether, dichloromethane, and pentane were passed through activated alumina columns and plumbed directly into a glovebox. Tetrahydrofuran and dichloromethane were stored over activated 3 Å molecular sieves in a dinitrogen-filled glovebox and, prior to use in spectroscopy and cyclic voltammetry experiments, filtered using a 25 mm diameter, 0.2 mm hydrophobic polytetrafluoroethylene (PTFE) syringe filter. Dry acetone was purchased from Sigma-Aldrich and used without purification. 2,4,6-tri-*t*-butylphenol (TTBP) and 2,4-di-*t*-butylphenol (DTBP) were recrystallized several times from saturated pentane solutions at -30 ˚C prior to use. LCu(MeCN)[26] and acetyl ferrocenium tetrakis(3,5-bis(trifluoromethyl)phenyl)borate ([AcFc][$BArF_{24}$])[34] were synthesized according to the published procedures. Bis(triphenylphosphine)iminium chloride (PPNCl), $AgNO_2$, [NBu_4][NO_2], Fc*, Fc, [NO][SbF_6], and trimethoxybenzene were purchased from Sigma-Aldrich and CoTPP was purchased from Strem Chemicals, and all were used without further purification.

UV-vis spectra were collected on a HP8453 (190 – 1100 nm) diode array spectrophotometer equipped with a Unisoku low-temperature UV-vis cell holder. EPR data were collected on frozen 1 mM samples with a CW Elexsys E500 EPR spectrometer using X-band (9.38 GHz) radiation at 35 dB and at 30 K. The microwave power, modulation amplitude, and modulation frequency were 0.0002 mW, 9.8 G, and 100 kHz, respectively. EPR spectral simulations were performed using the EasySpin EPR simulation package, v. 5.1, in Matlab.[196] NMR spectra were collected on a Varian Unity Inova (500 MHz) spectrometer. Deuterated chloroform ($CDCl_3$) was purchased from Cambridge Isotopes Laboratories, degassed, and dried over 3 Å molecular sieves prior to use. Cyclic voltammograms were recorded using an EC Epsilon potentiostat from BASi, a glassy carbon working electrode, a Pt counter electrode, and a Ag wire pseudoreference electrode. All cyclic voltammograms were performed in THF with 0.3 M tetrabutylammonium hexafluorophosphate (TBAP) electrolyte, which was recrystallized several times from ethanol and dried under high-vacuum before use, and were internally referenced to the ferrocene/ferrocenium (Fc/Fc^+) couple. The spectra were converted vs. the standard Fc/Fc^+ couple using standard conversion factors.[152] Elemental Analysis was performed by the CENTC Elemental Analysis Facility (University of Rochester).

For X-ray crystallography experiments, crystals were placed onto the tip of a MiTeGen cryoloop and mounted on a Bruker D8 VENTURE diffactometer equipped with a Photon III CMOS. The data collections were carried out using Mo Kα source using normal parabolic mirrors as monochromators at 173 K. Structure solutions were performed with SHELXT[153] using ShelXle[154] as a graphical interface. The structures were refined against F^2 on all data by full-matrix-least-squares with SHELXL.[155] The CCSD deposition number is: 2125948.

Resonance Raman spectra were obtained by collecting the collimated Raman scattering using a Plano convex lens (f = 10 cm, placed at an appropriate distance) through appropriate long-pass edge filter (Semrock). The spectra were collected by an Andor Shamrock 500i monochromator (SR-500I-A) with an Andor Newton 920 thermo-electric cooled CCD detector (DU920P-BU), which was cooled to -90 °C before collection. Data collection was interfaced with Andor Solis (s) software. Spectral data was collected on frozen samples at 77 K in EPR tubes using 135° backscattering geometry. Excitation at 660 nm was provided by a Cobolt Flamenco 660 nm 100 mW laser. Raman shifts were externally referenced to indene and internally referenced to solvent. Each spectrum was an accumulation of 450 spectra with 4 s acquisition times, resulting in 30 min collections. All spectra were baseline corrected using a multi-point correction within the software Spectragryph.[197]

3.7.2 Experimental procedures

Synthesis of [PPN][LCuNO$_2$]. A solution of PPNCl (1.696 g, 2.95 mmol) in anhydrous acetonitrile (5 mL) was added to 20 mL scintillation vial, covered in aluminum foil, containing $AgNO_2$ (0.500 g, 3.25 mmol) and acetonitrile (5 mL) and stirred for 1 h. The solvent was removed *in vacuo* and the pale orange, oily solid was dissolved in dry acetone (12 mL). Dry diethyl ether (8 mL) was slowly added down the side of the vial while crystals began to form. The vial was capped and stored at -30 °C overnight. The next day, the crystals were filtered, isolated, and residual solvents were removed *in vacuo*. After 1 week, the batch of crystals appeared to contain some silver decomposition products, so the batch was dissolved in CH_2Cl_2, filtered through a 25 mm diameter, 0.2 mm hydrophobic polytetrafluoroethylene (PTFE) syringe filter. LCuMeCN (50.0 mg, 0.085 mmol) was dissolved in THF (3 mL) in a 20 mL scintillation vial. To this vial, a slurry of [PPN][NO$_2$] (49.7 mg, 0.085 mmol) in THF (3 x 2 mL) was added quantitatively. After stirring for 1 h, the solution turned navy blue, and the solvent was removed *in vacuo*. The blue oil was triturated with pentane (2 x 5 mL) and the solvent was decanted and the resulting blue powder was dried *in vacuo* (83.5 mg, 87%). X-ray quality crystals were grown by dissolving the product in THF (1 mL) and using diethyl ether for vapor diffusion at room temperature over 3 days (navy blue/gray plates). UV-vis (THF, X °C) λ_{max}, nm (ε, M^{-1} cm^{-1}): 311 (8288), 385 (2509), 586 (454). Anal. calcd (%) for $C_{67}H_{67}CuN_5O_4P_2$: C, 71.10; H, 5.97; N, 6.19. Found: C, 70.73; H, 5.91; N, 5.91.

Synthesis of [NBu$_4$][LCuNO$_2$]. LCuMeCN (200.0 mg, 0.340 mmol) was dissolved in THF (4 mL) in a 20 mL scintillation vial. To this vial, a solution of [NBu$_4$][NO$_2$] (98.1 mg, 0.340 mmol) in THF (3 x 2 mL) was added quantitatively. After stirring for 1 h, the solution turned navy blue and the solvent was removed *in vacuo*. The oily product was triturated with pentane (2 x 5 mL) and the solvent was decanted then further removed *in vacuo* yielding a powder blue powder (253.0 mg, 89%). UV-vis (THF, -80 °C) λ_{max}, nm (ε, M^{-1} cm^{-1}): 311 (8594), 385 (2614), 586 (470). Anal. calcd (%) for $C_{47}H_{75}CuN_5O_5$ (as [NBu4][LCuNO2] $\bullet$ H_2O): C, 66.13; H, 8.86; N, 8.20. Found: C, 66.58; H, 8.57; N, 8.08.

General procedure for the generation of LCuNO$_2$. A solution of [NBu$_4$][LCuNO$_2$] in THF (0.2 mL, 2 mM) was injected into a UV-vis cuvette under Ar containing THF (1.6 mL) at -80 °C, set by the Unisoku low temperature UV-vis cell holder. After stirring and temperature equilibration (5 min), a UV-vis spectrum was recorded. With stirring, a solution of [AcFc][BArF$_{24}$] in THF (0.1 mL, 4 mM) was added to the cuvette (final concentration of 0.2 mM) and a spectrum was immediately recorded. For titration experiments, solution of [NBu$_4$][LCuNO$_2$] in THF (0.2 mL, 2 mM) was injected into a UV-vis cuvette under Ar containing THF (1.3 mL) at -80 °C, set by the Unisoku low temperature UV-vis cell holder. After stirring and temperature equilibration (5 min), a UV-vis spectrum was recorded. With stirring, aliquots of an [AcFc][BArF$_{24}$] solution in THF (0.8 mM) were added in 0.1 mL increments (0.2 eq.), up to 1.8 eq., to the cuvette and a spectrum was immediately recorded after each injection. A resonance Raman sample was prepared by cooling an EPR tube under Ar containing a solution of [NBu4][LCuNO$_2$] in THF (0.4 mL, 4 or 8 mM) and a stir bar to -78 °C in an acetone/dry ice-cold bath. A solution of [AcFc][BArF$_{24}$] in THF (0.4 mL, 4 or 8 mM) was slowly added down the side of the EPR tube and a magnetic stir bar retriever was submerged into the cold bath and used to thoroughly mix the contents of EPR tube. In rapid succession, the Ar supply and stir bar were removed, the outside of the EPR tube was wiped free of acetone and the tube was dunked into liquid nitrogen to freeze the sample.

General procedure for the reversible oxidation/reduction of [NBu_4][$LCuNO_2$]. A solution of [NBu_4][$LCuNO_2$] in THF (0.2 mL, 2 mM) was injected into a UV-vis cuvette under Ar containing THF (1.7 mL) at -80 °C, set by the Unisoku low temperature UV-vis cell holder. After stirring and temperature equilibration (5 min), a UV-vis spectrum was recorded. With stirring, a solution of [AcFc][$BArF_{24}$] in THF (0.1 mL, 4 mM) was added to the cuvette and a spectrum was immediately recorded. An aliquot of a Fc* solution in THF (0.1 mL, 4 mM) was added to the cuvette with stirring and another spectrum was immediately recorded. The chemical oxidation and reduction processes were repeated twice more, and spectra were recorded after each addition of reagent.

General procedure for the reactions between $LCuNO_2$ and phenol. A UV-vis cuvette under Ar containing THF (1.6 mL) at -80 °C (TTBP) or -40 °C (DTBP), set by the Unisoku low temperature UV-vis cell holder, was charged with a THF solution of [$LCuNO_2$][NBu_4] (0.2 mL, 2mM). The solution was allowed to cool (5 min) with stirring and a continuous collection of spectra was initiated. Quickly after, a THF solution of [AcFc][$BArF_{24}$] (0.1 mL, 4 mM) was injected into the cuvette. When the new features were fully formed, a THF solution of phenol (0.1 mL, various eq.) was quickly added, and the decay was observed until no further changes were observed. The k_2 values for the reactions between $LCuNO_2$ and TTBP (50 eq.) were calculated by using ReactLab Kinetics[188] using the known concentrations. EPR product analysis and quantification of the phenoxyl radical from the reaction between $LCuNO_2$ and TTBP were carried out by adding THF (0.3 mL) and a THF solution of [$LCuNO_2$][NBu_4] (0.1 mL, 0.6 mM) to an EPR tube containing a stir bar in the glovebox. The EPR tube was sealed with a septum cap, removed from the glovebox, and put under Ar on a Schlenk line. The tube was cooled to -78 °C in an acetone/dry ice-cold bath for 15 min when a THF solution of [AcFc][$BArF_{24}$] (0.1 mL, 0.6 mM) was slowly added down the side of the tube. A magnetic stir bar retriever was dunked into the cold bath and used to mix the solution. A THF solution of TTBP (0.1 mL, 30 mM, 50 eq.) was then slowly added down the side of the tube and the magnetic stir bar retriever was once again used to mix the solution. The reaction was allowed to proceed for 15 mins then frozen by, in rapid succession, removing the Ar flow, septum cap, and magnetic stir bar, wiping off the acetone from the outside of the tube, and dunking the tube into liquid nitrogen. The yield of the phenoxyl radical was calculated by finding the relative intensities of the double integration spectra for the reaction (0.1 mM in Cu, 5 mM in TTBP), TEMPO· (0.1 mM), and [PPN][$LCuNO_2$] (1 mM) and using them in the following equation: [(intensity of reaction spectrum - spectrum - [intensity of [PPN][$LCuNO_2$] spectrum/10])/(intensity of TEMPO·)]*100. The yield of NO released from the reaction between $LCuNO_2$ and TTBP (50 eq.) was found by placing a 1-dram vial inside a 20 mL vial that could be equipped with a cap containing a pierceable septum. THF (1.6 mL) was added to the inner 1-dram vial and a CH_2Cl_2 solution of CoTPP (0.2 mM, 2 mL) was added to the outer vial. The 2-vial setup and THF solutions of [NBu_4][$LCuNO_2$], [AcFc][$BArF_{24}$], and TTBP were cooled to -40 °C in a cold-well using an acetonitrile/dry ice-cold bath for 15 min. At -40 °C, the THF solutions of [NBu_4][$LCuNO_2$] (2 mM, 0.2 mL) and [AcFc][$BArF_{24}$] (4 mM, 0.1 mL) were syringed into the inner 1-dram vial to generate $LCuNO_2$. The 2-vial setup was capped with a pierceable septum cap and the THF solution of TTBP (50 eq., 200 mM, 0.1 mL) was spiked into the inner 1-dram vial. The reaction setup was allowed to come to room temperature for 1 h. An aliquot of the CH_2Cl_2 solution of CoTPP in the outer vial was diluted with CH_2Cl_2 (final concentration of 5 µM) and a room temperature UV-vis spectrum was recorded. The resulting spectrum was compared to pure CoTPP and (NO)CoTPP, which was generated via the same 2-vial setup using Fc and [NO][SbF_6] (50 eq.) in the inner 1-dram vial, using the Gaussian fitting function in Origin 2021b. The reactions between $LCuNO_2$ and various equivalents of DTBP (1 – 60 eq.) were analyzed using the natural log of the absorbance at a single wavelength (655 nm) over time. These plots were fit to a linear decay to attempt to derive pseudo-first order k_{obs} values for the various equivalents. The fits were found to be inappropriate because the data deviates from linearity due to more complicated kinetics occurring.

General procedure for organic product analysis of the reactions between $LCuNO_2$ and DTBP. THF solutions of [NBu_4][$LCuNO_2$], [AcFc][$BArF_{24}$], DTBP, a clean 20 mL scintillation vial were cooled for 10 minutes in a -41 °C coldwell generated by an acetonitrile/dry ice bath. The 20 mL scintillation vial was charged with the THF solution of $[NBu_4][LCuNO_2]$ (8 mM, 1 mL) followed by the THF solution of $[AcFc][BArF_{24}]$ (8 mM, 1 mL) to generate $LCuNO_2$. Then, the THF solution of DTBP (80 mM, 1 mL for 10 eq.; 8 mM, 1 mL for 1 eq.; 4 mM, 1 mL for 0.5 eq.) was immediately injected into the vial and the reaction was allowed to proceed in the coldwell for an allotted time (1 h when 10 eq. employed; 2 h when either 1 eq. or 0.5 eq. employed). The reaction mixture was brought to room temperature when the solvent was removed *in vacuo*. The residue was dissolved in CH_2Cl_2 (1 mL) and the solution was run through a 3-inch silica plug in a pipette. The vial and plug were rinsed with CH_2Cl_2 (2 x 1 mL). A THF solution of trimethoxybenzene (8 mM, 1 mL) was added to the resulting CH_2Cl_2 solution and the solvent was removed *in vacuo*. The residue was dissolved in $CDCl_3$ (1 mL) and a quantitative ^1H NMR spectrum was obtained.

Chapter 4

Exploration of high-valent Cu-amide complexes

4.1 Introduction

A myriad of pyridine-dicarboxamide copper-oxygen complexes have been synthesized and studied as mimics for enzyme active sites and for their proton-coupled electron transfer (PCET) reactivity.[21,23–26,28,29,33,34,198] The pyridine-dicarboxamide ligand, bis(2,6-diisopropylphenylcarboxamido)pyridine (L), has been shown to stabilize the Cu(III) oxidation state sufficiently enough to characterize over 10 different examples of Cu(III) complexes *in situ*.[24–28,30,31,33,34,40] We sought to extend the LCuX system to nitrogen-bound X ligands, amides or -NRR' (Figure 4.1), to understand if these species are accessible, as they are often proposed intermediates in copper-mediated transformations,[74,199,200] and to compare them to the oxygen-based complexes.

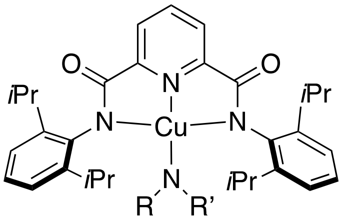

Figure 4.1. Target structure for LCuNRR' complexes.

Cu-amide complexes have been implicated as intermediates in chemical transformations, particularly C–N bond formation reactions.[74,199,200] Two common C–N bond forming reactions that use Cu are Ullmann couplings and Chan-Evans-Lam couplings.[73,76] Both types of reactions have been extensively studied and mechanisms have been proposed that include Cu(II) to Cu(III) transformations via disproportionation of two Cu(II) adducts (Scheme 4.1). The Cu(III) complexes, bound to both coupling partners and one being an amide, are then proposed to undergo reductive elimination to yield the product.[201]

Scheme 4.1. Proposed catalytic cycle for Chan-Evans-Lam couplings. Adapted from ref. 202.

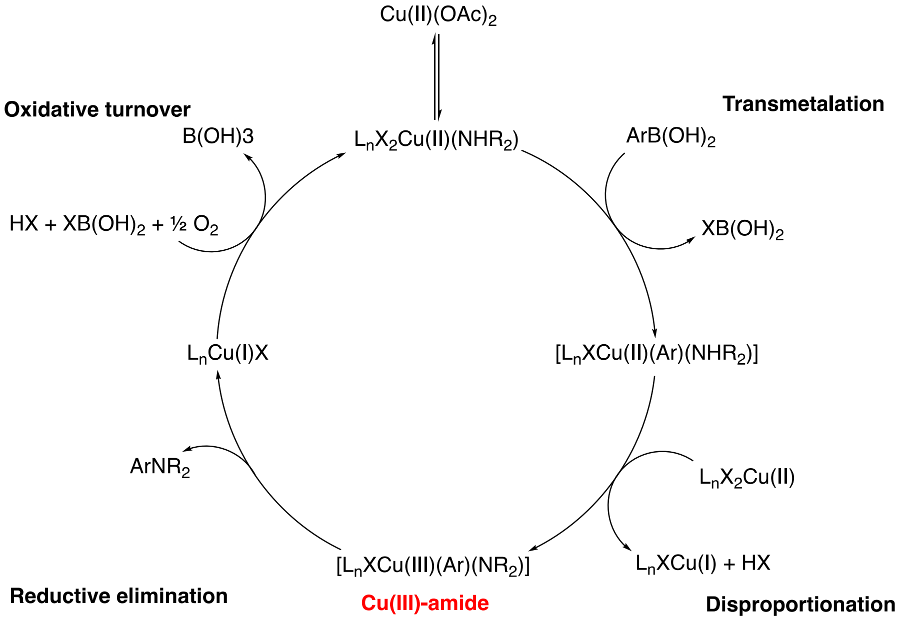

Cu(III) complexes have rarely been studied for their ability to perform C–N bond formation.[200] An organometallic Cu(III) complex was synthesized and reported to react with nitrogen nucleophiles to form C–N bonds (Scheme 2.2).[200] The complex featured a square planar Cu(III) with a Cu–C(aryl) bond, a good model for proposed intermediates in coupling reactions. When reacted with amides, conversion to the amidated ligand was observed. One of the proposed mechanisms for this transformation involves an unobserved Cu(III)(aryl)(amide) species that undergoes reductive elimination to yield the product. However, isolated and characterized Cu(III)-amide complexes, outside of the ancillary ligand, have not been reported, to the best of our knowledge.

Scheme 2.2. C-N bond coupling reaction performed by an aryl-Cu(III) complex.[200]

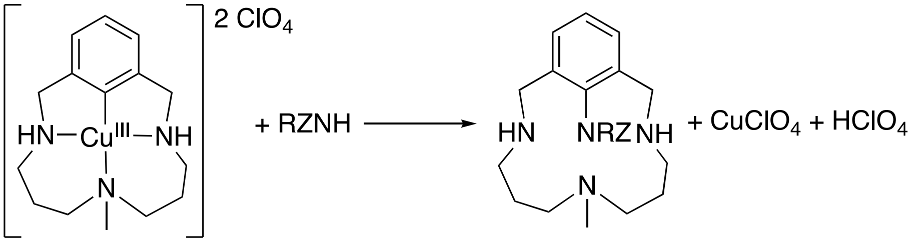

With the goal of trying to generate Cu(III)-amide complexes, we selected nitrogen-based ligands for the $[CuNRR']^+$ core that had diminished basicity to prevent reduction of

Cu(II) and resembled putative intermediates in C–N bond forming reactions. The usage of amidate moieties (deprotonated amides) fulfill these design criteria along with featuring a carbonyl as an α-substituent that could partake in HAA reactivity, as seen for the carbonyl O atoms in the $LCuO_2CR$ complexes. LCu-amidate complexes can be directly compared to the structures, spectroscopic properties, and HAA reactivity with the previously reported $LCuO_2CR$ complexes because of the shared functionality. Therefore, initial synthetic efforts focused on the preparation of complexes featuring N-methylbenzamide, N(Me)COPh, and acetanilide, N(Ph)COMe, substituted X ligands (Figure 4.2). Additionally, since LCuX complexes and high-valent Cu-nitrogen species are known to perform HAA, the LCuNRR' complexes were tested for their propensity toward HAA reactions and compared to the previously published reactions.

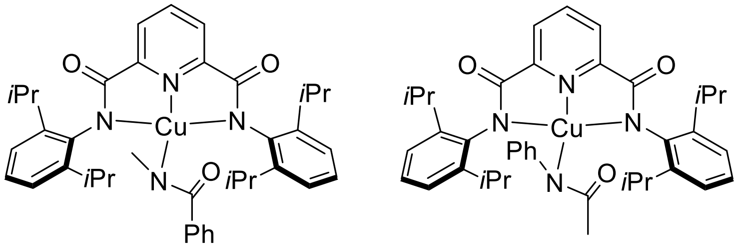

LCuN(Me)COPh
Cu(III)-N-methylbenzamide

LCuN(Ph)COMe
Cu(III)-acetanilide

Figure 4.2. Target LCu-amidate complexes

4.2 Synthesis and characterization of $[NBu_4][LCuN(Me)COPh]$ and $[NBu_4][LCuN(Ph)COMe]$

4.2.1 Synthesis of $[NBu_4][LCuN(Me)COPh]$ and $[NBu_4][LCuN(Ph)COMe]$

Protonolysis of $[NBu_4][LCuOH]$ with the corresponding amine, N-methylbenzamide or acetanilide, in the presence of 3 Å molecular sieves in THF yielded $[NBu_4][LCuN(Me)COPh]$ (77%) and $[NBu_4][LCuN(Ph)COMe]$ (84%), which were isolated as green powders after removing the THF and triturating with pentane (Scheme 4.3). Both complexes were characterized by UV-vis and EPR spectroscopy and elemental analysis. The elemental analysis results revealed that both complexes, having the same elemental composition, were within 0.5% of the theoretical values of C = 71.56%, H = 9.12%, N = 7.45%, indicating high bulk purity. $[NBu_4][LCuN(Me)COPh]$ was characterized by X-ray crystallography but $[NBu_4][LCuN(Ph)COMe]$ did not yield high-quality crystals. Therefore, [K(Krypt)][LCuN(Ph)COMe] was synthesized in hopes of obtaining diffraction quality crystals of the [LCuN(Ph)COMe]$^-$ core. We first generated [K][N(Ph)COMe] in situ by reacting KHMDS with acetanilide in THF. LCuMeCN was added to the THF solution and the green reaction mixture was stirred for 30 min before the solvent and HMDS byproduct were removed *in vacuo*. One equivalent of Krypt was added to a concentrated THF solution of the green oily product and recrystallized by a vapor diffusion of pentane in the THF solution at room temperature, resulting in green crystalline needles that were of suitable quality for X-ray diffraction.

Scheme 4.3. Syntheses of [NBu$_4$][LCuN(Me)COPh] and [NBu$_4$][LCuN(Ph)COMe]

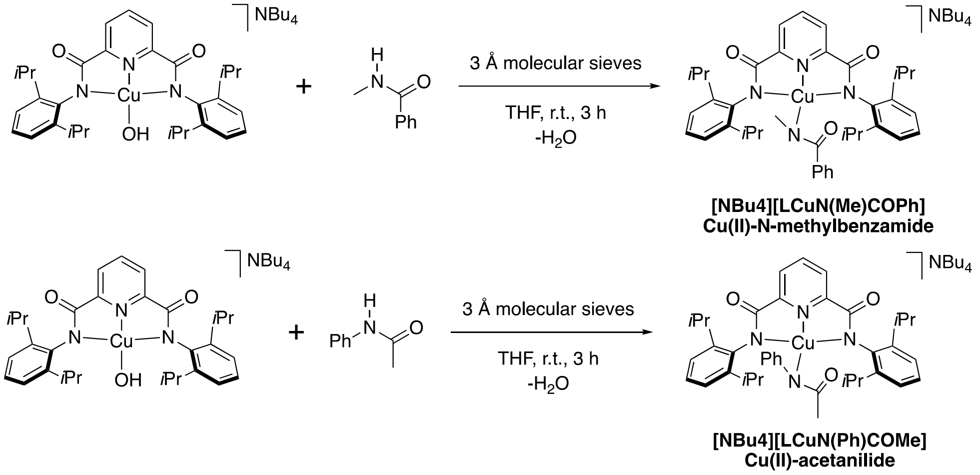

4.2.2 X-ray crystallography of [NBu$_4$][LCuN(Me)COPh] and [K(Krypt)][LCuN(Ph)COMe]

Multichroic, dark crystalline blocks of [NBu$_4$][LCuN(Me)COPh] and green needles of [K(Krypt)][LCuN(Ph)COMe], both grown from THF/pentane vapor diffusions, yielded high-quality solid-state structures (Figure 4.3). Both structures contain distorted square planar Cu(II) ions with τ_4 values of 0.21 and 0.23 for [NBu$_4$][LCuN(Me)COPh] and [K(Krypt)][LCuN(Ph)COMe], respectively. The bond distances from the Cu center to the pyridine dicarboxamide ligand in the two complexes are essentially identical and are comparable to other $[LCuX]^+$ structures.[23,27–29,31,37,40] The -NRR' ligands are bound in a κ^1 fashion through the central amide-N and have similar bond lengths: for [NBu$_4$][LCuN(Me)COPh] Cu1–N4 is 1.918(3) Å and for [K(Krypt)][LCuN(Ph)COMe] Cu1–N4 is 1.938(3) Å. These bond lengths are on the shorter side of the reported C–N bond length range, 1.912 Å to 2.039 Å, in Cu(II)-amide complexes.[23,28,203–206,29,31,33,34,40,92,127,147] Analogously to the binding motif found in the structures of [LCuNO$_2$] and [LCuO$_2$CR], there is a weak interaction between the carbonyl-O atom and the Cu center: for [NBu$_4$][LCuN(Me)COPh] Cu1–O3 is 2.683(3) Å and for [K(Krypt)][LCuN(Ph)COMe] Cu1–O3 is 2.654(4) Å. Both structures also reveal trigonal planar geometries of the N atoms on the amidate ligands, $\Sigma(\angle N) = 359.6^\circ$ in [NBu$_4$][LCuN(Me)COPh] and $\Sigma(\angle N) = 359.72^\circ$ in [K(Krypt)][LCuN(Ph)COMe], indicative of sp^2 character on the N atoms with a filled p-orbital in the Cu d_{x2-y2} plane. Of note, the π-aryl plane of the amide ligand in [K(Krypt)][LCuN(Ph)COMe] is twisted almost orthogonally to the arylamido arms of the pyridine dicarboxamide ligand and out of the N trigonal plane. This angle results in the aryl ring being out of conjugation with the amide, which is different from what is observed in [NBu$_4$][LCuN(Me)COPh] and the [LCuO$_2$CAr]$^-$ complexes.[30,31]

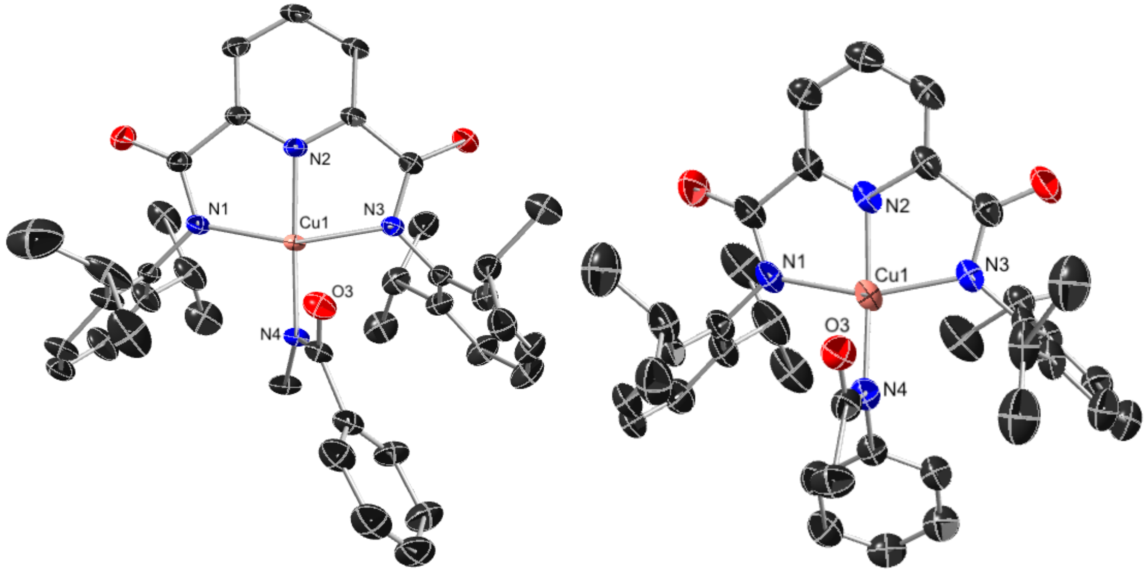

Figure 4.3. X-ray crystal structures of [NBu$_4$][LCuN(Me)COPh] and [K(Krypt)][LCuN(Ph)COMe]. H atoms and counter ions are omitted for clarity, and all non-H atoms are shown as 30% thermal ellipsoids. Selected bond distances (Å) and angles (deg) for [NBu$_4$][LCuN(Me)COPh]: Cu1–N1, 2.020(3); Cu1–N2, 1.931(3); Cu1–N3, 2.036(3); Cu1–N4, 1.918(3); Cu1–O3, 2.683(3); N1–Cu1–N3, 156.99(11); N2–Cu1–N4, 174.11(12). Selected bond distances (Å) and angles (deg) for [K(Krypt)][LCuN(Ph)COMe]: Cu1–N1, 2.037(4); Cu1–N2, 1.938(4); Cu1–N3, 2.028(4); Cu1–N4, 1.959(4); Cu1–O3, 2.654(4); N1–Cu1–N3, 156.99(17); N2–Cu1–N4, 170.71(17).

4.2.3 UV-vis and EPR spectroscopy of [NBu$_4$][LCuN(Me)COPh] and [NBu$_4$][LCuN(Ph)COMe]

[NBu$_4$][LCuN(Me)COPh] and [NBu$_4$][LCuN(Ph)COMe] display low absorbing, low energy peaks at 663 nm (ε = 443 M^{-1} cm^{-1}) and 711 nm (ε = 397 M^{-1} cm^{-1}), respectively (Figure 4.4). These features are assigned as *d-d* transitions, typical for square planar, d^9 Cu(II) complexes. These values are red-shifted from most LCuX complexes (Table 4.1, except [LCuOOtBu]$^-$ and [LCuOOCumyl]$^-$), consistent with a weaker ligand field and a stabilization of the Cu d$_{x2-y2}$ orbital. Both EPR spectra for [NBu$_4$][LCuN(Me)COPh] and [NBu$_4$][LCuN(Ph)COMe] show rhombic signals that are typical for S = ½ tetragonal Cu(II) complexes (Figure 4.5). Spectral simulations (Table 4.2) were performed on the spectra and good fits required inclusion of superhyperfine coupling to 4 N atoms, consistent with spin density delocalized to all four N-donor ligands.

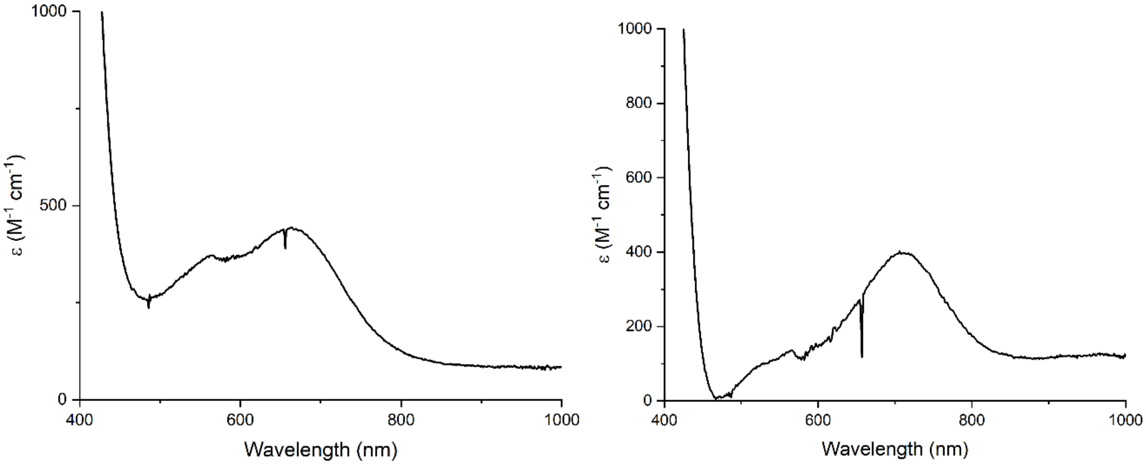

Figure 4.4. UV-vis spectra of [NBu$_4$][LCuN(Me)COPh] (left) and [NBu$_4$][LCuN(Ph)COMe] (right). Conditions: THF at -80 °C.

Table 4.1. UV-vis *d*-*d* peaks for [NBu4][LCuX] complexes.

-X ligand in [NBu4][LCuX]	UV-vis peak (nm)	Ref.
-SH	559[a]	40
-ONO	586[a]	Chapter 3
-OH	597[b]	24
$-O_2CC_6F_5$	598[b]	31
$-O_2CC_6H_4(NO_2)$	600[b]	31
$-O_2CC_6H_4(Cl)$	610[a]	30
$-O_2CC_6H_5$	615[b]	31
$-O_2CC_6H_4(OMe)$	618[b]	31
$-O_2CCH_3$	619[b]	31
-Br	625[c]	27
-Cl	635[c]	27
-F	655[c]	27
-N(Me)COPh	663[a]	This work
-OO*t*Bu	694[a]	28
-OOCumyl	698[a]	28
-N(Ph)COMe	711[a]	This work

[a] Measured in THF at -80 ˚C. [b] Measured in THF at room temperature. [c] Measured in CH_2Cl_2 at room temperature.

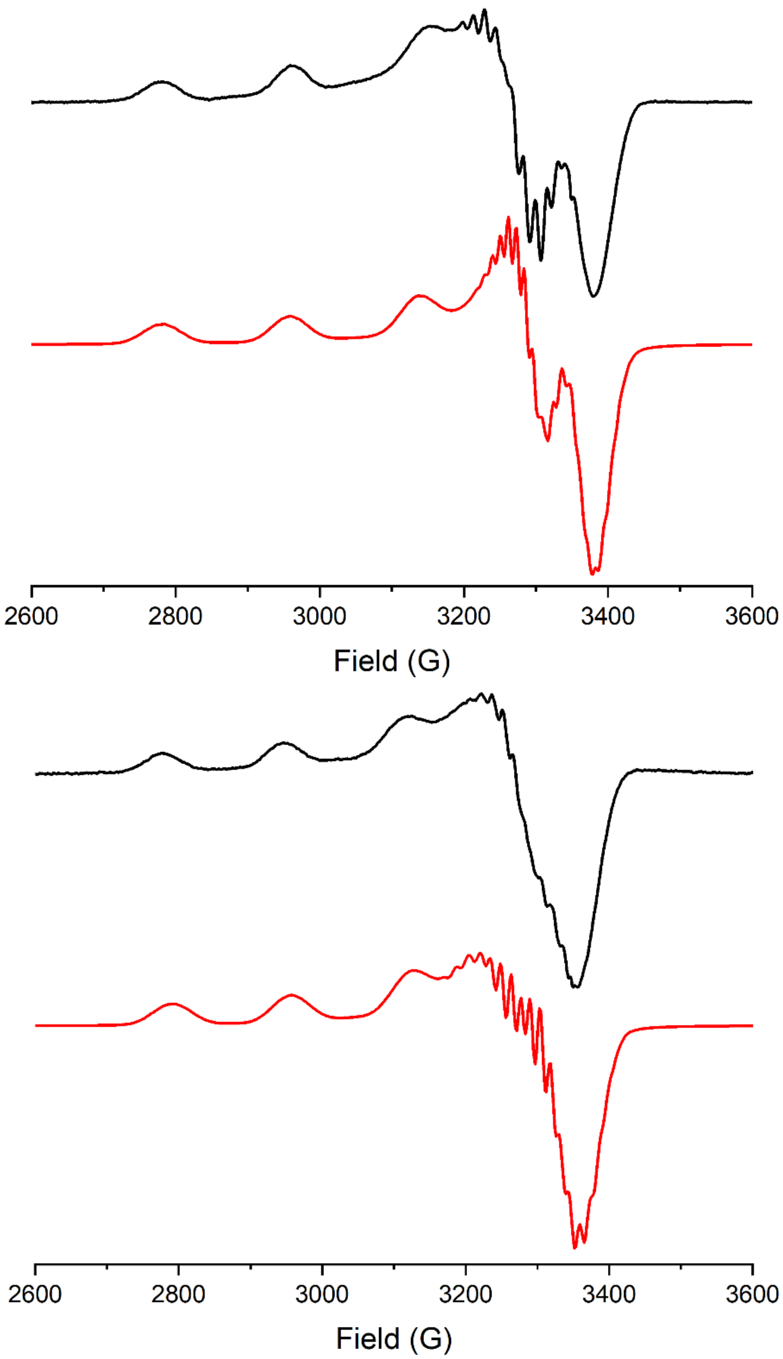

Figure 4.5. (top) Continuous wave X-band EPR spectrum of 1 mM $[NBu_4][LCuN(Me)COPh]$ in THF at 30 K (black) and the simulation of $[LCuN(Me)COPh]^-$ (red). Parameters: 30 K; microwave frequency 9.38 GHz; microwave power 0.0002 mW; modulation amplitude 9.8 G; modulation frequency 100 kHz. Parameters from the simulation are listed in Table 4.2. (bottom) Continuous wave X-band EPR spectrum of 1 mM $[NBu_4][LCuN(Ph)COMe]$ in THF at 30 K (black) and the simulation of $[LCuN(Ph)COMe]^-$ (red). Parameters: 30 K; microwave frequency 9.38

GHz; microwave power 0.0002 mW; modulation amplitude 9.8 G; modulation frequency 100 kHz. Parameters from the simulation are listed in Table 4.2.

Table 4.2. Simulated g-values and hyperfine/superhyperfine parameters (MHz) for Cu, $N^{pyridine}$, $N^{L\text{-}amide}$, and $N^{X\text{-}amide}$ nuclei for $[NBu_4][LCuN(Me)COPh]$ and $[NBu_4][LCuN(Ph)COMe]$ in THF at 30 K.

Compound	**$[NBu_4][LCuN(Me)COPh]$**	**$[NBu_4][LCuN(Ph)COMe]$**
g_x	2.082	2.095
g_y	2.102	2.113
g_z	2.262	2.267
$A^{Cu}{}_x$	10	55
$A^{Cu}{}_y$	35	60
$A^{Cu}{}_z$	550	515
$A^{py}{}_x$	35	45
$A^{py}{}_y$	30	50
$A^{py}{}_z$	40	30
$A^{L\text{-}am}{}_x$	30	40
$A^{L\text{-}am}{}_y$	35	55
$A^{L\text{-}am}{}_z$	40	50
$A^{X\text{-}am}{}_x$	35	40
$A^{X\text{-}am}{}_y$	30	45
$A^{X\text{-}am}{}_z$	40	30

4.2.4 Electrochemistry of $[NBu_4][LCuN(Me)COPh]$ and $[NBu_4][LCuN(Ph)COMe]$

Cyclic voltammetry (CV) was performed on THF solutions of $[NBu_4][LCuN(Me)COPh]$ (Figure 4.6, 2 mM [Cu], 300 mM $[NBu_4][PF_6]$, glassy-carbon working electrode) and $[NBu_4][LCuN(Ph)COMe]$ (Figure 4.7, 1 mM [Cu], 200 mM $[NBu_4][PF_6]$, Pt working electrode) to determine if $Cu^{II/III}$ couples were accessible. Both complexes displayed waves that exhibite linear current variation with increasing scan rate, although the cathodic peaks are diminished at moderate scan rates (~250 mV s^{-1}) for $[NBu_4][LCuN(Me)COPh]$. Therefore, the oxidation of $[NBu_4][LCuN(Me)COPh]$ is characterized as psuedoreversible while that of $[NBu_4][LCuN(Ph)COMe]$ is reversible. $[NBu_4][LCuN(Me)COPh]$ displayed an $E_{1/2}$ of 23 mV vs. $Fc^{+/0}$ in THF and $[NBu_4][LCuN(Ph)COMe]$ displayed an $E_{1/2}$ of 92 mV vs. $Fc^{+/0}$ in THF. These potentials fall in the range of measured potentials for $[LCuX]^-$ complexes (select values in Table 4.3). Previously, a trend between the basicity of the O-based ligand (aqueous pK_a values) and the $E_{1/2}$ of $[LCuO_2R]^{-/0}$ complexes was found (more basic ligand, lower potential).[31] The trend is also apparent between $[LCuOR]^-$ complexes and the ligand pK_a values in DMSO (Table 4.3). However, the trend does not seem to uphold with the N-based ligands since $[NBu_4][LCuN(Ph)COMe]$ contains the more basic ligand but the higher potential (pK_a of acetanilide = 21.5 in DMSO; pK_a of N-methylbenzamide between 24.5 and 27.5 in DMSO).[200] More Cu(II)-amide complexes would have to be synthesized and analyzed to understand if there is a true trend here. The CV experiments helped us determine that the Cu(III) formal oxidation state could be accessed at moderate potentials, so we attempted to generate the LCuNRR' complexes chemically.

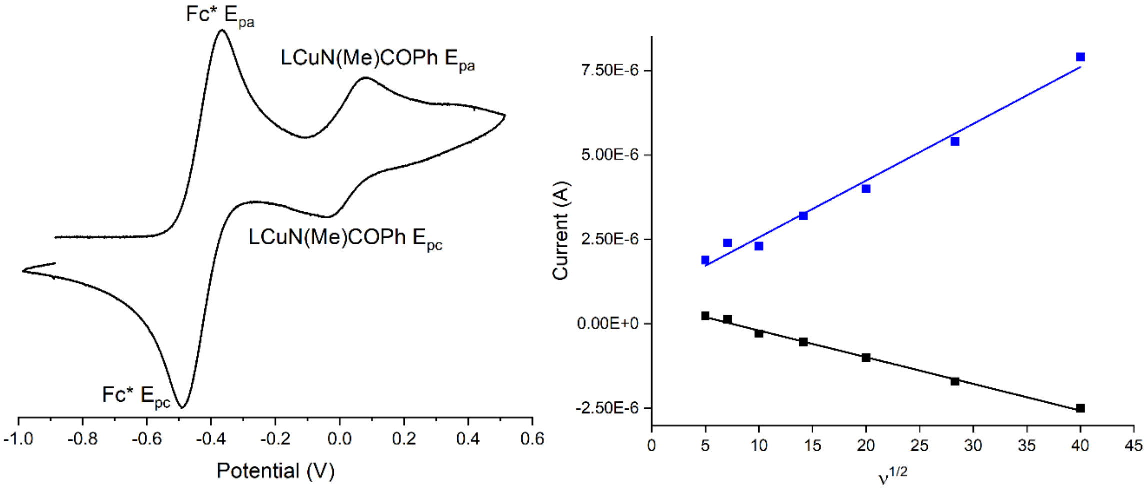

Figure 4.6. (Left) Cyclic voltammogram collected of $[NBu_4][LCuN(Me)COPh]$. Conditions: 2 mM [Cu], 0.3 M TBAP, THF, 25 °C, glassy-carbon working electrode, 100 mV/s scan rate. (Right) Anodic and cathodic current response as a function of the square root of the scan rate.

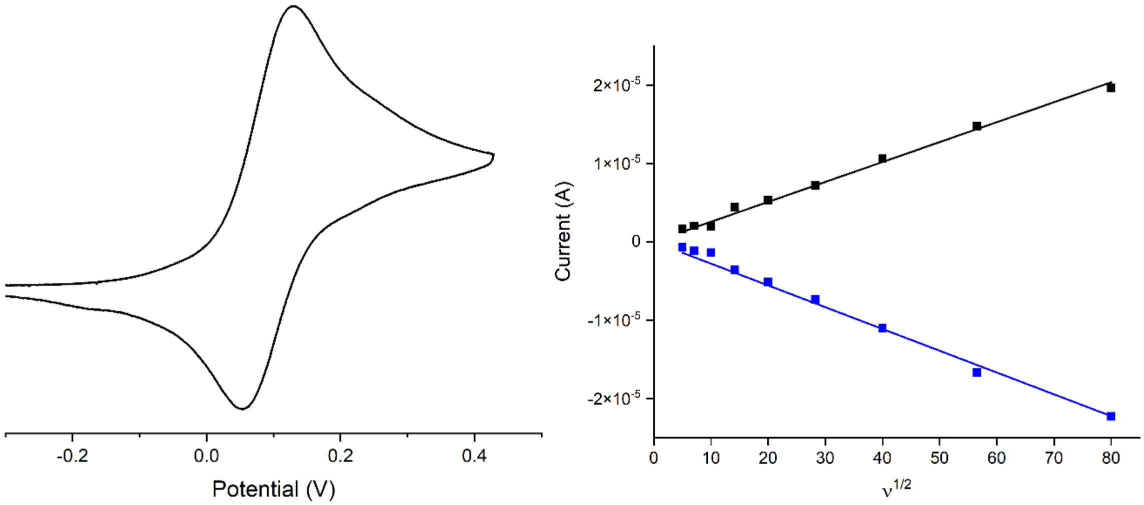

Figure 4.7. (Left) Cyclic voltammogram collected of [NBu$_4$][LCuN(Ph)COMe]. Conditions: 1 mM [Cu], 0.2 M TBAP, THF, 25 °C, Pt working electrode, 100 mV/s scan rate. (Right) Anodic and cathodic current response as a function of the square root of the scan rate.

Table 4.3. Cyclic voltammetry data for [LCuX]$^{-/0}$ and pK_a (DMSO) data for the associated ligands

Complex	$E_{1/2}$ (mV in THF)[a]	Ref.	pK_a of ligand (DMSO)	Ref.
[LCuOH]$^-$	-167	[29]	31.4	[207]
[LCuOCH$_2$CF$_3$]$^-$	37	[29]	23.5	[208]
[LCuO$_2$CCH$_3$]$^-$	150	[31]	12.6	[209]
[LCuO$_2$CC$_6$H$_5$]$^-$	169	[31]	11.1	[210]
[LCuO$_2$CC$_6$H$_4$(NO$_2$)]$^-$	239	[31]	9.1	[211]
[LCuN(Me)COPh]$^-$	23	This work	24.5-27.5	[200]
[LCuN(Ph)COMe]$^-$	92	This work	21.5	[200]

4.3 Generation and characterization of LCuN(Me)COPh and LCuN(Ph)COMe

The chemical oxidant [AcFc][BArF$_{24}$] (270 mV vs. Fc$^{0/+}$ in CH$_2$Cl$_2$)[212] was chosen as an oxidant for [NBu$_4$][LCuN(Me)COPh] and [NBu$_4$][LCuN(Ph)COMe] based on the observed $E_{1/2}$ values. When 1 eq. of [AcFc][BArF$_{24}$] was added to THF solutions of the complexes at -80 °C, new features in the UV-vis spectrum appeared. The oxidation of [NBu$_4$][LCuN(Me)COPh] gave way to a dark purple solution with intense features at 412 (ε = 4245 M^{-1} cm^{-1}) and 595 (ε = 8944 M^{-1} cm^{-1}) nm with a shoulder at 716 (ε = 6136 M^{-1} cm^{-1}) nm (Figure 4.8). The oxidation of [NBu$_4$][LCuN(Ph)COMe] yielded a dark gray solution with intense features across the visible spectrum at 478 (ε = 8556 M^{-1} cm^{-1}), 645 (ε = 9595 M^{-1} cm^{-1}), and 734 (ε = 9094 M^{-1} cm^{-1}) nm (Figure 4.9). A titration of [AcFc]$^+$ to THF solutions of both complexes at -80 °C revealed maximum absorbances of the new features when 1 eq. of [AcFc]$^+$ was added (Figures 4.8 and 4.9). Additionally, the new features bleached when 1 eq. of Fc* was added to the new species and regenerated again when another equivalent of [AcFc]$^+$ was added, a process that could be repeated (~2 times, Figures 4.10 and 4.11). Thus, the UV-vis titration data for [NBu$_4$][LCuN(Me)COPh] and [NBu$_4$][LCuN(Ph)COMe] with [AcFc]$^+$ revealed that a 1-electron oxidation is required for the generation of the new species. However, when the second and third eq. of [AcFc]$^+$ was added to [NBu$_4$][LCuN(Me)COPh] in the chemical oxidation/reduction titration experiments, there was less of the oxidized species present than in the re-oxidation of [NBu$_4$][LCuN(Ph)COMe], indicative of some instability or decomposition processes for the former oxidized complex. These experiments corroborate the cyclic voltammetry experiments, showing [NBu$_4$][LCuN(Me)COPh] to have a quasi-reversible oxidation.

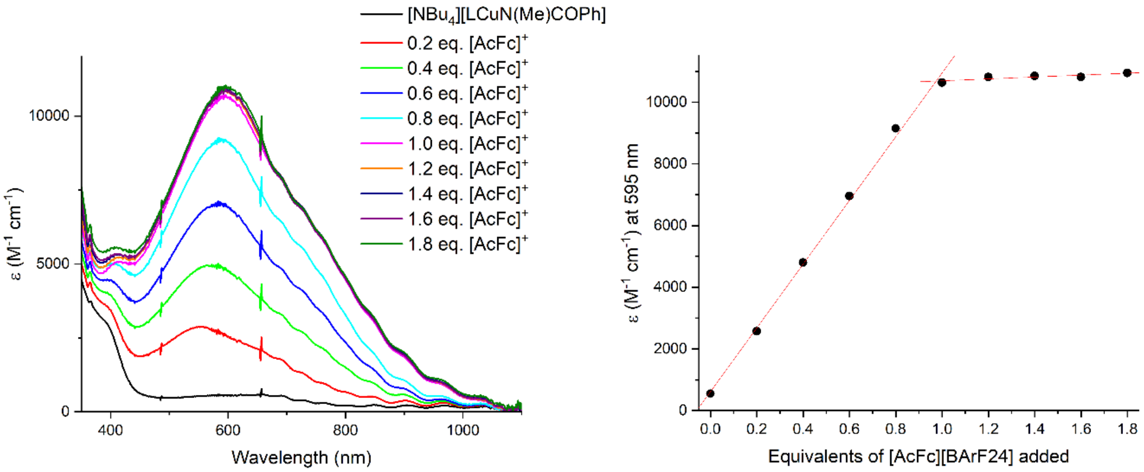

Figure 4.8. (right) Overlay of UV-vis spectra upon addition of incremental equivalents of [AcFc][BArF$_{24}$] to [NBu$_4$][LCuN(Me)COPh] at -80 °C in THF. (left) Plot of corresponding molar absorptivity values at λ = 595 nm vs. equivalents of [AcFc][BArF$_{24}$] added to [NBu$_4$][LCuN(Me)COPh] at -80 °C in THF.

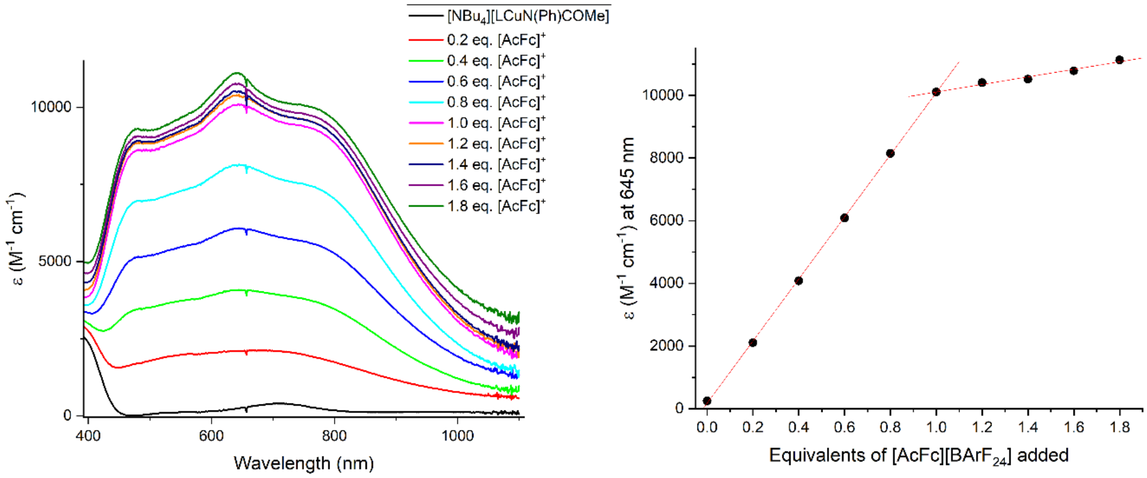

Figure 4.9. (right) Overlay of UV-vis spectra upon addition of incremental equivalents of [AcFc][BArF$_{24}$] to [NBu$_4$][LCuN(Ph)COMe] at -80 °C in THF. (left) Plot of corresponding molar absorptivity values at λ = 595 nm vs. equivalents of [AcFc][BArF$_{24}$] added to [NBu$_4$][LCuN(Ph)COMe] at -80 °C in THF.

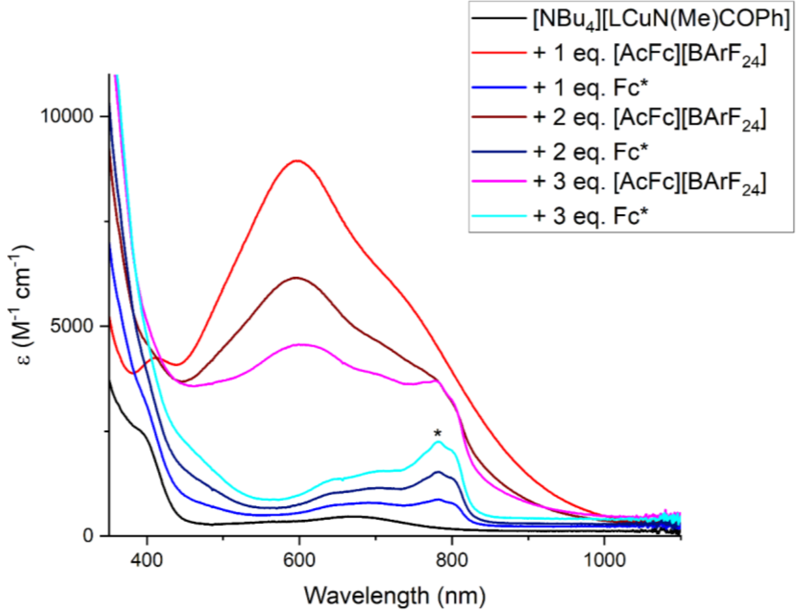

Figure 4.10. UV-vis chemical oxidation/reduction titration where up to 3 eq. of [AcFc][BArF$_{24}$] and Fc* were added to [NBu$_4$][LCuN(Me)COPh] in THF at -80 °C (*denotes Fc*$^+$ signal).

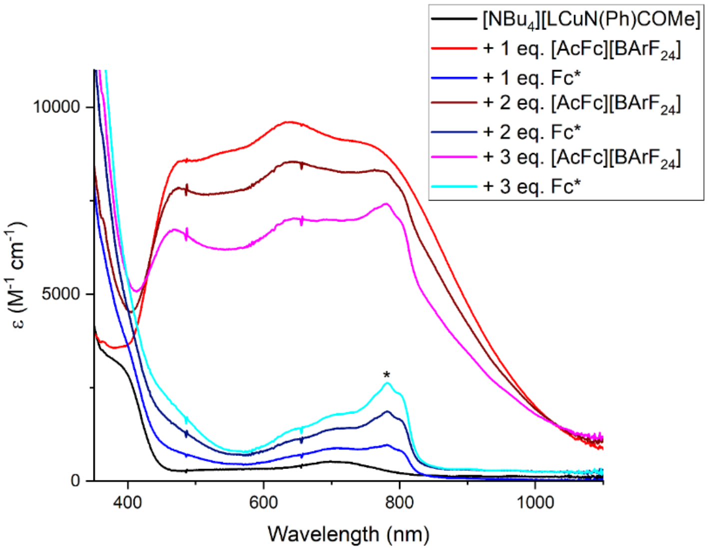

Figure 4.11. UV-vis chemical oxidation/reduction titration where up to 3 eq. of [AcFc][BArF$_{24}$] and Fc* were added to [NBu$_4$][LCuN(Ph)COMe] in THF at -80 °C (*denotes Fc*$^+$ signal).

The new intense features that appear after the oxidations of [NBu$_4$][LCuN(Me)COPh] and [NBu$_4$][LCuN(Ph)COMe] are analogous to the features found for LCuOR complexes that have been assigned by TD-DFT as Ligand to Metal Charge Transfer (LMCT) transitions from the arylamido arms of the pyridine dicarboxamide ligands to the Cu d-orbitals. Thus, by analogy to the [LCuOR]$^-$ systems, we assign the 1-electron oxidation products of [NBu$_4$][LCuN(Me)COPh] and [NBu$_4$][LCuN(Ph)COMe] as LCuN(Me)COPh and LCuN(Ph)COMe, respectively, formally Cu(III) products.

The pyridine dicarboxamide ligand allowed a platform for accessing Cu(III)-amide species for the first time, to our knowledge. With the abundance of characterization data known for LCuX complexes, we were able to recognize and understand the LCuNRR' species. For example, the presence of the high-absorbing UV-vis peaks that are characteristic for LCuX complexes helps us assign the formal Cu(III) oxidation state in LCuNRR'. Additionally, the Cu(III)-amide species that are proposed for C–N bond forming reactions are square planar Cu species with three overall anionic donor ligands,[200,202] similar electronic environments found in the LCuNRR' complexes. Thus, the

LCuNRR’ complexes support the possibility of Cu(III)-amide species as intermediates in Cu catalysis.

4.4 PCET reactivity of LCuN(Me)COPh and LCuN(Ph)COMe

As previously discussed, LCuOR species act as potent PCET reagents, and we sought to determine if LCuNRR’ species could also perform PCET reactions and to compare those reactions to analogous ones with LCuOR complexes. Reacting LCuN(Me)COPh with TTBP in THF at -80 °C resulted in the decay of the UV-vis features of LCuN(Me)COPh over ~25 min (Figure 4.12). The decay spectra were fit to a second order reaction model using a global-fitting program, ReactLab Kinetics, and a k_2 value of 3(1) x 10^{-1} M^{-1} s^{-1} was determined (from triplicate runs). LCuN(Ph)COMe was also reacted with TTBP in THF at -80 °C and a rapid decay of the UV-vis features of LCuN(Ph)COMe was observed. A global fit of the decay spectra over 25 seconds to a second order reaction model yielded a k_2 value of 5(1) x 10^{1} M^{-1} s^{-1} (>150 times faster decay, from triplicate runs). However, the fitted data does not overlay with the experimental data particularly well (relatively large residuals). We believe this is due to the speed of the reaction relative to the collection rate. A much faster sampling time could help improve the fits to the experimental data, requiring a stop-flow instrument. While stop-flow experiments for the reaction are ongoing, we can estimate the lower boundary of the second-order rate constant for the reaction between LCuN(Ph)COMe and TTBP to be 5(1) x 10^{1} M^{-1} s^{-1}. Two products of the reactions were identified as the 2,4,6-tri-*t*-butylphenoxyl radical (UV-vis peaks around 400 and 660 nm) and LCu(THF) (UV-vis peak at 570 nm), expected and typical products of a PCET reaction involving LCuX and TTBP in THF.

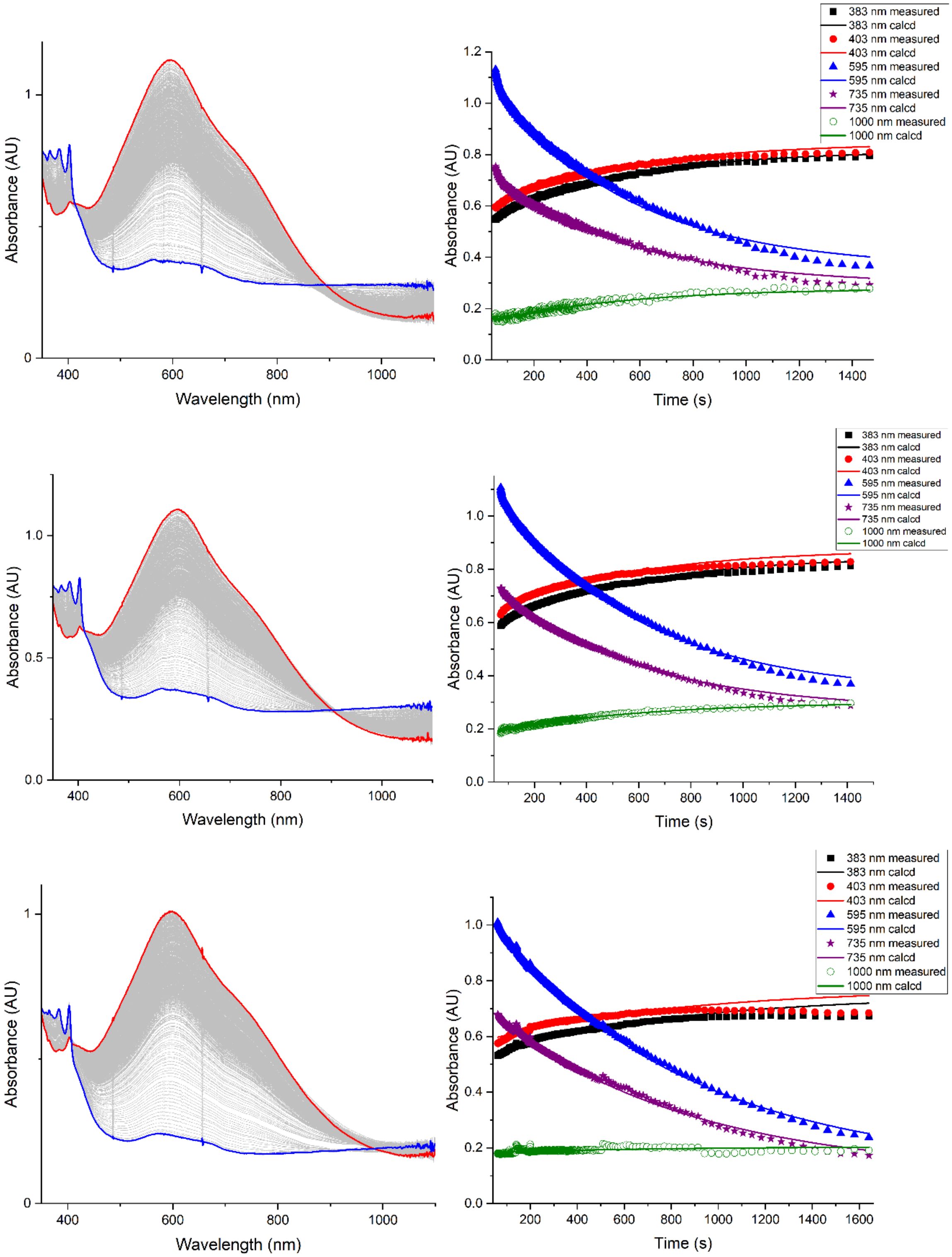

Figure 4.12. (Left column) Triplicate UV-vis spectra as a function of time for the reactions of LCuN(Me)COPh (red) with TTBP (50 eq.) in THF at -80 °C. The product spectrum (blue) is assigned as LCuTHF and the phenoxyl radical of TTBP. (Right column) Plots of

absorbance vs. time at representative wavelengths (λ = 383, 403, 595, 735, and 1000 nm) for the respective decay plots in the right column. The plots contain an overlay of experimental (scatter plots) and calculated (lines) data to represent the accuracy of the fit from ReactLab Kinetics, which was used to calculate the k_2 value discussed in the text.

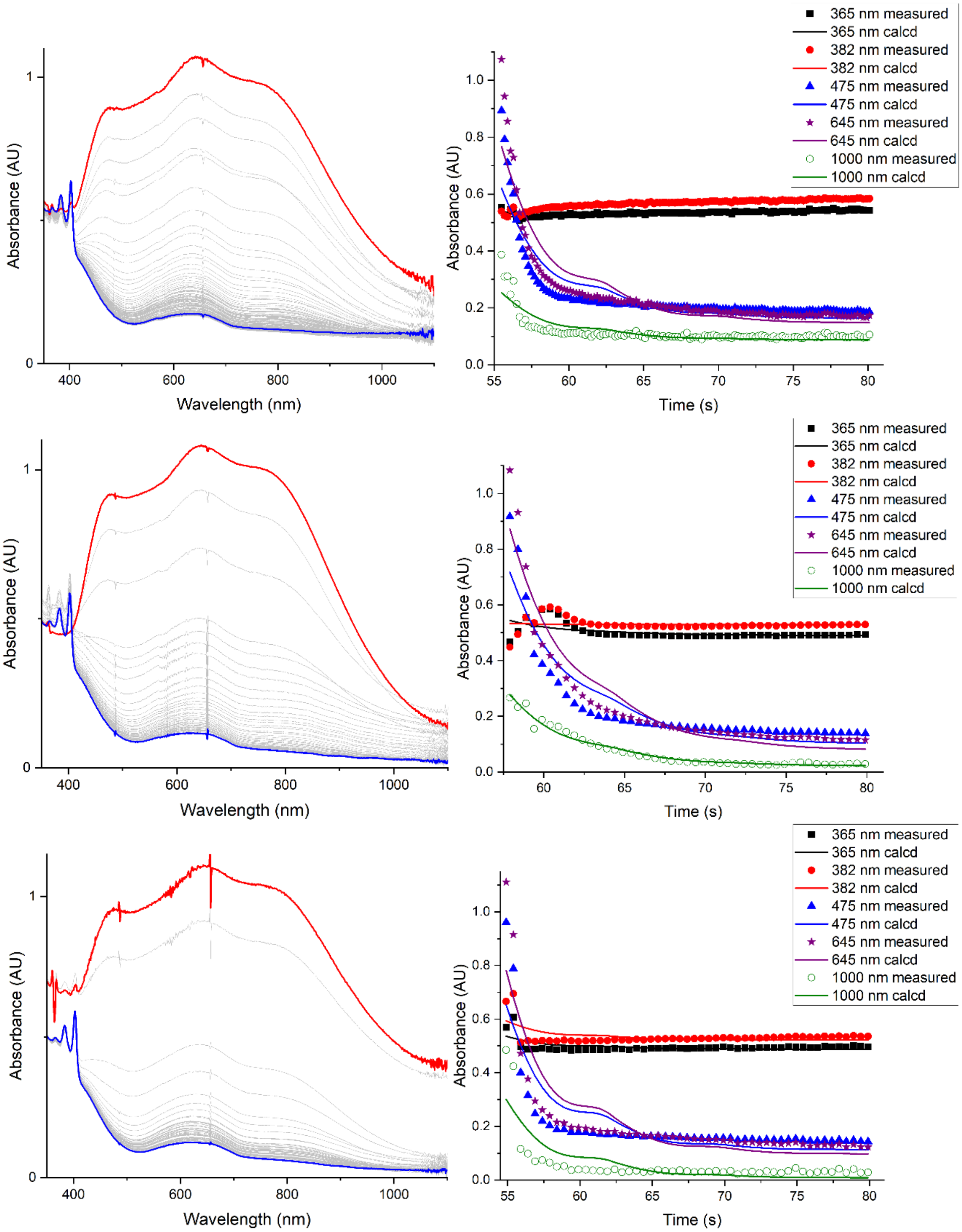

Figure 4.13. (Left column) Triplicate UV-vis spectra as a function of time for the reactions of LCuN(Ph)COMe (red) with TTBP (50 eq.) in THF at -80 °C. The product spectrum (blue) is assigned as LCuTHF and the phenoxyl radical of TTBP. (Right column) Plots of absorbance vs. time at representative wavelengths (λ = 365, 382, 475, 645, and 1000 nm) for the respective decay plots in the right column. The plots contain an overlay of

experimental (scatter plots) and calculated (lines) data to represent the accuracy of the fit from ReactLab Kinetics, which was used to calculate the k_2 value discussed in the text.

The reaction rates reveal that LCuN(Ph)COMe reacts about 150 times faster with TTBP than LCuN(Me)COPh. The second order rate constant for the reaction between LCuN(Me)COPh and TTBP resembles the rate constants found for $LCuO_2CC_6H_4(Cl)$ (0.3 M^{-1} s^{-1}),[30,31] $LCuO_2CC_6H_4(NO_2)$ (0.23 M^{-1} s^{-1}),[31] and $LCuNO_2$ (0.1 M^{-1} s^{-1}, Chapter 3). On the other hand, the rate constant calculated for the reaction between LCuN(Me)COPh and TTBP resembles the rate constant found for LCuOH (20 M^{-1} s^{-1}).[30] The basis for the large difference in rate constants is unknown. One factor could be the dearomatization of the aryl ring from the amide-N in LCuN(Ph)COMe that would make the reaction highly favorable upon rearomatization of acetanilide, although we are unsure if the angle observed in the solid state of $[LCuN(Ph)COMe]^-$ persists in solution and in the Cu(III) state. Previously, the reaction between $LCuO_2CC_4H_4(Cl)$ and TTBP was investigated *in silico* to understand which O atom in the carboxylate ligand was the reactive site and it was discovered that the distal-O atom was the reactive site, favored by 8.7 kcal mol^{-1} over the proximal-O atom.[30] Similarly, the LCuNRR' complexes have multiple sites in which the hydrogen atom could be transferred to, the carbonyl-O and the amide-N. Given the drastic disparities in the rate constants for the two complexes, the H-atom acceptor site may differ between the two complexes. Perhaps, since LCuN(Me)COPh has similar rate constants as the $LCuO_2CR$ complexes, the reaction proceeds according to the findings for $LCuO_2CC_4H_4(Cl)$, through the distal carbonyl-O. Likewise, given that the second order rate constants for the reactions between TTBP and LCuOH and LCuN(Ph)COMe are similar, the H-atom acceptor site could be the atom bound to the Cu. Furthermore, high-valent Cu-nitrogen complexes are known to be highly reactive with R-H substrates via HAA, although the resulting products react further and complicate studying the HAA step.[79] LCuN(Me)COPh and LCuN(Ph)COMe give way to studying HAA chemistry in detail easily since the products of HAA via LCuNRR' yield stable products (LCu(II) adducts and HNRR').

4.5 Summary and conclusions

We synthesized and characterized two $[NBu_4]$[LCuNRR'] complexes, $[NBu_4]$[LCuN(Me)COPh] and $[NBu_4]$[LCuN(Ph)COMe]. While

$[NBu_4][LCuN(Me)COPh]$ yielded X-ray quality crystals, [K(Krypt)][LCuN(Ph)COMe] was synthesized for accessing high quality crystals containing $[LCuN(Ph)COMe]^-$. The X-ray structure of $[LCuN(Ph)COMe]^-$ showed the -N(Ph)COMe ligand with the aryl ring twisted out of the trigonal plane of the N, a unique feature and the consequences of which are still unknown. The two Cu(II) complexes were oxidized by one electron to yield LCuN(Me)COPh and LCuN(Ph)COMe, assigned as formally Cu(III) species. The Cu(III)-amidate complexes were characterized by UV-vis, becoming the first characterized Cu(III)-amidate complexes (outside of other LCuX complexes, L containing two amidates), and bear resemblance to LCuX complexes. The successful generation of Cu(III)-amidates helps support the hypothesis that Cu(III)-amidate species are accessible intermediates in Cu mediated C–N bond coupling reactions. Additionally, LCuN(Me)COPh and LCuN(Ph)COMe were both found to react with TTBP yielding PCET products. The second order rate constants uncover a large difference in PCET reactivity of the two complexes with LCuN(Ph)COMe reacting with TTBP magnitudes faster than LCuN(Me)COPh. However, the underlying reason for the large difference is still unknown and could be subject to further experimental and computational studies.

4.6 Experimental section

4.6.1 Materials and methods

Metal complexes were synthesized and handled under a dinitrogen atmosphere in a Vacuum Atmospheres glovebox or an argon atmosphere using Schlenk techniques. All reagents and solvents were purchased from commercial sources unless otherwise noted. Tetrahydrofuran and pentane were passed through activated alumina columns and plumbed directly into a glovebox. Tetrahydrofuran was stored over activated 3 Å molecular sieves in a dinitrogen-filled glovebox and, prior to use in spectroscopy and cyclic voltammetry experiments, filtered using a 25 mm diameter, 0.2 mm hydrophobic polytetrafluoroethylene (PTFE) syringe filter. 2,4,6-tri-*t*-butylphenol (TTBP) was recrystallized several times from saturated pentane solutions at -30 °C prior to use. KHMDS was recrystallized from saturated toluene solutions at -30 °C prior to use. LCu(MeCN)[26] and acetyl ferrocenium tetrakis(3,5-bis(trifluoromethyl)phenyl)borate ($[AcFc][BArF_{24}]$)[34] were synthesized according to the published procedures. N-methylbenzamide, acetanilide, Kryptofix 222, Fc*, and Fc were purchased from Sigma-Aldrich and were used without further purification.

UV-vis spectra were collected on a HP8453 (190 – 1100 nm) diode array spectrophotometer equipped with a Unisoku low-temperature UV-vis cell holder. EPR data were collected on frozen 1 mM samples with a CW Elexsys E500 EPR spectrometer using X-band (9.38 GHz) radiation at 35 dB and at 30 K. The microwave power, modulation amplitude, and modulation frequency were 0.0002 mW, 9.8 G, and 100 kHz, respectively. Cyclic voltammograms were recorded using an EC Epsilon potentiostat from BASi, a glassy carbon working electrode or a Pt working electrode, a Pt counter electrode, and a Ag wire pseudoreference electrode. All cyclic voltammograms were performed in THF with 0.3 or 0.2 M tetrabutylammonium hexafluorophosphate (TBAP) electrolyte, which was recrystallized several times from ethanol and dried under high-vacuum before use, and were internally referenced to the ferrocene/ferrocenium (Fc/Fc^+) couple. The spectra were converted vs. the standard Fc/Fc^+ couple using standard conversion factors.[152] Elemental Analysis was performed by the CENTC Elemental Analysis Facility (University of Rochester).

For X-ray crystallography experiments, crystals were placed onto the tip of a MiTeGen cryoloop and mounted on a Bruker D8 VENTURE diffactometer equipped with a Photon III CMOS. The data collections were carried out using Mo Kα source using normal parabolic mirrors as monochromators at 173 K. Structure solutions were performed with SHELXT[153] using ShelXle[154] as a graphical interface. The structures were refined against F^2 on all data by full-matrix-least-squares with SHELXL.[155]

4.6.2 Experimental procedures

Synthesis of [NBu$_4$][LCuN(Me)COPh]. A scintillation vial was charged with a stir bar, [NBu$_4$][LCuOH] (100 mg, 0.124 mmol), 1 cm of 3 Å molecular sieves, and THF (2 mL). N-methylbenzamide (17 mg, 0.124 mmol) was dissolved in THF (3 mL) and added dropwise to the reaction vial. The reaction was stirred for 3 h at room temperature then filtered using a 25 mm diameter, 0.2 mm hydrophobic polytetrafluoroethylene (PTFE) syringe filter. The solvent was removed *in vacuo* yielding a dark green oil. The oil was triturated with pentane (5 mL) and the pentane was decanted (x 3) to yield a gray-green powder (89 mg, 0.095 mmol, 77%). X-ray quality crystals were obtained by dissolving the oil in minimal THF and vapor diffusion of pentane at -35 °C for 3 days, which yielded an oil that grew multichroic, dark, blocky crystals after sitting at room temperature overnight. UV-vis (THF, -80 °C) λ_{max}, nm (ε, M^{-1} cm^{-1}): 663 (443). Anal. calcd (%) for $C_{56}H_{85}CuN_5O_3$: C, 71.56; H, 9.12; N, 7.45. Found: C, 71.11; H, 8.64; N, 7.24.

Synthesis of [NBu$_4$][LCuN(Ph)COMe]. A scintillation vial was charged with a stir bar, [NBu$_4$][LCuOH] (102 mg, 0.124 mmol), 1 cm of 3 Å molecular sieves, and THF (2 mL). Acetanilide (17 mg, 0.124 mmol) was dissolved in THF (3 mL) and added dropwise to the reaction vial. The reaction was stirred for 3 h at room temperature then filtered using a 25 mm diameter, 0.2 mm hydrophobic polytetrafluoroethylene (PTFE) syringe filter. The solvent was removed *in vacuo* yielding an emerald oil. The oil was triturated with pentane and the pentane (5 mL) was decanted (x 3) to yield a pale green powder (98 mg, 0.104 mmol, 84%). Crystals of [NBu$_4$][LCuN(Ph)COMe] were obtained through a THF/pentane vapor diffusion at -35 °C and were subjected to X-ray diffraction but yielded a low quality structure. However, we obtained a high quality structure of [K(Krypt)][LCuN(Ph)COMe], allowing inspection of the [LCuN(Ph)COMe]$^-$ unit. [K(Krypt)][LCuN(Ph)COMe] was synthesized by deprotonating acetanilide with KHMDS (1 eq.) in THF and adding that mixture to LCuMeCN (1 eq.) in THF. The green solution was stirred for 30 min and the solvent was removed *in vacuo*. Kryptofix 222 (1 eq.) in minimal THF was added to the Cu complex and a pentane vapor diffusion at room temperature resulted in green needles. UV-vis (THF, -80 °C) λ_{max}, nm (ε, M^{-1} cm^{-1}): 711 (397). Anal. calcd (%) for $C_{56}H_{85}CuN_5O_3$: C, 71.56; H, 9.12; N, 7.45. Found: C, 71.58; H, 8.97; N, 7.53.

General procedure for the generation of LCuNRR'. A solution of [NBu$_4$][LCuNRR'] in THF (0.1 mL, 2 mM) was injected into a UV-vis cuvette under Ar containing THF (1.7 mL) at -80 °C, set by the Unisoku low temperature UV-vis cell holder. After stirring and temperature equilibration (5 min), a UV-vis spectrum was recorded. With stirring, a solution of [AcFc][BArF$_{24}$] in THF (0.1 mL, 2 mM) was added to the cuvette (final concentration of 0.1 mM) and a spectrum was immediately recorded. For titration experiments, solution of [NBu$_4$][LCuNRR'] in THF (0.1 mL, 2 mM) was injected into a UV-vis cuvette under Ar containing THF (1.4 mL) at -80 °C, set by the Unisoku low temperature UV-vis cell holder. After stirring and temperature equilibration (5 min), a UV-vis spectrum was recorded. With stirring, aliquots of an [AcFc][BArF$_{24}$] solution in THF (0.4 mM) were added in 0.1 mL increments (0.2 eq.), up to 1.8 eq., to the cuvette and a spectrum was immediately recorded after each injection.

General procedure for the reversible oxidation/reduction of [NBu$_4$][LCuNRR']. A solution of [NBu$_4$][LCuNRR'] in THF (0.1 mL, 2 mM) was injected into a UV-vis cuvette under Ar containing THF (1.8 mL) at -80 °C, set by the Unisoku low temperature UV-vis cell holder. After stirring and temperature equilibration (5 min), a UV-vis spectrum was recorded. With stirring, a solution of [AcFc][BArF$_{24}$] in THF (0.1 mL, 2 mM) was added to the cuvette and a spectrum was immediately recorded. An aliquot of a Fc* solution in THF (0.1 mL, 2 mM) was added to the cuvette with stirring and another spectrum was immediately recorded. The chemical oxidation and reduction processes were repeated twice more, and spectra were recorded after each addition of reagent.

General procedure for the reactions between LCuNRR' and TTBP. A UV-vis cuvette under Ar containing THF (1.6 mL) at -80 °C, set by the Unisoku low temperature UV-vis cell holder, was charged with a THF solution of [NBu$_4$][LCuNRR'] (0.2 mL, 2mM). The solution was allowed to cool (5 min) with stirring and a continuous collection of spectra was initiated. Quickly after, a THF solution of [AcFc][BArF$_{24}$] (0.1 mL, 2 mM) was injected into the cuvette. When the new features were fully formed, a THF solution of TTBP (0.1 mL, 100 mM, 50 eq.) was quickly added, and the decay was observed until no further changes were observed. The k_2 values for the reactions between LCuNRR' and TTBP were calculated by using ReactLab Kinetics[188] using the known concentrations.

References

(1) Crichton, R. *Biological Inorganic Chemistry: A New Introduction to Molecular Structure and Function*, Third Edit.; 2018. https://doi.org/https://doi.org/10.1016/C2016-0-01804-1.

(2) Solomon, E. I.; Heppner, D. E.; Johnston, E. M.; Ginsbach, J. W.; Cirera, J.; Qayyum, M.; Kieber-Emmons, M. T.; Kjaergaard, C. H.; Hadt, R. G.; Tian, L. Copper Active Sites in Biology. *Chem. Rev.* **2014**, *114* (7), 3659–3853. https://doi.org/10.1021/CR400327T.

(3) Concia, A. L.; Beccia, M. R.; Orio, M.; Ferre, F. T.; Scarpellini, M.; Biaso, F.; Guigliarelli, B.; Réglier, M.; Simaan, A. J. Copper Complexes as Bioinspired Models for Lytic Polysaccharide Monooxygenases. *Inorg. Chem.* **2017**, *56*, 1023–1026. https://doi.org/10.1021/acs.inorgchem.6b02165.

(4) Castillo, I.; Torres-Flores, A. P.; Abad-Aguilar, D. F.; Berlanga-Vázquez, A.; Orio, M.; Martínez-Otero, D. Cellulose Depolymerization with LPMO-Inspired Cu Complexes. *ChemCatChem* **2021**, *13* (22), 4700–4704. https://doi.org/10.1002/CCTC.202101169.

(5) Span, E. A.; Suess, D. L. M.; Deller, M. C.; Britt, R. D.; Marletta, M. A. The Role of the Secondary Coordination Sphere in a Fungal Polysaccharide Monooxygenase. *ACS Chem. Biol.* **2017**, *12*, 1095–1103. https://doi.org/10.1021/acschembio.7b00016.

(6) Hedegård, E. D.; Ryde, U. Targeting the Reactive Intermediate in Polysaccharide Monooxygenases. *J. Biol. Inorg. Chem.* **2017**, *22* (7), 1–9. https://doi.org/10.1007/s00775-017-1480-1.

(7) Elwell, C. E.; Gagnon, N. L.; Neisen, B. D.; Dhar, D.; Spaeth, A. D.; Yee, G. M.; Tolman, W. B. Copper-Oxygen Complexes Revisited: Structures, Spectroscopy, and Reactivity. *Chem. Rev.* **2017**, *117* (3), 2059–2107. https://doi.org/10.1021/acs.chemrev.6b00636.

(8) Liviu M. Mirica; Xavier Ottenwaelder, A.; Stack, T. D. P. Structure and Spectroscopy of Copper−Dioxygen Complexes. *Chem. Rev.* **2004**, *104* (2), 1013–1045. https://doi.org/10.1021/CR020632Z.

(9) Frandsen, K. E. H.; Simmons, T. J.; Dupree, P.; Poulsen, J.-C. N.; Hemsworth, G. R.; Ciano, L.; Johnston, E. M.; Tovborg, M.; Johansen, K. S.; von Freiesleben, P.; Marmuse, L.; Fort, S.; Cottaz, S.; Driguez, H.; Henrissat, B.; Lenfant, N.; Tuna, F.; Baldansuren, A.; Davies, G. J.; Lo Leggio, L.; Walton, P. H. The Molecular Basis of Polysaccharide Cleavage by Lytic Polysaccharide Monooxygenases. *Nat. Chem. Biol.* **2016**, *12* (4), 298–303. https://doi.org/10.1038/nchembio.2029.

(10) Vermaas, J. V.; Crowley, M. F.; Beckham, G. T.; Payne, C. M. Effects of Lytic Polysaccharide Monooxygenase Oxidation on Cellulose Structure and Binding of Oxidized Cellulose Oligomers to Cellulases. *J. Phys. Chem. B* **2015**, *119* (20), 6129–6143. https://doi.org/10.1021/acs.jpcb.5b00778.

(11) Villares, A.; Moreau, C.; Bennati-Granier, C.; Garajova, S.; Foucat, L.; Falourd, X.; Saake, B.; Berrin, J.-G.; Cathala, B. Lytic Polysaccharide Monooxygenases Disrupt the Cellulose Fibers Structure. *Sci. Rep.* **2017**, *7*, 40262. https://doi.org/10.1038/srep40262.

(12) Frommhagen, M.; Koetsier, M. J.; Westphal, A. H.; Visser, J.; Hinz, S. W. A.; Vincken, J.-P.; van Berkel, W. J. H.; Kabel, M. A.; Gruppen, H. Lytic Polysaccharide Monooxygenases from Myceliophthora Thermophila C1 Differ in Substrate Preference

and Reducing Agent Specificity. *Biotechnol. Biofuels* **2016**, *9* (1), 186. https://doi.org/10.1186/s13068-016-0594-y.

(13) Johansen, K. S. Lytic Polysaccharide Monooxygenases: The Microbial Power Tool for Lignocellulose Degradation. *Trends Plant Sci.* **2016**, *21* (11), 926–936. https://doi.org/10.1016/j.tplants.2016.07.012.

(14) Ciano, L.; Davies, G. J.; Tolman, W. B.; Walton, P. H. Bracing Copper for the Catalytic Oxidation of C–H Bonds. *Nat. Catal.* **2018**, *1*, 571–577. https://doi.org/10.1038/s41929-018-0110-9.

(15) Lo Leggio, L.; Simmons, T. J.; Poulsen, J.-C. N.; Frandsen, K. E. H.; Hemsworth, G. R.; Stringer, M. A.; von Freiesleben, P.; Tovborg, M.; Johansen, K. S.; De Maria, L.; Harris, P. V.; Soong, C.-L.; Dupree, P.; Tryfona, T.; Lenfant, N.; Henrissat, B.; Davies, G. J.; Walton, P. H. Structure and Boosting Activity of a Starch-Degrading Lytic Polysaccharide Monooxygenase. *Nat. Commun.* **2015**, *6*, 5961–5969. https://doi.org/10.1038/ncomms6961.

(16) Cao, L.; Caldararu, O.; Rosenzweig, A. C.; Ryde, U. Quantum Refinement Does Not Support Dinuclear Copper Sites in Crystal Structures of Particulate Methane Monooxygenase. *Angew. Chemie - Int. Ed.* **2018**, *130*, 168–172. https://doi.org/10.1002/ange.201708977.

(17) Ross, M. O.; MacMillan, F.; Wang, J.; Nisthal, A.; Lawton, T. J.; Olafson, B. D.; Mayo, S. L.; Rosenzweig, A. C.; Hoffman, B. M. Particulate Methane Monooxygenase Contains Only Mononuclear Copper Centers. *Science (80-.).* **2019**, *364* (6440), 566–570. https://doi.org/10.1126/SCIENCE.AAV2572/SUPPL_FILE/AAV2572-ROSS-SM.PDF.

(18) Bacik, J. P.; Mekasha, S.; Forsberg, Z.; Kovalevsky, A. Y.; Vaaje-Kolstad, G.; Eijsink, V. G. H.; Nix, J. C.; Coates, L.; Cuneo, M. J.; Unkefer, C. J.; Chen, J. C. H. Neutron and Atomic Resolution X-Ray Structures of a Lytic Polysaccharide Monooxygenase Reveal Copper-Mediated Dioxygen Binding and Evidence for N-Terminal Deprotonation. *Biochemistry* **2017**, *56* (20), 2529–2532. https://doi.org/10.1021/acs.biochem.7b00019.

(19) Haddad Momeni, M.; Fredslund, F.; Bissaro, B.; Raji, O.; Vuong, T. V.; Meier, S.; Nielsen, T. S.; Lombard, V.; Guigliarelli, B.; Biaso, F.; Haon, M.; Grisel, S.; Henrissat, B.; Welner, D. H.; Master, E. R.; Berrin, J. G.; Abou Hachem, M. Discovery of Fungal Oligosaccharide-Oxidising Flavo-Enzymes with Previously Unknown Substrates, Redox-Activity Profiles and Interplay with LPMOs. *Nat. Commun. 2021 121* **2021**, *12* (1), 1–13. https://doi.org/10.1038/s41467-021-22372-0.

(20) Kjaergaard, C. H.; Qayyum, M. F.; Wong, S. D.; Xu, F.; Hemsworth, G. R.; Walton, D. J.; Young, N. A.; Davies, G. J.; Walton, P. H.; Johansen, K. S.; Hodgson, K. O.; Hedman, B.; Solomon, E. I. Spectroscopic and Computational Insight into the Activation of O2 by the Mononuclear Cu Center in Polysaccharide Monooxygenases. *Proc. Natl. Acad. Sci.* **2014**, *111* (24), 8797–8802. https://doi.org/10.1073/pnas.1408115111.

(21) Bailey, W. D.; Dhar, D.; Cramblitt, A. C.; Tolman, W. B. Mechanistic Dichotomy in Proton-Coupled Electron-Transfer Reactions of Phenols with a Copper Superoxide Complex. *J. Am. Chem. Soc.* **2019**, *141*, 5470–5480. https://doi.org/10.1021/jacs.9b00466.

(22) Dietl, N.; van der Linde, C.; Schlangen, M.; Beyer, M. K.; Schwarz, H. Diatomic [CuO]+ and Its Role in the Spin-Selective Hydrogen- and Oxygen-Atom Transfers in the Thermal

Activation of Methane. *Angew. Chem., Int. Ed.* **2011**, *50*, 4966–4969.

(23) Donoghue, P. J.; Tehranchi, J.; Cramer, C. J.; Sarangi, R.; Solomon, E. I.; Tolman, W. B. Rapid C-H Bond Activation by a Monocopper(III)-Hydroxide Complex. *J. Am. Chem. Soc.* **2011**, *133* (44), 17602–17605. https://doi.org/10.1021/ja207882h.

(24) Dhar, D.; Tolman, W. B. Hydrogen Atom Abstraction from Hydrocarbons by a Copper(III)-Hydroxide Complex. *J. Am. Chem. Soc.* **2015**, *137* (3), 1322–1329. https://doi.org/10.1021/ja512014z.

(25) Dhar, D.; Yee, G. M.; Markle, T. F.; Mayer, J. M.; Tolman, W. B. Reactivity of the Copper(III)-Hydroxide Unit with Phenols. *Chem. Sci.* **2017**, *8* (2), 1075–1085. https://doi.org/10.1039/C6SC03039D.

(26) Donoghue, P. J.; Gupta, A. K.; Boyce, D. W.; Cramer, C. J.; Tolman, W. B. An Anionic , Tetragonal Copper(II) Superoxide Complex. *J. Am. Chem. Soc.* **2010**, *132* (45), 15869–15871.

(27) Bower, J. K.; Cypcar, A. D.; Henriquez, B.; Stieber, S. C. E.; Zhang, S. C(Sp3)-H Fluorination with a Copper(II)/(III) Redox Couple. *J. Am. Chem. Soc.* **2020**, *142* (18), 8514–8521. https://doi.org/10.1021/jacs.0c02583.

(28) Neisen, B. D.; Gagnon, N. L.; Dhar, D.; Spaeth, A. D.; Tolman, W. B. Formally Copper(III)-Alkylperoxo Complexes as Models of Possible Intermediates in Monooxygenase Enzymes. *J. Am. Chem. Soc.* **2017**, *139* (30), 10220–10223. https://doi.org/10.1021/jacs.7b05754.

(29) Krishnan, V. M.; Shopov, D. Y.; Bouchey, C. J.; Bailey, W. D.; Parveen, R.; Vlaisavljevich, B.; Tolman, W. B. Structural Characterization of the [CuOR]2+Core. *J. Am. Chem. Soc.* **2021**, *143* (9), 3295–3299. https://doi.org/10.1021/jacs.0c13470.

(30) Mandal, M.; Elwell, C. E.; Bouchey, C. J.; Zerk, T. J.; Tolman, W. B.; Cramer, C. J. Mechanisms for Hydrogen-Atom Abstraction by Mononuclear Copper(III) Cores: Hydrogen-Atom Transfer or Concerted Proton-Coupled Electron Transfer? *J. Am. Chem. Soc.* **2019**, *141* (43), 17236–17244. https://doi.org/10.1021/jacs.9b08109.

(31) Elwell, C. E.; Mandal, M.; Bouchey, C. J.; Que, L.; Cramer, C. J.; Tolman, W. B. Carboxylate Structural Effects on the Properties and Proton-Coupled Electron Transfer Reactivity of [CuO2CR]2+ Cores. *Inorg. Chem.* **2019**, *58* (23), 15872–15879. https://doi.org/10.1021/acs.inorgchem.9b02293.

(32) Bailey, W. D.; Gagnon, N. L.; Elwell, C. E.; Cramblitt, A. C.; Bouchey, C. J.; Tolman, W. B. Revisiting the Synthesis and Nucleophilic Reactivity of an Anionic Copper Superoxide Complex. *Inorg. Chem.* **2019**, *58*, 4706–4711. https://doi.org/10.1021/acs.inorgchem.9b00090.

(33) Dhar, D.; Yee, G. M.; Tolman, W. B. Effects of Charged Ligand Substituents on the Properties of the Formally Copper(III)-Hydroxide ([CuOH] 2+) Unit. *Inorg. Chem.* **2018**, *57* (16), 9794–9806. https://doi.org/10.1021/acs.inorgchem.8b01529.

(34) Dhar, D.; Yee, G. M.; Spaeth, A. D.; Boyce, D. W.; Zhang, H.; Dereli, B.; Cramer, C. J.; Tolman, W. B. Perturbing the Copper(III)-Hydroxide Unit through Ligand Structural Variation. *J. Am. Chem. Soc.* **2016**, *138* (1), 356–368. https://doi.org/10.1021/jacs.5b10985.

(35) Spaeth, A. D.; Gagnon, N. L.; Dhar, D.; Yee, G. M.; Tolman, W. B. Determination of the Cu(III)-OH Bond Distance by Resonance Raman Spectroscopy Using a Normalized Version of Badger's Rule. *J. Am. Chem. Soc.* **2017**, *139* (12), 4477–4485. https://doi.org/10.1021/jacs.7b00210.

(36) Zerk, T. J.; Saouma, C. T.; Mayer, J. M.; Tolman, W. B. Low Reorganization Energy for Electron Self-Exchange by a Formally Copper(III,II) Redox Couple. *Cite This Inorg. Chem* **2019**, *58*, 14151–14158. https://doi.org/10.1021/acs.inorgchem.9b02185.

(37) Mandal, M.; Elwell, C. E.; Bouchey, C. J.; Zerk, T. J.; Tolman, W. B.; Cramer, C. J. Mechanisms for Hydrogen-Atom Abstraction by Mononuclear Copper(III) Cores: Hydrogen-Atom Transfer or Concerted Proton-Coupled Electron Transfer? *J. Am. Chem. Soc.* **2019**, *141* (43), 17236. https://doi.org/10.1021/jacs.9b08109.

(38) Badiei, Y. M.; Dinescu, A.; Dai, X.; Palomino, R. M.; Heinemann, F. W.; Cundari, T. R.; Warren, T. H. Copper-Nitrene Complexes in Catalytic C-H Amination. *Angew. Chemie - Int. Ed.* **2008**, *47* (51), 9961–9964. https://doi.org/10.1002/anie.200804304.

(39) Carsch, K. M.; DiMucci, I. M.; Iovan, D. A.; Li, A.; Zheng, S. L.; Titus, C. J.; Lee, S. J.; Irwin, K. D.; Nordlund, D.; Lancaster, K. M.; Betley, T. A. Synthesis of a Copper-Supported Triplet Nitrene Complex Pertinent to Copper-Catalyzed Amination. *Science (80-.).* **2019**, *365* (6458), 1138–1143. https://doi.org/10.1126/SCIENCE.AAX4423/SUPPL_FILE/AAX4423_CARSCH_SM.PDF.

(40) Wu, W.; Tehranchi De Hont, J.; Vlaisavljevich, B.; Tolman, W. B. Sulfur-Containing Analogues of the Reactive [CuOH]2+ Core. *Inorg. Chem.* **2021**, *60* (7), 5217–5223. https://doi.org/10.1021/acs.inorgchem.1c00216.

(41) Merkle, A. C.; Lehnert, N. Binding and Activation of Nitrite and Nitric Oxide by Copper Nitrite Reductase and Corresponding Model Complexes. *Dalt. Trans.* **2012**, *41* (12), 3355–3368. https://doi.org/10.1039/c1dt11049g.

(42) Suzuki, S.; Kataoka, K.; Yamaguchi, K. Metal Coordination and Mechanism of Multicopper Nitrite Reductase. *Acc. Chem. Res.* **2000**, *33* (10), 728–735. https://doi.org/10.1021/ar9900257.

(43) Rose, S. L.; Antonyuk, S. V.; Sasaki, D.; Yamashita, K.; Hirata, K.; Ueno, G.; Ago, H.; Eady, R. R.; Tosha, T.; Yamamoto, M.; Samar Hasnain, S. An Unprecedented Insight into the Catalytic Mechanism of Copper Nitrite Reductase from Atomic-Resolution and Damage-Free Structures. *Sci. Adv.* **2021**, *7* (1). https://doi.org/10.1126/sciadv.abd8523.

(44) Yokoyama, H.; Yamaguchi, K.; Sugimoto, M.; Suzuki, S. CuI and CuII Complexes Containing Nitrite and Tridentate Aromatic Amine Ligand as Models for the Substrate-Binding Type-2 Cu Site of Nitrite Reductase. *Eur. J. Inorg. Chem.* **2005**, *2* (8), 1435–1441. https://doi.org/10.1002/ejic.200400808.

(45) Hsu, S. C. N.; Chang, Y.; Chuang, W.; Chen, H.; Lin, I.; Chiang, M. Y.; Kao, C.; Chen, H. Copper(I) Nitro Complex with an Anionic [HB(3,5-Me2Pz)3]- Ligand: A Synthetic Model for the Copper Nitrite Reductase Active Site. *Inorg. Chem.* **2012**, *51* (17), 9297–9308.

(46) Kujime, M.; Izumi, C.; Tomura, M.; Hada, M.; Fujii, H. Effect of a Tridentate Ligand on the Structure, Electronic Structure, and Reactivity of the Copper(I) Nitrite Complex: Role

of the Conserved Three-Histidine Ligand Environment of the Type-2 Copper Site in Copper-Containing Nitrite Reductases. *J. Am. Chem. Soc.* **2008**, *130* (19), 6088–6098. https://doi.org/10.1021/JA075575B.

(47) Halfen, J. A.; Mahapatra, S.; Wilkinson, E. C.; Gengenbach, A. J.; Young, V. G.; Que Jnr, L.; Tolman, W. B. Synthetic Modeling of Nitrite Binding and Activation by Reduced Copper Proteins. Characterization of Copper(I)-Nitrite Complexes That Evolve Nitric Oxide. *J. Am. Chem. Soc.* **1996**, *118* (4), 763–776. https://doi.org/10.1021/ja952691i.

(48) Kataoka, K.; Furusawa, H.; Takagi, K.; Yamaguchi, K.; Suzuki, S. Functional Analysis of Conserved Aspartate and Histidine Residues Located around the Type 2 Copper Site of Copper-Containing Nitrite Reductase. *J. Biochem.* **2000**, *127* (2), 345–350. https://doi.org/10.1093/oxfordjournals.jbchem.a022613.

(49) Lehnert, N.; Cornelissen, U.; Neese, F.; Ono, T.; Noguchi, Y.; Okamoto, K. I.; Fujisawa, K. Synthesis and Spectroscopic Characterization of Copper(II)-Nitrito Complexes with Hydrotris(Pyrazolyl)Borate and Related Coligands. *Inorg. Chem.* **2007**, *46* (10), 3916–3933. https://doi.org/10.1021/ic0619355.

(50) Tocheva, E. I.; Rosell, F. I.; Mauk, A. G.; Murphy, M. E. P. Side-On Copper-Nitrosyl Coordination by Nitrite Reductase. *Science (80-.).* **2004**, *304* (5672), 867–870. https://doi.org/10.1126/SCIENCE.1095109/SUPPL_FILE/TOCHEVA_SOM.PDF.

(51) Sakhaei, Z.; Kundu, S.; Donnelly, J. M.; Bertke, J. A.; Kim, W. Y.; Warren, T. H. Nitric Oxide Release via Oxygen Atom Transfer from Nitrite at Copper(II). *Chem. Commun.* **2017**, *53*, 549. https://doi.org/10.1039/c6cc08745k.

(52) Chen, C. S.; Yeh, W. Y. Coordination of NO2- Ligand to Cu(I) Ion in an O,O-Bidentate Fashion That Evolves NO Gas upon Protonation: A Model Reaction Relevant to the Denitrification Process. *Chem. Commun.* **2010**, *46* (18), 3098–3100. https://doi.org/10.1039/b927513d.

(53) Chuang, W. J.; Narwane, M.; Chen, H. Y.; Kao, C. L.; Huang, B.; Hsu, K. M.; Wang, Y. M.; Hsu, S. C. N. Nitric Oxide-Release Study of a Bio-Inspired Copper(i)-Nitrito Complex under Chemical and Biological Conditions. *Dalt. Trans.* **2018**, *47* (37), 13151–13157. https://doi.org/10.1039/c8dt02281j.

(54) Kumar, M.; Dixon, N. A.; Merkle, A. C.; Zeller, M.; Lehnert, N.; Papish, E. T. Hydrotris(Triazolyl)Borate Complexes as Functional Models for Cu Nitrite Reductase: The Electronic Influence of Distal Nitrogens. *Inorg. Chem.* **2012**, *51* (13), 7004–7006. https://doi.org/10.1021/ic300160c.

(55) Beretta, M.; Bouwman, E.; Casella, L.; Douziech, B.; Driessen, W. L.; Gutierrez-Soto, L.; Monzani, E.; Reedijk, J. Copper Complexes of a New Tridentate Imidazole-Containing Ligand: Spectroscopy, Structures and Nitrite Reductase Reactivity: The Molecular Structures of [Cu(Biap)(NO2)2] and [Cu(Biap)Br2]. *Inorganica Chim. Acta* **2000**, *310* (1), 41–50. https://doi.org/10.1016/S0020-1693(00)00271-1.

(56) Monzani, E.; Koolhaas, G. J. A. A.; Spandre, A.; Leggieri, E.; Casella, L.; Gullotti, M.; Nardin, G.; Randaccio, L.; Fontani, M.; Zanello, P.; Reedijk, J. Binding of Nitrite and Its Reductive Activation to Nitric Oxide at Biomimetic Copper Centers. *J. Biol. Inorg. Chem.* **2000**, *5* (2), 251–261. https://doi.org/10.1007/s007750050369.

(57) Maji, R. C.; Barman, S. K.; Roy, S.; Chatterjee, S. K.; Bowles, F. L.; Olmstead, M. M.; Patra, A. K. Copper Complexes Relevant to the Catalytic Cycle of Copper Nitrite Reductase: Electrochemical Detection of NO(g) Evolution and Flipping of NO 2 Binding Mode upon CuII → CuI Reduction. *Inorg. Chem.* **2013**, *52* (19), 11084–11095. https://doi.org/10.1021/ic401295t.

(58) Maji, R. C.; Mishra, S.; Bhandari, A.; Singh, R.; Olmstead, M. M.; Patra, A. K. A Copper(II) Nitrite That Exhibits Change of Nitrite Binding Mode and Formation of Copper(II) Nitrosyl Prior to Nitric Oxide Evolution. *Inorg. Chem.* **2018**, *57* (3), 1550. https://doi.org/10.1021/acs.inorgchem.7b02897.

(59) Cioncoloni, G.; Roger, I.; Wheatley, P. S.; Wilson, C.; Morris, R. E.; Sproules, S.; Symes, M. D. Proton-Coupled Electron Transfer Enhances the Electrocatalytic Reduction of Nitrite to NO in a Bioinspired Copper Complex. *ACS Catal.* **2018**, *8* (6), 5070–5084. https://doi.org/10.1021/acscatal.8b00361.

(60) Moore, C. M.; Szymczak, N. K. Nitrite Reduction by Copper through Ligand-Mediated Proton and Electron Transfer. *Chem. Sci.* **2015**, *6*, 3373. https://doi.org/10.1039/c5sc00720h.

(61) Maria, S.; Chattopadhyay, T.; Ananya, S.; Kundu, S. Reduction of Nitrite to NO at a Mononuclear Copper(II)-Phenolate Site. *Inorganica Chim. Acta* **2020**, *506* (January). https://doi.org/10.1016/j.ica.2020.119515.

(62) Kundu, S.; Kim, W. Y.; Bertke, J. A.; Warren, T. H. Copper(II) Activation of Nitrite: Nitrosation of Nucleophiles and Generation of NO by Thiols. *J. Am. Chem. Soc.* **2017**, *139* (3), 1045–1048. https://doi.org/10.1021/jacs.6b11332.

(63) Sakhaei, Z.; Kundu, S.; Bertke, J. A.; Warren, T. H. Nitrite-Phenol-NO Crosstalk: Phenol Oxidation and NO Generation from Nitrite at Copper(II) Sites. *ChemRxiv* **2019**.

(64) Mondal, A.; Reddy, K. P.; Bertke, J. A.; Kundu, S. Phenol Reduces Nitrite to NO at Copper(II): Role of a Proton-Responsive Outer Coordination Sphere in Phenol Oxidation. *J. Am. Chem. Soc.* **2020**, *142* (4), 1726–1730. https://doi.org/10.1021/jacs.9b11597.

(65) Hili, R.; Yudin, A. K. Making Carbon-Nitrogen Bonds in Biological and Chemical Synthesis. *Nat. Chem. Biol. 2006 26* **2006**, *2* (6), 284–287. https://doi.org/10.1038/nchembio0606-284.

(66) Yamaguchi, J.; Yamaguchi, A. D.; Itami, K.; Yamaguchi, J.; Itami, K.; Yamaguchi, A. D. C-H Bond Functionalization: Emerging Synthetic Tools for Natural Products and Pharmaceuticals. *Angew. Chemie Int. Ed.* **2012**, *51* (36), 8960–9009. https://doi.org/10.1002/ANIE.201201666.

(67) Roughley, S. D.; Jordan, A. M. The Medicinal Chemist's Toolbox: An Analysis of Reactions Used in the Pursuit of Drug Candidates. *J. Med. Chem.* **2011**, *54* (10), 3451–3479. https://doi.org/10.1021/JM200187Y/SUPPL_FILE/JM200187Y_SI_001.PDF.

(68) Ohata, J.; Minus, M. B.; Abernathy, M. E.; Ball, Z. T. Histidine-Directed Arylation/Alkenylation of Backbone N-H Bonds Mediated by Copper(II). *J. Am. Chem. Soc.* **2016**, *138* (24), 7472–7475. https://doi.org/10.1021/JACS.6B03390/SUPPL_FILE/JA6B03390_SI_001.PDF.

(69) Yamaguchi, J.; Yamaguchi, A. D.; Itami, K.; Yamaguchi, J.; Itami, K.; Yamaguchi, A. D.

C-H Bond Functionalization: Emerging Synthetic Tools for Natural Products and Pharmaceuticals. *Angew. Chemie Int. Ed.* **2012**, *51* (36), 8960–9009. https://doi.org/10.1002/ANIE.201201666.

(70) Hartwig, J. F. Carbon–Heteroatom Bond Formation Catalysed by Organometallic Complexes. *Nat. 2008 4557211* **2008**, *455* (7211), 314–322. https://doi.org/10.1038/nature07369.

(71) Kim, Y.; Lin, Z.; Jeon, I.; Van Voorhis, T.; Swager, T. M. Polyaniline Nanofiber Electrodes for Reversible Capture and Release of Mercury(II) from Water. *J. Am. Chem. Soc.* **2018**, *140* (43), 14413–14420. https://doi.org/10.1021/JACS.8B09119/SUPPL_FILE/JA8B09119_SI_001.PDF.

(72) Ohata, J.; Minus, M. B.; Abernathy, M. E.; Ball, Z. T. Histidine-Directed Arylation/Alkenylation of Backbone N-H Bonds Mediated by Copper(II). *J. Am. Chem. Soc.* **2016**, *138* (24), 7472–7475. https://doi.org/10.1021/JACS.6B03390/SUPPL_FILE/JA6B03390_SI_001.PDF.

(73) Chen, J. Q.; Li, J. H.; Dong, Z. B. A Review on the Latest Progress of Chan-Lam Coupling Reaction. *Adv. Synth. Catal.* **2020**, *362* (16), 3311–3331. https://doi.org/10.1002/ADSC.202000495.

(74) Park, Y.; Kim, Y.; Chang, S. Transition Metal-Catalyzed C-H Amination: Scope, Mechanism, and Applications. *Chem. Rev.* **2017**, *117* (13), 9247–9301. https://doi.org/10.1021/acs.chemrev.6b00644.

(75) Chen, J. Q.; Li, J. H.; Dong, Z. B. A Review on the Latest Progress of Chan-Lam Coupling Reaction. *Adv. Synth. Catal.* **2020**, *362* (16), 3311–3331. https://doi.org/10.1002/ADSC.202000495.

(76) Sambiagio, C.; Marsden, S. P.; Blacker, A. J.; McGowan, P. C. Copper Catalysed Ullmann Type Chemistry: From Mechanistic Aspects to Modern Development. *Chem. Soc. Rev.* **2014**, *43* (10), 3525–3550. https://doi.org/10.1039/C3CS60289C.

(77) Sambiagio, C.; Marsden, S. P.; Blacker, A. J.; McGowan, P. C. Copper Catalysed Ullmann Type Chemistry: From Mechanistic Aspects to Modern Development. *Chem. Soc. Rev.* **2014**, *43* (10), 3525–3550. https://doi.org/10.1039/C3CS60289C.

(78) Carsch, K. M.; DiMucci, I. M.; Iovan, D. A.; Li, A.; Zheng, S. L.; Titus, C. J.; Lee, S. J.; Irwin, K. D.; Nordlund, D.; Lancaster, K. M.; Betley, T. A. Synthesis of a Copper-Supported Triplet Nitrene Complex Pertinent to Copper-Catalyzed Amination. *Science (80-.).* **2019**, *365* (6458), 1138–1143. https://doi.org/10.1126/SCIENCE.AAX4423/SUPPL_FILE/AAX4423_CARSCH_SM.PDF.

(79) Aguila, M. J. B.; Badiei, Y. M.; Warren, T. H. Mechanistic Insights into C-H Amination via Dicopper Nitrenes. *J. Am. Chem. Soc.* **2013**, *135* (25), 9399–9406. https://doi.org/10.1021/ja400879m.

(80) Badiei, Y. M.; Krishnaswamy, A.; Melzer, M. M.; Warren, T. H. Transient Terminal Cu-Nitrene Intermediates from Discrete Dicopper Nitrenes. *J. Am. Chem. Soc.* **2006**, *128* (47), 15056–15057. https://doi.org/10.1021/JA065299L/SUPPL_FILE/JA065299LSI20061027_011721.PDF.

(81) Desnoyer, A. N.; Nicolay, A.; Ziegler, M. S.; Lakshmi, K. V.; Cundari, T. R.; Tilley, T. D. A Dicopper Nitrenoid by Oxidation of a CuICuICore: Synthesis, Electronic Structure, and Reactivity. *J. Am. Chem. Soc.* **2021**, *143* (18), 7135–7143. https://doi.org/10.1021/JACS.1C02235/SUPPL_FILE/JA1C02235_SI_001.PDF.

(82) Carsch, K. M.; Lukens, J. T.; Dimucci, I. M.; Iovan, D. A.; Zheng, S. L.; Lancaster, K. M.; Betley, T. A. Electronic Structures and Reactivity Profiles of Aryl Nitrenoid-Bridged Dicopper Complexes. *J. Am. Chem. Soc.* **2020**, *142* (5), 2264–2276. https://doi.org/10.1021/JACS.9B09616/SUPPL_FILE/JA9B09616_SI_002.CIF.

(83) Badiei, Y. M.; Krishnaswamy, A.; Melzer, M. M.; Warren, T. H. Transient Terminal Cu-Nitrene Intermediates from Discrete Dicopper Nitrenes. *J. Am. Chem. Soc.* **2006**, *128* (47), 15056–15057. https://doi.org/10.1021/JA065299L/SUPPL_FILE/JA065299LSI20061027_011721.PDF.

(84) Vaaje-Kolstad, G.; Westereng, B.; Horn, S. J.; Liu, Z.; Zhai, H.; Sorlie, M.; Eijsink, V. G. H. An Oxidative Enzyme Boosting the Enzymatic Conversion of Recalcitrant Polysaccharides. *Science (80-.).* **2010**, *330*, 219–222. https://doi.org/10.1126/science.1192231.

(85) Walton, P. H.; Davies, G. J. On the Catalytic Mechanisms of Lytic Polysaccharide Monooxygenases. *Curr. Opin. Chem. Biol.* **2016**, *31*, 195–207.

(86) Meier, K. K.; Jones, S. M.; Kaper, T.; Hansson, H.; Koetsier, M. J.; Karkehabadi, S.; Solomon, E. I.; Sandgren, M.; Kelemen, B. Oxygen Activation by Cu LPMOs in Recalcitrant Carbohydrate Polysaccharide Conversion to Monomer Sugars. *Chem. Rev.* **2018**, *118* (5), 2593–2635. https://doi.org/10.1021/acs.chemrev.7b00421.

(87) Bertini, L.; Breglia, R.; Lambrughi, M.; Fantucci, P.; Gioia, L. De; Borsari, M.; Sola, M.; Bortolotti, C. A.; Bruschi, M. Catalytic Mechanism of Fungal Lytic Polysaccharide Monooxygenases Investigated by First-Principles Calculations. *Inorg. Chem.* **2017**, *57* (1), 86–97. https://doi.org/10.1021/ACS.INORGCHEM.7B02005.

(88) Lee, J. Y.; Karlin, K. D. Elaboration of Copper-Oxygen Mediated CH Activation Chemistry in Consideration of Future Fuel and Feedstock Generation. *Curr. Opin. Chem. Biol.* **2015**, *25*, 184–193. https://doi.org/10.1016/j.cbpa.2015.02.014.

(89) Kim, S.; Stahlberg, J.; Sandgren, M.; Paton, R. S.; Beckham, G. T. Quantum Mechanical Calculations Suggest That Lytic Polysaccharide Monooxygenases Use a Copper-Oxyl, Oxygen-Rebound Mechanism. *Proc. Natl. Acad. Sci.* **2014**, *111* (1), 149–154. https://doi.org/10.1073/pnas.1316609111.

(90) Schröder, D.; Holthausen, M. C.; Schwarz, H. Radical-Like Activation of Alkanes by the Ligated Copper Oxide Cation (Phenanthroline)CuO+. *J. Phys. Chem. B* **2004**, *108* (38), 14407–14416. https://doi.org/10.1021/JP0496452.

(91) Shaffer, C. J.; Schröder, D.; Gütz, C.; Lützen, A. Intramolecular C-H Bond Activation through a Flexible Ester Linkage. *Angew. Chemie Int. Ed.* **2012**, *51* (32), 8097–8100. https://doi.org/10.1002/ANIE.201203163.

(92) Tehranchi, J.; Donoghue, P. J.; Cramer, C. J.; Tolman, W. B. Reactivity of (Dicarboxamide)M(II)–OH (M = Cu, Ni) Complexes – Reaction with Acetonitrile to Yield M(II)–Cyanomethides. *Eur. J. Inorg. Chem.* **2013**, No. 22–23, 4077–4084.

https://doi.org/10.1002/EJIC.201300328.

(93) Wu, T.; MacMillan, S. N.; Rajabimoghadam, K.; Siegler, M. A.; Lancaster, K. M.; Garcia-Bosch, I. Structure, Spectroscopy, and Reactivity of a Mononuclear Copper Hydroxide Complex in Three Molecular Oxidation States. *J. Am. Chem. Soc.* **2020**, *142* (28), 12265–12276. https://doi.org/10.1021/JACS.0C03867.

(94) Itoh, S. Developing Mononuclear Copper-Active-Oxygen Complexes Relevant to Reactive Intermediates of Biological Oxidation Reactions. *Acc. Chem. Res.* **2015**, *48*, 2066–2074. https://doi.org/10.1021/acs.accounts.5b00140.

(95) Noh, H.; Cho, J. Synthesis, Characterization and Reactivity of Non-Heme 1st Row Transition Metal-Superoxo Intermediates. *Coord. Chem. Rev.* **2019**, *382*, 126–144. https://doi.org/10.1016/j.ccr.2018.12.006.

(96) Reynolds, A. M.; Gherman, B. F.; Cramer, C. J.; Tolman, W. B. Characterization of a 1:1 Cu-O2 Adduct Supported by an Anilido Imine Ligand. *Inorg. Chem.* **2005**, *44* (20), 6989–6997. https://doi.org/10.1021/ic050280p.

(97) Gherman, B. F.; Tolman, W. B.; Cramer, C. J. Characterization of the Structure and Reactivity of Monocopper-Oxygen Complexes Supported by b-Diketiminate and Anilido-Imine Ligands. *J. Comput. Chem.* **2006**, *27* (16), 1950–1961. https://doi.org/10.1002/jcc.

(98) Hill, L. M. R.; Gherman, B. F.; Aboelella, N. W.; Cramer, C. J.; Tolman, W. B. Electronic Tuning of β-Diketiminate Ligands with Fluorinated Substituents: Effects on the O2-Reactivity of Mononuclear Cu(I) Complexes. *Dalt. Trans.* **2006**, No. 41, 4944–4953. https://doi.org/10.1039/B609939D.

(99) M. Reynolds, A.; A. Lewis, E.; W. Aboelella, N.; B. Tolman, W. Reactivity of a 1∶1 Copper–Oxygen Complex: Isolation of a Cu(II)-o-Iminosemiquinonato Species. *Chem. Commun.* **2005**, No. 15, 2014–2016. https://doi.org/10.1039/B418939F.

(100) Csay, T.; Kripli, B.; Giorgi, M.; Kaizer, J.; Speier, G. A Flexible Hydroxy-Bridged Dicopper Complex as Catechol Oxidase Mimic. *Inorg. Chem. Commun.* **2010**, *13* (2), 227–230. https://doi.org/10.1016/j.inoche.2009.11.018.

(101) Pap, J. S.; Kripli, B.; Bányai, V.; Giorgi, M.; Korecz, L.; Gajda, T.; Árus, D.; Kaizer, J.; Speier, G. Tetra-, Penta- and Hexacoordinate Copper(II) Complexes with N3 Donor Isoindoline-Based Ligands: Characterization and SOD-like Activity. *Inorganica Chim. Acta* **2011**, *376* (1), 158–169. https://doi.org/10.1016/j.ica.2011.06.001.

(102) Balogh-Hergovich, É.; Kaizer, J.; Speier, G.; Huttner, G.; Jacobi, A. Preparation and Oxygenation of (Flavonolato)Copper Isoindoline Complexes with Relevance to Quercetin Dioxygenase. *Inorg. Chem.* **2000**, *39* (19), 4224–4229. https://doi.org/10.1021/IC990521R.

(103) Babu, H. V.; Muralidharan, K. Zn(II), Cd(II) and Cu(II) Complexes of 2,5-Bis{N-(2,6-Diisopropylphenyl)Iminomethyl}pyrrole: Synthesis, Structures and Their High Catalytic Activity for Efficient Cyclic Carbonate Synthesis. *Dalt. Trans.* **2012**, *42* (4), 1238–1248. https://doi.org/10.1039/C2DT31755A.

(104) Daneshmand, P.; Fortun, S.; Schaper, F. Diiminopyrrolide Copper Complexes: Synthesis, Structures, and Rac-Lactide Polymerization Activity. *Organometallics* **2017**, *36* (19), 3860–3877. https://doi.org/10.1021/ACS.ORGANOMET.7B00609.

(105) Daneshmand, P.; Est, A. van der; Schaper, F. Mechanism and Stereocontrol in Isotactic Rac-Lactide Polymerization with Copper(II) Complexes. *ACS Catal.* **2017**, *7* (9), 6289–6301. https://doi.org/10.1021/ACSCATAL.7B02049.

(106) Fortun, S.; Daneshmand, P.; Schaper, F. Isotactic Rac-Lactide Polymerization with Copper Complexes: The Influence of Complex Nuclearity. *Angew. Chemie Int. Ed.* **2015**, *54* (46), 13669–13672. https://doi.org/10.1002/ANIE.201505674.

(107) Sahu, R.; Padhi, S. K.; Jena, H. S.; Manivannan, V. Conversion of 2-(Aminomethyl) Substituted Pyridine and Quinoline to Their Dicarbonyldiimides Using Copper(II) Acetate. *Inorganica Chim. Acta* **2010**, *363* (7), 1448–1454. https://doi.org/10.1016/J.ICA.2010.01.028.

(108) Pap, J. S.; Bányai, V.; Szilvási, D. S.; Kaizer, J.; Speier, G.; Giorgi, M. Influence of Meridional N3-Ligands on Supramolecular Assembling and Redox Behavior of Carboxylatocopper(II) Complexes. *Inorg. Chem. Commun.* **2011**, *14* (11), 1767–1772. https://doi.org/10.1016/J.INOCHE.2011.08.005.

(109) Kaizer, J.; Pap, J.; Speier, G.; Réglier, M.; Giorgi, M. Synthesis, Properties, and Crystal Structure of a Novel 3-Hydroxy-(4H)-Benzopyran-4-One Containing Copper(II) Complex, and Its Oxygenation and Relevance to Quercetinase. *Transit. Met. Chem. 2004 296* **2004**, *29* (6), 630–633. https://doi.org/10.1007/S11243-004-2794-8.

(110) Engle, J. T.; Martić, G.; Ziegler, C. J. Investigations into the Coordination Chemistry of 1,3-Bis(2'-Benzimidazolylimino)Isoindoline. *Macroheterocycles* **2013**, *6* (4), 353–359. https://doi.org/10.6060/mhc131265z.

(111) Sauer, D. C.; Wadepohl, H. Variable Coordination Modes of an Active Ligand Periphery in 1,3-Bis(2-Pyridylimino)Isoindolato Copper(II) Complexes. *Polyhedron* **2014**, *81*, 180–187. https://doi.org/10.1016/J.POLY.2014.06.001.

(112) Taghvaee, M.; Rodríguez-Álvarez, M. J.; García-Álvarez, J.; del Río, I.; Lough, A. J.; Gossage, R. A. Amido-Pincer Complexes of Cu(II): Synthesis, Coordination Chemistry and Applications in Catalysis. *J. Organomet. Chem.* **2017**, *845*, 107–114. https://doi.org/10.1016/j.jorganchem.2017.03.021.

(113) Deng, Q.-H.; Wadepohl, H.; Gade, L. H. Highly Enantioselective Copper-Catalyzed Alkylation of β-Ketoesters and Subsequent Cyclization to Spirolactones/Bi-Spirolactones. *J. Am. Chem. Soc.* **2012**, *134* (6), 2946–2949. https://doi.org/10.1021/JA211859W.

(114) Chuang, W.-J.; Hsu, S.-P.; Chand, K.; Yu, F.-L.; Tsai, C.-L.; Tseng, Y.-H.; Lu, Y.-H.; Kuo, J.-Y.; Carey, J. R.; Chen, H.-Y.; Chen, H.-Y.; Chiang, M. Y.; Hsu, S. C. N. Reactivity Study of Unsymmetrical β-Diketiminato Copper(I) Complexes: Effect of the Chelating Ring. *Inorg. Chem.* **2017**, *56* (5), 2722–2735. https://doi.org/10.1021/ACS.INORGCHEM.6B02876.

(115) Barbe, J.-M.; Habermeyer, B.; Khoury, T.; Gros, C. P.; Richard, P.; Chen, P.; Kadish, K. M. Three-Metal Coordination by Novel Bisporphyrin Architectures. *Inorg. Chem.* **2010**, *49* (19), 8929–8940. https://doi.org/10.1021/IC101170K.

(116) Faizi, M. S. H.; Sen, P. [Bis(Quinolin-2-Ylcarbon-yl)Amido-K3N,N′,N″]Bromido-(N,N-Di-methyl-formamide-KO)Copper(II). *Acta Crystallogr. Sect. E* **2014**, *70* (6), m206–m207. https://doi.org/10.1107/S1600536814010058.

(117) Hurley, N. J.; Hayward, J. J.; Rawson, J. M.; Murrie, M.; Pilkington, M. Exploring the Coordination Chemistry of 3,3′-Di(Picolinamoyl)-2,2′-Bipyridine: One Ligand, Multiple Nuclearities. *Inorg. Chem.* **2014**, *53* (16), 8610–8623. https://doi.org/10.1021/IC501224Q.

(118) Kan, W.-Q.; Xia, D.-C.; Ma, J.-F. Crystal Structure of N-(5-((Pyridin-2-Yl)Methoxy)-4-Ethynyl-2,3-Dihydro-2-(Pyridin-2-Yl)Benzofuran-3-Yl)Picolinamidecopper(I) Chloride—Methanol, Cu(C26H16O3N5)Cl · CH3OH. *Zeitschrift für Krist. - New Cryst. Struct.* **2010**, *225* (1), 97–98. https://doi.org/10.1524/NCRS.2010.0041.

(119) Wu, C. Y.; Su, C. C. Electronic and Bonding Properties of Mixed-Ligand Copper(II) Complexes of N-(2-Pyridylethyl)Picolinamide (Pepa). Molecular Structures of [Cu(Pepa)(3-Methyl-Pyridine) (H2O)](ClO4), [Cu(Pepa)(4-Methylpyridine) (H2O)](ClO4) and [Cu(Pepa)(4-Methylimidazole) (H2O)](H2O)(ClO4). *Polyhedron* **1997**, *16* (14), 2465–2474. https://doi.org/10.1016/S0277-5387(96)00569-4.

(120) Brown, S. J.; Tao, X.; Stephan, D. W.; Mascharak, P. K. Synthetic Analog Approach to Metallobleomycins. 1. Syntheses, Structures and Properties of the Copper Complexes of Two Peptides Related to Bleomycins. *Inorg. Chem.* **1986**, *25* (19), 3377–3384. https://doi.org/10.1021/IC00239A013.

(121) Brown, S. J.; Tao, X.; Wark, T. A.; Stephan, D. W.; Mascharak, P. K. Synthetic Analog Approach to Metallobleomycins. 4. New Halobridged Dimeric and Polymeric (Infinite Zigzag Chain) Complexes of Copper(II) with Peptide Ligands Related to Bleomycins. *Inorg. Chem.* **1988**, *27* (9), 1581–1587. https://doi.org/10.1021/IC00282A014.

(122) Wang, J.; Djukic, B.; Cao, J.; Alberola, A.; Razavi, F. S.; Pilkington, M. A Novel Bis Tridentate Bipyridine Carboxamide Ligand and Its Complexation to Copper(II): Synthesis, Structure, and Magnetism. *Inorg. Chem.* **2007**, *46* (21), 8560–8568. https://doi.org/10.1021/IC700469V.

(123) Anderson, O. P.; La Cour, A.; Dodd, A.; Garrett, A. D.; Wicholas, M. Syntheses and Structures of Isoindoline Complexes of Zn(II) and Cu(II): An Unexpected Trinuclear Zn(II) Complex. *Inorg. Chem.* **2003**, *42* (1), 122–127. https://doi.org/10.1021/ic011246n.

(124) Folgado, J. V.; Martínez-Tamayo, E.; Beltrán-Porter, A.; Beltrán-Porter, D.; Fuertes, A.; Miravitlles, C. Crystal Structure and Spectroscopic Study of [Cu(BPCA)(OH2)(O2CCH3)·H2O Complex; BPC = N-2-Pyridinylcarbonyl-2-Pyridinecarboximidate Anion. *Polyhedron* **1989**, *8* (8), 1077–1083. https://doi.org/10.1016/S0277-5387(00)81122-5.

(125) Pandiri, H.; Gonnade, R. G.; Punji, B. Synthesis of Quinolinyl-Based Pincer Copper(Ii) Complexes: An Efficient Catalyst System for Kumada Coupling of Alkyl Chlorides and Bromides with Alkyl Grignard Reagents. *Dalt. Trans.* **2018**, *47* (46), 16747–16754. https://doi.org/10.1039/C8DT03210F.

(126) Jana, O.; Mani, G. New Types of Cu and Ag Clusters Supported by the Pyrrole-Based NNN-Pincer Type Ligand. *New J. Chem.* **2017**, *41* (17), 9361–9370. https://doi.org/10.1039/c7nj01009e.

(127) Elwell, C. E.; Neisen, B. D.; Tolman, W. B. Copper Complexes of Multidentate Carboxamide Ligands. *Inorganica Chim. Acta* **2019**, *485*, 131–139. https://doi.org/10.1016/j.ica.2018.10.011.

(128) Meder, M. B.; Gade, L. H. Coordination Chemistry of 1,3-Bis(2-Pyridylimino)- and 1,3-Bis(2-Thiazolylimino)Soindole Copper Complexes: Investigation of Their Catalytic Behavior in Oxidation Reactions. *Eur. J. Inorg. Chem.* **2004**, No. 13, 2716–2722. https://doi.org/10.1002/EJIC.200400012.

(129) Bereman, R. D.; Shields, G. D.; Dorfman, J. R.; Bordner, J. Stereoelectronic Properties of Metalloenzymes. 10. a Refined Model That Mimics the Type II Copper(II) Site in Galactose Oxidase. *J. Inorg. Biochem.* **1983**, *19* (1), 75–93. https://doi.org/10.1016/0162-0134(83)85014-4.

(130) Addison, A. W.; Burke, P. J.; Henrick, K. Crystal and Molecular Structure of Dipolar Spin-Coupled Dimers of an Irregularly Pentaccordinate Copper(II) Complex, [Cu(5-MeIin)(DBM)]. *Inorg. Chem.* **2002**, *21* (1), 60–63. https://doi.org/10.1021/IC00131A011.

(131) Lee, W. C. C.; Shen, Y.; Gutierrez, D. A.; Li, J. J. 2-Aminophenyl-1H-Pyrazole as a Removable Directing Group for Copper-Mediated C-H Amidation and Sulfonamidation. *Org. Lett.* **2016**, *18* (11), 2660–2663. https://doi.org/10.1021/acs.orglett.6b01105.

(132) Duncan Lyngdoh, R. H.; Schaefer, H. F.; King, R. B. Metal-Metal (MM) Bond Distances and Bond Orders in Binuclear Metal Complexes of the First Row Transition Metals Titanium through Zinc. *Chem. Rev.* **2018**, *118* (24), 11626–11706. https://doi.org/10.1021/ACS.CHEMREV.8B00297/SUPPL_FILE/CR8B00297_SI_001.PDF.

(133) Carrier, S. M.; Ruggiero, C. E.; Houser, R. P.; Tolman, W. B. Synthesis, Structural Characterization, and Electrochemical Behavior of Copper(I) Complexes of Sterically Hindered Tris(3-Ferf-Butyl-and 3,5-Diphenylpyrazolyl)Hydroborate Ligands. *Inorg. Chem* **1993**, *32*, 4889–4899.

(134) Mealli, C.; Arcus, C. S.; Wilkinson, J. L.; Marks, T. J.; Tbers, J. A. Structural Studies of Copper(I) Binding by Hydrotris(l-Pyrazolyl)Borate and Hydrotris(3,5-Dimethyl-l-Pyrazolyl)Borate in the Solid State and in Solution.

(135) Chang, Y. L.; Lin, Y. F.; Chuang, W. J.; Kao, C. L.; Narwane, M.; Chen, H. Y.; Chiang, M. Y.; Hsu, S. C. N. Structure and Nitrite Reduction Reactivity Study of Bio-Inspired Copper(i)-Nitro Complexes in Steric and Electronic Considerations of Tridentate Nitrogen Ligands. *Dalt. Trans.* **2018**, *47* (15), 5335–5341. https://doi.org/10.1039/c7dt03843g.

(136) Fujisawa, K.; Tanaka, M.; Moro-oka, Y.; Kitajima, N. A Monomeric Side-On Superoxocopper(II) Complex: Cu(02)(HB(3-TBu-5-IPrpz)3). *J. Am. Chem. Soc* **1994**, *116* (2), 1277.

(137) Chen, P.; Root, D. E.; Campochiaro, C.; Fujisawa, K.; Solomon, E. I. Spectroscopic and Electronic Structure Studies of the Diamagnetic Side-on CuII-Superoxo Complex Cu(O2)[HB(3-R-5-IPrpz)3]: Antiferromagnetic Coupling versus Covalent Delocalization. *J. Am. Chem. Soc.* **2003**, *125* (2), 466–474. https://doi.org/10.1021/JA020969I/SUPPL_FILE/JA020969I_S.PDF.

(138) Hueso-urena, F.; Esteve, V.; Debaerdemaeker, T. Copper(II) Complexes with the N,N,O-Tridentate Ligand 6-Amino-5-Formyl- Studies. *Polyhedron* **1999**, *18*, 3629–3636.

(139) Jia, W.-G.; Li, D.-D.; Dai, Y.-C.; Zhang, H.; Yan, L.-Q.; Sheng, E.-H.; Wei, Y.; Mu, X.-L.; Huang, K.-W. Synthesis and Characterization of Bisoxazolines- and Pybox-Copper(II)

Complexes and Their Application in the Coupling of α-Carbonyls with Functionalized Amines. *Org. Biomol. Chem.* **2014**, *12* (29), 5509–5516. https://doi.org/10.1039/C4OB01027B.

(140) Kwiatkowski, E.; Kwiatkowski, M.; Olechnowicz, A.; Mroziński, J.; Ho, D. M.; Deutsch, E. Synthesis, Structure and Magnetic Properties of a New Chloro-Bridged Dimeric Copper Complex, Bis(μ-Chloro)Bis(8-Amino-5-Aza-4-Methyl-3-Octene-2-Onato)Dicopper(II). *Inorganica Chim. Acta* **1989**, *158* (1), 37–42. https://doi.org/10.1016/S0020-1693(00)84012-8.

(141) Bu, X.-H.; Du, M.; Zhang, L.; Shang, Z.-L.; Zhang, R.-H.; Shionoya, M. Novel Copper(II) Complexes with Diazamesocyclic Ligands Functionalized by Additional Donor Group(s): Syntheses, Crystal Structures and Magnetic Properties. *J. Chem. Soc. Dalt. Trans.* **2001**, No. 5, 729–735. https://doi.org/10.1039/B007424L.

(142) Bu, X. H.; Du, M.; Shang, Z. L.; Zhang, L.; Zhao, Q. H.; Zhang, R. H.; Shionoya, M. Novel Diazamesocyclic Ligands Functionalized with Pyridyl Donor Group(s) - Synthesis, Crystal Structures, and Properties of Their Copper(II) Complexes. *Eur. J. Inorg. Chem.* **2001**, No. 6, 1551–1558. https://doi.org/10.1002/1099-0682(200106)2001:6<1551::AID-EJIC1551>3.0.CO;2-8.

(143) Tuna, F.; Patron, L.; Journaux, Y.; Andruh, M.; Plass, W.; Trombe, J.-C. Synthesis and Magnetic Properties of a Series of Bi-and Tri-Nuclear Complexes of Copper(II) with the Unsymmetrical Tetradentate Schiff-Base Ligand 3-[N-2-(Pyridylethyl)Formimidoyl]Salicylic Acid, H 2 Fsaaep, and Crystal Structures of [{Cu(Hfsaaep)Cl} 2] . *J. Chem. Soc* **1999**, No. 4, 539–545.

(144) Jürgens, E.; Back, O.; Mayer, J. J.; Heinze, K.; Kunz, D. Synthesis of Copper(II) and Gold(III) Bis(NHC)-Pincer Complexes. *Zeitschrift fur Naturforsch. - Sect. B J. Chem. Sci.* **2016**, *71* (10), 1011–1018. https://doi.org/10.1515/znb-2016-0158.

(145) Sathyadevi, P.; Krishnamoorthy, P.; Butorac, R. R.; Cowley, A. H.; Dharmaraj, N. Novel ONN Pincer Type Copper(II) Hydrazide Complexes: An Investigation on the Effect of Electronegativity and Ring Size of Heterocyclic Hydrazides towards Nucleic Acid/Protein Binding, Free Radical Scavenging and Cytotoxicity. *Inorganica Chim. Acta* **2014**, *409*, 185–194. https://doi.org/10.1016/j.ica.2013.09.015.

(146) Yang, L.; Powell, D. R.; Houser, R. P. Structural Variation in Copper(i) Complexes with Pyridylmethylamide Ligands: Structural Analysis with a New Four-Coordinate Geometry Index, T4. *J. Chem. Soc. Dalt. Trans.* **2007**, No. 9, 955–964. https://doi.org/10.1039/b617136b.

(147) Boyce, D. W.; Salmon, D. J.; Tolman, W. B. Linkage Isomerism in Transition-Metal Complexes of Mixed (Arylcarboxamido)(Arylimino)Pyridine Ligands. *Inorg. Chem.* **2014**, *53* (11), 5788–5796. https://doi.org/10.1021/ic500638z.

(148) Shi, Y. C.; Cheng, H. J.; Zhang, S. H. Syntheses and Crystal Structures of Copper Mixed-Ligand Complexes of Multidentate Enaminones and Acetate Anions. *Polyhedron* **2008**, *27* (16), 3331–3336. https://doi.org/10.1016/j.poly.2008.04.057.

(149) Kitajima, N.; Fujisawa, K.; Fujimoto, C.; Hashimoto, S.; Kitagawa, T.; Toriumi, K.; Tatsumi, K.; Nakamura, A. A New Model for Dioxygen Binding in Hemocyanin . Synthesis , Characterization , and Molecular Structure of the μ- 2 : 2 Peroxo Dinuclear

Copper (II) Complexes , z-Pr and Ph). *J. Am. Chem. Soc.* **1992**, *114* (4), 1277–1291. https://doi.org/10.1021/ja00030a025.

(150) Kubas, G. Tetrakis (Acetonitrile) Copper (I) Hexafluorophosphate. *Inorg. Synth.* **1979**, *19*, 90–92. https://doi.org/10.1002/9780470132500.ch18.

(151) Lebœuf, D.; Huang, J.; Gandon, V.; Frontier, A. J. Using Nazarov Electrocyclization to Stage Chemoselective. *Angew. Chemie - Int. Ed.* **2011**, *50*, 10981–10985. https://doi.org/10.1002/anie.201104870.

(152) Noviandri, I.; Brown, K. N.; Fleming, D. S.; Gulyas, P. T.; Lay, P. A.; Masters, A. F.; Phillips, L. The Decamethylferrocenium/Decamethylferrocene Redox Couple: A Superior Redox Standard to the Ferrocenium/Ferrocene Redox Couple for Studying Solvent Effects on the Thermodynamics of Electron Transfer. **1999**. https://doi.org/10.1021/jp991381.

(153) Sheldrick, G. M. SHELXT – Integrated Space-Group and Crystal-Structure Determination. *Acta Crystallogr. Sect. A* **2015**, *71* (1), 3–8. https://doi.org/10.1107/S2053273314026370.

(154) Hübschle, C. B.; Sheldrick, G. M.; Dittrich, B. ShelXle: A Qt Graphical User Interface for SHELXL. *J. Appl. Crystallogr.* **2011**, *44* (6), 1281–1284. https://doi.org/10.1107/S0021889811043202.

(155) Sheldrick, G. M. A Short History of SHELX. *Acta Crystallogr. Sect. A* **2007**, *64* (1), 112–122. https://doi.org/10.1107/S0108767307043930.

(156) Kujime, M.; Fujii, H. Spectroscopic Characterization of Reaction Intermediates in a Model for Copper Nitrite Reductase. *Angew. Chemie - Int. Ed.* **2006**, *45* (7), 1089–1092. https://doi.org/10.1002/anie.200503555.

(157) Scarpellini, M.; Neves, A.; Castellano, E. E.; De Almeida Neves, E. F.; Franco, D. W. A Structural Model for Oxidized Type II Copper Nitrite Reductase with a Polyimidazole Tripodal Ligand. *Polyhedron* **2004**, *23* (4), 511–518. https://doi.org/10.1016/j.poly.2003.09.036.

(158) Halfen, J. A.; Tolman, W. B. Synthetic Model of the Substrate Adduct to the Reduced Active Site of Copper Nitrite Reductase. *J. Am. Chem. Soc.* **1994**, *116* (12), 5475–5476.

(159) Tolman, W. B. A Model for the Substrate Adduct of Copper Nitrite Reductase and Its Conversion to a Novel Tetrahedral Copper(II) Triflate Complex. *Inorg. Chem.* **1991**, *30* (26), 4880. https://doi.org/10.1021/ic00026a005.

(160) Casella, L.; Carugo, O.; Gullotti, M.; Doldi, S.; Frassoni, M. Synthesis, Structure, and Reactivity of Model Complexes of Copper Nitrite Reductase. *Inorg. Chem.* **1996**, *35* (5), 1101–1113. https://doi.org/10.1021/ic950392o.

(161) Arnold, P. J.; Davies, S. C.; Durrant, M. C.; Griffiths, D. V.; Hughes, D. L.; Sharpe, P. C. Copper(II) Nitrite Complexes of Tripodal Ligands Derived from 1,1,1-Tris(2-Pyridyl)Methylamine. *Inorganica Chim. Acta* **2003**, *348*, 143–149. https://doi.org/10.1016/S0020-1693(02)01487-1.

(162) Mondal, A.; Reddy, K. P.; Kundu, S. Phenol Reduces Nitrite to NO at Copper(II): Role of a Proton- Responsive Outer Coordination Sphere in Phenol Oxidation. *J. Am. Chem. Soc.* **2020**, *142*, 1726. https://doi.org/10.1021/jacs.9b11597.

(163) Moore, C. M.; Szymczak, N. K. Nitrite Reduction by Copper through Ligand-Mediated Proton and Electron Transfer. *Chem. Sci.* **2015**, *6* (6), 3373–3377. https://doi.org/10.1039/c5sc00720h.

(164) Halfen, J. A.; Mahapatra, S.; Olmstead, M. M.; Tolman, W. B. Synthetic Analogues of Nitrite Adducts of Copper Proteins: Characterization and Interconversion of Dicopper(I,I) and -(I,II) Complexes Bridged Only by NO2-. *J. Am. Chem. Soc.* **1994**, *116* (5), 4407–4408.

(165) Chuang, W. J.; Lin, I. J.; Chen, H. Y.; Chang, Y. L.; Hsu, S. C. N. Characterization of a New Copper(I)-Nitrito Complex That Evolves Nitric Oxide. *Inorg. Chem.* **2010**, *49* (12), 5377–5384. https://doi.org/10.1021/ic100083b.

(166) Maia, L. B.; Moura, J. J. G. How Biology Handles Nitrite. *Chem. Rev.* **2014**, *114* (10), 5273–5357. https://doi.org/10.1021/cr400518y.

(167) Zhao, Y.; Lukoyanov, D. A.; Toropov, Y. V.; Wu, K.; Shapleigh, J. P.; Scholes, C. P. Catalytic Function and Local Proton Structure at the Type 2 Copper of Nitrite Reductase: The Correlation of Enzymatic PH Dependence, Conserved Residues, and Proton Hyperfine Structure. *Biochemistry* **2002**, *41* (23), 7464–7474. https://doi.org/10.1021/bi0256274.

(168) Fukuda, Y.; Tse, K. M.; Nakane, T.; Nakatsu, T.; Suzuki, M.; Sugahara, M.; Inoue, S.; Masuda, T.; Yumoto, F.; Matsugaki, N.; Nango, E.; Tono, K.; Joti, Y.; Kameshima, T.; Song, C.; Hatsui, T.; Yabashi, M.; Nureki, O.; Murphy, M. E. P.; Inoue, T.; Iwata, S.; Mizohata, E. Redox-Coupled Proton Transfer Mechanism in Nitrite Reductase Revealed by Femtosecond Crystallography. *Proc. Natl. Acad. Sci. U. S. A.* **2016**, *113* (15), 2928–2933. https://doi.org/10.1073/pnas.1604061113.

(169) Ghosh, S.; Dey, A.; Sun, Y.; Scholes, C. P.; Solomon, E. I. Spectroscopic and Computational Studies of Nitrite Reductase: Proton Induced Electron Transfer and Backbonding Contributions to Reactivity. *J. Am. Chem. Soc.* **2009**, *131* (1), 277–288. https://doi.org/10.1021/ja806873e.

(170) Radi, R. Nitric Oxide, Oxidants, and Protein Tyrosine Nitration. *Proc. Natl. Acad. Sci. U. S. A.* **2004**, *101* (12), 4003–4008. https://doi.org/10.1073/pnas.0307446101.

(171) Ferrer-Sueta, G.; Campolo, N.; Trujillo, M.; Bartesaghi, S.; Carballal, S.; Romero, N.; Alvarez, B.; Radi, R. Biochemistry of Peroxynitrite and Protein Tyrosine Nitration. *Chem. Rev.* **2018**, *118* (3), 1338–1408. https://doi.org/10.1021/acs.chemrev.7b00568.

(172) Qiao, L.; Lu, Y.; Liu, B.; Girault, H. H. Copper-Catalyzed Tyrosine Nitration. *J. Am. Chem. Soc.* **2011**, *133* (49), 19823–19831. https://doi.org/10.1021/ja206980q.

(173) Warren, J. J.; Tronic, T. a.; Mayer, J. M.; Bond, S. V. G. Thermochemistry of Proton-Coupled Electron Transfer Reagents and Its Implications. *Chem. Rev.* **2010**, *110* (12), 6961–7001. https://doi.org/10.1021/cr100085k.

(174) Mayer, J. M. PROTON-COUPLED ELECTRON TRANSFER: A Reaction Chemist's View. *Annu. Rev. Phys. Chem.* **2004**, *55*, 363–390. https://doi.org/10.1146/ANNUREV.PHYSCHEM.55.091602.094446.

(175) Yosca, T. H.; Rittle, J.; Krest, C. M.; Onderko, E. L.; Silakov, A.; Calixto, J. C.; Behan, R. K.; Green, M. T. Iron(IV)Hydroxide PKa and the Role of Thiolate Ligation in C-H Bond

Activation by Cytochrome P450. *Science (80-.).* **2013**, *342* (6160), 825–829. https://doi.org/10.1126/SCIENCE.1244373/SUPPL_FILE/YOSCA.SM.PDF.

(176) Lee, N. F.; Malone, J.; Jeddi, H.; Kwong, K. W.; Zhang, R. Visible-Light Photolysis of Corrole-Manganese(IV) Nitrites to Generate Corrole-Manganese(V)-Oxo Complexes. *Inorg. Chem. Commun.* **2017**, *82*, 27–30. https://doi.org/10.1016/j.inoche.2017.05.001.

(177) Shi, K.; Mathivathanan, L.; Boudalis, A. K.; Turek, P.; Chakraborty, I.; Raptis, R. G. Nitrite Reduction by Trinuclear Copper Pyrazolate Complexes: An Example of a Catalytic, Synthetic Polynuclear NO Releasing System. *Inorg. Chem.* **2019**, *58* (11), 7537–7544. https://doi.org/10.1021/acs.inorgchem.9b00748.

(178) Dulong, F.; Pouessel, J.; Thuéry, P.; Berthet, J. C.; Ephritikhine, M.; Cantat, T. Nitrite Complexes of Uranium and Thorium. *Chem. Commun.* **2013**, *49* (24), 2412–2414. https://doi.org/10.1039/c3cc39163a.

(179) Bouchey, C. J.; Tolman, W. B. Involvement of a Formally Copper(III) Nitrite Complex in Proton-Coupled Electron Transfer and Nitration of Phenols. *Inorg. Chem.* **2022**, acs.inorgchem.1c03790. https://doi.org/10.1021/ACS.INORGCHEM.1C03790.

(180) Allmann, R.; Kremer, S.; Kucharzcyk, D. The Crystal Structure and EPR G-Tensors of [Cuterpy(ONO)OH2]NO2 H20. *Inorganica Chim. Acta* **1984**, *85*, 19–21.

(181) Hill, S. J.; Hubberstey, P.; Li, W. Bis (Diimine)Nitritocopper(Ll) Cations : Crystal and Molecular Structures of [Cu(Phen)2(ONO)] BF4 H20 and [Cu(Bipy)2(ONO)]HSO4 {phen = 1,10 Phenanthroline, Bipy = 2,2’-Bipyridine}. *Polyhedron* **1997**, *16* (14), 2447–2453.

(182) Lal, T. K.; Richardson, J. F.; Mashuta, M. S.; Buchanan, R. M.; Mukherjee, R. Synthesis, X-Ray Structure and Properties of a New Nitrite-Bound Copper(II) Complex with 2-(3,5-Dimethylpyrazol-1-Ylmethyl)Pyridine in a CuN4(O) Coordination. *Polyhedron* **1997**, *16* (24), 4331–4336. https://doi.org/10.1016/s0277-5387(97)00201-5.

(183) Komeda, N.; Nagao, H.; Kushi, Y.; Adachi, G.; Suzuki, M.; Uehara, A.; Tanaka, K. Molecular Structure of Nitro- and Nitrito-Copper Complexes as Reaction Intermediates in Electrochemical Reduction of Nitrite to Dinitrogen Oxide. *Bulletin of the Chemical Society of Japan*. 1995, pp 581–589. https://doi.org/10.1246/bcsj.68.581.

(184) Sarkar, B.; Konar, S.; Gomez-Garcia, C. J.; Ghosh, A. Rare Example of U-Nitrito-1-k-2O,O’:2KO Coordinating Mode in Copper(II) Nitrite Complexes with Monoanionic Tridentate Schiff-Base Ligands: Structure, Magnetic, and Electrochemical Properties. *Inorg Chem* **2008**, *47* (24), 11611–11619. https://doi.org/10.1080/00958970802216685.

(185) Jian, F.; Conry, R. R.; Bubacco, L.; Tyeklar, Z.; Jacobson, R. R.; Karlin, K. D.; Peisach, J. Crystal Structure and Electron Spin Echo Envelope Modulation Study of [Cu(II)(TEPA)(NO2)]PF6 (TEPA = Tris[2-(2-Pyridyl)Ethyl]Amine): A Model for the Purported Structure of the Nitrite Derivative of Hemocyanin. *J. Am. Chem. Soc.* **1993**, *115* (6), 2093–2102. https://doi.org/10.1126/science.7.165.272.

(186) Prakash, G. K. S.; Hu, J. Pentafluorobenzoic Acid. In *Encyclopedia of Reagents for Organic Synthesis, (Ed).*; 2006.

(187) Da Silva, G.; Kennedy, E. M.; Dlugogorski, B. Z. Ab Initio Procedure for Aqueous-Phase PKa Calculation: The Acidity of Nitrous Acid. *J. Phys. Chem. A* **2006**, *110* (39), 11371–

11376. https://doi.org/10.1021/jp0639243.

(188) Maeder, M.; King, P. Reactlab. Jplus Consulting Pty Ltd: East Freemantle, WA. Australia 2009.

(189) Manner, V. W.; Markle, T. F.; Freudenthal, J. H.; Roth, J. P.; Mayer, J. M. The First Crystal Structure of a Monomeric Phenoxyl Radical: 2,4,6-Tri-Tert-Butylphenoxyl Radical. *Chem. Commun.* **2008**, *246* (2), 256–258. https://doi.org/10.1039/b712872j.

(190) Porter, T. R.; Capitao, D.; Kaminsky, W.; Qian, Z.; Mayer, J. M. Synthesis, Radical Reactivity, and Thermochemistry of Monomeric Cu(II) Alkoxide Complexes Relevant to Cu/Radical Alcohol Oxidation Catalysis. *Inorg. Chem.* **2016**, *55* (11), 5467–5475. https://doi.org/10.1021/acs.inorgchem.6b00491.

(191) Park, J. Y.; Lee, Y. N. Solubility and Decomposition Kinetics of Nitrous Acid in Aqueous Solution. *J. Phys. Chem.* **1988**, *92* (22), 6294–6302. https://doi.org/10.1021/j100333a025.

(192) Chen, X.; Fuller, M. E.; Franklin Goldsmith, C. Decomposition Kinetics for HONO and HNO2. *React. Chem. Eng.* **2019**, *4* (2), 323–333. https://doi.org/10.1039/c8re00201k.

(193) Astolfi, P.; Panagiotaki, M.; Greci, L. New Insights into the Reactivity of Nitrogen Dioxide with Substituted Phenols: A Solvent Effect. *European J. Org. Chem.* **2005**, No. 14, 3052–3059. https://doi.org/10.1002/ejoc.200500016.

(194) Puthiyaveetil Yoosaf, M. A.; Ghosh, S.; Narayan, Y.; Yadav, M.; Sahoo, S. C.; Kumar, P. Finding a New Pathway for Acid-Induced Nitrite Reduction Reaction: Formation of Nitric Oxide with Hydrogen Peroxide. *Dalt. Trans.* **2019**, *48* (37), 13916–13920. https://doi.org/10.1039/c9dt02834j.

(195) Osako, T.; Ohkubo, K.; Taki, M.; Tachi, Y.; Fukuzumi, S.; Itoh, S. Oxidation Mechanism of Phenols by Dicopper-Dioxygen (Cu2/O 2) Complexes. *J. Am. Chem. Soc.* **2003**, *125* (36), 11027–11033. https://doi.org/10.1021/ja029380+.

(196) Stoll, S.; Schweiger, A. EasySpin, a Comprehensive Software Package for Spectral Simulation and Analysis in EPR. *J. Magn. Reson.* **2006**, *178* (1), 42–55. https://doi.org/10.1016/J.JMR.2005.08.013.

(197) Menges, F. Spectragryph - Optical Spectroscopy Software. 2020.

(198) Pirovano, P.; Magherusan, A. M.; McGlynn, C.; Ure, A.; Lynes, A.; McDonald, A. R. Nucleophilic Reactivity of a Copper(II)-Superoxide Complex. *Angew. Chemie* **2014**, *126* (23), 6056–6060. https://doi.org/10.1002/ange.201311152.

(199) Ribas, X.; Güell, I. Cu(I)/Cu(III) Catalytic Cycle Involved in Ullmann-Type Cross-Coupling Reactions. *Pure Appl. Chem.* **2014**, *86* (3), 345–360. https://doi.org/10.1515/PAC-2013-1104/PDF.

(200) Huffman, L. M.; Stahl, S. S. Carbon-Nitrogen Bond Formation Involving Well-Defined Aryl-Copper(III) Complexes. *J. Am. Chem. Soc.* **2008**, *130*, 9196–9197.

(201) West, M. J.; Fyfe, J. W. B.; Vantourout, J. C.; Watson, A. J. B. Mechanistic Development and Recent Applications of the Chan–Lam Amination. *Chem. Rev.* **2019**, *119* (24), 12491–12523. https://doi.org/10.1021/ACS.CHEMREV.9B00491.

(202) West, M. J.; Fyfe, J. W. B.; Vantourout, J. C.; Watson, A. J. B. Mechanistic Development

and Recent Applications of the Chan–Lam Amination. *Chem. Rev.* **2019**, *119* (24), 12491–12523. https://doi.org/10.1021/ACS.CHEMREV.9B00491.

(203) Tran, B. L.; Li, B.; Driess, M.; Hartwig, J. F. Copper-Catalyzed Intermolecular Amidation and Imidation of Unactivated Alkanes. *J. Am. Chem. Soc.* **2014**, *136* (6), 2555–2563. https://doi.org/10.1021/JA411912P/SUPPL_FILE/JA411912P_SI_005.CIF.

(204) Faggi, E.; Gavara, R.; Bolte, M.; Fajarí, L.; Juliá, L.; Rodríguez, L.; Alfonso, I. Copper(II) Complexes of Macrocyclic and Open-Chain Pseudopeptidic Ligands: Synthesis, Characterization and Interaction with Dicarboxylates. *Dalt. Trans.* **2015**, *44* (28), 12700–12710. https://doi.org/10.1039/C5DT01496D.

(205) Halvagar, M. R.; Solntsev, P. V.; Lim, H.; Hedman, B.; Hodgson, K. O.; Solomon, E. I.; Cramer, C. J.; Tolman, W. B. Hydroxo-Bridged Dicopper(II,III) and -(III,III) Complexes: Models for Putative Intermediates in Oxidation Catalysis. *J. Am. Chem. Soc.* **2014**, *136* (20), 7269–7272. https://doi.org/10.1021/JA503629R/SUPPL_FILE/JA503629R_SI_002.PDF.

(206) Donoghue, P.; Gupta, A. An Anionic, Tetragonal Copper (II) Superoxide Complex. *J. Am. Chem. Soc.* **2010**, *132*, 15869–15871.

(207) Olmstead, W. N.; Margolin, Z.; Bordwell, F. G. Acidities of Water and Simple Alcohols in Dimethyl Sulfoxide Solution. *J. Org. Chem.* **2002**, *45* (16), 3295–3299. https://doi.org/10.1021/JO01304A032.

(208) Bordwell, F. G. Equilibrium Acidities in Dimethyl Sulfoxide Solution. *J. Am. Chem. Soc.* **1988**, *110* (9), 2964–2968. https://doi.org/10.1021/ar00156a004.

(209) Bordwell, F. G.; Algrim, D. Nitrogen Acids. 1. Carboxamides and Sulfonamides. *J. Org. Chem.* **2002**, *41* (14), 2507–2508. https://doi.org/10.1021/JO00876A042.

(210) Olmstead, W. N.; Bordwell, F. G. Ion-Pair Association Constants in Dimethyl Sulfoxide. *J. Org. Chem.* **1980**, *45* (16), 3299–3305. https://doi.org/10.1021/JO01304A033.

(211) Reich, H. Equilibrium pKa Table (DMSO Solvent and Reference) https://organicchemistrydata.org/hansreich/resources/pka/pka_data/pka-compilation-reich-bordwell.pdf.

(212) Connelly, N. G.; Geiger, W. E. Chemical Redox Agents for Organometallic Chemistry. *Chem. Rev.* **1996**, *96* (2), 877–910. https://doi.org/10.1021/CR940053X.

(213) Popowski, Y.; Moreno, J. J.; Nichols, A. W.; Hooe, S. L.; Bouchey, C. J.; Rath, N. P.; Machan, C. W.; Tolman, W. B. Mechanistic Insight into Initiation and Regioselectivity in the Copolymerization of Epoxides and Anhydrides by Al Complexes. *Chem. Commun.* **2020**, *56* (90), 14027–14030. https://doi.org/10.1039/d0cc05652a.

(214) Luke, A. M.; Peterson, A.; Chiniforoush, S.; Mandal, M.; Popowski, Y.; Sajjad, H.; Bouchey, C. J.; Shopov, D. Y.; Graziano, B. J.; Yao, L. J.; Cramer, C. J.; Reineke, T. M.; Tolman, W. B. Mechanism of Initiation Stereocontrol in Polymerization of Rac-Lactide by Aluminum Complexes Supported by Indolide-Imine Ligands. *Macromolecules* **2020**, *53* (5), 1809–1818. https://doi.org/10.1021/acs.macromol.0c00092.

(215) Zhong, X.; Bouchey, C. J.; Kabir, E.; Tolman, W. B. Using a Monocopper-Superoxo Complex to Prepare Multicopper-Peroxo Species Relevant to Proposed Enzyme

Intermediates. *J. Inorg. Biochem.* **2021**, *222*, 111498. https://doi.org/10.1016/j.jinorgbio.2021.111498.

(216) Addison, A. W.; Rao, T. N.; Reedijk, J.; Van Rijn, J.; Verschoor, G. C. Synthesis, Structure, and Spectroscopic Properties of Copper(II) Compounds Containing Nitrogen–Sulphur Donor Ligands; the Crystal and Molecular Structure of Aqua[1,7-Bis(N-Methylbenzimidazol-2′-Yl)-2,6-Dithiaheptane]Copper(II) Perchlorate. *J. Chem. Soc. Dalt. Trans.* **1984**, No. 7, 1349–1356. https://doi.org/10.1039/DT9840001349.

(217) Spek, A. L. PLATON SQUEEZE: A Tool for the Calculation of the Disordered Solvent Contribution to the Calculated Structure Factors. *Acta Crystallogr. Sect. C* **2015**, *C71*, 9–18. https://doi.org/10.1107/S2053229614024929.

(218) Bruker X-Ray Analytical. Madison, WI 2016.

(219) Dolomanov, O. V.; Bourhis, L. J.; Gildea, R. J.; Howard, J. A. K.; Puschmann, H. OLEX2: A Complete Structure Solution, Refinement and Analysis Program. *J. Appl. Crystallogr.* **2009**, *42*, 339–341. https://doi.org/10.1107/S0021889808042726.

(220) Parsell, T. H.; Yang, M. Y.; Borovlk, A. S. C-H Bond Cleavage with Reductants: Re-Investigating the Reactivity Ofmonomeric Mn III/IV - Oxo Complexes and the Role of Oxo Ligandbasicity. *J. Am. Chem. Soc.* **2009**, *131* (8), 2762–2763. https://doi.org/10.1021/JA8100825/SUPPL_FILE/JA8100825_SI_001.PDF.

Appendix[a]

[a]The results presented in this chapter were previously published in:

1. Popowski, Y.; Moreno, J. J.; Nichols, A. W.; Hooe, S. L.; Bouchey, C. J.; Rath, N. P.; Machan, C. W.; Tolman, W. B. Mechanistic Insight into Initiation and Regioselectivity in the Copolymerization of Epoxides and Anhydrides by Al Complexes. *Chem. Commun.* **2020**, *56* (90), 14027–14030.
2. Luke, A. M.; Peterson, A.; Chiniforoush, S.; Mandal, M.; Popowski, Y.; Sajjad, H.; Bouchey, C. J.; Shopov, D. Y.; Graziano, B. J.; Yao, L. J.; Cramer, C. J.; Reineke, T. M.; Tolman, W. B. Mechanism of Initiation Stereocontrol in Polymerization of Rac-Lactide by Aluminum Complexes Supported by Indolide-Imine Ligands. *Macromolecules* **2020**, *53* (5), 1809–1818.
3. Bailey, W. D.; Gagnon, N. L.; Elwell, C. E.; Cramblitt, A. C.; Bouchey, C. J.; Tolman, W. B. Revisiting the Synthesis and Nucleophilic Reactivity of an Anionic Copper Superoxide Complex. *Inorg. Chem.* **2019**, *58*, 4706–4711.
4. Krishnan, V. M.; Shopov, D. Y.; Bouchey, C. J.; Bailey, W. D.; Parveen, R.; Vlaisavljevich, B.; Tolman, W. B. Structural Characterization of the $[CuOR]^{2+}$ Core. *J. Am. Chem. Soc.* **2021**, *143* (9), 3295–3299.
5. Zhong, X.; Bouchey, C. J.; Kabir, E.; Tolman, W. B. Using a Monocopper-Superoxo Complex to Prepare Multicopper-Peroxo Species Relevant to Proposed Enzyme Intermediates. *J. Inorg. Biochem.* **2021**, *222*, 111498.
6. Mandal, M.; Elwell, C. E.; Bouchey, C. J.; Zerk, T. J.; Tolman, W. B.; Cramer, C. J. Mechanisms for Hydrogen-Atom Abstraction by Mononuclear Copper(III) Cores: Hydrogen-Atom Transfer or Concerted Proton-Coupled Electron Transfer? *J. Am. Chem. Soc.* **2019**, *141* (43), 17236–17244.
7. Elwell, C. E.; Mandal, M.; Bouchey, C. J.; Que, L.; Cramer, C. J.; Tolman, W. B. Carboxylate Structural Effects on the Properties and Proton-Coupled Electron Transfer Reactivity of $[CuO_2CR]^{2+}$ Cores. *Inorg. Chem.* **2019**, *58* (23), 15872.

In addition to my main projects in Chapters 2, 3, and 4, I collected various pieces of data that contributed to the results of several publications.[29,31,32,37,213–215] For these projects, I collected X-ray crystal structures, resonance Raman spectra, kinetic runs via UV-visible and stopped-flow UV-visible spectroscopy, and product yields via gas chromatography-mass spectrometry. The results and conclusions from these data are briefly described herein.

A.1 X-ray crystallography

There are several projects in the Tolman group that are funded by the Center of Sustainable Polymers, a National Science Foundation center, that explore the development of aluminum-based catalysts for ring-opening polymerization reactions of bio-renewable resources. Of specific interest to our group, we have designed catalysts that have been used to glean mechanistic details into the initiation steps of polymerization reactions, which are ring-opening nucleophilic attacks from the $[\text{Al-X}]^{2+}$ units (X = Cl, O^{i}Pr, OBn) on cyclic monomers (lactide or cyclic anhydrides).[213,214] I collected and solved a crystal structure of L^3AlCl (Figure A.1, L^3 = tetradentate bipyridine-bis(phenoxide) ligand) which was found to be an active catalyst for the ring-opening copolymerization of epoxides and cyclic anhydrides.[213] The crystal structure revealed two crystallographically distinct molecules of L^3AlCl in the unit cell with geometric parameters for 5-coordinate atoms, τ_5, about the Al atoms of 0.14 and 0.18. A τ_5 value is calculated by the equation $(\alpha - \beta)/60$, where α is the largest valence angle about the central atom and β is the second largest valence angle about the central atom. A value closer to 0 indicates square pyramidal character, where a value closer to 1 indicates trigonal bipyramidal character.[216] The calculated values of the molecules of L^3AlCl indicate square pyramidal character about the Al atoms. Two level B alerts were generated in the CheckCif for this crystal structure: the first alert indicated there was unaccounted electron density and the second alert indicated there was a large Ueq for two carbon atoms. Both alerts arise from small components of disorder that were not modeled and do not impact the structure or analysis. The alerts are due to a disordered chlorine atom in a CH_2Cl_2 molecule and a disordered *t*-butyl substituent on the ligand, respectively.[213]

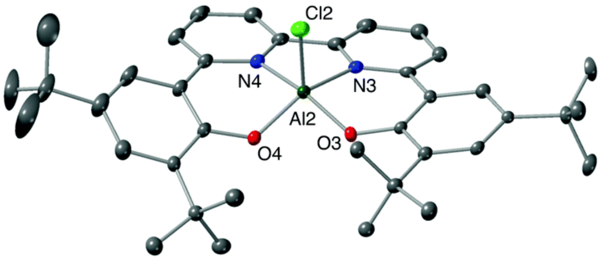

Figure A.1. Representation of the X-ray crystal structure of L^3AlCl, showing non-hydrogen atoms for one of two molecules in the unit cell as 50% ellipsoids. Selected interatomic distances (Å) and angles (deg): Al2–Cl2, 2.174(2); Al2–O3, 1.767(3); Al2–O4, 1.792(3); Al2–N4, 2.020(4); Al2–N3, 2.031(4); O3–Al2–O4, 91.01(14); O3–Al2–N4, 155.4(2); O4–Al2–N4, 87.5(1); O3–Al2–N3, 88.2(1); O4–Al2–N3, 144.6(2); N4–Al2–N3, 79.1(1); O3–Al2–Cl2, 105.9(1); O4–Al2–Cl2, 111.1(1); N4–Al2–Cl2, 97.6(1); N3–Al2–Cl2, 103.1(1). Reprinted with permission from ref. 213. Copyright 2020 Royal Society of Chemistry.

I also collected and helped solve three structures of Al complexes that resulted from reactions where Al-O^{i}Pr complexes were used to ring-open cyclic anhydrides. The crystal structures revealed the products to be L^{3}Al(oCPMA-O^{i}Pr) (o = open, CPMA = carbic anhydride) and L^{4}Al(oCPCA-O^{i}Pr) (L^4 = ^{t}BuSalph, Salph = N,N′-o-phenylenebis[salicylideneimine], CPCA = 2-methyl-norborn-5-ene-2,3-dicarboxylic acid-anhydride) as seen in Figure A.2. and L^{4}Al(oCHCA-O^{i}Pr) (CHCA = 3-methyl-bicyclo[2.2.2]oct-5-ene-2,3-dicarboxylic anhydride) as seen in Figure A.3. The quality of the data for these complexes was poor due to various issues with diffraction resolution, disorder, and/or twinning. Specifically, the crystal quality for L^{3}Al(oCPMA-O^{i}Pr) was poor and diffracted weakly at resolutions greater than 1.5 Å. The quality of the data led us to analyze this structure only for connectivity purposes. The refinement required the SWAT instruction to model solvent disorder. The crystal containing L^{4}Al(oCPCA-O^{i}Pr) was a pseudo-merohedral twin containing 1 molecule of L^{4}Al(oCPCA-O^{i}Pr) and 1 molecule of the starting material, L^{4}AlO^{i}Pr, in the asymmetric unit. The crystal was disordered in a solvent molecule, the supporting salph ligand, and in the starting material, L^{4}AlO^{i}Pr. The structure also has low C–C bond precision due to low resolution data. The various issues with the crystal led us to only analyze the connectivity and did not enable us to distinguish between the enantiomers formed upon anhydride ring-opening. The crystal was refined as a two-component inversion twin. PLATON SQUEEZE[217] was used to model the diffused solvent molecule contribution. EADP, DFIX, SADI, SIMU, and RIGU restraints were used to model disordered atoms. The crystal containing L^{4}Al(oCHCA-O^{i}Pr) was also a pseudo-merohedral twin containing 1 molecule of L^{4}Al(oCHCA-O^{i}Pr) and 1 molecule of the starting material, L^{4}AlO^{i}Pr, in the asymmetric unit. The crystal was similarly disordered in a solvent molecule, the supporting salph ligand, and in the starting material, L^{4}AlO^{i}Pr. The structure also has low C–C bond precision due to low resolution data. The various issues with the crystal led us to only analyze the connectivity and did not enable us to distinguish between the enantiomers formed upon anhydride ring-opening. The crystal was refined as a two-component inversion twin. PLATON SQUEEZE[217] was used to model the diffused solvent molecule contribution. EADP, DFIX, SAME, and SADI restraints were used to model disordered atoms.[213]

Nevertheless, the connectivity details provided key conclusions to the project. The crystals revealed the ring-opened anhydrides bound to the Al atoms through a carboxylate O-atom, and the isopropoxide units were bound to carbonyl C-atoms from the ring-opened anhydrides, confirming nucleophilic attack from the isopropoxide units on the anhydrides. The structures show that the complexes with CPCA and CHCA contain the more sterically hindered carbonyl proximal to the Al center, consistent with nucleophilic attack of the isopropoxide ligand at the less sterically hindered carbonyl. Overall, the crystal structures provided key information on regio- and stereochemical details in the copolymerization mechanism of epoxides and cyclic anhydrides.[213]

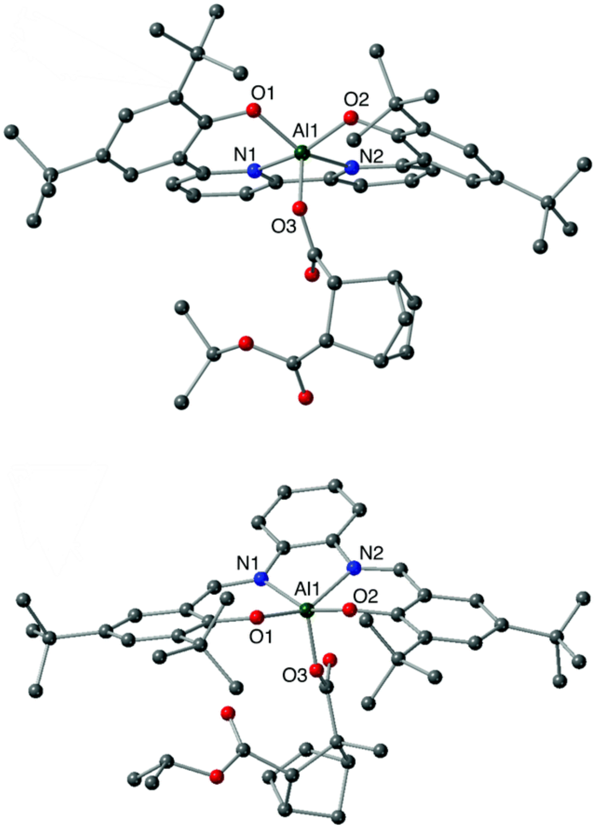

Figure A.2. Ball-and-stick representation of the X-ray crystal structures of (top) $L^3Al(oCPMA\text{-}O^iPr)$ and (bottom) $L^4Al(oCPCA\text{-}O^iPr)$, showing all non-hydrogen atoms as isotropic spheres. Reprinted with permission from ref. 213. Copyright 2020 Royal Society of Chemistry.

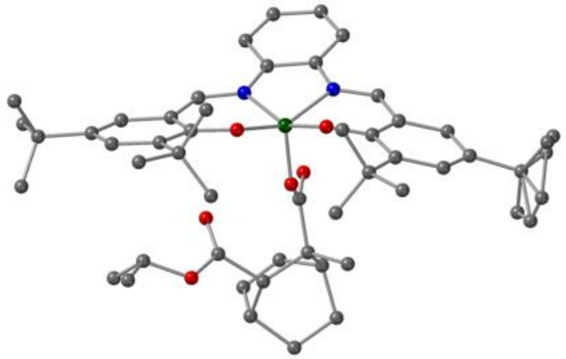

Figure A.3. Representation of the X-ray crystal structure of L^{4}Al(oCHCA-O^{i}Pr), showing all nonhydrogen atoms as isotropic spheres (green = Al, blue = N, red = O, gray = C). Reprinted with permission from ref. 213. Copyright 2020 Royal Society of Chemistry.

In a separate project investigating the stereocontrol of polymerization reactions of *rac*-lactide (LA), an Al complex, L^{5}AlOBn (L^5 = ethylenediamine backbone with flanking indole groups connected at the 2-position), was used to ring-open *rac*-lactide and the resulting complex was crystallized.[214] I collected and solved the crystal structure of the product, which was revealed to be L^{5}Al(oLA-OBn) (Figure A.4). The crystals were comprised of a pair of enantiomers contained in each unit cell, P$_{-1}$ space group, with the two molecules about the inversion center inherent to the space group. The lactide ligand was bound to the Al atom via two O atoms in the lactide unit, one being an alkoxide-O, rendering the geometry of the Al atom octahedral. This structure was a breakthrough in the field as it was a rare example of a high-quality structure of ring-opened lactide bound to a metal complex. Ultimately, the structure revealed the stereochemistry of the initiation of *rac*-lactide by L^{5}AlOBn providing mechanistic information on the synthesis of sustainable polymers.[214]

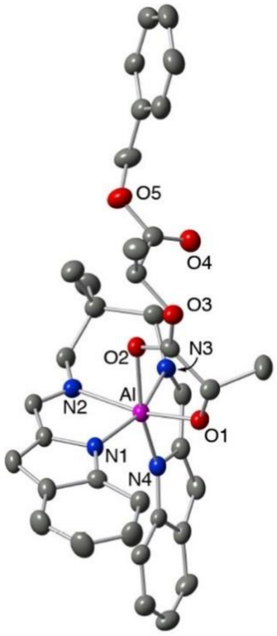

Figure A.4. X-ray crystal structure of L^5Al(oLA-OBn). Only a single enantiomer is shown but the other enantiomer is present in the unit cell. All atoms are shown as 50% ellipsoids and hydrogen atoms are omitted for clarity. Selected bond distances (Å) and angles (deg): (a) Al1–O1, 1.804(2); Al1–N1, 1.932(3); Al1–N2, 2.058(5); Al1–N3, 2.054(1); Al1–N4, 1.945(0); N3–Al1–N1, 160.070(6); N3–Al1–O1, 99.876(5); N3–Al1–O2, 88.536(1); N3–Al1–N2, 79.984(0); N3–Al1–N4, 80.830(1); N2–Al1–N4, 100.140(0); O2–Al1–O1, 81.204(6); N2–Al1–O2, 84.416(7); N4–Al1–O1, 94.002(8); N4–Al1–O2, 167.451(7); N1–Al1–N4, 102.280(5), N1–Al1–N2, 80.091(8); N1–Al1–O2, 89.986(1); N1–Al1–O1, 99.531(4). Reprinted with permission from ref. 214. Copyright 2020 American Chemical Society.

A.2 Resonance Raman spectroscopy

During my time in the Tolman group, I acted as the resonance Raman spectroscopist for multiple years, in which I was able to build and use a new resonance Raman lab. The spectra I collected contributed to the characterization data of multiple complexes, which are described below. In 2019, a new method was found to generate $[LCuOO]^-$ (L = bis(2,6-diisopropylphenylcarboxamido)pyridine): preforming a soluble superoxide salt, K(Krypt)O_2, then adding the superoxide solution to LCuMeCN.[32] Frozen resonance Raman samples containing the complex generated by the new method in MeCN were made in order to confirm the nature of species and ensure the spectrum matched the data collected for the species generated by the previously published method.[206] The spectrum (Figure A.5) revealed a signal at 1102 cm^{-1} assigned as ν(O–O) (λ_{ex} = 660 nm) based on precedence of the previously found isotopically sensitive feature ν(O–O) =1104 cm^{-1} ($\Delta_{16O\text{-}18O}$ = 60 cm^{-1}, λ_{ex} = 647.1 nm).[32,206] This data helped confirm that the new method yielded the intended species, [LCuOO]$^{-}$, so reactivity experiments of the biomimetic complex could commence.[32]

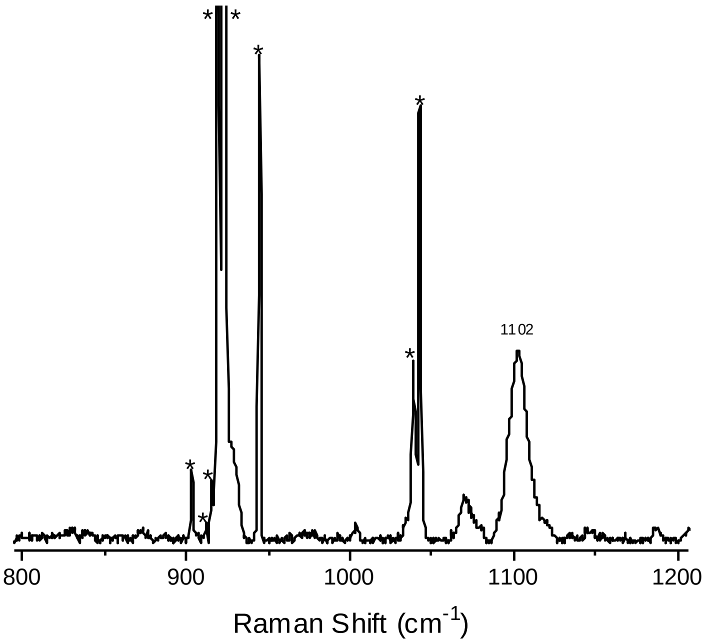

Figure A.5. Resonance Raman spectrum of [K(Krypt)][LCuOO] in MeCN (10 mM). Laser excitation at 660 nm at 77 K (* denotes solvent). Reprinted with permission from ref. 32. Copyright 2019 American Chemical Society.

Investigation of structural data on LCuOR complexes was undertaken to gain a deeper understanding of the oxidized species.[29] Thus, ligand perturbations of L^{2-} and the R group were made to enhance the stability of the complexes, which would make available the use of structural characterization techniques, like X-ray crystallography and NMR spectroscopy, that were thwarted previously. The complexes ^{OMe}LCuOH, $LCuCH_2CF_3$, and $^{OMe}LCuCH_2CF_3$ (^{OMe}L = L with a *para* methoxy substituent on the pyridine ring) were accessed via the 1-electron oxidation of their Cu(II) percursors.[29] I collected resonance Raman spectra on frozen samples of ^{OMe}LCuOH, $LCuOCH_2CF_3$, $^{OMe}LCuOCH_2CF_3$ and LCuOH (for comparison purposes) to identify ν(Cu–O) signals. Previously, an isotopically sensitive feature at 633 cm^{-1} ($\Delta_{16O\text{-}18O}$ = 26 cm^{-1}, λ_{ex} = 515 nm) was found in the resonance Raman spectra of LCu$^{16/18}$OH.[35] This feature was assigned as a ν(Cu–O) signal based on the energy and calculated isotope shift. I recollected this spectrum in THF (Figure A.6) and found the ν(Cu–O) signal at 634 cm^{-1} (λ_{ex} = 561 nm). The spectra that I collected for ^{OMe}LCuOH (Figure A.7), LCuOCH$_2$CF$_3$ (Figure A.8), and ^{OMe}LCuOCH$_2$CF$_3$ (Figure A.9) displayed nearly identical features at 634 cm^{-1} (λ_{ex} = 561 nm) (overlay can be seen in Figure A.10) that we assigned as ν(Cu–O) by analogy. These results were also verified by DFT calculated spectra. Additionally, the spectra of ^{OMe}LCuOH, LCuOCH$_2$CF$_3$, and ^{OMe}LCuOCH$_2$CF$_3$ displayed more overall signals between 400 and 1000 cm^{-1} than LCuOH, which DFT calculations accounted for. The calculated spectrum of LCuOH only contains one ν(Cu–O) signal and four ν(Cu–N) signals. Comparatively, the calculated spectra of ^{OMe}LCuOH, LCuOCH$_2$CF$_3$, and ^{OMe}LCuOCH$_2$CF$_3$ contain multiple ν(Cu–O) signals and similar amounts of ν(Cu–N) signals.[29] Generally, the resonance Raman spectra contribute to the characterization data known for Cu(III) complexes in the literature.

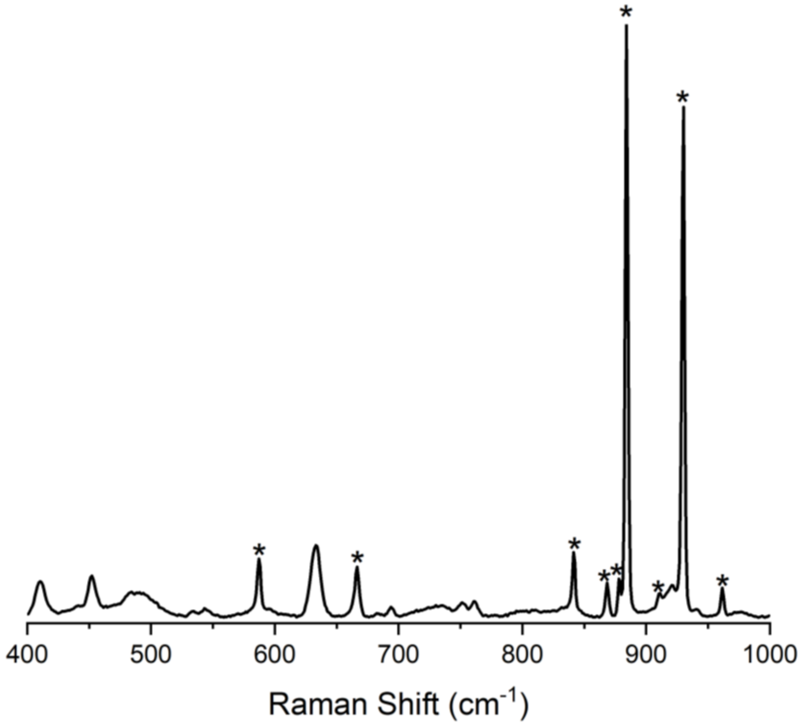

Figure A.6. Resonance Raman spectrum of LCuOH (5 mM in THF, λ_{ex} = 561 nm) at 77 K. ν(Cu–O) signal is assigned as 634 cm^{-1}. Asterisks indicate solvent peaks. Reprinted with permission from ref. 29. Copyright 2021 American Chemical Society.

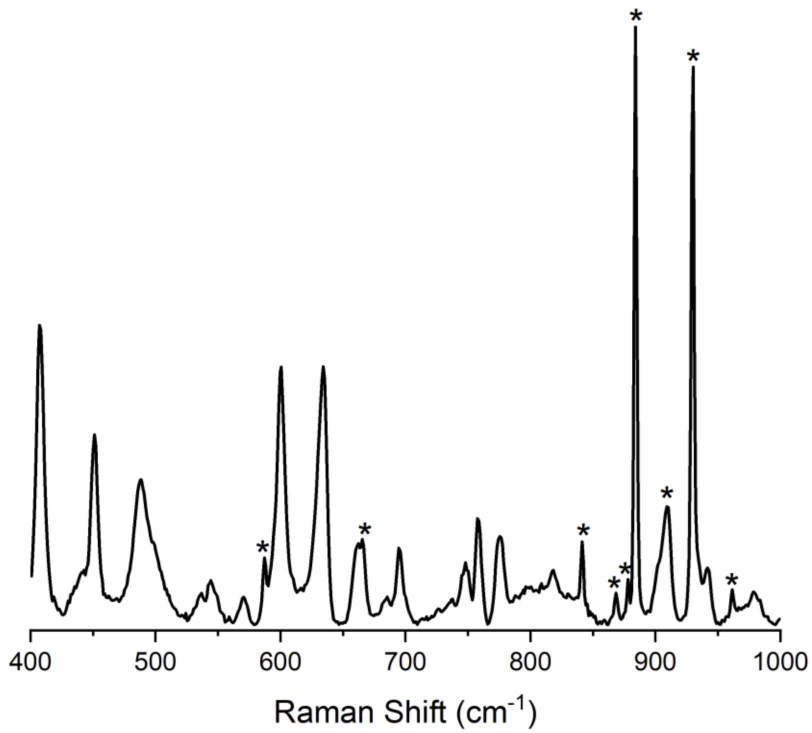

Figure A.7. Resonance Raman spectrum of L^{OMe}CuOH (4.4 mM in THF, λ_{ex} = 561 nm) at 77 K. ν(Cu–O) signal is assigned as 634 cm^{-1}. Asterisks indicate solvent peaks. Reprinted with permission from ref. 29. Copyright 2021 American Chemical Society.

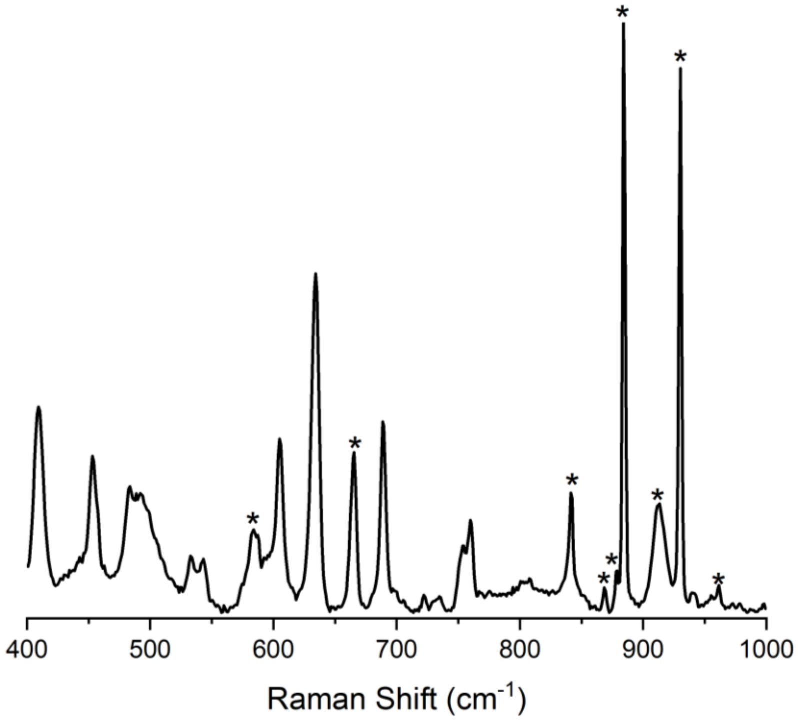

Figure A.8. Resonance Raman spectrum of $LCuOCH_2CF_3$ (4 mM in THF, λ_{ex} = 561 nm) at 77 K. ν(Cu–O) signal is assigned as 634 cm^{-1}. Asterisks indicate solvent peaks. Reprinted with permission from ref. 29. Copyright 2021 American Chemical Society.

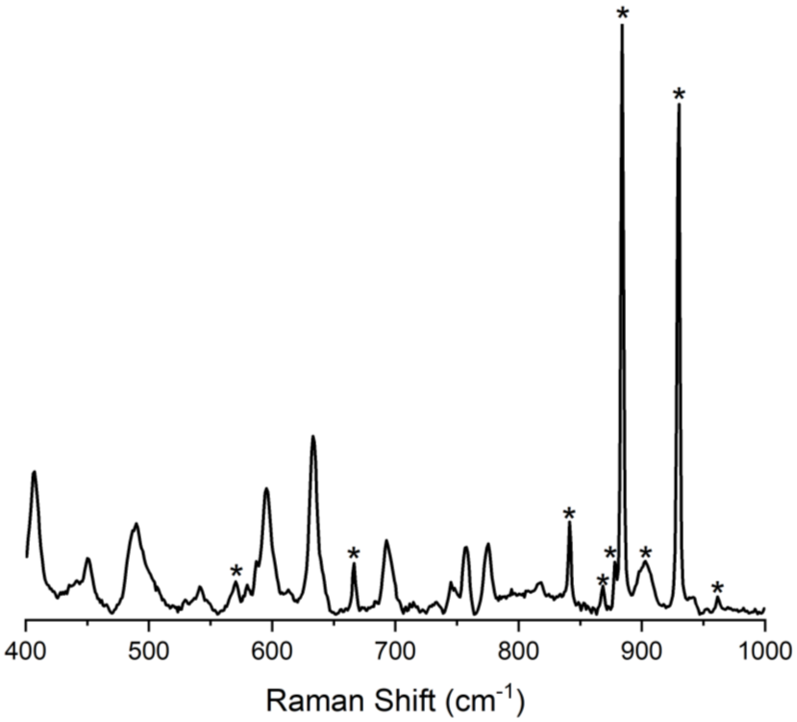

Figure A.9. Resonance Raman spectrum of $L^{OMe}CuOCH_2CF_3$ (4 mM in THF, λ_{ex} = 561 nm) at 77 K. ν(Cu–O) signal is assigned as 634 cm^{-1}. Asterisks indicate solvent peaks. Reprinted with permission from ref. 29. Copyright 2021 American Chemical Society.

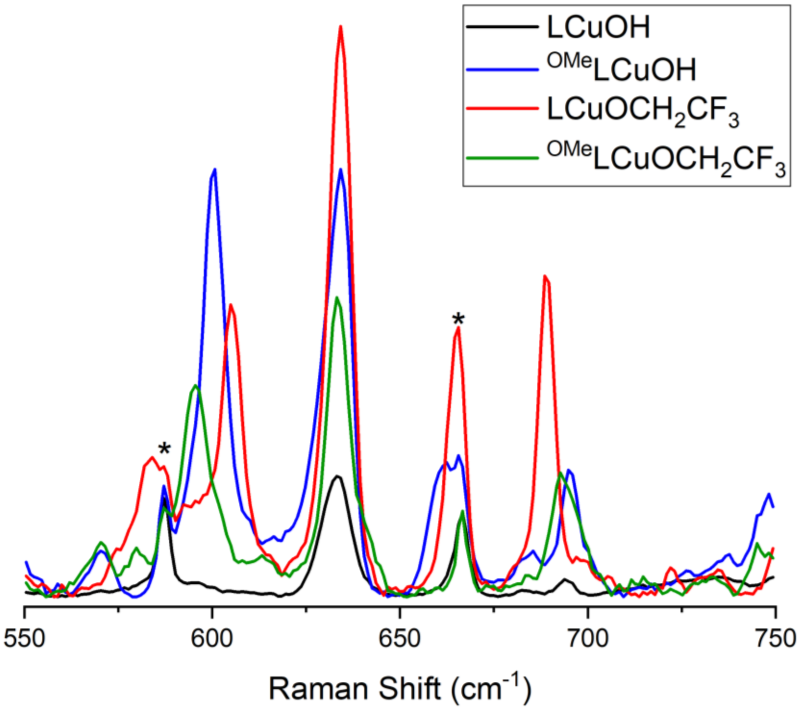

Figure A.10. Overlay of LCuOR resonance Raman spectra between 550 – 750 cm^{-1} (THF, 77 K, λ_{ex} = 561 nm). Signals attributed to ν(Cu–O) for each complex at 634 cm^{-1}. Asterisks indicate solvent peaks. Reprinted with permission from ref. 29. Copyright 2021 American Chemical Society.

Recently, our group published on attempts to generate a multicopper oxygen core that models the proposed "Peroxy Intermediate" (PI) in the mechanism for O_2 reduction by multicopper oxidases.[215] The proposed PI core contains a η^1:η^1:η^2-peroxide bound to one Cu(I) and two Cu(II) ions. Reacting a Cu(II)-superoxide complex with a dicopper(I) complex could theoretically provide a modular route to accessing a PI model. Thus, [K(Krypt)][LCuOO] was reacted with the dicopper(I) complex [(TPBN)Cu_2(MeCN)$_2$][PF_6]$_2$ ([TPBN = *N*,*N*,*N′*,*N′*-tetrakis-(2-pyridylmethyl)-1,4-diaminobutane]) at low temperatures and generation of new UV-vis features were observed. However, a UV-vis titration study revealed only ½ of an eq. of [(TPBN)Cu_2(MeCN)$_2$][PF_6]$_2$ reacts with 1 eq. of [K(Krypt)][LCuOO], inconsistent with a tricopper complex and consistent with 1:1 Cu(II)-superoxide/Cu(I) adduct. A control experiment for observing a 1:1 Cu(II)-superoxide/Cu(I) adduct was performed by reacting [K(Krypt)][LCuOO] with the monocopper(I) complex [(BPMA)Cu(MeCN)][PF_6] (BPMA

= *N*,*N*-bis(2-pyridylmethyl)-methyl-amine) at low temperatures and was also monitored by UV-vis spectroscopy, resulting in a new UV-vis active species.[215] To gain insight into the nature of the oxygen ligand in the new species, I ran resonance Raman spectroscopy on frozen samples of the new species and the isotopically labeled species. The spectrum for the product of the reaction between [K(Krypt)][LCuOO] and [(TPBN)Cu_2(MeCN)$_2$][PF_6]$_2$ revealed two isotopically sensitive features at 771 cm^{-1} ($\Delta_{16O-18O}$ = 40 cm^{-1}) and 562 cm^{-1} ($\Delta_{16O-18O}$ = 22 cm^{-1}), assigned as ν(O–O) and ν(Cu–O) signals, respectively, by their energies and calculated isotope shifts (Figure A.11 (a)). The spectrum for the product of the control reaction between [K(Krypt)][LCuOO] and [(BPMA)Cu(MeCN)][PF_6] also revealed two isotopically sensitive features at 787 cm^{-1} ($\Delta_{16O-18O}$ = 44 cm^{-1}) and 559 cm^{-1} ($\Delta_{16O-18O}$ = 30 cm^{-1}), assigned as ν(O–O) and ν(Cu–O) signals, respectively, as well by their energies and calculated isotope shifts (Figure A.11 (b)). The energy of the ν(O–O) signals for both complexes were found to be different than the starting material, [K(Krypt)][LCuOO] ν(O–O) =1104 cm^{-1},[32] and categorize the oxygen ligands as peroxide ligands. Furthermore, both signals fall below the range of known η^1:η^1-peroxide Raman signals (797 – 849 cm^{-1}) and fall in between the ranges known for η^1:η^2-peroxide (790 – 839 cm^{-1}) and η^2:η^2-peroxide Raman signals (714–765 cm^{-1}). Thus, the products for the reactions between [K(Krypt)][LCuOO] and [(TPBN)Cu_2(MeCN)$_2$][PF_6]$_2$ and [(BPMA)Cu(MeCN)][PF_6] are identified as η^1:η^2-peroxides with η^2 bonding to the (TBPN)Cu(II)/(BPMA)Cu(II) units and an η^1 bonding to the LCu(II) units, where a second weak interaction to the LCu(II) units is possible.[215] In brief, the resonance Raman spectra of the products were integral in determining the nature of the species and confirming the modular reactions are viable synthetic routes to new copper-oxygen species.

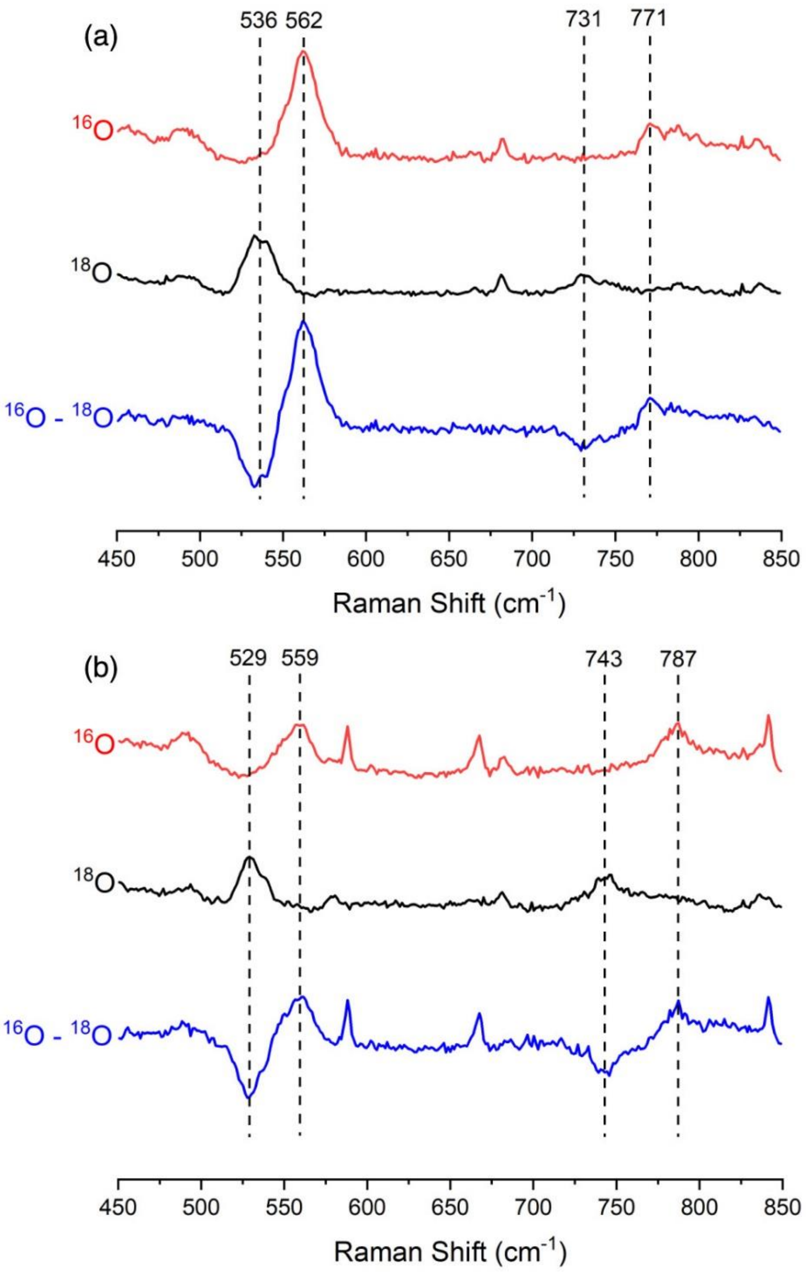

Figure A.11. Resonance Raman spectra of frozen solutions (3:1 THF/MeCN, 8 mM, 77 K, λ_{ex} = 515 nm) of the products of the reaction between [K(Krypt)][LCuOO] (^{16}O, red; ^{18}O, black; difference ^{16}O-^{18}O, blue) with (a) [(TPBN)Cu_2(MeCN)$_2$][PF_6]$_2$ and (b) [(BPMA)Cu(MeCN)][PF_6]. Reprinted with permission from ref. 215. Copyright 2021 Elsevier.

A.3 Experiments performed to augment $LCuO_2CR$ PCET chemistry

In 2019, our group published on the reactive species $LCuO_2CR$, generated by 1-electron oxidations of the corresponding Cu(II) complexes.[31,37] In these publications, the mechanistic details of the proton-coupled electron transfer (PCET) chemistry of LCu*m*CBA (*m*CBA = meta-chlorobenzoate) with O–H and C–H substrates were investigated.[37] I performed multiple experiments to supplement the results and bolster the conclusions. Firstly, I quantified the anthracene formed from the HAA reaction between LCu*m*CBA and 10 eq. of dihydroanthracene (DHA) in 1,2-difluorobenzene (DFB) at -25 °C. GC-MS integrations from the reaction were compared to a standard chromatogram of DHA in order to account for anthracene contamination in the starting material. After this correction, the results indicated that of the 10 eq. of DHA added, 0.6 eq. of DHA were converted to anthracene, a 60% yield of anthracene.[37]

Furthermore, I was able to collect kinetic isotope effects (KIEs) for the reactions between LCu*m*CBA and TEMPO–H and DHA. Previously, my colleague monitored the reaction between LCu*m*CBA and TEMPO–H in THF at -80 °C using stopped-flow UV-vis spectroscopy ($k_2 = 5.8(2) \times 10^3$ M^{-1} s^{-1}). I synthesized TEMPO–D, quantified the deuterium incorporation (95.3%, Figure A.12), and monitored the reaction between LCu*m*CBA and TEMPO–D (25 eq.) via stopped-flow UV-vis spectroscopy (Figure A.13). A global analysis on triplicate kinetic runs was performed using ReactLab Kinetics, taking into consideration the 4.7% TEMPO–H, producing a second-order rate constant of $2.2(5) \times 10^3$ M^{-1} s^{-1} and a normal KIE of 2.6. In order to calculate the KIE for the reaction between LCu*m*CBA and DHA, I monitored the reactions between LCu*m*CBA and DHA (500 eq.) and LCu*m*CBA and DHA-d_4 (500 eq.) in DFB at -25 °C using benchtop UV-vis spectroscopy. A global analysis was applied to one kinetic run for each reaction using ReactLab Kinetics. Second-order rate constants for the reactions between LCu*m*CBA and DHA and LCu*m*CBA and DHA-d_4 were calculated to be 3.2×10^{-2} M^{-1} s^{-1} and 5.2×10^{-4} M^{-1} s^{-1}, respectively, revealing a KIE of 62.[37] Both KIE results indicate HAA takes place in the rate determining step.

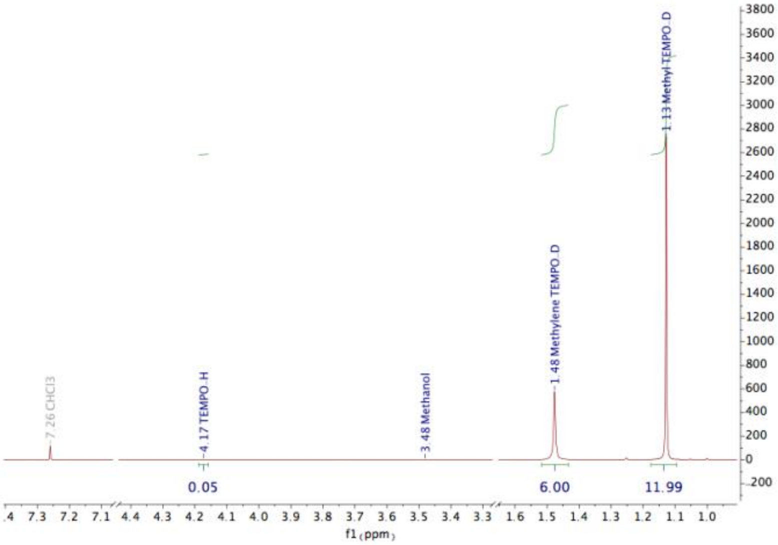

Figure A.12. ^{1}H NMR spectrum of 95.3% incorporated TEMPO–D. Reprinted with permission from ref. 30. Copyright 2019 American Chemical Society.

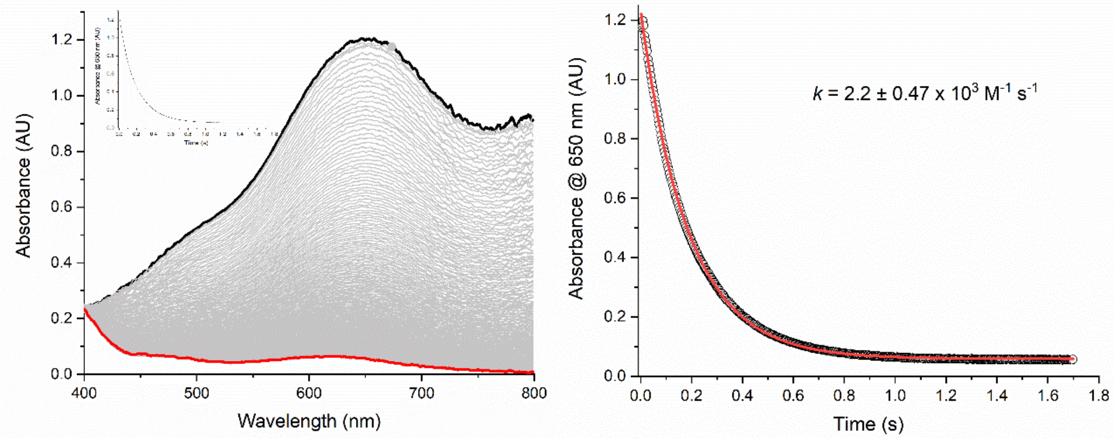

Figure A.13. Representative UV-vis spectra and decay traces of LCu*m*CBA with 25 eq. TEMPO–D (95.3% incorporation) in THF at –80 °C; (left) overlay of experimental UV-vis spectra from t = 0 (black) to t = 1.65 s (red); (right) experimental decay trace at 650 nm (black circles) overlaid with a calculated decay trace at 650 nm (red line). Reprinted with permission from ref. 30. Copyright 2019 American Chemical Society.

Lastly, ligand perturbations of $LCuO_2CR$ by way of the carboxylate ligands were made and the impacts of the perturbations on reactivity with substrates were investigated.[31] Considering the second-order rate constants for the reactions between $LCuO_2CR$ and 2,4,6-tri-*t*-butylphenol in THF at -80 °C, linear relationships were found when plotting the $E_{1/2}$ values of the $LCuO_2CR^{-/0}$ couples vs $\log(k_2)$ and the H–O_2CR pK_a values (H_2O) vs $\log(k_2)$.[31] However, the same relationship was not observed when plotting the $E_{1/2}$ values of the $LCuO_2CR^{-/0}$ couples vs log(k_2) of the reactions between $LCuO_2CR$ and DHA in DFB at -25 °C. A hypothesis proffered was that steric effects confound a relationship between electronic influences induced by the carboxylate ligand and the rate of reactions with DHA.[31] To test this hypothesis, I reacted 1,4-cyclohexadiene (CHD, 200 eq.), a less sterically crowded C–H substrate with a similar BDE to DHA, with LCu*m*CBA in DFB at -25 °C and monitored the reactions using UV-vis spectroscopy. Three kinetic runs were examined and contained an apparent induction period. However, they were fit to a second-order reaction model anyway using the global fitting software, Reactlab Kinetics, and a k_2 of 4.6×10^{-2} M^{-1} s^{-1} was calculated. This rate constant was about 2 times smaller than the rate constant found for the reaction between LCu*m*CBA and DHA under the same conditions, $k_2 = 1.1 \times 10^{-1}$ M^{-1} s^{-1}. Considering only steric effects in the two reactions, we would expect the rate constant for CHD to be larger than for DHA. Thus, it was concluded that steric effects are not likely the cause for a lack of trend between electronic influences induced by the carboxylate ligands and the rate of reactions with DHA.[31] The experiments I performed for these two projects provided further details on PCET reactions of $LCuO_2CR$, which contributes to the deeper understanding of oxidation reactions in general.

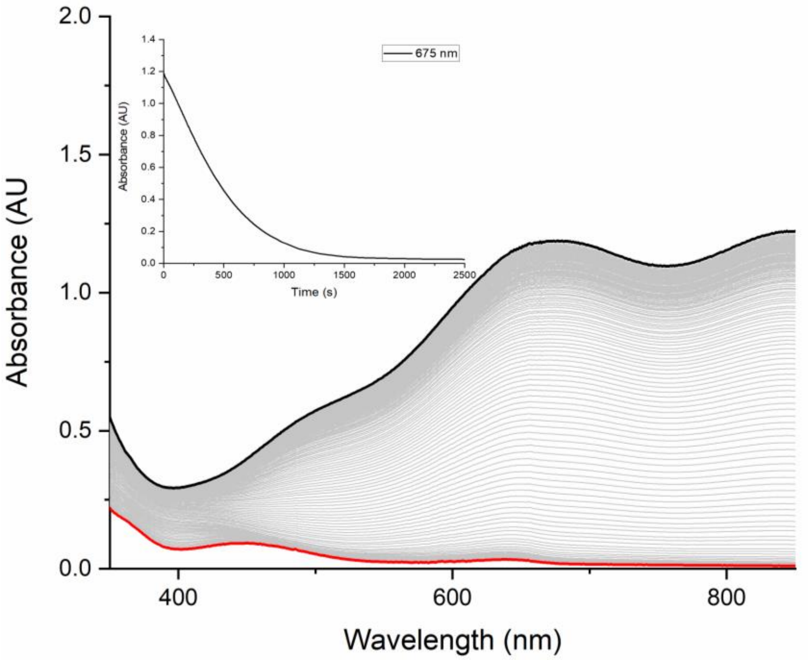

Figure A.14. Overlay of the UV-vis spectra for the reaction of LCu*m*CBA with 200 eq. of CHD in DFB at –25 °C (inset: UV-vis decay trace at 675 nm). Reprinted with permission from ref. 31. Copyright 2019 American Chemical Society.

A.4 Experimental methods

X-ray diffraction measurements were collected with Mo Kα or Cu Kα source and a Bruker X8 diffractometer equipped with a Kappa Apex II CCD using a graphite monochromator and an Oxford Cryostream LT device. Apex III and SAINT software packages were used for data collection and data integration.[218] Structure solutions were performed with SHELXT[153] or SHELXS[155] using OLEX[219] or ShelXle[154] as graphical interfaces. The structures were refined against F2 on all data by full matrix least squares with SHELXL.[155] Resonance Raman spectra were obtained by collecting the collimated Raman scattering using a Plano convex lenses (f = 10 cm or f = 12 cm, placed at an appropriate distance) through a long-pass edge filter (Semrock). The spectra were collected by an Andor Shamrock SR-500i monochromator with a Newton 920 thermo-electrically cooled CCD detector (DU920-BU) (cooled to -90 °C before collection) interfaced with Solis S software or by an Acton AM506 monochromator with a Princeton Instruments liquid N2-cooled (LN-1100PB) CCD detector (cooled to -120 °C before collection) and ST-1385 controller interfaced with Winspec software. The spectra were obtained on frozen samples at 77 K using a 135° backscattering geometry. Excitation at 515 nm, 561 nm, or 660 nm was provided by a Cobolt Jive 150 mW laser, a Cobolt Fandango 50 mW laser, or a Cobolt Flamenco 100 mW laser, respectively. Raman shifts were externally referenced to indene and internally referenced to solvent. Each spectrum was an accumulation of 450 spectra with 4s acquisition times or an accumulation of 900 spectra with 2s acquisition times, resulting in 30 min collections. Spectra were baseline corrected using a multipoint correction process using Origin (2018b) or SpectraGryph.[197] The GC/MS experiments were conducted with an Agilent Technologies 7890A GC system containing an HP-5 ms column (30 m x 0.25 mm) and detected by a 5975C VL MSD. The method used in the experiment consisted of an initial temperature of 80 °C held for 2 mins, then a 20 °C/min ramp to 200 °C, held for 2 min, followed by a 20 °C/min ramp to 300 °C, and held for 2 min. DHA and anthracene eluted at 9.5 and 10.6 mins, respectively. TEMPO–D was obtained by stirring TEMPO–H in CH_3OD (Sigma-Aldrich, 99.5 atom % D) for 3 hours and the solvent was removed in vacuo. This process was repeated once more, twice total. Stopped-flow measurements were performed at –80°C in THF using a TgK CryoStopped-Flow instrument equipped with a Xenon lamp and photodiode array detector in double mixing mode. In a typical experiment, 0.4 mM solutions of $[NBu_4]$[LCu*m*CBA] and acetylferrocenium tetrakis(3,5-bis(trifluoromethyl)phenyl)borate ([AcFc]$[BArF_{24}]$) in THF were initially mixed by syringes A and B, respectively, for 1 second leading to quantitative formation of LCu*m*CBA; this was verified independently by single mixing measurements. Finally, a 5.0 mM solution of TEMPO–D in THF was co-injected via syringe C. Thus, the concentrations of LCu*m*CBA and TEMPO–D before reacting were 0.1 mM and 2.5 mM, respectively. Spectra were recorded every 3.4 ms during the reaction and the cell pathlength was 10 mm. The rate constant for the reaction between LCu*m*CBA and TEMPO–D was obtained by global analysis of the data (400 – 800 nm) using ReactLab Kinetics.[188] The 95.3% deuterium incorporation was accounted for when fitting the data by indicating there was 4.7% (0.1175 mM) of TEMPO–H in the mixture that undergoes a second order reaction with LCu*m*CBA at a rate constant of $5.8(2) \times 10^3$ M^{-1} s^{-1} . With this correction applied, the rate constant for the second order reaction between TEMPO–D and LCu*m*CBA, obtained by global analysis of three separate data sets, is $2.2(5) \times 10^3$ M^{-1} s^{-1}, affording k_H/k_D = 2.6. UV-vis spectra were collected on a HP8453 (190 - 1100 nm) diode array spectrophotometer. Low temperature UV-vis experiments were performed using a Unisoku low-temperature UV-vis cell holder. The substrate d_4-dihydroanthracene was synthesized by a published procedure.[220] A reaction between LCu*m*CBA and 500 eq. of DHA was performed by cooling a UV-vis cuvette under Ar and containing a stir bar and DFB (1.8 mL) to -25 °C. A solution of $[NBu_4]$[LCu*m*CBA] in DFB (0.05 mL, 4 mM) was added to the cuvette. Continuous collection of the UV-vis spectrum was initiated as soon as an aliquot of [AcFc]$[BArF_{24}]$ in DFB (0.05 mL, 4mM) was injected into the cuvette. When the growth of the UV-vis signal attributed to LCu*m*CBA was complete, a DHA solution in DFB (0.1 mL, 1 M) was added to the cuvette and the collection of the spectra continued until full decay of the signal from LCu*m*CBA was observed. The same procedure was adopted for monitoring the reaction between LCu*m*CBA and 500 eq. of d_4-DHA except for the following changes: the cuvette contained 1.6 mL of DFB when cooled, 0.1 mL of a 4 mM DFB solution of $[NBu_4]$[LCu*m*CBA], 0.1 mL of a 4 mM DFB solution of [AcFc]$[BArF_{24}]$, and 0.2 mL of a 1 M DFB d_4-DHA were used for the reaction, and the collection of the spectra was stopped before full decay of the UV-vis signal of LCu*m*CBA. The self-decay of LCu*m*CBA in DFB at -25 °C was also collected by the same procedure as described above but without the addition of substrate. The self-decay of LCu*m*CBA in these conditions was found to have a k_0 of 1 x 10^{-4} s^{-1} and was accounted for when calculating the k_2 values for the reactions between LCu*m*CBA and DHA and d_4-DHA. The kinetics obtained from these reactions were fit to a second order reaction model using global analysis of the data (350 - 850 nm) using ReactLab Kinetics.[188] The k_2 values were calculated to be 3.2 x 10^{-2} M-1 s^{-1} and 5.2 x 10^{-4} M^{-1} s^{-1} for the reaction between LCu*m*CBA and DHA and the reaction between LCu*m*CBA and d_4-DHA, respectively, affording k_H/k_D = 62. 1,4-Cyclohexadiene (CHD) was purchased from Sigma-Aldrich and dried over $MgSO_4$, degassed by three freeze-pump-thaw cycles, and vacuum transferred. The CHD was then brought into a nitrogen-filled glovebox, stored over activated 3 Å molecular sieves, and filtered using a 25 mm diameter, 0.2 mm hydrophobic polytetrafluoroethylene (PTFE) syringe filter before use. A reaction between LCu*m*CBA and 200 eq. of CHD was performed by cooling a UV-vis cuvette under Ar and containing a stir bar and DFB (1.8

mL) to –25 °C. A solution of $[NBu_4][LCu\textit{m}CBA]$ in DFB (0.05 mL, 8 mM) was added to the cuvette. An aliquot of $[AcFc][BArF_{24}]$ in DFB (0.05 mL, 8 mM) was injected into the cuvette. Continuous collection of the UV-vis spectrum was initiated as soon as a CHD solution in DFB (0.1 mL, 800 mM) was added to the cuvette. The collection of the spectra continued until full decay of the signal from LCu*m*CBA was observed. The experiment was repeated two more times under the same conditions. The kinetics obtained from this reaction were analyzed by a global analysis (350 - 850 nm) of the data using ReactLab Kinetics.[188] The average k_2 value was calculated to be 4.6 x 10^{-2} M^{-1} s^{-1}.